CR-86197

07398-6027-R0-00

RADIO/OPTICAL/STRAPDOWN INERTIAL GUIDANCE STUDY FOR ADVANCED KICK STAGE APPLICATIONS

FINAL REPORT

Volume II — Detailed Study Results (Tasks III and IV)
November 1968

PART I DERIVATION OF GUIDANCE AND CONTROL FUNCTIONAL AND PERFORMANCE REQUIREMENTS

Contract No. NAS 12-141

Prepared for
NATIONAL AERONAUTICS AND SPACE ADMINISTRATION
ELECTRONICS RESEARCH CENTER
Cambridge, Massachusetts

TRW
SYSTEMS GROUP
ONE SPACE PARK · REDONDO BEACH, CALIFORNIA

276P.

07398-6027-R0-00

RADIO/OPTICAL/STRAPDOWN INERTIAL GUIDANCE STUDY FOR ADVANCED KICK STAGE APPLICATIONS

FINAL REPORT

Volume II—Detailed Study Results (Tasks III and IV)
November 1968

PART I DERIVATION OF GUIDANCE AND CONTROL FUNCTIONAL AND PERFORMANCE REQUIREMENTS

Contract No. NAS 12-141
Prepared for
NATIONAL AERONAUTICS AND SPACE ADMINISTRATION
ELECTRONICS RESEARCH CENTER
Cambridge, Massachusetts

TRW
SYSTEMS GROUP
ONE SPACE PARK · REDONDO BEACH, CALIFORNIA

FOREWORD

This final report documents the results of the work accomplished under Tasks III and IV of a study of Radio/Optical/Strapdown Inertial Guidance Systems for future unmanned space missions, conducted by TRW Systems for the NASA Electronics Research Center under Contract NAS 12-141. This effort expands and extends the work accomplished previously under Tasks I and II of the same contract.

Volume I summarizes both the results of the study and recommendations reached, including those developed under Tasks I and II. Volume II documents the detailed study results for Tasks III and IV.

CONTENTS

VOLUME II – PART I

CONTENTS (Continued)

CONTENTS (Continued)

CONTENTS (Continued)

VOLUME II – PART II

CONTENTS (Continued)

CONTENTS (Continued)

ILLUSTRATIONS

ILLUSTRATIONS (Continued)

ILLUSTRATIONS (Continued)

ILLUSTRATIONS (Continued)

TABLES (Continued)

ILLUSTRATIONS (Continued)

TABLES

1. INTRODUCTION

This TRW Systems final report documents the detailed results of the work accomplished for the NASA Electronics Research Center under Tasks III and IV of a study of "Radio/Optical/Strapdown Inertial Guidance Systems" for application to future unmanned space missions. This effort extends and refines the work previously carried out and documented under Tasks I and II (see Ref. 1-1).

1.1 STUDY OBJECTIVES

The primary objective of the study was to evaluate the feasibility of the "integrated modular design" concept for the guidance and control of launch vehicles and spacecraft for specified NASA unmanned space missions by means of analysis and design of a responsive system. Detailed study objectives were to:

- Establish the guidance and control requirements for a selected group of future NASA space missions.
- Investigate possible guidance concepts based on the appropriate use of radio, inertial, and optical techniques, with the further objective of establishing the functional role, the capabilities, limitations, and constraints of each of these elements in the overall guidance system concept.
- Define feasible radio/optical/strapdown inertial navigation, guidance and control system "conceptual designs."
- Perform analyses to establish the feasibility (performance) of the selected conceptual designs and to establish the significant performance characteristics of each component and subsystem.
- Perform a "Preliminary modular design" of the radio/optical/strapdown inertial system meeting the composite requirements of all the missions considered, configured so that specific components may be interchangeably combined into given operational systems.
- Perform preliminary design studies of the inertial and electro-optical sensor subsystems and indicate areas of technology where state-of-the-art advances are necessary.

- Establish the performance capabilities of the preliminary modular design and verify by performance analyses that this design meets the performance requirements for each mission.

A "conceptual design" is a functional representation of the guidance and control system component configuration responsive to a given mission, and includes 1) a functional schematic blocking out each component subsystem, the mechanization of the various operational computations, all data flow, and all moding and switching functions, 2) functional descriptions, performance characteristics and development status for each component subsystem.

A "preliminary modular design" is a selection of specific components, meeting the composite requirements for all the missions considered, that may be interchangeably combined into given operational systems for specific applications. Such a design includes 1) block schematics of the complete complement of guidance and control components selected on the basis of the analysis leading to, and the evaluation of, the various conceptual designs, 2) functional descriptions, physical characteristics, performance specifications and interface characteristics for each of the modular elements, 3) specification of the mechanical and electrical interfaces between the modular elements of the system and between the system and the launch vehicle or spacecraft.

The initial objective of Task III was to formulate the requirements for an integral modular guidance, navigation, and control system capable of meeting the mission requirements of Earth low-altitude polar and synchronous equatorial orbits, lunar orbit, Mars orbit, and solar probe (Jupiter flyby) missions. The results of Tasks I and II (see Ref. 1-1) provided the basis for this Task III formulation. Conceptual designs responsive to these requirements were then to be developed. Parametric variations of the performance characteristics of each of the critical components and subsystems of these conceptual designs were to be analyzed so as to permit the establishment of specific performance requirements relative to mission accuracy, fuel expenditure, system reliability, and

weight. These analyses were to be used under the Task IV effort in specifying a "Preliminary Modular Design" and in assuring a technically sound rationale for the equipment specifications.

The study constraints and the scope of work applicable to Task III can be summarized as follows:

a) The representative missions to be studied were

   1) Earth-Polar Orbit-Injection Mission utilizing Atlas/SLV3A/Burner II.

   2) Synchronous Equatorial Earth-Orbit Mission utilizing the Atlas SLV3X/Centaur. (Both direct ascent and parking orbit modes were to be considered.)

   3) Mars Orbiter Mission (Voyager spacecraft launched by Saturn V).

   4) Lunar Orbiter Mission (Lunar orbiter spacecraft launched by Atlas SLV3C/Centaur).

   5) Solar-Probe Mission using Jupiter assist (advanced planetary probe spacecraft launched by Saturn IB/Centaur). (Close-in solar probe (0.1 AU) and out-of-ecliptic missions were to be considered.)

b) The resultant guidance and control instrumentation for a given set of launch vehicles, upper stages, unmanned spacecraft, and missions was to be based upon the boost phase (launch through injection) requirements as well as those for midcourse, target approach, encounter, and deboost into orbit phases of flight.

c) The choice of inertial systems was to be limited to strapdown systems.

d) Only the existing NASA and DOD radio tracking systems were to be considered. (See Ref. 1-1.)

e) Specific control system design concepts and interfaces with existing boost-vehicle control system elements were to be established for each of the launch vehicles. No attempt was to be made to optimize the total control system design.

f) Onboard computational requirements (memory capacity, word length, and execution time) were to be established utilizing the NASA-ERC United Aircraft computer concept described in Ref. 1-2. Sizing studies were to be based on guidance equations previously developed by TRW plus the control equations developed in this study.

g) Computer interfaces were to be defined with respect to the NASA-ERC UAC computer concept defined in Ref. 1-2. Interface hardware (input/output) preliminary design was to be accomplished, but no specific design information for the computer was required.

h) The planet tracker used in the approach guidance system for the Mars mission was to be the NASA-ERC Kollsman sensor currently under advanced development. This is the only practical approach to the problem of planet tracking to have been developed to date.

1.2 STUDY IMPLEMENTATION

In accordance with the objectives stated above, the study effort was divided into two groups:

- Derivation of Guidance and Control Functional and Performance Requirements (Vol. II, Part I)
    - Definition of Mission Characteristics
    - Conceptual Design
    - System Performance Analyses
- Preliminary Modular Design (Vol. II, Part II)
    - System Configuration and Interfaces
    - Subsystem Design Studies
    - Performance Analyses of Modular Design

Vol. II of this report contains the detailed study results obtained under the Task III and IV effort, and is published in two parts as indicated above. The following paragraphs describe briefly the implementation of each of these groups of tasks.

1.2.1 Derivation of Guidance and Control Functional and Performance Requirements (Vol. II, Part I, Secs. 2 Through 5)

1.2.1.1 Mission Characteristics (Sec. 2)

Reference trajectories for the five basic missions were developed by TRW through the use of its Multivehicle N-Stage (MVNS) and Space Navigation Simulation (SNS) precision integration programs (Refs. 1-3 and 1-4). However, for the earth-synchronous-orbit and lunar-orbit

missions, utilizing the Atlas/Centaur launch vehicle, TRW used the trajectories generated under the previous study effort (see Ref. 1-1). New trajectories generated under Task III were:

Reference Powered Trajectories

a) Atlas Burner II – Low altitude earth-circular polar orbit mission launched from WTR.

b) Saturn V – Launch-to-injection trajectory, with earth-injection conditions determined to match the interplanetary trajectories defined below.

c) Saturn IB/Centaur – Launch-to-injection trajectory with earth-injection conditions chosen to match the interplanetary trajectories defined below.

Reference Interplanetary Trajectories

a) Mars Orbiter Missions – Based on trajectory and mission analyses conducted for the Mars 1975 launch opportunity under the TRW Voyager Task D study (Ref. 1-5), Types I and II reference trajectories were selected for the two Mars orbiter missions to be considered. The rationale for selection of the reference trajectories is presented together with a comparison of the heliocentric trajectory characteristics of both mission types in sec. 2 of this report. Injection state vectors for these Mars missions were computed analytically assuming a Saturn V launch vehicle and a 100-n. mi., short-coast, circular parking orbit.

b) Jupiter Flyby Missions – Trajectory data for Jupiter flyby missions during the 1972 launch opportunity were generated for the two specified flyby missions. Reference trajectories were selected and an analytic computation of the injection state vector was performed assuming a Saturn IB/Centaur launch vehicle and a 100-n. mi., short-coast, circular parking orbit.

In addition to generation of the analytic state vector required at injection, the vehicle's position with respect to the sun, earth, target planet, and Canopus was determined for all reference trajectories analyzed. Time histories of these quantities were developed for both the near-earth and heliocentric phases of the missions. Target planet approach geometry was defined for all reference trajectories and capture conditions and orbit orientation geometry were developed for the Mars orbit missions.

Characteristics of the powered flight and interplanetary trajectories are described in sec. 2 of this volume and in subsecs. 2.3 and 2.5 of Ref. 1-1. Characteristics of the Lunar and Mars orbits used for orbit determination performance studies are described in subsec. 4.7.

1.2.1.2 Guidance and Control System Conceptual Designs (Sec. 3)

The implications of mission objectives on variable versus fixed time-of-arrival midcourse guidance schemes were examined for the Mars Type I mission, including tradeoffs between midcourse correction capabilities and requirements, and for the particular guidance schemes.

Earth-based tracking and computation was established as the primary navigation mode for the lunar and interplanetary missions and for the determination of orbital parameters for the Mars orbiter missions.

The booster and spacecraft attitude control system concepts were examined, and a digital system was selected as the most appropriate for the applications considered. Control system interface tradeoff studies were conducted to define the functional interfaces between the ROI guidance and control system and the existing or modified boost vehicle control electronics and thrust vector and reaction control systems.

Special emphasis was placed on studies relating to attitude-fixed versus attitude-maneuvering spacecraft/payloads and gimbaled versus fixed optical sensors. For the translunar and interplanetary coast phases, body-fixed optical sensors were selected as the most appropriate spacecraft attitude references. For the Mars approach guidance, high-precision optical measurements are required. Gimbaled Canopus and planet sensors were chosen as the most appropriate for this application.

For each mission/booster/payload, an overall functional description and schematic of the radio/optical/strapdown inertial guidance system were developed. These include the general signal flow, and moding and switching functions. Detailed mechanization equations were defined as required to define the data flow between subsystems and the operational moding and sequencing functions.

1.2.1.3 Guidance and Navigation Performance Analyses (Sec. 4)

a) Sun-Sighting Time-Updating Technique
The time-updating technique for the multiparking orbit earth-synchronous missions was analyzed in detail. The accuracy of this method and the impact on overall system accuracy were assessed.

b) Powered Flight Performance Analysis
For those missions in which the guidance, navigation, and control system under study has prime control over the boost and injection phase, the GEAP II error analysis program (Ref. 1-6) was used to evaluate injection accuracy and to establish the requirements for midcourse velocity corrections. Parametric tradeoff studies involving strapdown inertial instrument quality, and prelaunch azimuth alignment errors, were performed. Midcourse correction, deboost maneuver, and orbital transfer maneuver accuracies were also evaluated.

c) Interplanetary and Approach Navigation Analysis
The SVEAD program (Ref. 1-7) for estimating navigation accuracy was modified to give it the capability of handling closed orbits around Mars. The analyses made earlier under Task II for the Mars mission were extended both to incorporate variations in optical sensor accuracies and to examine the implications of Type I versus Type II trajectories.

1.2.1.4 Control System Performance Analyses (Sec 5)

Bending modes were generated for the Saturn V/Voyager vehicle configuration, and existing bending data, propellant sloshing data, aerodynamic and mass properties data, and thrust vector control characteristics for each launch vehicle were assembled for use in subsequent control system analyses (see apps. C, D, E).

Stability margins of the linear control system for the first stages of the selected boost-vehicle configurations were determined (see app. A). A comparison was made between the use of first-stage rate gyros and upper-stage gyros, and the digital compensation required under these conditions established. Stability margins for the Voyager spacecraft were also determined.

Coast-flight attitude-reference acquisition, maneuvers, and normal mode operations were analyzed.

1.2.2 Preliminary Modular Design (Vol. II, Part II, Secs, 6 Through 11)

Preliminary modular designs were developed for each mission based on the conceptual designs. Interface definitions were established for the onboard computer; the control system; and the telemetry, tracking, and command system. Detailed equipment descriptions and specifications were developed for the electro-optical sensors and the inertial reference unit.

1.2.2.1 System Configuration and Interfaces (Sec. 6)

a) Modularity Concept
An equipment modularity concept for the total radio/optical/strapdown inertial guidance system was established in accordance with the basic ROI Study objectives. For each of the missions, TRW established the equipment utilization concept, and defined the interconnections and interfaces of the various units comprising the system.

b) Vehicle Interfaces and Mechanical Mounting Considerations
Physical locations and interconnections of the modular radio/optical/strapdown inertial guidance system components were established for each of the five launch vehicle/mission combinations, considering the optical sensor line-of-sight requirements and other location and mounting constraints. Interfaces with existing vehicle control system elements were established in accordance with the control system conceptual and modular design studies.

c) Guidance Equipment Mechanical Interface and Packaging Considerations
Sensor mounting provisions (necessary for adequate mounting stability) were established including the requirements for precision navigation base assemblies. An electronics packaging modular design concept was also established.

d) Thermal Design Considerations
For each mission, the expected thermal environment conditions and constraints were established for the guidance and control equipment at the appropriate location in the launch vehicle, upper stage, or spacecraft. A survey was conducted to establish the approximate operating temperature range for the most critical optical sensors, and thermal control

concepts established to the extent possible using available design data on various boost vehicles and spacecraft. (See Appendix F)

Temperature control requirements and concepts were established for such units as the IRU, where the required performance can be achieved only through precise thermal control of critical elements.

1.2.2.2 Onboard Computational Elements (Sec. 7)

Onboard computational requirements (memory size, word length, and speed requirements) were established for the NASA-ERC UAC computer concept (Ref. 1-2). These studies were based on equations previously developed by TRW for the LM Abort Guidance System (attitude reference navigation computations) (Ref. 1-8), Advanced Centaur Studies (steering and guidance computations) (Ref. 1-9) plus the control equations developed in this study.

Major emphasis was placed on defining in detail the I/O interfaces between the computer and the electro-optical sensors, the inertial reference unit, the control system components, and the telemetry, tracking and command subsystems. A conceptual design of a computer interface unit (CIU) was developed providing interface compatibility with the NASA-ERC UAC Advanced Kick Stage Guidance Computer (Ref. 1-2). A reliability estimate for this computer was developed for use in mission reliability studies.

1.2.2.3 Control System Design (Sec. 8)

Tradeoffs were made between control system digital autopilot equation complexity and computational-time and memory-storage requirements. Several digital compensation filters were considered to determine the cost of added flexibility in the digital control system.

The interface between the computer and the control system hardware was defined with considerations given to signal levels issued to the thrust-vector actuation system and to the receipt of signals from interfacing gyro packages. An evaluation was made of the signal mixing requirement, either within or outside the computer for differential roll control; the problem of interfacing with a varying number of boost-vehicle engines was also addressed.

Functional schematics of the Atlas/Centaur, Saturn V/Voyager, and Saturn IB/Centaur digital control systems were generated showing signal flow, and moding and switching functions.

1.2.2.4 Electro-Optical Sensor Designs (Sec. 9)

The optical sensors selected under Tasks I and II (Ref. 1-1) were reviewed both in light of recent state-of-the-art developments and of new requirements resulting from present mission specifications. Specifically, the applicability of gimbaled Canopus and planet approach sensors and the use of a very narrow field sun sensor were considered.

Based on this review, TRW chose a set of sensors appropriate to the study effort and established a configuration for each mission. Sensor specifications were prepared covering functional description, accuracy, physical performance, and reliability. Emphasis was placed both upon a preliminary description of data interface characteristics and upon the accuracy of the sensor configuration for the Mars orbit mission necessary for support of the guidance accuracy studies. The state of development of each of the sensor elements was evaluated.

For each sensor required by the several missions, a preliminary design was generated using available data on existing equipment, where applicable, plus additional preliminary design effort as required. The following characteristics were established for each sensor:

a) Sensor operating modes

b) Sensor accuracy

c) Final data interface characteristics

d) Weight, dimensions, electrical power requirements

e) Sensor reliability models and numerical parameters

f) Mechanical and electrical mounting characteristics consistent with required physical interchangeability

g) Physical description consisting of a preliminary design drawing for each sensor.

1.2.2.5 Inertial Reference Unit (Sec. 10)

A preliminary design was generated of a strapdown IRU meeting the performance requirements of the several missions based on the previous studies carried out under Tasks I and II (see Ref. 1-1). The following characteristics were established for this unit:

a) Sensor and electronics accuracy including environmental sensitivities (linear and rotational acceleration and vibration environments).

b) Data interface characteristics

c) Weight, dimensions, electrical power requirements

d) Mechanical mounting characteristics

e) Mechanical electrical packaging and thermal control concepts

f) Reliability estimate.

1.2.2.6 Performance Characteristics of Modular Design (Sec. 11)

A performance analysis summary for the preliminary modular design was established based on the recommended sensor selections and specifications, demonstrating that the preliminary modular design satisfies the guidance and control requirements for the five missions studied. The overall system performance characteristics were related to trajectory accuracy and fuel required for correction of guidance, navigation and control errors.

Weight, power, and total failure-rate estimates were made for each of the elements comprising the modular system and the results used to estimate the overall system reliability, weight, and power for each of the five missions considered.

1.3 DEFINITION OF TERMS

Certain of the definitions pertaining to the missions, the launch vehicle, mission events, and trajectories used throughout this report are summarized below.

1.3.1 Missions

In general, the term "mission" is used in this report to encompass and describe the events which are associated with directing the launch vehicle or the spacecraft from the earth and which terminate with the accomplishment of the mission objectives. In the analysis of the various missions described in the ROI Study, the following terms are used:

Synchronous Earth Orbit Mission	In the synchronous earth orbit mission, the launch vehicle is used to place the satellite payload into an earth-synchronous (24-hr period) equatorial orbit at a desired longitude. The injected payload (satellite) is assumed to have orbit trim and stationkeeping capability.
Orbiter Missions	In an orbiter mission, approximately at the time when the spacecraft is closest to the target body (moor or planet), its trajectory is deliberately altered by a propulsive maneuver so that it remains in an orbit about the target body as a satellite.
Solar Probe Mission	In a solar probe mission the spacecraft is injected into a heliocentric orbit that passes within a specified distance of the sun. This is an untargeted mission requiring no trajectory alterations subsequent to injection.
Flyby Mission	In a flyby mission, the spacecraft passes close to the target planet. No propulsion forces are employed to alter the trajectory so as to remain in the vicinity of the target planet. The spacecraft departs from the region of the target planet, although its trajectory will have been perturbed.
Solar Probe with Planetary Swingby	In this type of mission the spacecraft passes close to a planet with the purpose of significantly altering the spacecraft trajectory. After departure from the target planet, the spacecraft continues on a heliocentric trajectory to within a prescribed distance from the sun. No propulsive forces are employed to

Solar Probe with Planetary Swingby (Continued)	alter the trajectory in the vicinity of the target planet. For a given distance of closest approach to the sun, this technique may be used to significantly reduce the launch vehicle ΔV requirements, usually at the expense of considerably longer mission durations.

1.3.2 Vehicle Terms

Launch Vehicle	The launch vehicle includes the multistage boost vehicle which injects the spacecraft into the desired trajectory and includes all hardware up to the interface where the spacecraft is mated and the payload shroud attaches which protects the spacecraft. Generically, the launch vehicle system also includes all appropriate ground support and test equipment.
Kick Stage	For the purposes of this study, "kick stage" refers to the final powered stage of the launch vehicle (the payload spacecraft is assumed to have only limited velocity capability for incremental orbit corrections). The kick stage is assumed to provide complete three-axis guidance, navigation and control capability for all launch vehicle stages except for the Saturn V (Mars orbiter mission).
High Energy Upper Stage (HEUS)	This is a particular kick stage concept using an advanced propulsion system burning high-energy propellants such as H_2/F_2. Typical gross weight is 3200 kg. The thrust to weight ratio is approximately 1.
Spacecraft	The spacecraft system encompasses the payload itself and all its component subsystems, the science payload, the adapter which is mounted to the kick stage, and limited propulsion capability for orbital corrections.

Launch Operations System	The launch operations system does not include any flight hardware, but constitutes the operational responsibility for supporting and conducting the launch of the combined launch vehicle and spacecraft through the separation of the spacecraft from the launch vehicle.
Mission Operations Systems	Operational responsibility for supporting and conducting the mission after the spacecraft is separated from the launch vehicle is borne by the mission operations system.

1.3.3 Mission Events

In the analysis of the various mission events described in the ROI Study, the following terms are used:

Prelaunch	Collectively, all events before liftoff.
Launch	Collectively, all events from liftoff to injection.
Liftoff and Ascent	Departure of the combined launch vehicle-spacecraft from the ground and ascent to a parking orbit of specified altitude (typically 185 km (100 n. mi).
Injection (synchronous earth orbit mission)	Thrust termination of the kick stage, placing the kick stage/payload into a transfer trajectory to synchronous altitude from the parking orbit or, alternately, into the final synchronous earth orbit.
Injection (lunar or interplanetary mission)	Thrust termination of the lower stages of the launch vehicle, placing the kick stage/payload into an interplanetary or translunar trajectory, from the parking orbit.
Separation (shroud)	Detachment of the nose fairing from the launch vehicle during ascent.
Separation (spacecraft)	Detachment of the spacecraft from the spacecraft kick stage adapter after injection.

Orientation Maneuver	A programmed alteration of the injection stage or spacecraft attitude to cause it to return to a desired orientation such as the cruise orientation.
Midcourse Trajectory Correction Maneuver	A propulsive maneuver performed to compensate for inaccuracies or perturbations so as to redirect the spacecraft toward the intended aiming point. Generally, it requires orientation to a specific attitude, operation of the rocket engine, and reorientation to the cruise attitude. The time of this maneuver is during the interplanetary or translunar flight, but not necessarily at the midpoint.
Encounter	Generally, encounter encompasses events occurring when the spacecraft is near the target planet. Specifically, it refers to the time when the spacecraft is at its point of closest approach (periapsis).
Orbit Insertion	The propulsive braking maneuver by which the (orbiter) spacecraft trajectory at the target planet is changed from approach (hyperbolic) to orbital (elliptical).

1.3.4 Trajectory Terms

In discussing the trajectories possible for the various missions of the ROI Study, the following terms are used:

Direct Trajectory	An interplanetary trajectory from the earth to a target planet, in which no intermediate planets (or satellites) are approached closely enough to significantly influence the trajectory.
Swingby Trajectory	An interplanetary trajectory from the earth to a target planet, in which an intermediate planet is passed sufficiently closely to exploit the effect of its gravitational attraction. This exploitation may provide reduced mission duration, reduced launch energy, or an opportunity for scientific observations of the intermediate planet.

Launch Opportunity	The time during which trajectories to a target planet may be initiated from the earth, with reasonable launch energies. A launch opportunity is usually identified by the year in which it occurs, and the target planet.
Launch Period	The space in arrival date-launch date coordinates in which earth-planet trajectories are possible in a given launch opportunity; specifically, the number of days from the earliest possible launch date to the latest.
Launch Window	The time in hours during which a launch is possible on a particular day.
Geocentric (heliocentric, planetocentric)	Described or measured with respect to inertial coordinates centered with the earth (sun, planet). Pertaining to the portion of the flight in which the trajectory is dominated by the gravitation of the earth (sun, planet).
C3, Launch Energy, Injection Energy	Twice the geocentric energy-per-unit mass, of the injected spacecraft. This is equivalent to the square of the geocentric asymptotic departure velocity.
Asymptote	The line that is the limiting position which the tangent to a hyperbolic (escape) trajectory approaches at large distances from the attracting center.
DLA	Declination of the outgoing geocentric launch asymptote.
ZAL	Angle between the outgoing geocentric asymptote and the sun-earth vector.
ZAP	Angle between the incoming planetocentric asymptote (at the target planet) and the planet-sun vector.

ZAE	Angle between the incoming planetocentric asymptote (at the target planet) and the planet-earth vector.
V_∞ or V_{HP}	Planetocentric asymptotic approach velocity.
Parking Orbit	An unpowered, geocentric, approximately circular orbit, separating the powered portions of the launch and injection sequence.
Type I, Type II Interplanetary Trajectories	Type I transfers are defined as those in which the vehicle traces a central angle of less than 180° about the Sun between departure from the Earth and arrival at the planet. In Type II transfers, the angle is greater than 180°.

1.3.5 Coordinate Systems

The various coordinate systems used in specifying performance requirements and powered flight performance analysis results obtained during the ROI Study are defined as follows:

ECI (Earth-Centered-Inertial)	This is a right-handed coordinate system, in which Z lies along the earth's polar axis and X and Y lie in the earth's equatorial plane. The X-axis passes through the Greenwich meridian or in the direction of the Vernal Equinox at the time of launch, (specified in text).
RTN (Radial-Tangential-Normal)	A right-handed orthogonal coordinate system in which R lies in the direction of the nominal position vector from the center of the earth, and N lies in the direction of the orbital angular momentum. T forms a right-handed orthogonal set with R and N.
(X, Y, Z) Selenographic	Moon-Centered Inertial Coordinates. This is a right-handed orthogonal coordinate system in which Z lies along lunar polar axis, and X, Y lie in the lunar equatorial plane with X passing through zero lunar longitude (Sinus Medii).

$\bar{B} \cdot \bar{R}$, $\bar{B} \cdot \bar{T}$	For a given interplanetary trajectory, the impact parameter vector $\bar{B}$ specifies in which direction from the planet and what distance the approach asymptote lies. $\bar{B}$ is commonly expressed in components $\bar{B} \cdot \bar{R}$ and $\bar{B} \cdot \bar{T}$, where $\bar{R}$, $\bar{S}$, $\bar{T}$ are a right-hand set of mutually orthogonal unit vectors aligned as follows: $\bar{S}$ is parallel to the planet centered approach asymptote, $\bar{T}$ is parallel to the plane of the ecliptic and positive eastward, and $\bar{R}$ completes the set and has a positive southerly component.

REFERENCES

1-1 "Radio/Optical/Strapdown Inertial Guidance Study for Advanced Kick Stage Applications," Final Report, TRW Document No. 07398-6017-R000, 30 June 1967.

1-2 "Specification for the NASA-ERC UAC Advanced Kick Stage Guidance Computer," (Rough Draft), United Aircraft Document No. SCS 2260B, no date.

1-3 "Digital Computer Program for General Missile Dynamics Simulation (N-Stage), Summary of Equations;" TRW Systems Report No. 9830.4-22, 11 December 1961.

1-4 D. C. Leonard, "The TRW Space Navigation Simulation Program, A Descriptive Survey," TRW Systems Report No. 9990-6987-TU-000, August 1965.

1-5 "Voyager Spacecraft Phase B, Task D, Final Report," prepared by TRW Systems for NASA-MSFC, October 1967.

1-6 D. F. McAllister and J. C. Wilcox, "Digital Computer Program for a Generalized Inertial Guidance System Error Analysis, Version II (GEAP II)," TRW Document No. 08768-6009-T000, 11 May 1967.

1-7 W. M. Lear, "SVEAD Users Manual," TRW Systems Report No. 7221.11-10, 28 April 1967.

1-8 LM AGS Programmed Equations Document, Flight Program 3," TRW Systems Report No. 05952-6201-T000, May 1968.

1-9 "Centaur Explicit Guidance Equation Study, Final Report," TRW Systems Report No. 08768-6002-R000, 17 January 1967.

2. MISSION CHARACTERISTICS

2.1 INTRODUCTION

The five basic missions to be investigated under Task III of this study determined the specific launch vehicle/payload combinations described in this section. Table 2-I summarizes the mission-related data pertaining to the launch vehicles and the location of the Radio/Optical/Strapdown Inertial Guidance System (ROI) for each of these missions. The table also delineates the specific TRW assumptions made relative to the guidance regime.

Those specific mission characteristics added to Task III or different from those used in the Tasks I and II portions of the overall study are examined in detail in the following subsections. However, the earth-synchronous satellite and lunar orbiter missions are substantially the same as those used in Tasks I and II; descriptions of their characteristics are contained in subsecs 2.3 and 2.5 of Ref. 2-1.

2.2 EARTH LOW-ALTITUDE POLAR-ORBIT MISSION

The earth low-altitude polar-orbit mission typifies one that might be used for earth resources studies and was added to the repertory of the basic Tasks I and II missions for more complete coverage of the spectrum of possible unmanned space missions. This study assumed that the orbiting satellite payload is capable of correcting for orbit-insertion errors. Typically, this ΔV capability can be on the order of 10 to 20 m/sec. The modular guidance system must then provide the guidance function from launch through orbit insertion with accuracy sufficient to ensure that the payload ΔV capability is not exceeded.

For this mission, the Atlas/Burner II launch vehicle is assumed to be launched from the Western Test Range (WTR). The Atlas stages inject the Burner II/payload combination into a coast up to the apogee altitude of 927 km. At that altitude the Burner II provides the velocity increment for circularizing the payload orbit. The actual sequence of events is summarized in Table 2-II. Basic data used to define the launch and injection trajectory and this sequence of events were obtained from Refs. 2-2 through 2-5.

TABLE 2-I

RADIO/OPTICAL/STRAPDOWN INERTIAL TASK III MISSION SUMMARIES

Mission	Trajectory Characteristics	Booster	Guidance Package Location	Approximate Payload Weight	Guidance Regime
Earth Low-Altitude Polar Orbit	WTR Launch; ~927 km near polar circular orbit	Atlas SLV-3A/ Burner II	Burner II	2,500	Launch through insertion of payload into desired earth orbit (payload assumes orbit trim and stationkeeping functions after separation from last booster stage)
Earth-Synchronous Orbit a) Direct Ascent b) Parking Orbit Ascent	Same as used in Tasks I and II (See Ref. 2-1)	Atlas SLV-3C/ Centaur	Centaur	400	
Lunar Orbiter	Same as used in Tasks I and II	Atlas SLV-3X/ Centaur	Payload	2,000	Launch through insertion into final desired selenocentric or areocentric orbit, including all midcourse corrections and orbit change maneuvers
Mars Orbiter, 1975 a) Type I Trajectory b) Type II Trajectory	Saturn V injects spacecraft with desired C_3 into Type I or Type II interplanetary trajectory; spacecraft performs M/C and deboost into 1100 x 10,000-km orbit and subsequent injection into 500-km orbit	Saturn V	Payload	40,000	
Jupiter Flyby a) 0.1 — AU Probe b) Cross Ecliptic Probe	S-IB/Centaur injects spacecraft onto a high-energy interplanetary trajectory (C_3 = 121 km^2/sec^2, T = 464 days) post Jupiter trajectory determined by targeted $\vec{B} \cdot \vec{T}$, $\vec{B} \cdot \vec{R}$	Saturn IB/ Centaur	Payload	800	Launch through injection into interplanetary orbit and pre-encounter midcourse correction(s); post-encounter attitude control only

TABLE 2-II

ATLAS SLV-3A/BURNER II SEQUENCE OF EVENTS

Event	Description	Time (sec from Liftoff)
T_{LO}	Liftoff	0.0
BECO	Booster engine cutoff (sustainer operation)	148.4
JBP	Jettison booster package and shroud	151.4
SECO	Sustainer engine cutoff	361.4
VECO	Vernier engine cutoff (begin coast to apogee)	381.1
B2IG	Burner II ignition	1107.1
B2BO	Burner II burnout (circular orbit injection)	1153.1

The characteristics of the actual orbit obtained from the TRW/ N-Stage program include the following:

Injected weight	2513 lb
Inclination	99^{o}
Apogee/perigee	954/900 km
Eccentricity	0.0037
Orbital period	103.54 min

This is not a perfectly circular orbit. Since the above orbit was adequate for error analysis purposes, further iterations of the N-Stage program to achieve a more circular orbit were not attempted.

2.3 MARS ORBITER MISSIONS

Two 1975 Mars orbiter missions, corresponding to Type I and Type II transfers,* have been selected from the optimum 20-day launch periods identified during the Voyager Task D study (Ref. 2-6). These two types of trajectories were chosen to examine the sensitivity of the trajectory determination errors (and hence the fuel required for corrective maneuvers) to guidance and control errors. For either type of trajectory, the basic mission phases listed below are identical:

a) Launch, parking orbit, and injection into interplanetary trajectory

b) Separation from booster and first-cruise phase

c) Midcourse execution

d) Subsequent cruise and midcourse corrections

e) Approach

f) Deboost velocity application (into 1,100 x 10,000-km orbit)

g) Doppler tracking in elliptic orbit

h) Transfer into 500-km altitude circular orbit

Within each launch period, the critical mission was identified as that Earth-Mars trajectory which requires the maximum short coast Earth parking orbit. Table 2-III summarizes the Saturn V launch vehicle characteristics used to compute these coast times. The basic booster data was obtained from Refs. 2-3 and 2-7. Specific launch sequence event times for the Type II transfer are summarized in Table 2-IV.

Table 2-V lists the pertinent trajectory characteristics of each critical mission; Figures 2-1 and 2-2 illustrate the heliocentric transfer

*Type I transfers are defined as those in which the vehicle traces a central angle of less than 180° about the sun between departure from the Earth and arrival at Mars. In Type II trajectories, the angle is greater than 180°. The two types are effectively noncontiguous: when the heliocentric central angle is very near 180°, the position of Mars out of the ecliptic causes the interplanetary trajectory to be highly inclined to the ecliptic, leading to excessive launch energy requirements.

geometry of each mission. Time histories of the following trajectory characteristics are displayed in Figures 2-3 and 2-4 for the transit phase of each mission:

a) Sun-spacecraft distance
b) Sun-Mars distance
c) Spacecraft-Earth distance
d) Earth-Mars distance
e) Spacecraft-Mars distance
f) Sun-spacecraft-Earth angle
g) Sun-Mars-Earth angle

In addition, the Sun-Mars distance, Earth-Mars distance, and Sun-Mars-Earth angle plots have been extended to include the first 200 days of the orbiting phase of each mission.

TABLE 2-III

SATURN V LAUNCH AND INJECTION TRAJECTORY CHARACTERISTICS

1975 MARS TRANSFERS			
Phase	Duration (min)	Angle (deg)	Altitude (n. mi.)
Type I Mars Transfer			
Total powered flight	17.28	49.80*	
Circular parking orbit	58.02	236.84*	100.0
Injection		8.0**	180.0
Type II Mars Transfer			
Total powered flight	17.20	49.20*	
Circular parking orbit	24.83	101.34*	100.0
Injection		8.0**	180.0

* Angle traversed, measured in earth-centered inertial coordinates.

** Flight path angle at injection, measured (+) above the local horizontal.

TABLE 2-IV

SATURN V SEQUENCE OF EVENTS
(TYPE II TRANSFER TRAJECTORY)

Event	Description	Time (sec from liftoff)
T_{LO}	Liftoff	0.0
IECO	S-IC inboard engine cutoff	154.6
OECO	S-IC outboard engine cutoff	158.6
T_{IG2}	S-II stage ignition	164.1
T_{JFI}	Jettison S-IC/S-II forward interstage	194.1
T_{JHS}	Jettison heat shroud	214.1
S2CO	S-II stage cutoff	538.1
T_{IG3}	S-IVB stage first ignition	543.6
T_{BO3}	S-IVB stage first cutoff (parking orbit injection)	686.2
T_{2IG3}	S-IVB stage second ignition	2184.9
S4CO	S-IVB stage final cutoff (transfer orbit injection)	2491.3

The distances plotted in Figures 2-3 and 2-4 affect communications characteristics (spacecraft-earth distance) and relate to solar radiation and wind intensities (spacecraft-sun distance). The sun-spacecraft-earth angle is significant because of its effect on the transfer of attitude reference from earth to sun for the performance of midcourse maneuvers.

2.4 SOLAR PROBE (WITH JUPITER ASSIST) MISSIONS

It has been shown (Ref. 2-8) that the gravitational field of Jupiter may be employed to obtain solar probe and out-of-ecliptic postencounter trajectories following a close flyby past that planet. A 1972 solar impact mission and a 1972 90° out-of-ecliptic mission have been analyzed assuming the Saturn IB/Centaur launch vehicle characteristics given in Table 2-VI (Refs. 2-3, 2-9, and 2-10).

TABLE 2-V

CHARACTERISTICS OF 1975 EARTH-MARS TRAJECTORIES

	Type I Transfer	Type II Transfer
Departure date	1975 September 19	1975 September 22
Arrival date	1976 May 1	1976 September 5
Time of flight, days	224.75	348.32
Departure asymptote (from earth)		
V_∞, km/sec	4.45	3.85
C_3, km^2/sec^2	19.76	14.83
Angle to equatorial plane, deg	50.12	5.13
Angle to sun-earth line, deg	248.94	255.14
Heliocentric Orbit		
True anomaly at departure, deg	1.565	0.899
True anomaly at arrival, deg	7.204	-8.558
Heliocentric transfer angle, deg	150.68	203.32
Inclination to ecliptic, deg	3.751	2.083
Perihelion distance from sun, AU	1.003	1.003
Aphelion distance from sun, AU	1.705	1.675
Eccentricity	0.2594	0.2510
Approach Asymptote (to Mars)		
V_∞, km/sec	3.09	2.80
Angle to plane of Mars' orbit, deg	-20.22	26.83
Angle to Mars-Sun line, deg	138.76	54.71

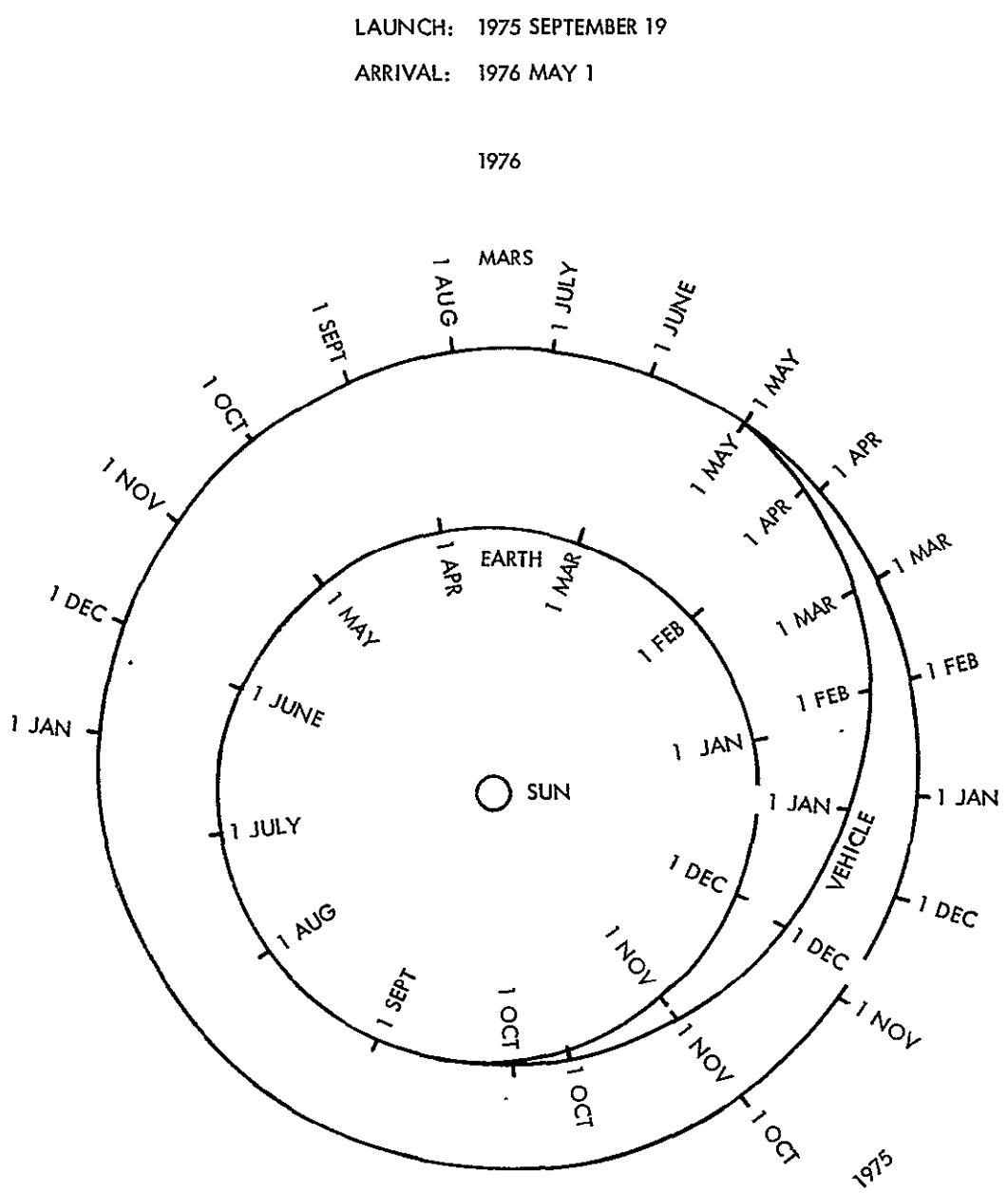

Figure 2-1. Ecliptic Projection of Sample 1975 Type I Mars Mission, Showing Relative Heliocentric Positions of Earth, Vehicle, and Mars

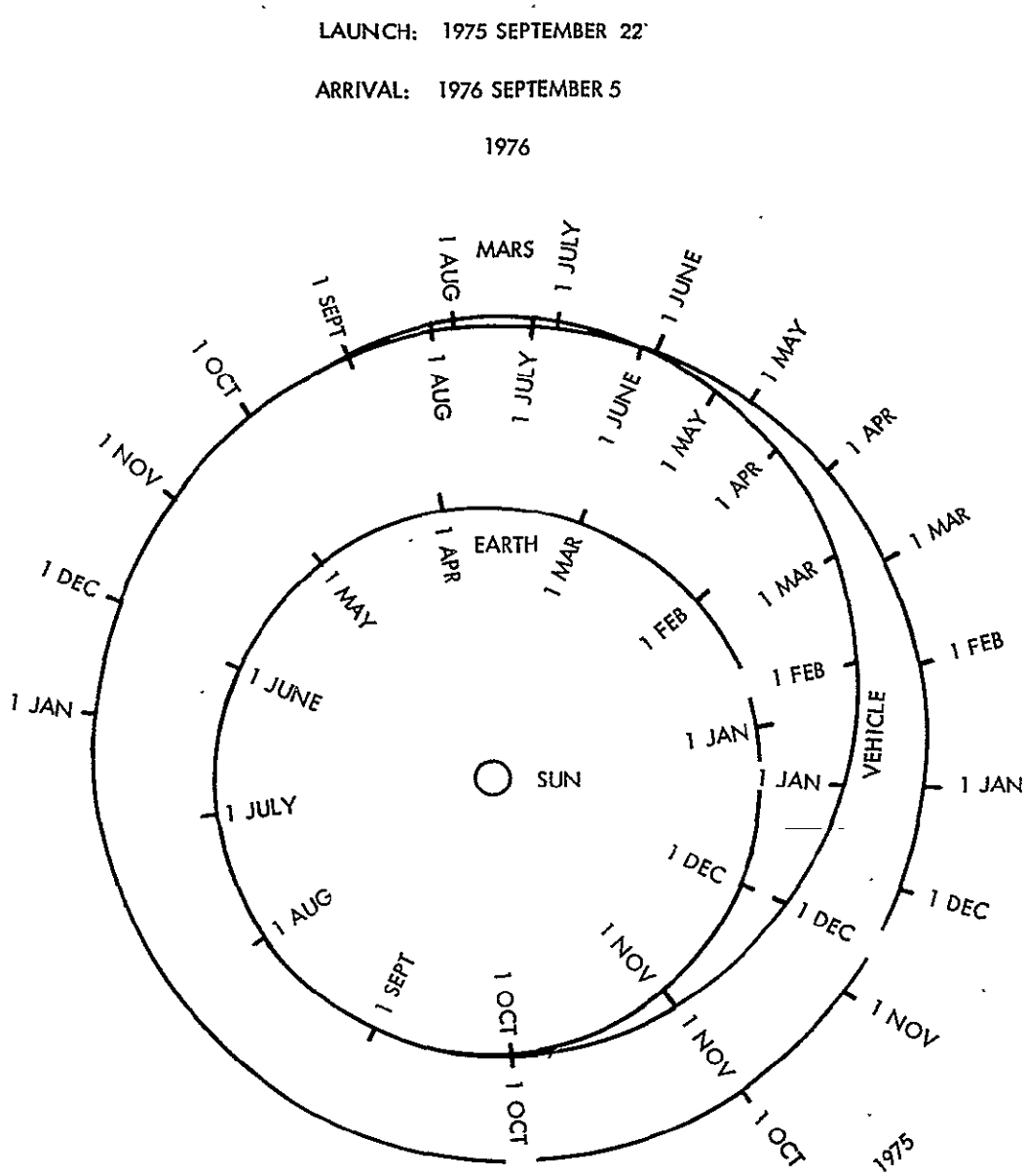

Figure 2-2. Ecliptic Projection of Sample 1975 Type II Mars Mission, Showing Relative Heliocentric Positions of Earth, Vehicle, and Mars

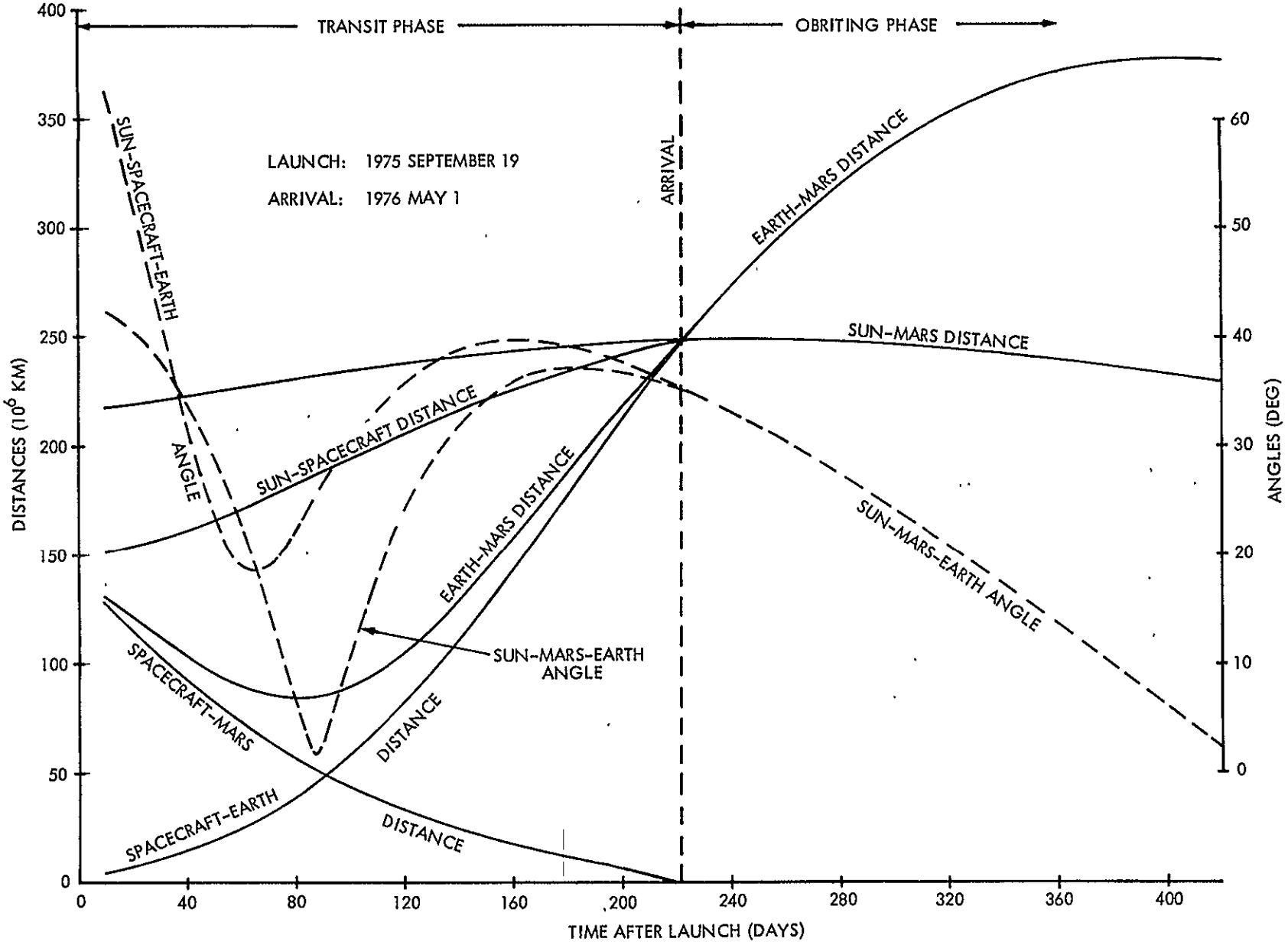

Figure 2-3. Time Histories of Heliocentric Orientation Angles and Distances for 1975 Type I Mars Mission

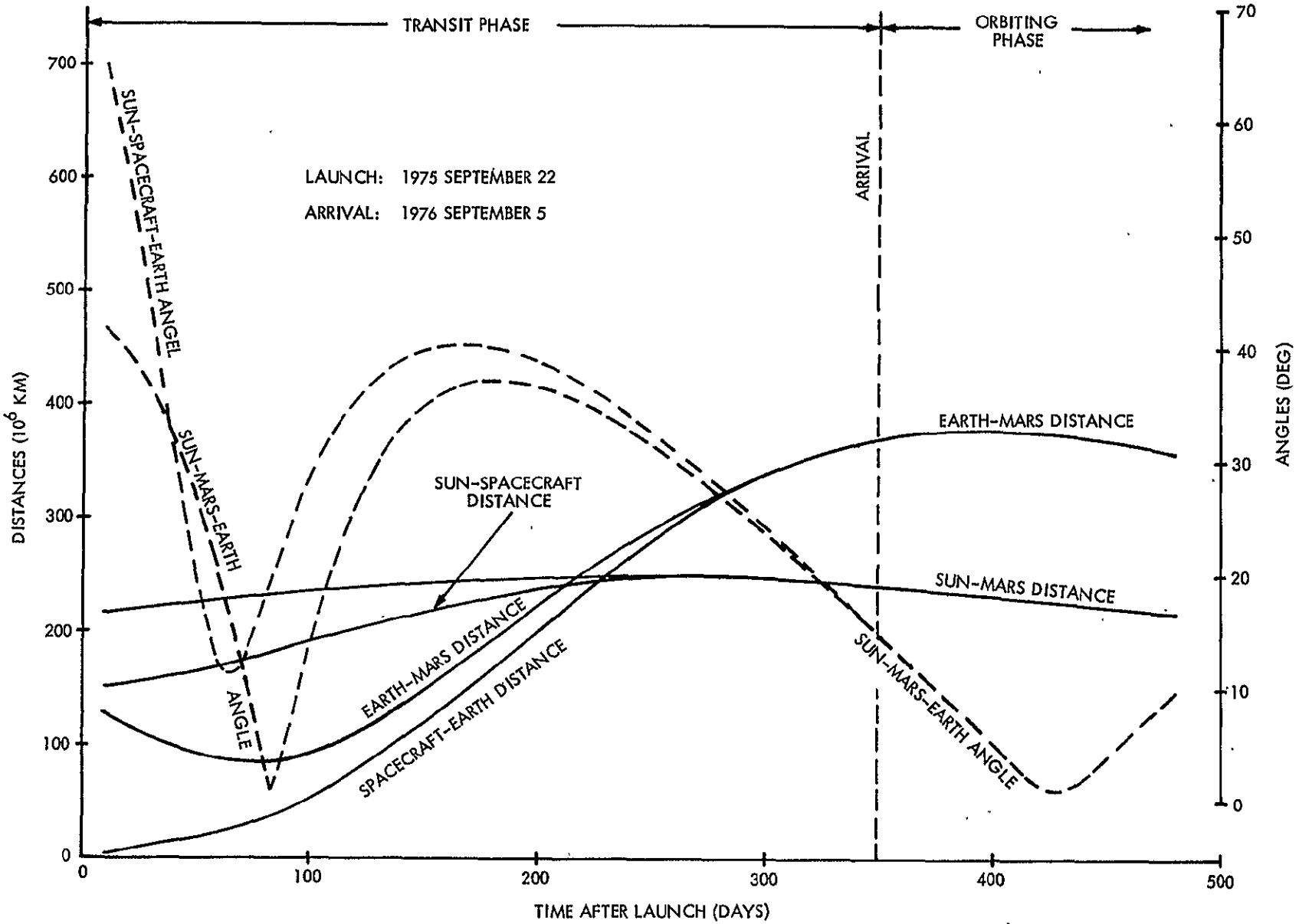

Figure 2-4. Time Histories of Heliocentric Orientation Angles and Distances for 1975 Type II Mars Mission

TABLE 2-VI

SATURN IB/CENTAUR LAUNCH AND INJECTION TRAJECTORY CHARACTERISTICS

Phase	Duration (min)	Angle (deg)	Altitude (n. mi.)
Total powered flight	18.12	53.70*	
Circular parking orbit	1.08	4.42*	100.0
Injection		12.7 **	313.0

* Angle traversed, measured in earth-centered inertial coordinates.

** Flight path angle at injection, measured (+) above the local horizontal.

Specific launch sequence event times for the Saturn IB/Centaur are summarized in Table 2-VII.

TABLE 2-VII

SATURN IB/CENTAUR SEQUENCE OF EVENTS

Event	Description	Time (sec from liftoff)
T_{LO}	Liftoff	0.0
IECO	S-IB inboard engine cutoff	139.5
OECO	S-IB outboard engine cutoff	146.0
T_{IG2}	S-IVB ignition	151.5
JHS	Jettison heat shroud	181.5
4BCO	S-IVB cutoff	643.0
CI	Centaur first ignition	654.5
CECO	Centaur first shutdown (parking orbit injection)	660.4
CI_2	Centaur second ignition	725.4
$CECO_2$	Centaur second cutoff	1152.4

Following the Centaur second cutoff, the payload coasts in the heliocentric transfer ellipse to Jupiter encounter. The earth-centered and heliocentric transfer trajectory characteristics of both missions are essentially the same. The altitude of closest approach at Jupiter and the components $\bar{B} \cdot \bar{T}$ and $\bar{B} \cdot \bar{R}$ of the impact parameter $\bar{B}$ determine the postencounter trajectories. The impact parameter, $\bar{B}$, is defined as a vector originating at the center of the target and is perpendicular to the incoming asymptote, $\bar{V}_\infty$ (see Figure 2-5). A unit vector $\bar{T}$ is defined as lying in a plane parallel to the ecliptic according to

$$\bar{T} = \frac{\bar{V}_\infty \times \bar{k}}{|\bar{V}_\infty \times \bar{k}|}$$

where $\bar{k}$ is a unit vector normal to the ecliptic plane and pointing towards the north. The $\bar{R}$ axis is defined by

$$\bar{R} = \frac{\bar{V}_\infty \times \bar{T}}{|\bar{V}_\infty \times \bar{T}|}$$

The impact parameter, $\bar{B}$, lies in the $\bar{R}$-$\bar{T}$ plane and has components $\bar{B} \cdot \bar{T}$ and $\bar{B} \cdot \bar{R}$.

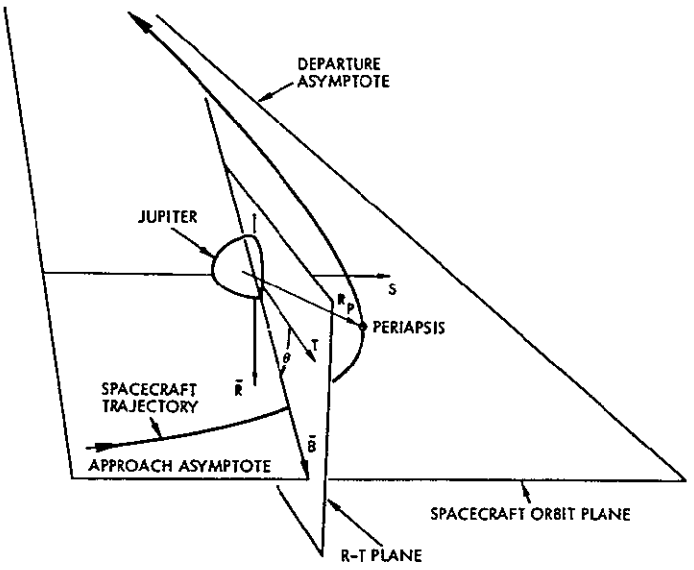

Figure 2-5. Encounter Geometry

Table 2-VIII summarizes the pertinent trajectory characteristics of each mission. The velocity of the solar probe as it becomes enveloped in the sun's photosphere is 617.45 km/sec; the total flight time beginning from injection is 2.762 yr.

TABLE 2-VIII

CHARACTERISTICS OF 1972 JUPITER PROBES

Departure date	1972 March 16	
Arrival date	1973 June 23	
Time of flight, days	463.97	
Departure asymptote (from earth)		
V_∞, km/sec	10.93	
C_3, km^2/sec^2	119.38	
Angle to equatorial plane, deg	-24.49	
Angle to sun-earth line, deg	254.54	
Heliocentric orbit		
True anomaly at departure, deg	4.799	
True anomaly at arrival, deg	57.593	
Heliocentric transfer angle, deg	128.21	
Inclination to ecliptic, deg	0.664	
Perihelion distance from sun, AU	0.987	
Aphelion distance from sun, AU	12.603	
Eccentricity	0.8547	
Approach asymptote (to Jupiter)		
V_∞, km/sec	13.99	
Angle to plane of Jupiter's orbit, deg	0.90	
Angle to plane of Jupiter-Sun line, deg	157.49	
Target parameters (at Jupiter)	Solar Probe	Out-of-Ecliptic Probe
Altitude of closest approach, Jupiter radii	3.03	6.23
$\bar{B} \cdot \bar{T}$, km	-674,781	-899,392
$\bar{B} \cdot \bar{R}$, km	14,787	-352,550

REFERENCES

2-1 "Radio/Optical/Strapdown Inertial Guidance Study for Advanced Kick-Stage Applications, Volume II: Detailed Study Results," TRW Final Report 07398-6017-R000, 30 June 1967.

2-2 "Program 720 Data Book." Convair Division of General Dynamics, GDC-BNZ67-020, 13 October 1967.

2-3 "Characteristics of Launch Vehicle Selected for High Speed Reentry Testing Studies (U)," Missiles and Space Division, LTV Aerospace Corporation, MSD Report No. 00.840, April 1967. (Confidential)

2-4 "Burner II Performance Handbook," The Boeing Company, D2-82601-2, August 1966.

2-5 "Burner II General Description," The Boeing Company, D2-82601-1, May 1966.

2-6 "Voyager Spacecraft Phase B, Task D, Final Report, Vol. II, Spacecraft Design and Performance," TRW Systems Report prepared for Marshall Space Flight Center, October 1967.

2-7 "Saturn V Payload Planner's Guide," Douglas Missile and Space Systems Division, SM-47274, November 1965.

2-8 M. Minovitch, "Utilizing Large Planetary Perturbations for the Design of Deep-Space, Solar Probe, and Out-of-Ecliptic Trajectories," Technical Memorandum No. 312-514, JPL, 15 February 1965.

2-9 "Saturn 1-B Payload Planner's Guide," Douglas Missile and Space Systems Division, SM-47010, June 1965.

2-10 "Centaur Technical Handbook," Revision B, General Dynamics/Astronautics, GD/A-BPM64-001-1, 24 January 1966.

3. GUIDANCE AND CONTROL SYSTEM CONCEPTUAL DESIGNS

3.1 INTRODUCTION

This section presents the recommended guidance and control system conceptual designs for each of the five missions considered in this study. A conceptual design is defined as a functional representation of the component configuration responsive to a specific mission, and consists of the following:

1) A functional schematic of the complete guidance, navigation, and control system indicating all informational loops.

2) Performance descriptions of each component and component subsystem in terms of its functional description, accuracy, physical parameters, and reliability.

3) Statement of development status of each component.

Functional schematics for each of the missions are presented in subsec. 3.3 following. Component descriptions, performance characteristics, and development status supporting the conceptual designs are presented in secs. 7, 9, and 10.

The guidance and control conceptual designs presented in this section are based on the operational sequences and the guidance performance requirements developed under Tasks I and II (Ref. 3-1). These requirements have been refined and extended to reflect the revised mission definitions* and the five specific launch vehicle/payload combinations defined in subsec. 1.1. Subsec. 3.2 summarizes the guidance and control requirements on which the conceptual designs are based. Subsec. 3.3 presents the conceptual designs for each mission.

The guidance system core concept adopted during the Tasks I and II studies was retained in this study. However, some of the basic functional concepts have been modified. In particular, the utilization of the

*The characteristics of the missions that differ from those that were used in the Task I and II studies (Ref. 3-1) are described in sec. 2 of this volume. A summary of the characteristics of all the missions is given in sec. 3 of vol. I.

inertial measurement unit and digital computer of the core configuration was extended to cover the launch and boost phases of all the missions. This modification of concept was made to examine the feasibility of performing launch/boost/injection guidance and control with a strapdown inertial package. In most instances, it is difficult to justify (on the basis of cost, performance requirements, and payload weight and size) the need, or use, for a complete three-axis inertial measurement unit to be used solely for attitude control and midcourse velocity corrections in interplanetary missions. The addition of the launch and boost-phase guidance and control functions to the total set of functions to be performed by the system thus provides a tenable basis for including the three-axis inertial measurement unit for these missions.

The recommended conceptual guidance system and control configurations developed in this study for the boost vehicles considered herein ignores the basic fact that all these boosters already have highly developed or proven guidance packages of their own. However, it was not intended to propose replacement of the existing systems with the strapdown system of this study. Rather, the boosters used in this study served primarily as vehicles or bases from which the analytical and preliminary design studies could proceed.

3.2 GUIDANCE AND CONTROL REQUIREMENTS

This subsection summarizes the guidance and control requirements which form the basis for the conceptual designs presented in subsec. 3.3. Guidance system performance (accuracy) requirements are summarized in vol. I, sec. 3.

The control subsystem conceptual designs presented in this section are based on the functional requirements defined in this subsection, the performance (stability) requirements defined in app. A, and the control system interface considerations and tradeoffs discussed in sec. 8.

3.2.1 Guidance and Control System Operational Sequences

The functional requirements for the ROI Guidance and Control System are developed from the operational sequences necessary to accomplish the objectives of the various missions with the postulated launch vehicles.

The operational sequences are presented in sec. 3 of vol. I for each of the five missions considered. A brief summary of these sequences is given here.

For the lunar and interplanetary orbiting missions, the general operational sequence may be summarized as follows:

a) Launch and Boost into Parking Orbit. The ROI strapdown inertial guidance and control subsystem will provide the guidance and control functions for this phase for all the missions.

b) Coast in Parking Orbit. The spacecraft, together with injection stage, will coast in the parking orbit until translunar or interplanetary orbit injection. The inertial guidance subsystem serves as an attitude reference during this phase.

c) Translunar or Interplanetary Orbit Injection. The injection stage is ignited to inject the spacecraft into the translunar or interplanetary trajectory. Attitude and burn control will be provided by the strapdown inertial guidance subsystem.

d) Coast Until First Midcourse Correction. Following injection burn, the spacecraft is separated from the injection, stage, a celestial reference acquisition sequence is initiated, and the spacecraft becomes attitude fixed to the sun and star Canopus via body-fixed sun and star sensors. The strapdown accelerometers can be turned off (except for heaters), and the flight computer algorithm for updating the direction cosines can be placed in a standby mode.

   Deep-Space Network (DSN) tracking is used during this coast phase to determine the orbit and compute the midcourse velocity correction required to reduce the effects of injection errors. The midcourse thrust vector pointing and magnitude commands and time of execution command are transmitted to the ROI guidance system.

e) First Midcourse Correction. At a predetermined time from injection, the first midcourse correction is executed. Ten to thirty minutes prior to the time of execution, the strapdown inertial reference unit is turned on, the direction cosine solution algorithm is initialized, and vehicle rotations are commanded to orient the thrust vector in the required inertial direction. The midcourse burn is initiated at the correct time when the proper attitude is achieved, and is designed to null selected miss components at lunar or planetary intercept.

f) Second Coast Phase and Second Midcourse Correction. After completion of the first midcourse correction, the spacecraft is "unwound" to the original Sun/Canopus reference attitude and continues in a cruise phase identical to the first. A second midcourse burn may be performed prior to lunar or planetary injection if required.

g) Coast Until Deboost Maneuver Into Intermediate Lunar or Planetary Orbit. This phase is identical to the other coast phases.

h) Deboost Into Intermediate Orbit. Based on the DSN tracking data obtained during the previous phase, the deboost maneuver is calculated and the spacecraft is deboosted into an intermediate orbit, under control of the inertial guidance system.

i) Coast in Intermediate Orbit. The spacecraft is tracked by DSN stations to determine orbital parameters and the retromaneuver required to place the payload into the final orbit.

j) Retro Into Final Orbit. Based on the orbital estimates obtained from DSN tracking data and controlled by the strapdown inertial guidance system, the spacecraft is injected into the final orbit.

For the Solar Probe (with Jupiter assist) missions, the operational sequence is similar except that no further powered maneuvers are required subsequent to the last midcourse corrections.

The operational sequence for the earth orbiting missions consists basically of:

a) Launch and boost into parking orbit

b) Coast in parking orbit

c) Injection into transfer orbit

d) Transfer orbit coast

e) Injection into final orbit

Functionally, the operations in each of these phases is the same as for the corresponding phases in the lunar and interplanetary missions except that earth-based tracking is not utilized.

For the low-altitude polar-orbit mission utilizing the Atlas/Burner II, a direct ascent mode is utilized (no parking orbit is required).

3.2.2 Control System Functional Requirements

The conceptual guidance and control system designs defined in subsec. 3.3 are based on the requirement for stabilizing and controlling each stage of the boost vehicle and also any spacecraft stage that employs the system during both powered and coast phases. Booster operation is assumed to include all mission phases between liftoff and separation of the spacecraft. In the event that the last stage of the boost vehicle is used as a spacecraft, the spacecraft functional requirements would be applicable to that stage.

In addition to the functional requirements defined below, the control system designs must meet the specific performance (stability) requirements defined in app. A. No attempt has been made to optimize interfaces between the ROI guidance and control system and the existing boost vehicle control systems components. Existing boost vehicle control electronics and actuators are used where possible, however, some modifications are suggested to simplify the overall control system and to achieve interface compatibility. Interface tradeoffs are discussed in sec. 8 of this volume.

3.2.2.1 Boost Vehicle Functional Requirements

Multistage launch vehicles often employ coast phases between the upper-stage powered flight phases, particularly if third or fourth stages are used. Requirements for control during these coast phases are included within the booster stage control requirements.

Powered Flight. The ROI Guidance and Control System must maintain vehicle control throughout powered booster flight from liftoff to separation of the spacecraft. Adequate stability margins, as described in app. A, must be maintained throughout this phase. Shortly after liftoff, the system must initiate a pitch program to achieve the desired vehicle trajectory. Closed-loop guidance steering during first-stage operations is optional and dependent upon mission requirements.

Vehicle control must be maintained in the presence of disturbances such as those due to winds, nose-fairing jettison, and stage separation. A control system autopilot design intended to relieve structural loads resulting from high-wind shears is required only for those vehicles

presently incorporating a load relief design. Of the candidate vehicle configurations, only the Saturn IB booster employs such a system.

The control system autopilot must have a minimum capability of two changes in the gain and filter coefficients per stage, one change during each stage operation and one change at the start of each stage operation, excluding a change at liftoff. Increases in these requirements are to be made to satisfy the stability requirements given in app. A.

In addition to control loop gains and stability compensation filters, the autopilot must contain attitude-command error limits and thrust-vector deflection-command limits which are capable of being changed at the start of each stage operation. The autopilot control laws must be capable of accomplishing vehicle control through linear thrust-vector deflections as well as pulsed reaction jet control. Linear thrust-vector control techniques include thrust deflection by means of liquid injection, gimbaled engine, and gimbaled nozzle control. However, for the boost vehicles under consideration here, only gimbaled engine control is required. The pulsed jet control laws must be applicable for coast phase as well as powered phase operation through changes made in autopilot coefficients.

Coast Flight Operations. During the coast phases of boost flight, the control system must maintain three-axis attitude control of the booster, through the use of reaction control jets. It must also be capable of accomplishing attitude change maneuvers to attain the desired orientations for subsequent powered flight operations. The coast phase limit cycle performance prior to spacecraft separation must be within acceptable staging requirements for the particular launch vehicle design. Such requirements will be strongly dependent upon the means adapted for spacecraft separation.

In addition to attitude control, the coast phase control system must be capable of accomplishing forward translational acceleration for propellant settling operations to facilitate main engine operations and for adding low forward velocity increments.

3.2.2.2 Spacecraft Functional Requirements

Spacecraft functional requirements are given below with both digital and analog control modes included. The analog control modes serve as either backup modes selectable upon ground command or as primary modes during mission phases when the digital computer is deactivated.

Launch Vehicle Separation. The tip off rates imparted to the spacecraft during separation from the launch vehicle are removed by the ROI Guidance and Control System through the use of the spacecraft reaction control devices.

Digital Control Inertial Hold. Subsequent to separation from the launch vehicle, the digital control system must provide three-axis attitude control of the spacecraft employing signals from the inertial sensors in an attitude hold mode.

During all phases of the mission in which the digital computer is active, the digital control inertial hold mode must be capable of selection through ground commands or onboard sequencing commands.

Acquisition of Celestial References. The ROI Guidance and Control System must reorient the spacecraft to the desired orientation to enable acquisition of the celestial references (i.e., earth, sun, stars, planets) through onboard preprogrammed command angles or through ground commanded angles. In the event that one of these references is not directly obtainable, a search mode must be provided in which the vehicle is either librated or slowly spun about the search axis.

Acquisition of the celestial references through both digital and analog control must be provided by the ROI Guidance and Control System. The analog control would be a backup system selectable upon ground command. Acquisition of celestial sensors would be accomplished or completed through use of the electro-optical sensors.

Analog Control Inertial Hold. During all phases of the mission in which the digital computer is inactive, an analog control inertial hold mode must be capable of selection through ground commands or onboard sequencing commands. This inertial hold mode must provide three-axis attitude control of the spacecraft through use of signals from inertial instruments.

Digital and Analog Celestial Hold. After acquisition of the celestial references and through use of the electro-optical sensors, the ROI Guidance and Control System must maintain a celestial hold mode through both digital and analog control selectable upon ground command. During earth and planetary orbits, if one of these bodies were employed as a reference,

the celestial hold mode would entail one spacecraft rotation per orbit to maintain a specific control axis aligned to the planet geocenter.

Reorientation Maneuvers. In addition to maneuvers for celestial reference acquisitions, the ROI Guidance and Control System must accomplish additional spacecraft reorientation maneuvers through digital or back-up analog control employing inertial instruments. The additional maneuvers include reorientation for: powered flight firings; acquisition of solar power; improvement of communication strength; experiment pointing or tracking.

Thermal Control Mode. As a means of reducing the thermal gradient between the sunlit and shadowed portions of the spacecraft, the ROI Guidance System must be capable of maintaining a low-spin rate on the spacecraft. This mode is to be employed over long-mission durations in which the digital computer is deactivated, hence, analog control must be employed with electro-optical sensing for spin control.

Spacecraft Powered Flight Operation. During the phases when trajectory and orbit changes are accomplished, the ROI Guidance and Control System must maintain three-axis attitude control through the use of spacecraft reaction control devices or through deflection of the main engine thrust. The use of the inertial sensors would be made for these firings. These firing phases include orbit transfer, orbit circularization, orbit-trim, translunar and interplanetary orbit injection, midcourse correction, and lunar and planetary deboost firings.

The powered flight operation may include an attitude hold, or constant angular rate modes, as well as guidance commanded operation employing explicit guidance laws.

3.3 GUIDANCE AND CONTROL SYSTEM CONCEPTUAL DESIGNS

The composite conceptual equipment configuration depicted in Figure 3-1 was developed on the basis of the above premises and the performance analyses in secs. 4 and 5 and Ref. 3-1. The utilization of equipment for each mission is summarized in Table 3-I.

A digital control system concept was chosen for these studies because it provides a flexible means of implementing the control functions on a per flight basis without requiring hardware modifications. In this

2

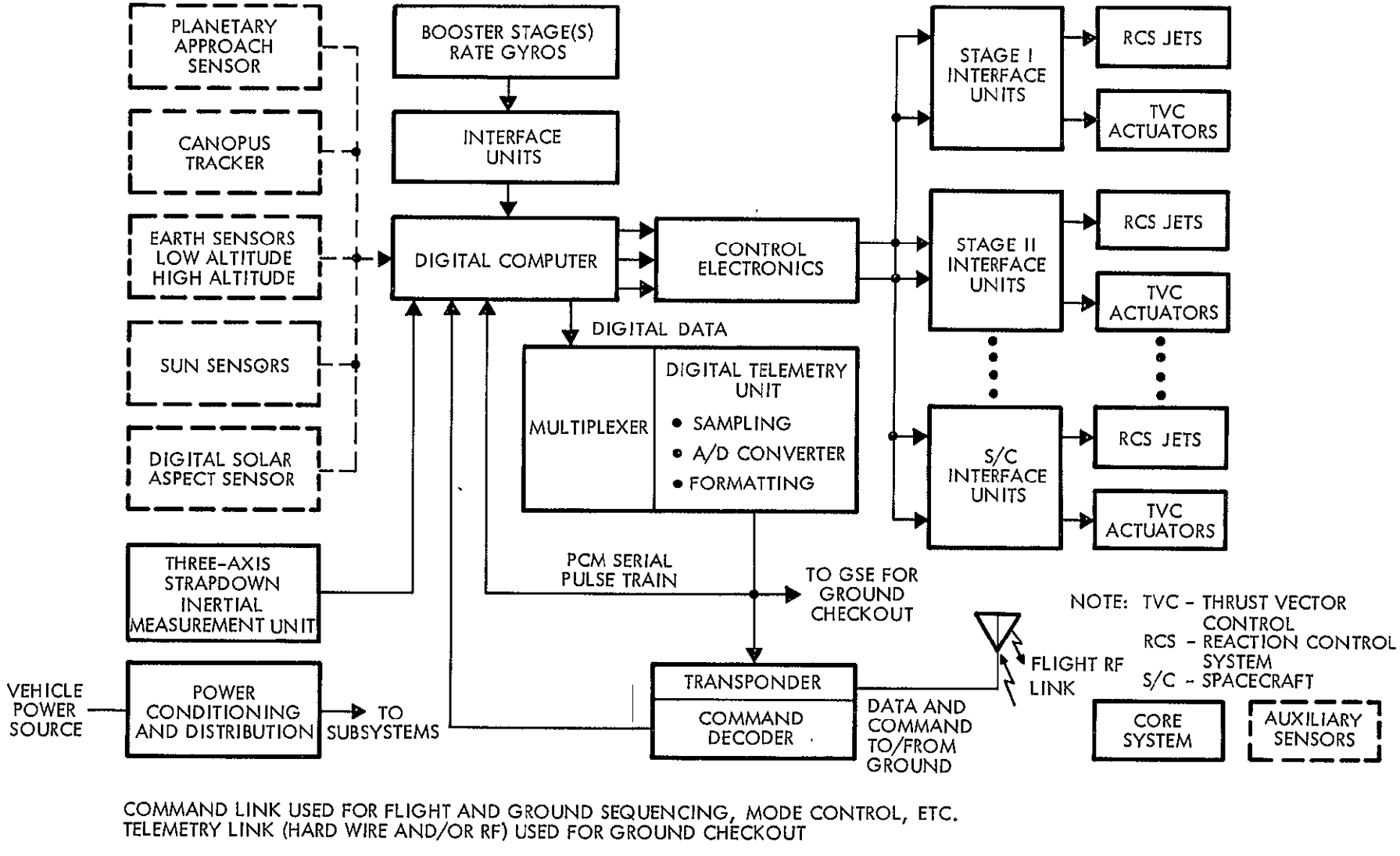

Figure 3-1. Composite Equipment Configuration

TABLE 3-I

EQUIPMENT UTILIZATION

Equipment		Near-Earth Polar Orbit	Earth-Synchronous Orbit	Lunar Orbit	Solar Probe (Jupiter Swing-by)	Mars Orbiter
Core System	3-axis strapdown inertial measurement unit	▲	▲	▲	▲	▲
	Digital Computer	▲	▲	▲	▲	▲
	S-band tracking transponder and command link		▲	▲	▲	▲
	Auxiliary equipment power conditioning and distribution, telemetry, etc.	▲	▲	▲	▲	▲
Auxiliary Sensors	Star (Canopus) tracker (attitude reference)			▲	▲	▲
	Earth sensor (horizon scanner) (local vertical reference) • Low Altitude • High Altitude		▲			
	Sun sensor (cruise attitude) reference)			▲	▲	▲
	Sun sensor solar aspect sensor for attitude reference and navigation fix (optional)		▲			
	Planetary approach sensor					▲

study, full advantage was taken of the digital computer existing within the ROI guidance system to accomplish the stabilization and control of the boost vehicle as well as of the spacecraft. With the use of the computer a single autopilot can be employed to control all the booster and spacecraft stages, thereby eliminating the need for multiple autopilots, which are often used in multistage space boosters. Other benefits of this approach include: 1) the elimination and/or simplification of certain items of booster control system hardware and 2) the ease with which the ROI guidance and control system can be adapted to the various booster/spacecraft TVC and RCS systems with a minimum of special-purpose interface hardware.

The recommended control system conceptual design configuration is shown in Figure 3-2. Control system interface considerations and trade-offs are discussed in sec. 8. Specific adaptations of this concept for each of the missions is given below.

3.4 NEAR-EARTH POLAR-ORBIT MISSION

The powered and coast phases of the near-earth polar-orbit mission up to injection of the payload into the design orbit is of short duration (19.2 min) with no inordinate demands exceeding state-of-the-art guidance capabilities. Electro-optical sensors are not required for any mission phase; therefore, guidance system for this mission is comprised of the core package of Table 3-I.

The integrated guidance and control configuration is indicated in Figure 3-3. The basic guidance package is installed in the Burner II and provides the guidance function for the Atlas stages as well. A control electronics package is required on the Burner II to interface between 1) the primary ROI computer and the Burner II attitude control system and 2) the ROI computer and the Atlas components, indicated in Figure 3-3, which are part of the existing Atlas system.

Autopilot stability studies indicate that the Atlas rate gyros should be retained, with considerations of possible relocation (see sec. 5). However, the Atlas position gyro functions can be taken over by the ROI core package. These comments pertaining to the Atlas hold for the two missions discussed in subsecs. 3.5 and 3.6.

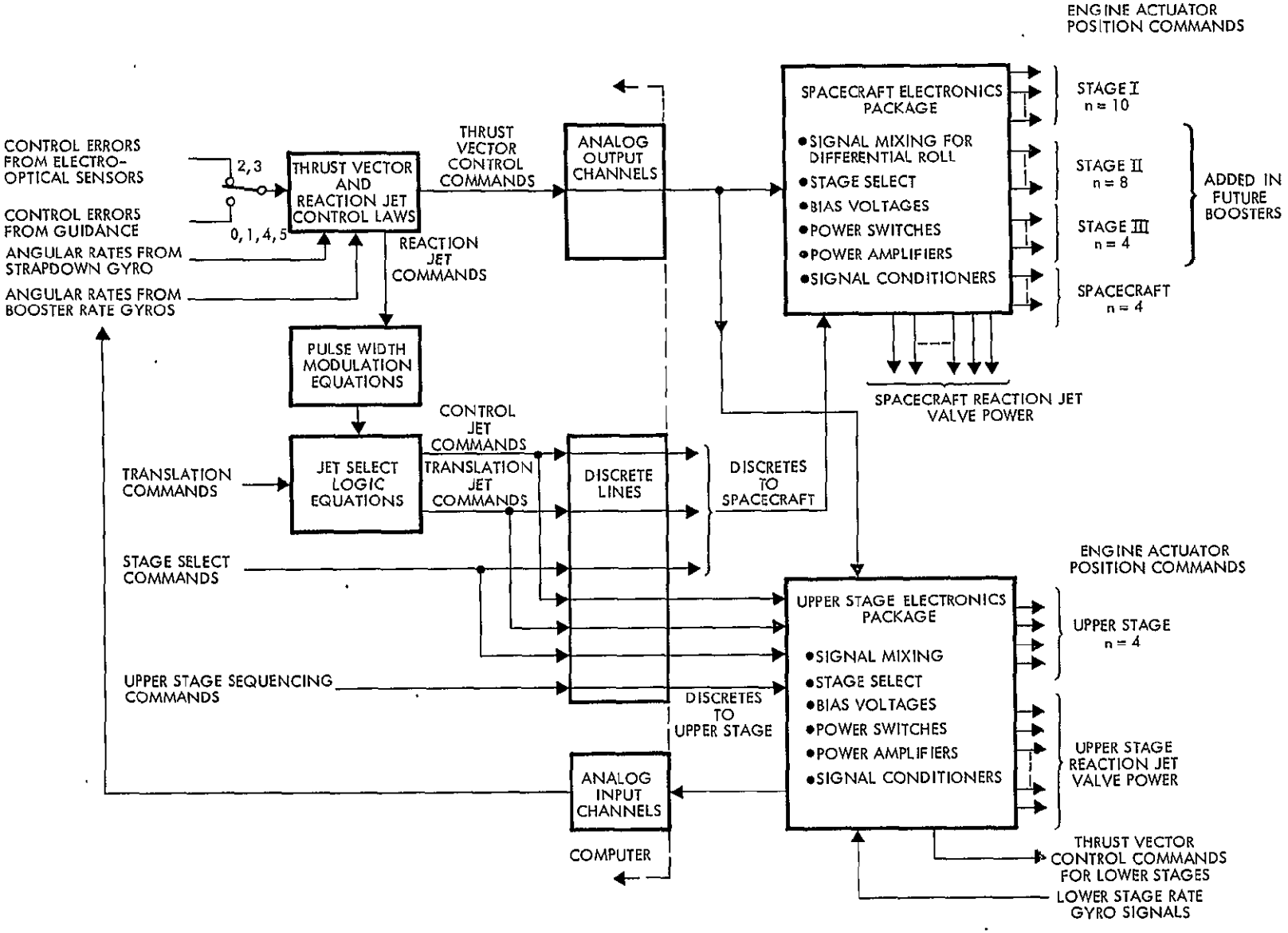

Figure 3-2. Control System Signal and Equation Flow Diagram

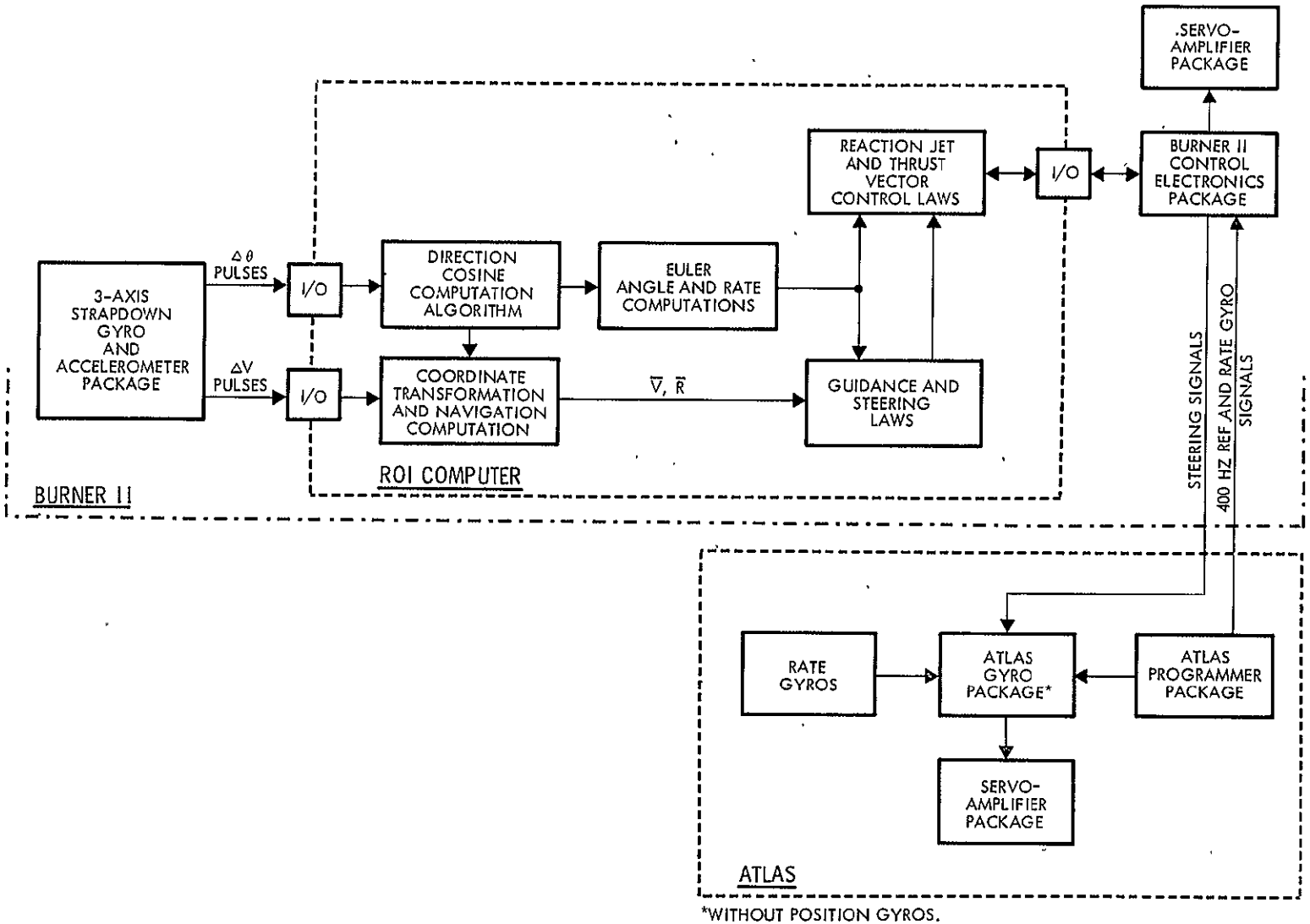

Figure 3-3. Basic Conceptual Design Configuration for the Near-Earth Polar-Orbit Mission

The guidance performance analysis of this conceptual design can be found in subsec. 4.2.

3.5 EARTH-SYNCHRONOUS SATELLITE MISSION

The integrated guidance and control conceptual configuration for the earth-synchronous satellite mission is indicated in Figure 3-4. An earth horizon scanner and a solar aspect sensor (see subsecs. 9.4 and 9.5 respectively) have been added to the core package. The core package, the electro-optical sensors, and an interface electronics package are installed on the Centaur. No changes are made to the basic Centaur control actuation system, and the Atlas control system configuration is the same as in the previous mission.*

The functioning of the various sensors can best be described with reference to the basic mission profile. During the Atlas and first Centaur burns to parking orbit injection, guidance and steering are controlled inertially. For the direct-ascent mission, the second Centaur burn is initiated at first equatorial crossing, approximately half an hour after launch. During the intermediate coasting period, constant attitude is maintained and the second Centaur burn for Hohmann transfer from parking orbit altitude to synchronous altitude is again controlled inertially. For this direct-ascent mission, no external attitude or timing update information is required (Ref. 3-1).

However, for the long parking orbit coast case, both an attitude and timing update are highly beneficial prior to the second Centaur, or perigee, burn (see Table 4-V). Both these updates can be obtained with the combination of the earth sensor and solar aspect sensor shown in Figure 3-4.

During the long (approximately 5.25-hr) Hohmann transfer coast to apogee at synchronous altitude, attitude is maintained inertially. However, prior to the third Centaur, or apogee, burn, an attitude update is accomplished again with the aid of the earth and sun sensors.

The performance achievable with this system configuration is discussed in subsec. 4.3.

---

*The control system design is discussed further in subsec. 8.2.

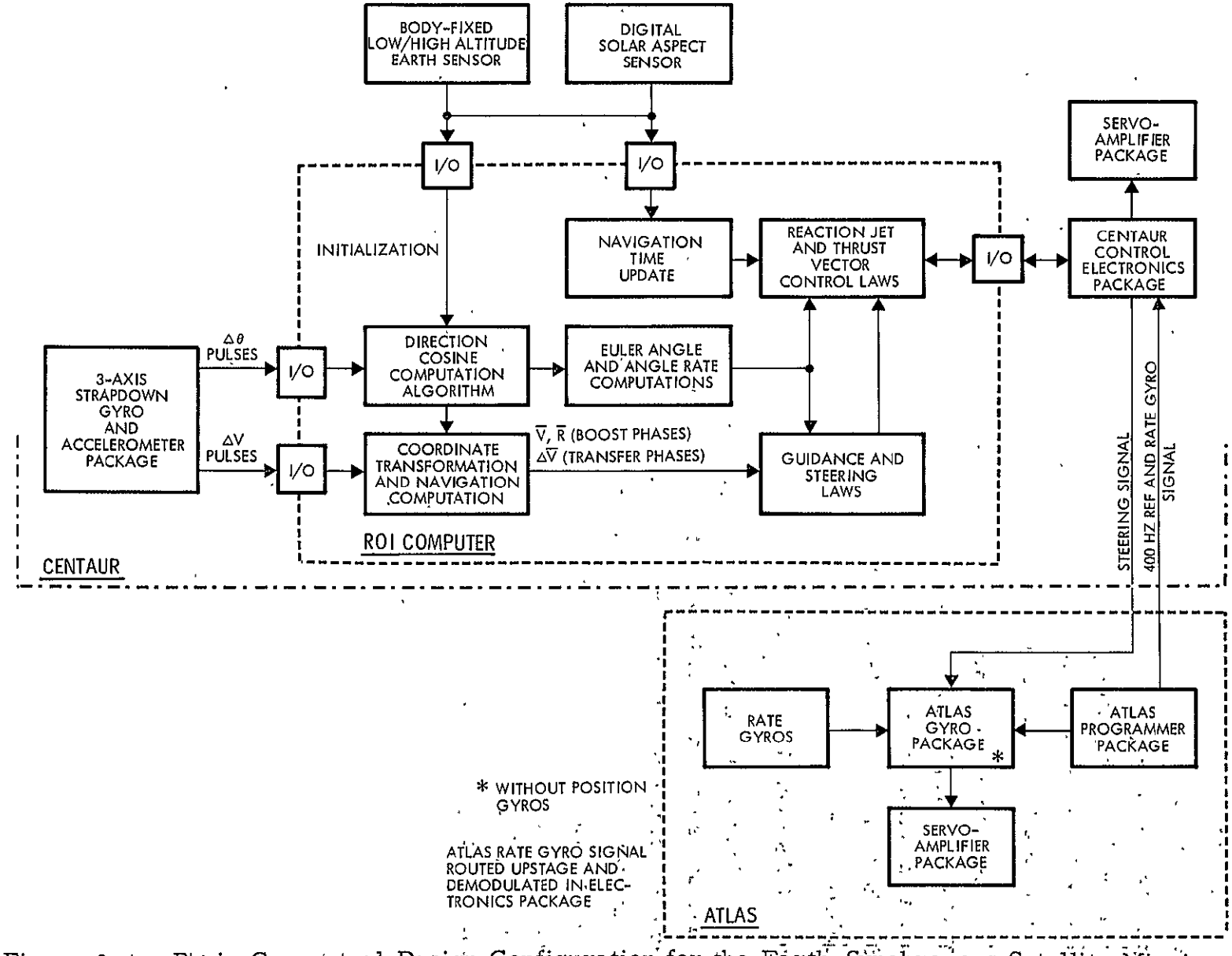

Figure 3-4. Basic Conceptual Design Configuration for the Earth-Synchronous Satellite Mission

3.6 LUNAR ORBITER MISSION

For the Lunar orbiter mission, the ROI guidance package is installed in the orbiter spacecraft, and data and signal transfer to the Atlas control system configuration is effected through a Centaur electronics interface package (Figure 3-5). The canopus tracker and sun sensor (see subsecs. 9.4 and 9.6 respectively) replace the earth sensor and solar aspect sensor of the previous mission. These sensors are used to establish the celestial attitude reference only during the translunar coasting phases.

Performance analyses for this mission were conducted during the Tasks I and II phases of this overall study. A summary of the translunar orbit injection analysis for the two strapdown inertial systems studied and for the Centaur gimbaled inertial guidance system is given in vol. 1, subsec. 5.4.

3.7 MARS ORBITER MISSION

The major difference in the system elements for the Mars orbiter mission as compared to those of the lunar orbiter mission is the possible addition of the planetary approach sensor. As shown in subsec. 4.6, data from this sensor in conjunction with data from the sun and Canopus sensors can be utilized by ground-based stations to improve the quality of the determination of the spacecraft approach orbit to Mars. However, for mission requirements comparable to those in use up to now, it is not clear that this improvement in approach orbit determination is absolutely essential. Thus, the planetary approach sensor shown in Figure 3-6 is included conditionally so that the implications on preliminary modular design can be investigated for applications to possible future missions with high-accuracy requirements.

Except for the planetary approach sensor, the functions and utilization of the total guidance and control system substantially parallel the functional operations of the lunar orbiter mission. As shown in sec. 5, the Saturn V rate gyros are retained to simplify the autopilot design problem.

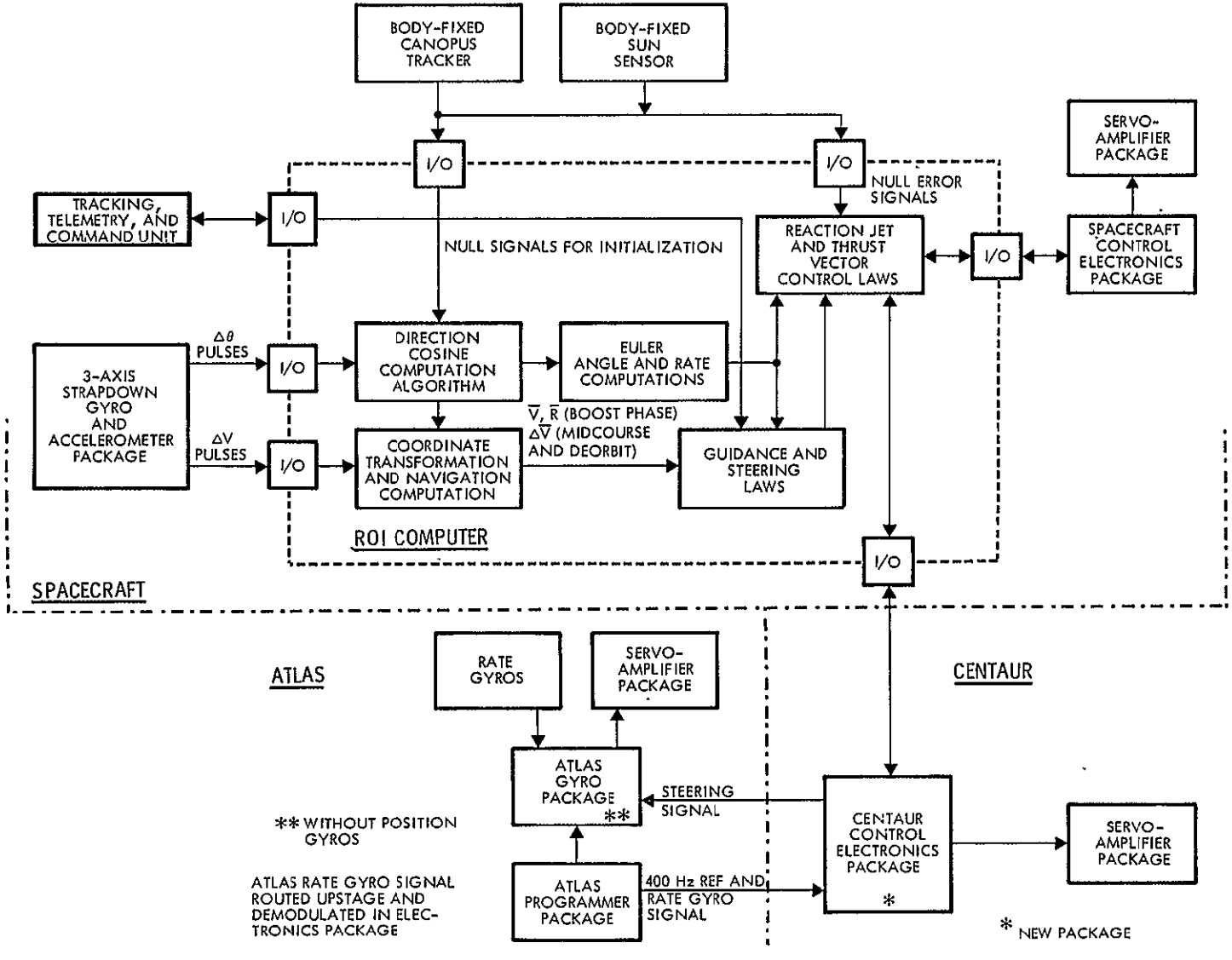

Figure 3-5. Basic Conceptual Design Configuration for the Lunar Orbiter Mission

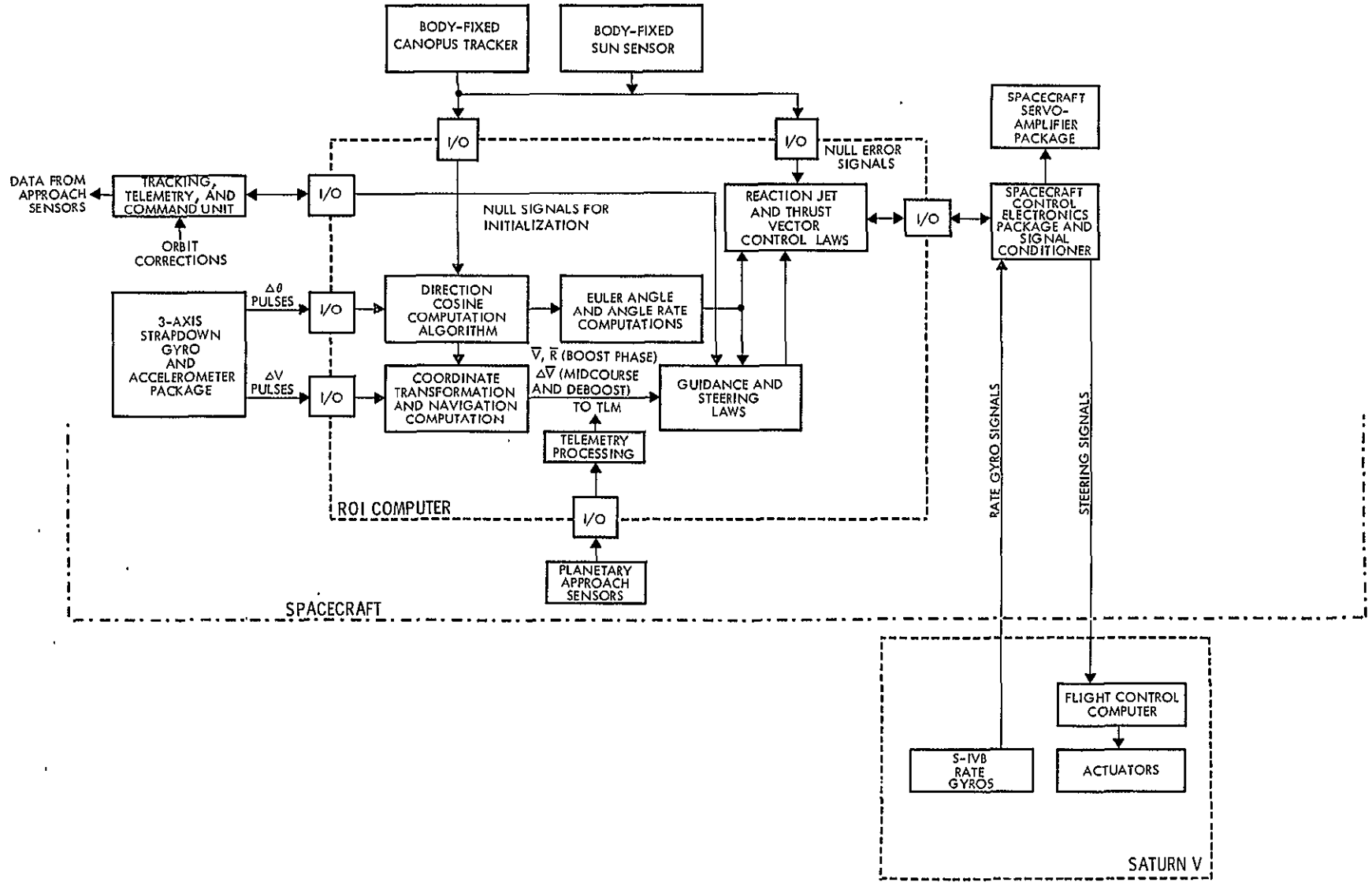

Figure 3-6. Basic Conceptual Design Configuration for the Mars Orbiter Mission

3.8 SOLAR PROBE MISSIONS (WITH JUPITER ASSIST)

Up to Jupiter encounter, the solar probe missions closely resemble the lunar mission. Therefore, the conceptual configuration, Figure 3-7, is very similar to that of the lunar mission, insofar as the guidance system is concerned.

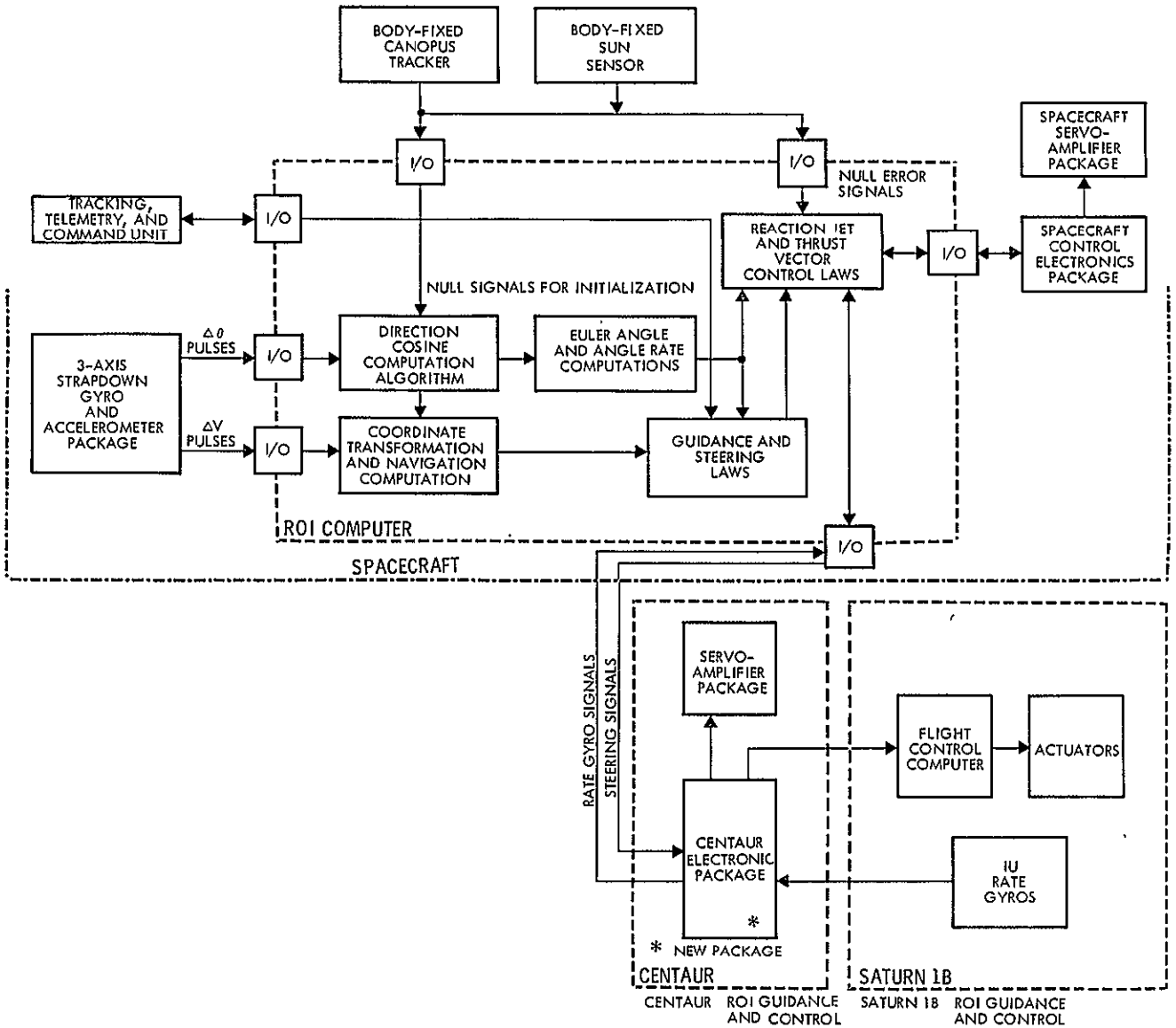

Figure 3-7. Basic Conceptual Design Configuration for the Jupiter Missions

REFERENCES

3-1 "Radio/Optical/Strapdown Inertial Guidance Study for Advanced Kick Stage Applications," Final Report, Volume II, TRW Systems Report No. 07398-6017-R000, 30 June 1967.

4. GUIDANCE AND NAVIGATION PERFORMANCE ANALYSES

4.1. INTRODUCTION AND SUMMARY

In secs. 7 and 8 of the Tasks I and II report (Ref. 4-1), performance analyses for the following missions/mission segments were obtained:

a) Injection of a payload into the earth-synchronous satellite orbit using Atlas/Centaur

b) Translunar orbit injection with the Atlas/Centaur

c) Midcourse and planetary orbit insertion maneuvers

Under the present study effort, the following performance analyses were conducted:

a) Injection accuracy and 95%-corrective ΔV requirements for the Atlas/Burner II near-earth polar mission (see subsec. 4.2)

b) Analysis of the sunsighting, perigee burn-time update technique for the synchronous satellite mission (see subsec. 4.3)

c) Injection accuracy, 95% first midcourse ΔV, and target miss analysis for the Saturn V/Mars orbiter mission (see subsec. 4.4)

d) Injection accuracy, 95% first midcourse ΔV, and target miss analysis for the Saturn-IB/Centaur/Jupiter missions (see subsec. 4.5)

e) Mars approach analysis (see subsec. 4.6)

The inertial instrument error models for these analyses are the same as those derived in sec. 4 of Ref. 4-1, and are summarized in Table 4-I. Both the TG-166 and TG-266 inertial system error models were used in the analyses. Either system is capable of providing adequate performance; the TG-166 is the less accurate of the two systems, but is available at lower cost, weight, size and power requirements. For the Earth polar and Mars missions, the error models were modified to the extent that initial azimuth alignment, error source No. 7, was varied parametrically to establish requirements on azimuth alignment. The error sources attributable to the electro-optical sensors were modified to reflect those developed in the present study.

TABLE 4-I

ERROR MODELS USED FOR STRAPDOWN INERTIAL GUIDANCE PERFORMANCE ANALYSIS

Number	TG-166	TG-266	Units	Type	Description
1	3	3	m	Initial	Vertical position
2, 3	15	15	m	Initial	East, north position
7, 8, 9*	20	20	arc sec	Initial	Orientation
10	600	600	arc sec	Optical	Roll axis at apogee
20, 30	180	180	arc sec	Optical	Yaw, pitch axes at apogee
11, 31	720	720	arc sec	Optical	Roll, pitch axes at perigee
21	180	180	arc sec	Optical	Yaw axis at perigee
39**	4.0†	4.0†	sec	Optical (Sun Sensor)	Update time
40, 51, 62	21	14	μg	Accelerometer	Bias
73, 77, 81	75	24	μg/g	Accelerometer	Scale factor
74	12	10	arc sec	Accelerometer	X accelerometer input axis rotation toward y-axis
75	12	10	arc sec	Accelerometer	X accelerometer input axis rotation toward z-axis
78	12	10	arc sec	Accelerometer	Y accelerometer input axis rotation toward z-axis
82, 83, 84	15	10	μg/g	Accelerometer	Pendulous axis g sensitivity
85, 86, 87	1	1	μg/g	Accelerometer	Output axis g sensitivity
91, 97, 103	50	30	$\mu g/g^2$	Accelerometer	Input-pendulous g-product sensitivity
92, 98, 104	0.5	0.5	$\mu g/g^2$	Accelerometer	Input-output g-product sensitivity
230, 241, 252	0.187	0.09	deg/hr	Gyro	Bias drift
263, 266, 269	0.627	0.16	deg/hr/g	Gyro	Input axis g-sensitive drift
264, 267, 270	0.627	0.16	deg/hr/g	Gyro	Spin axis g-sensitive drift
265, 268, 271	0.02	0	deg/hr/g	Gyro	Output axis g-sensitive drift
275, 281, 287	0.04	0.04	$deg/hr/g^2$	Gyro	Anisoelastic drift
290, 294, 298	57	26	ppm	Gyro	Scale factor.
291, 292, 293	10	10	arc sec	Gyro	Gyro input axis rotations toward each of other two axes
295, 296, 297	10	10	arc sec	Gyro	Gyro input axis rotations toward each of other two axes

*Initial azimuth alignment error (source No. 7) was varied parametrically between 10 and 180 arc sec.

**Applies only to the multi-parking orbit-synchronous satellite missions.

†0.238 sec used in previous error analyses (Ref. 4-1).

The error analyses were conducted with the aid of the GEAP II and SVEAD error analysis programs, as were Tasks I and II. The basic powered trajectories are those described in sec. 2.

4.2 POWERED PERFORMANCE ANALYSES OF THE NEAR-EARTH POLAR-ORBIT MISSION

For the near-earth polar-orbit mission, the basic guidance system is located in the Burner II. The guidance system configuration contains only the core package, comprised of the strapdown IMU package and the computer. No optical sensors are required; thus, error source Nos. 10, 11, 20, 21, 30, 31 and 39 of Table 4-I do not apply.

For an initial azimuth alignment error of 20 arc sec, the resulting 1-σ rss position and velocity component errors in radial, tangential, normal (RTN) coordinates for the two inertial systems are as indicated in Table 4-II.

TABLE 4-II

ATLAS/BURNER II NEAR-EARTH POLAR-ORBIT INJECTION ERRORS

System	Position (km)			Velocity (m/sec)		
	R	T	N	R	T	N
TG-166	1.28	1.59	4.01	3.28	1.50	6.05
TG-266	0.54	0.96	1.32	1.56	0.86	1.79

The major contributors to these totals are summarized in Tables 4-III and 4-IV for the TG-166 and TG-266 systems, respectively.

To relate these injection errors to mission performance, the 95% corrective ΔV required to correct the payload orbit was computed for both systems and for a range of initial azimuth accuracies (error source No. 7). The orbit correction scheme was assumed to be the same as that used in Ref. 4-1, i.e.,

1) Perform a Hohmann transfer from the perigee of the imperfect orbit to the desired 926.5-km (500 n. mi.) circular orbit altitude.

TABLE 4-III

SUMMARY OF ATLAS/BURNER II NEAR-EARTH POLAR-ORBIT MISSION ERROR ANALYSIS RESULTS

(TG-166 System with Initial Azimuth Alignment Error = 20 arc sec)

	Position (km)			Velocity (m/sec)			Orientation (arc sec)		
	R	T	N	R	T	N	Yaw	Roll	Pitch
7	-0.05	0	-0.81	0	0	-0.71	19.8	-22.6	0
8	0.29	-0.70	-0.07	0.73	-0.58	0	-2.5	-2.6	19.7
9	-0.09	0.16	-0.31	-0.20	0.14	0	-14.8	-12.9	0
40	0.09	0	0	0	0	0	0	0	0
62	0.04	-0.09	0	0	0	0	0	0	0
73	0.73	0	0	1.17	0	0	0	0	0
230	-0.03	0	-0.57	0	0	-1.46	192.8	38.0	-8.7
241	-0.90	1.31	0	-2.82	1.28	0	-9.1	-3.3	-215.0
252	0.07	0	1.02	0	0	1.02	-38.2	193.0	0
263	-0.21	-0.07	-3.76	-0.44	0	-5.73	518.0	180.5	24.6
268	-0.22	0.31	0	-0.52	0.30	0	0	0	-20.6
294	0.27	-0.44	0	0.55	-0.40	0	0	0	6.3

TABLE 4-IV

SUMMARY OF ATLAS/BURNER II NEAR-EARTH POLAR-ORBIT MISSION ERROR ANALYSIS RESULTS

(TG-266 System with Initial Azimuth Alignment Error = 20 arc sec)

	Position (km)			Velocity (m/sec)			Orientation (arc sec)		
	R	T	N	R	T	N	Yaw	Roll	Pitch
7	-0.05	0	-0.81	0	0	-0.71	19.8	-22.6	0
8	0.29	-0.70	-0.07	0.73	-0.58	0	0	0	19.7
9	-0.09	0.16	-0.31	-0.20	0.14	0	-14.8	-12.9	0
40	0.06	0	0	0	0	0	0	0	0
62	0.03	-0.06	0	0	0	0	0	0	0
73	0.23	0	0	0.37	0	0	0	0	0
230	-0.02	0	-0.27	0	0	0.70	93.0	18.0	0
241	-0.44	0.63	0	-1.37	0.61	0	0	0	-104.0
252	0.03	0	0.49	0	0	0.49	-18.0	93.0	0
263	-0.05	-0.02	-0.96	0	0	1.46	132.2	46.0	-6.3
294	0.12	-0.20	0	0.24	0	0	0	0	0

2) Circularize when the desired 926.5-km altitude is reached.

3) Perform the inclination correct at equatorial crossing.

The results from a 1000-run Monte Carlo analysis of the above correction sequence are indicated in Figure 4-1. Both the average ΔV and 95% ΔV requirements are shown. As expected, the TG-266 system shows a performance effectiveness two to three times better than the TG-166. The "knee" of the 95% ΔV curves occurs near 20 arc sec, however, no really significant degradation occurs before 1 arc min. Operationally, a value of 20 arc sec can be achieved by optical means and is a recommended prelaunch value.

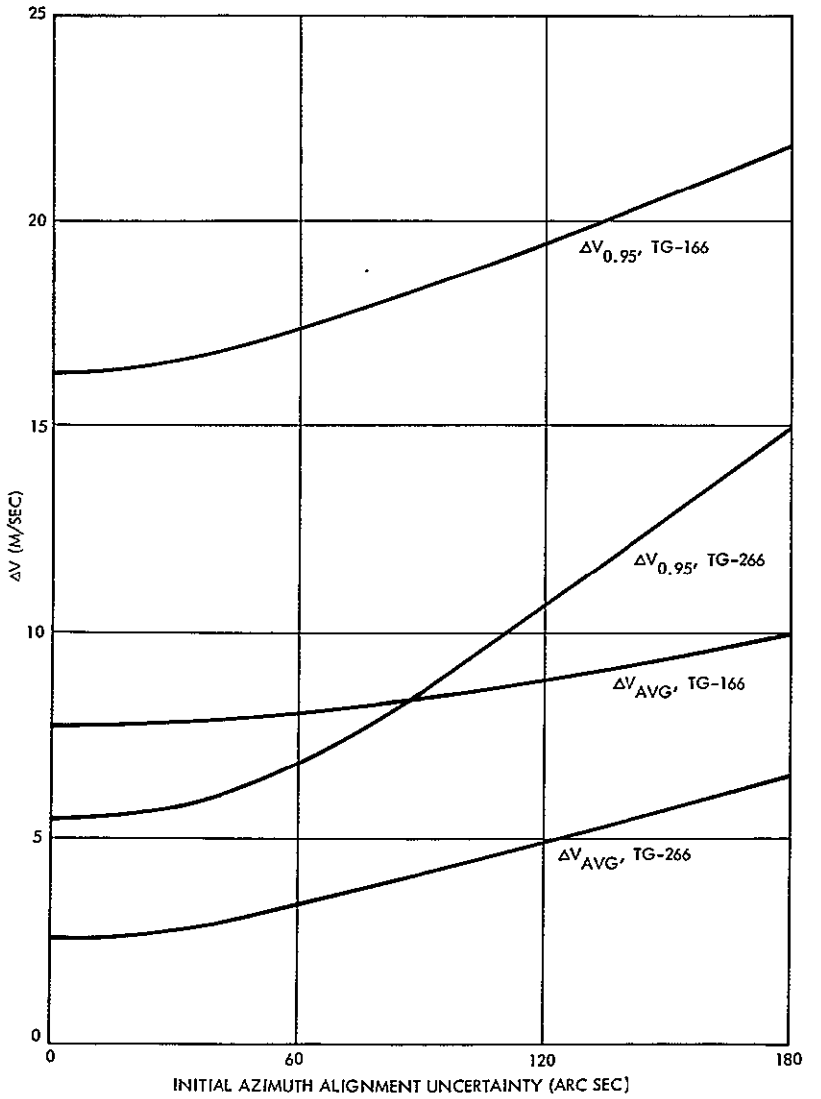

Figure 4-1. Corrective Velocity Requirements for Atlas/Burner II Near-Earth Polar-Orbit Mission

4.3 ANALYSIS OF THE SUN SIGHTING, PERIGEE BURN-TIME UPDATE

In the Task II report (Ref. 4-1), it was recommended that a time update be provided to ensure that Centaur ignition for the transfer from the 185-km parking orbit to synchronous altitude be executed at equatorial crossing. The benefits of this concept are evident, comparing the orbit trim 95% ΔV requirements shown in Table 4-V, which were extracted from the referenced report.

It was proposed that the time update be achieved by means of a sun/earth sighting technique. The pertinent geometry for this scheme is illustrated in Figure 4-2. At equatorial crossing, the angle E measured in the orbital plane from the ascending node is 0 or π, depending on whether ignition is desired at the ascending or descending node, respectively. Then the zenith angle at equatorial crossing is determined from

$$\cos A_o = \pm (\cos \Omega \cos \tau - \sin \Omega \sin \tau \cos i_e) \qquad (4\text{-}1)$$

where

Ω = longitude of the ascending node

τ = sun angle measured in the ecliptic plane from vernal equinox

i_e = obliquity of the ecliptic = 23.4^o

$+$ is used for ignition at the ascending node

$-$ is used for ignition at the descending node

Thus, with known nominal values for Ω and τ, A_o is precomputable. By continually comparing this value against the zenith angle, A, to the sun measured in orbit via the earth scanner/digital aspect sensor combination, ignition can be commanded when $A_o - A = 0$. The primary constraint on this proposed scheme is that for a period of 5 to 15 min prior to, and up to, equatorial crossing, $45 \leq A \leq 90^o$. The time update accuracy of this technique depends on sensor accuracies, the accuracy of the preknowledge of launch time (i.e., error in τ), and the accuracy of injection into the 185-km parking orbit (i.e., errors in Ω and i_s, the orbital inclination, nominally 28^o).

TABLE 4-V

SUMMARY OF SYNCHRONOUS MISSION PERFORMANCE ANALYSIS RESULTS

Run No.	Coast Orbits	System No.	Prelaunch Calibration	Time Update	Attitude Update		95% ΔV (m/sec) Required by Payload for Orbit Trim
					Perigee	Apogee	
1	0	166	No	No	No	No	73
2	0	166	No	No	No	Yes	13
3	0	166	Yes	No	No	No	75
4	0	166	Yes	No	No	Yes	9
5	0	266	No	No	No	No	35
6	0	266	No	No	No	Yes	8
7	8	166	No	No	Yes	Yes	163
8	8	166	No	Yes	Yes	Yes	22
9	8	166	Yes	No	Yes	Yes	109
10	8	166	Yes	Yes	Yes	Yes	19
11	8	266	No	No	Yes	Yes	83
12	8	266	No	Yes	Yes	Yes	19

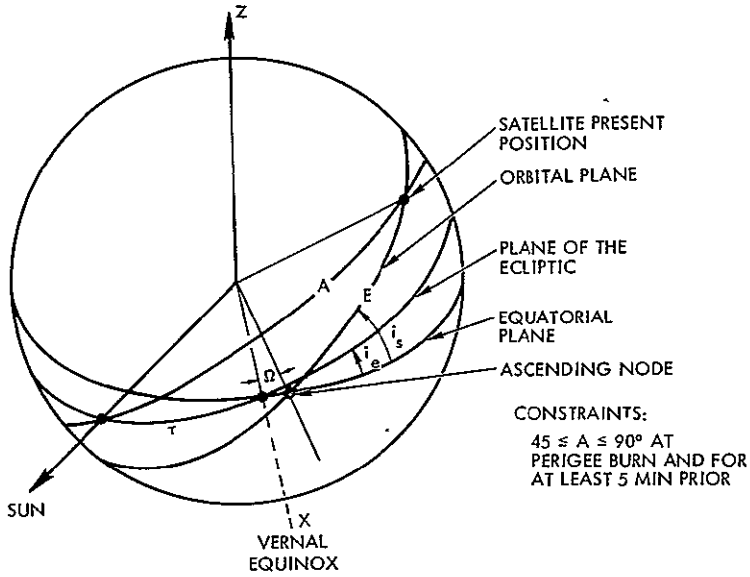

$$\cos A = (\cos \Omega \cos \tau - \sin \Omega \sin \tau \cos i_e) \cos E$$
$$- \left| (\sin \Omega \cos \tau + \cos \Omega \sin \tau \cos i_e) \cos i_s + \sin \tau \sin i_e \sin i_s \right| \sin E$$

Figure 4-2. Sun Sighting Time Update Technique for Multi-Parking Orbit Synchronous Satellite Mission

4.3.1 Visibility Constraints

The 90° limit on A is imposed to preclude the possibility of having to look through the earth's atmosphere and the attendant refraction effects. The lower limit is imposed to ensure a reasonable angular spread between the lines-of-sight to the sun and earth for accurate vehicle attitude updating (with A = 0, the earth and sun are 180° apart and no vehicle yaw attitude information can be obtained).

Equation (4-1) can be manipulated to determine those combinations of Ω and τ that satisfy the $45^{\circ} \leq A \leq 90^{\circ}$ constraint. Some typical results are shown in Figure 4-3. For illustrative purposes, consider the curve labeled (50°, A). Any Ω, τ combination falling on this curve gives an angle A of 50° at the ascending node and further, $45 \leq A \leq 90^{\circ}$ for at least 5 min prior to reaching the ascending node.

4.3.2 Accuracy Considerations

In general, satisfaction of $A_o - A = 0$ results in an error in E from the desired 0 or π value because of the errors mentioned previously. The possible errors in τ should be considered first.

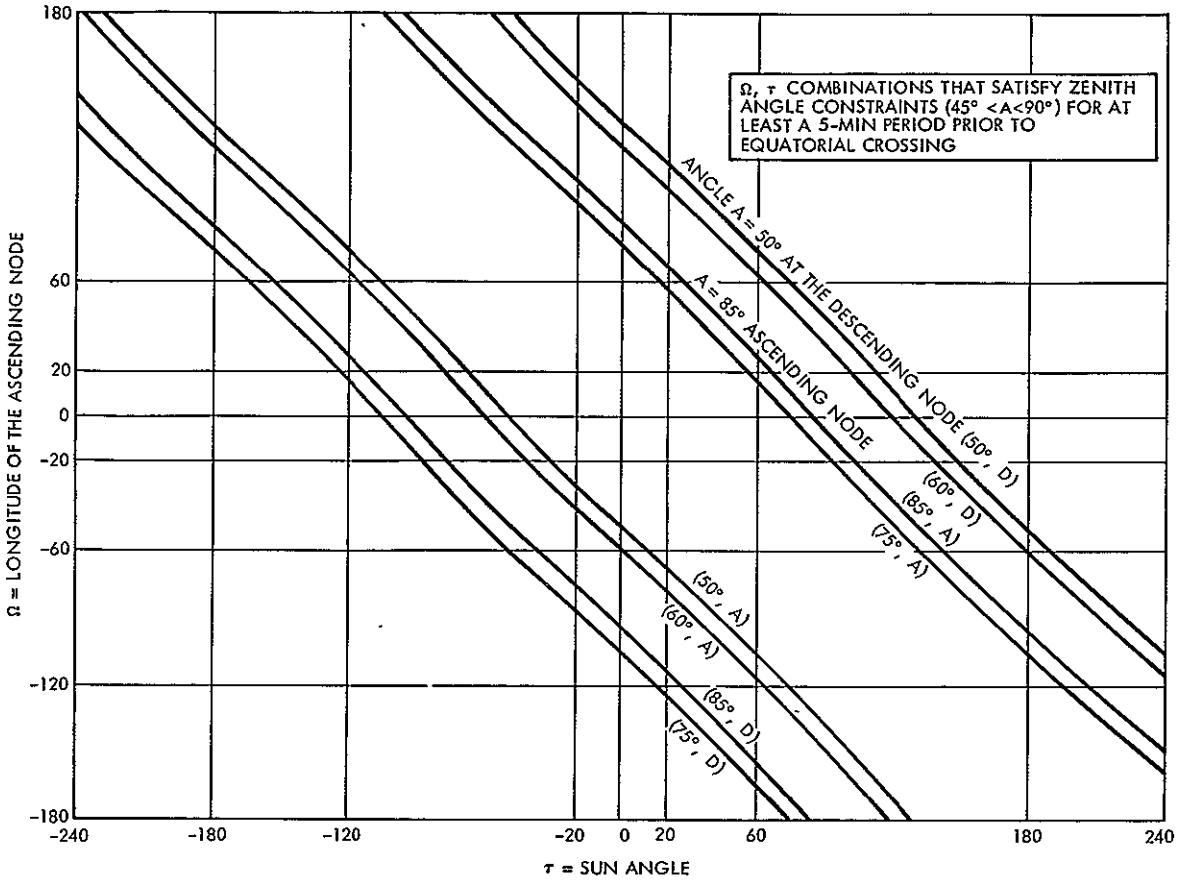

Figure 4-3. Combinations of Ω and τ that Satisfy the Visibility Constraints

If there were no error in launch time or orbital period, and if τ were known precisely at launch, it would be easy to compute the value of τ that would exist at any equatorial crossing. Errors in launch time or in orbital period would cause a deviation from this nominal value. But τ varies nearly linearly with time, so that if τ is known at <u>any</u> time, an accurate value of τ can always be obtained from the computer by periodically updating τ under control of the internal clock. If this scheme is used, the only errors in τ arise because of clock errors, and launch time and orbital period errors have no effect on τ.

The sun angle varies by only 360°/yr, or approximately 1°/day. If an update were performed every minute, the maximum error would be about 0.04 arc min. In practice, updates could be performed much more frequently if desired. The contribution of the clock error should be completely negligible.

If the method for updating τ described above is used, errors in τ become uncorrelated from the injection errors. Also, errors in the sensor measurement are uncorrelated with all other errors. Errors in Ω are a function of injection errors, and it will be shown that errors in the orbital inclination, i_s, have no effect. Thus, the total error in angle E can be written simply as

$$\delta E = \left(\frac{\partial E}{\partial \Omega}\right)\delta\Omega + \left(\frac{\partial E}{\partial \tau}\right)\delta\tau + \left(\frac{\partial E}{\partial A}\right)\delta A \qquad (4\text{-}2)$$

The various sensitivities may be determined by differentiating the complete expression for cos A shown in Figure 4-2 with respect to all the variables, and evaluating these derivatives at the nominal conditions (i.e., at $E = 0^{\circ}$). When this is done $\partial E/\partial i_s$ is seen to be zero. The other sensitivities are

$$\frac{\partial E}{\partial \Omega} = -\frac{\sin\Omega\cos\tau + \cos\Omega\sin\tau\ \sin i_e}{D} = K_1 \qquad (4\text{-}3)$$

$$\frac{\partial E}{\partial \tau} = -\frac{\cos\Omega\sin\tau + \sin\Omega\ \cos\tau\ \cos i_e}{D} = K_2 \qquad (4\text{-}4)$$

$$\frac{\partial E}{\partial A} = \frac{\sin A}{D} = K_3 \qquad (4\text{-}5)$$

where

$$D = (\sin\Omega\ \cos\tau + \cos\Omega\sin\tau\cos i_e)\cos i_s + \sin\tau\ \sin i_e\ \sin i_s \qquad (4\text{-}6)$$

Then, the variance of E is given by

$$\sigma_E^{\,2} = K_1^{\,2}\,\sigma_\Omega^{\,2} + K_2^{\,2}\,\sigma_\tau^{\,2} + K_3^{\,2}\,\sigma_A^{\,2} \qquad (4\text{-}7)$$

Since errors in measured A and τ are uncorrelated with each other and with anything else,

$$\sigma_\tau = \delta\tau$$

and

$$\sigma_A = \delta A$$

From the covariance matrix of RTN position and velocity error components at injection into the 185-km parking orbit, σ_Ω may be computed.

The angular momentum vector of a satellite is perpendicular to the orbit plane and is given by $\underline{H} = \underline{R} \times \underline{V}$, where $\underline{R}$ and $\underline{V}$ are the position and velocity vectors of the satellite. The cross product of a unit vector along the Z-axis ($\underline{\mu}_Z$) with the unit vector along the H vector ($\underline{\mu}_H$) results in a vector in a direction perpendicular to both of them ($\underline{\mu}_\Omega$). To be perpendicular to $\underline{H}$, it must lie in the orbit plane, and therefore passes through the ascending and descending nodes. Because of the order in which the cross products were taken, its positive direction is toward the ascending node. But the angle Ω is defined as the angle between the X-axis and the ascending node, so that

$$\cos\Omega = \underline{\mu}_X \cdot \underline{\mu}_\Omega \tag{4-8}$$

$$\delta\Omega = -\left[1 - (\underline{\mu}_X \cdot \underline{\mu}_\Omega)^2\right]^{-\frac{1}{2}} d(\underline{\mu}_X \cdot \underline{\mu}_\Omega) \tag{4-9}$$

But

$$d(\underline{\mu}_X \cdot \underline{\mu}_\Omega) = \underline{\mu}_X \cdot d(\underline{\mu}_\Omega) \tag{4-10}$$

since $\underline{\mu}_X$ is a constant, therefore

$$d(\underline{\mu}_\Omega) = d\left[\frac{(\underline{\mu}_Z \times \underline{\mu}_H)}{|\underline{\mu}_Z \times \underline{\mu}_H|}\right] \tag{4-11}$$

After the differentiation has been performed, the partial derivatives may be written as

$$
\begin{aligned}
\frac{\partial \Omega}{\partial X} &= \frac{-\dot{Z}\ T1}{B} \\
\frac{\partial \Omega}{\partial Y} &= \frac{\dot{Z}\ T2}{B} \\
\frac{\partial \Omega}{\partial Z} &= \frac{\dot{X}\ T1 - \dot{Y}\ T2}{B} \\
\frac{\partial \Omega}{\partial \dot{X}} &= \frac{Z\ T1}{B} \\
\frac{\partial \Omega}{\partial \dot{Y}} &= \frac{-Z\ T2}{B} \\
\frac{\partial \Omega}{\partial \dot{Z}} &= \frac{-X\ T1 + Y\ T2}{B}
\end{aligned}
\qquad (4\text{-}12)
$$

where

$$
\begin{aligned}
T1 &= Y\dot{Z} - Z\dot{Y} \\
T2 &= X\dot{Z} - Z\dot{X} \\
B &= T1^2 - T2^2
\end{aligned}
$$

and where X, Y, Z, $\dot{X}$, $\dot{Y}$, $\dot{Z}$ are the components of position and velocity.

Letting F denote the matrix of partial derivatives shown above, then

$$
\delta\Omega = F \begin{Bmatrix} \delta X \\ \delta Y \\ \delta Z \\ \delta \dot{X} \\ \delta \dot{Y} \\ \delta \dot{Z} \end{Bmatrix} \qquad (4\text{-}13)
$$

If C denotes the covariance of the state vector, then

$$
\sigma_\Omega^2 = F\, C\, F^T \qquad (4\text{-}14)
$$

The resulting value for σ_Ω is 5.2 arc min.

It was assumed that τ was updated as infrequently as every 15 sec. Then the maximum error $\delta\tau$ is approximately 0.01 arc min. The error in measured zenith angle attributable to the solar aspect and earth sensors

was taken to be conservatively 20 arc min (the solar aspect sensor accuracy is approximately 3 arc min and the earth horizon scanner accuracy is approximately 12 arc min).

Evaluation of the sensitivity coefficients, Equations (4-3) through (4-5), shows these to be all of approximate unity magnitude, and thus, σ_E is approximately 20.6 arc min. The timing error is related by

$$\sigma_T = \sigma_E / \dot{E}$$

or, for the 185-km parking orbit altitude,

$$\sigma_T \cong 4 \text{ sec}$$

In the Task II study, a value of $\sigma_T = 0.238$ sec was used; thus, the new value is a factor of 17 larger.

However, even this magnitude increase does not degrade ultimate performance as shown in Tables 4-VI and 4-VII. These tables summarize the major error contributors to Runs 8 and 12, respectively, of Table 4-V. The underlined error source, No. 39, is the time update error and the values correspond to those for $\sigma_T = 0.238$ sec. Increasing these by a factor of 17 results in the rss errors labeled "new" in Tables 4-VI and 4-VII. The resulting 95% ΔV requirements have increased by only 1 m/sec in each case. Thus, even with the relatively coarse time update of 4 sec, the total performance is still significantly improved over the cases without time update (see Runs 7, 9, and 11 of Table 4-V).

4.4 POWERED PERFORMANCE ANALYSES OF THE MARS MISSIONS

4.4.1 Injection Errors

Using the basic error source values of Table 4-I and the powered trajectory to injection into the heliocentric transfer orbit to Mars, the resulting 1-σ rss position and velocity component errors in the RTN coordinates for the two inertial systems are as indicated in Table 4-VIII. The major contributors to these totals are the same as for all previous powered error analysis runs, viz, initial alignment, x- and y-accelerometer biases, x-accelerometer scale factor, gyro bias drift, and y-gyro output axis g-sensitive drift and scale factor.

TABLE 4-VI

SUMMARY OF LONG COAST SYNCHRONOUS SATELLITE MISSION
ERROR ANALYSIS RESULTS (TG-166 SYSTEM)

	Error Source	Position (km)			Velocity (m/sec)			Orientation (arc sec)			95% ΔV (m/sec)
		R	T	N	R	T	N	Yaw	Roll	Pitch	
Initial orientation	9	-19.2	18.3	9.9	-2.6	0.6	0.3	0	0	0	
Roll attitude at apogee burn	10	0.1	0.0	0.0	3.8	-0.1	0.0	14	475	257	
Roll attitude at perigree burn	11	- 3.7	2.1	1.9	-0.5	-0.6	1.4	0	0	0	
Yaw attitude at apogee burn	20	0.0	0.0	0.0	0.0	-0.5	-1.0	120	-3	- 2	
Pitch attitude at apogee burn	30	0.0	0.0	0.0	-0.6	0.0	0.0	0	57	-106	
Pitch attitude at perigee burn	31	-12.1	117.6	63.7	-5.9	0.3	0.2	0	0	0	
Time Update	39	0.3	4.4	2.4	-0.2	0.0	0.0	0	0	0	
X- Accelerometer bias	40	5.4	- 7.0	- 3.8	0.8	-0.1	-0.1	0	0	0	
Y- Accelerometer bias	62	- 1.1	1.5	0.8	-0.2	0.0	0.0	0	0	0	
X- Accelerometer scale factor	73	27.1	-35.1	-19.0	4.2	-0.6	-0.4	0	0	0	
X- Bias drift	230	- 0.3	- 2.0	4.2	0.8	-0.1	-0.1	2	113	47	
Y- Bias drift	241	44.2	-22.0	-11.9	4.3	-1.4	-0.8	0	47	-113	
Z- Bias drift	252	0.5	3.9	- 8.3	0.1	0.5	0.8	-128	2	1	
Y- Gyro OA g-sensitive drift	268	8.4	- 6.5	- 3.5	1.0	-0.3	-0.2	0	-2	- 3	
Y- Gyro scale factor	294	-13.3	10.2	5.5	-1.7	0.4	0.2	0	0	0	
	RSS (old)	59.1	128.0	73.8	9.9	2.0	2.1				22
	RSS (new)	59.5	148.2	84.3	10.4	2.0	2.1				23

TABLE 4-VII

SUMMARY OF LONG COAST SYNCHRONOUS SATELLITE MISSION ERROR ANALYSIS RESULTS (TG-266 SYSTEM)

	Error Source	Position (km)			Velocity (m/sec)			Orientation (arc sec)			95% ΔV (m/sec)
		R	T	N	R	T	N	Yaw	Roll	Pitch	
Initial orientation	9	-19.2	18.3	9.9	-2.6	0.6	0.3	0	0	0	
Roll attitude at apogee burn	10	0.1	0.0	0.0	3.8	-0.1	0.0	14	475	257	
Roll attitude at perigree burn	11	- 3.7	2.1	1.9	-0.5	-0.6	1.4	0	0	0	
Yaw attitude at apogee burn	20	0.0	0.0	0.0	0.0	-0.5	-1.0	120	-3	- 2	
Pitch attitude at apogee burn	30	0.0	0.0	0.0	-0.6	0.0	0.0	0	57	-106	
Pitch attitude at perigee burn	31	-12.1	117.6	63.7	-5.9	0.3	0.2	0	0	0	
Time Update	39	0.3	4.4	2.4	-0.2	0.0	0.0	0	0	0	
X- Accelerometer bias	40	3.6	- 4.7	-2.5	0.5	-0.1	-0.1	0	0	0	
X- Accelerometer scale factor	73	8.7	-11.2	-6.1	1.3	-0.2	-0.2	0	0	0	
X- Bias drift	230	- 0.2	- 1.0	2.0	0.4	0.0	0.1	1	54	23	
Y- Bias drift	241	21.3	-10.6	-5.7	2.1	-0.7	-0.4	0	23	- 54	
Z- Bias drift	252	0.2	1.9	-4.0	0.0	0.3	0.4	-62	1	0	
Y- Gyro scale factor	294	- 6.1	4.7	2.5	-0.8	0.2	0.1	0	0	0	
	RSS (old)	33.2	121.0	66.0	8.0	1.3	1.8				19
	RSS (new)	33.6	142.2	77.6	8.7	1.3	1.8				20

TABLE 4-VIII

SATURN V MARS MISSION INJECTION ERRORS (INITIAL AZIMUTH ALIGNMENT ERROR = 20 ARC SEC)

System	Position (km)			Velocity (m/sec)		
	R	T	N	R	T	N
TG-166	7.1	2.01	3.37	7.96	2.89	4.84
TG-266	3.37	1.02	1.07	3.52	1.30	1.61

As the initial azimuth alignment value (error source No. 7) is varied parametrically, only the normal components of position and velocity in Table 4-VIII vary. The variation is as indicated in Figure 4-4. The 20-arc sec value again appears to be a satisfactory compromise between operational feasibility and system performance.

4.4.2 Target Misses Due to Injection Errors

The sensitivity matrix, C, relating injection errors to target misses in the commonly accepted $\overline{B} \cdot \overline{T}$ and $\overline{B} \cdot \overline{R}$ coordinates is

$$C = \begin{bmatrix} \frac{\partial(\overline{B} \cdot \overline{T})}{\partial X} & \frac{\partial(\overline{B} \cdot \overline{T})}{\partial Y} & \frac{\partial(\overline{B} \cdot \overline{T})}{\partial Z} & \frac{\partial(\overline{B} \cdot \overline{T})}{\partial \dot{X}} & \frac{\partial(\overline{B} \cdot \overline{T})}{\partial \dot{Y}} & \frac{\partial(\overline{B} \cdot \overline{T})}{\partial \dot{Z}} \\ \frac{\partial(\overline{B} \cdot \overline{R})}{\partial X} & \cdot & \cdot & \cdot & \cdot & \frac{\partial(\overline{B} \cdot \overline{R})}{\partial \dot{Z}} \end{bmatrix}$$

The numerical values of the sensitivity coefficients are obtained from the "Interplanetary Search Program" (ISP), and for the Type I and Type II transfer trajectories they are approximately

$$C_I = \begin{bmatrix} 0.1188E5 & -0.336E5 & -0.121E5 & 0.455E8 & -0.260E7 & 0.241E8 \\ -0.155E5 & 0.315E5 & 0.156E5 & -0.429E8 & -0.153E7 & -0.284E8 \end{bmatrix}$$

$$C_{II} = \begin{bmatrix} -0.962E5 & 0.164E6 & 0.943E5 & -0.224E9 & -0.156E9 & 0.685E8 \\ 0.267E5 & -0.424E5 & -0.274E5 & 0.610E8 & 0.387E8 & 0.183E8 \end{bmatrix}$$

where

the E denotes powers of 10, and the units are km/km and km/km/sec.

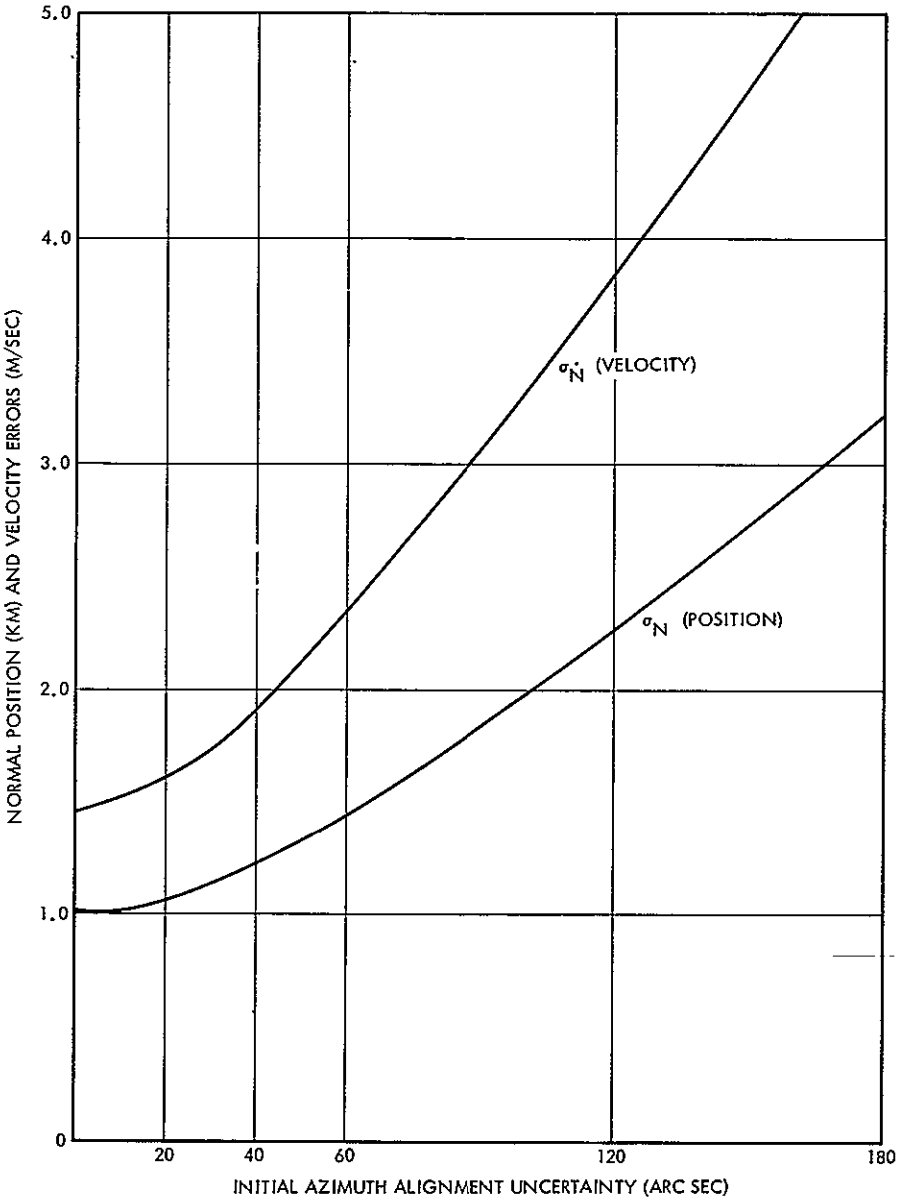

Figure 4-4. Normal Component Sensitivity to Initial Azimuth Uncertainty

The uncorrected target miss covariance matrix is

$$\Sigma_T = C\Sigma_{INJ}\, C^T \tag{4-15}$$

where

Σ_{INJ} is the 6 x 6 injection error covariance matrix obtained from GEAP II expressed in ECI coordinates.

Evaluation of Eq. (4-15) yields, for the Type I trajectory,

$$\Sigma_T = \begin{bmatrix} 7.8954E10 & -7.2562E10 \\ -7.2562E10 & 6.6956E10 \end{bmatrix} km^2 \qquad (4-16)$$

and for the Type II trajectory

$$\Sigma_T = \begin{bmatrix} 1.3754E12 & -3.7192E11 \\ -3.7192E11 & 1.0058E11 \end{bmatrix} km^2 \qquad (4-17)$$

The resulting error ellipses corresponding to the covariance matrices of Eqs. (4-16) and (4-17) are depicted in Figures 4-5 and 4-6, respectively.

4.4.3 Corrective Velocity Requirements

To determine the midcourse velocity required to correct for the injection errors, one of the options of GEAP II is used. This option requires the inputting of the 3 x 6 guidance sensitivity matrix G, which is composed of the partials of the three midcourse velocity components (ΔV_x, ΔV_y, and ΔV_z) with respect to the six injection error components. The matrix G is obtained from ISP for specific times of application of the midcourse correction. Two types of G can be obtained: one for miss plus time-of-arrival correction and one for miss only. The program outputs are $\Sigma_{\Delta V}$, the midcourse correction velocity covariance matrix, and the expected 95% ΔV value. The results obtained from this GEAP II option are summarized in Table 4-IX.

4.4.4 Corrected Target Miss

Inasmuch as the midcourse velocity corrections will not be applied perfectly, the target miss ellipses of par. 4.4.2 will not be eliminated completely. From subsec. 8.4 of Ref. 4-1, the velocity application error along the thrust and cross axis directions is

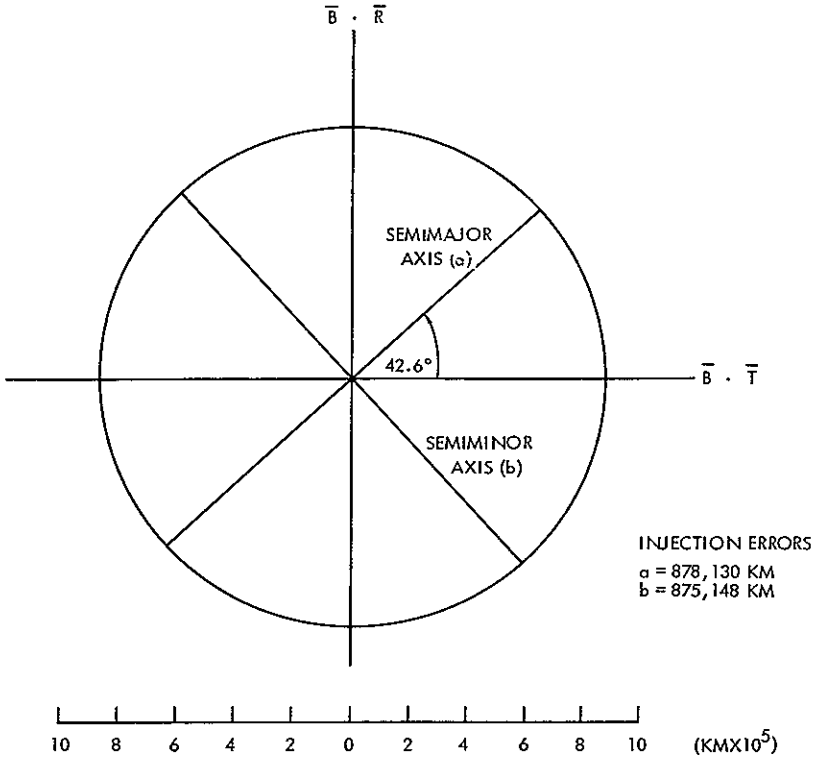

Figure 4-5. Mars Trajectory, Type I (Uncorrected Miss Ellipse)

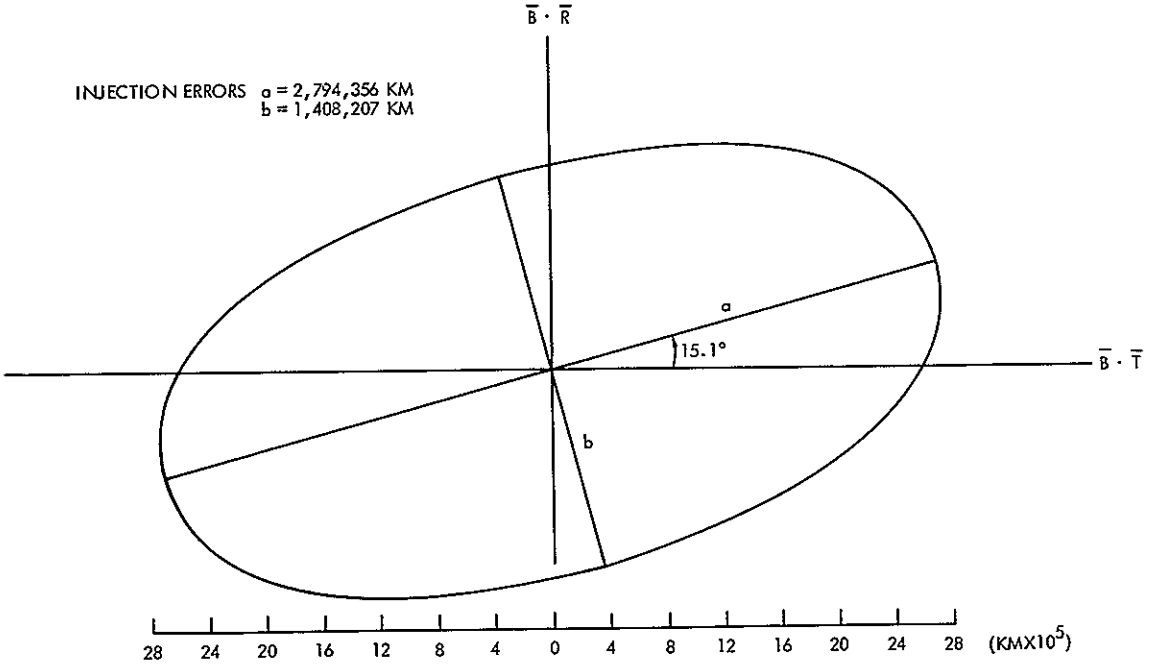

Figure 4-6. Mars Trajectory, Type II (Uncorrected Miss Ellipse)

TABLE 4-IX.

NINETY-FIVE PERCENT ΔV MIDCOURSE (5 DAYS) REQUIREMENTS FOR 1975 MARS MISSIONS

Trajectory Type	Correction Type	System	95% ΔV (m/sec)
I	M + T*	TG-166	77.8
I	M**	TG-166	70.5
II	M + T	TG-166	77.1
II	M	TG-166	57.6
I	M + T	TG-266	35.4
I	M	TG-266	32.0
II	M + T	TG-266	35.7
II	M	TG-266	26.6

*Miss plus time-of-flight correction.

**Miss correction only.

$$\frac{\epsilon(\Delta V)}{\Delta V} = 0.43 \times 10^{-3} = \sqrt{\sigma_s^2}$$

$$\frac{\epsilon(\Delta V_{\text{cross axis}})}{\Delta V} = 10^{-3} \text{ rad} = \sqrt{\sigma_p^2}$$

and the execution error covariance matrix is

$$\Sigma_e = (\sigma_s^2 - \sigma_p^2)\, \Sigma_{\Delta V} + \sigma_p^2 \left|\overline{V}\right|^2 I$$

where

$\left|\overline{V}\right|^2$ = expected value of V squared

I = unit matrix

The target miss covariance matrix following the imperfect midcourse correction is then

$$\Sigma_{TM} = M \Sigma_e M^T$$

where M is the sensitivity matrix relating midcourse velocity errors to target misses in the $\overline{B} \cdot \overline{T}$, $\overline{B} \cdot \overline{R}$ coordinates. At 5 days after injection, the numerical results for the Type I and Type II trajectories are, respectively,

$$\Sigma_{TM} = \begin{bmatrix} -1.616E5 & -1.484E5 \\ -1.484E5 & 1.370E5 \end{bmatrix} km^2$$

and

$$\Sigma_{TM} = \begin{bmatrix} 2.814E6 & -7.610E5 \\ -7.610E5 & 2.058E5 \end{bmatrix} km^2$$

The resulting error ellipses are depicted in Figures 4-7 and 4-8.

4.5 SUMMARY OF POWERED PERFORMANCE ANALYSES OF THE JUPITER MISSIONS

The Jupiter missions were analyzed for only one value of initial azimuth misalignment, viz, 20 arc sec. For this value, the Saturn IB/Centaur injection errors are those indicated in Table 4-X for the TG-266 system.

TABLE 4-X.

SATURN IB/CENTAUR JUPITER MISSIONS INJECTION ERRORS (RTN COORDINATES)

Position (km)			Velocity (m/sec)		
R	T	N	R	T	N
0.97	1.40	1.89	4.12	2.02	5.46

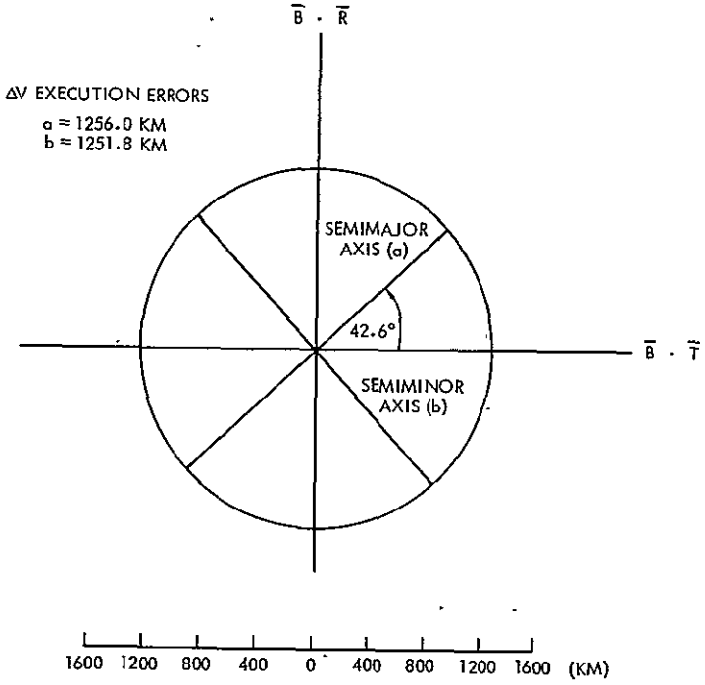

Figure 4-7. Mars Trajectory, Type I (Miss Ellipse After First Midcourse)

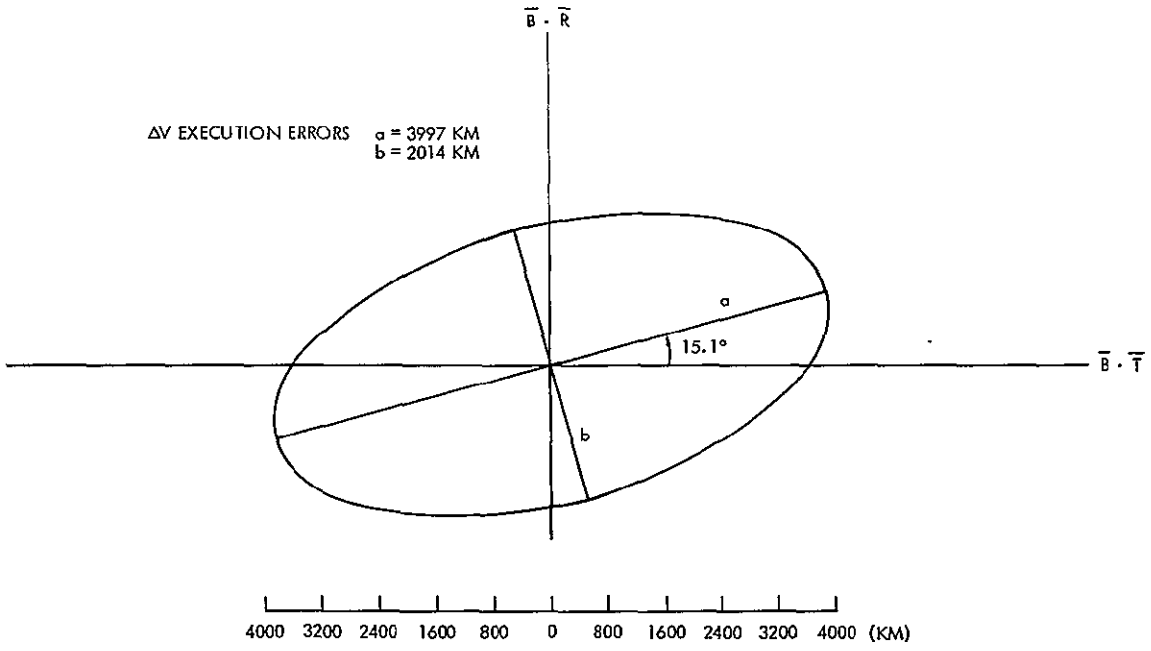

Figure 4-8. Mars Trajectory, Type II (Miss Ellipse After First Midcourse)

The resulting uncorrected target miss covariance matrices for the solar probe and the cross ecliptic probe are, respectively,

$$\Sigma_T = \begin{bmatrix} 2.551E10 & 7.144E9 \\ 7.144E9 & 2.121E9 \end{bmatrix} km^2$$

and

$$\Sigma_T = \begin{bmatrix} 2.328E10 & 6.65E9 \\ 6.65E9 & 2.023E9 \end{bmatrix} km^2$$

The corresponding error ellipses are shown in Figures 4-9 and 4-10. The midcourse 95% velocity requirements at 5 days after injection to correct for the injection errors are tabulated in Table 4-XI.

The corrected target miss ellipses are, respectively,

$$\Sigma_{TM} = \begin{bmatrix} 5.22E4 & 1.462E4 \\ 1.462E4 & 4.339E3 \end{bmatrix} km^2$$

and

$$\Sigma_{TM} = \begin{bmatrix} 4.763E4 & 1.361E4 \\ 1.361E4 & 4.14E3 \end{bmatrix} km^2$$

and the corresponding error ellipses are depicted in Figures 4-11 and 4-12.

4.6 MARS APPROACH ANALYSES

The navigation performance analyses for interplanetary and planet approach phases conducted under Tasks I and II of this study have been modified and extended to the extent summarized below:

a) New approach trajectories to Mars have been incorporated (nominal perifocus altitude of 1100 km for both Type I and II trajectories, see sec. 2).

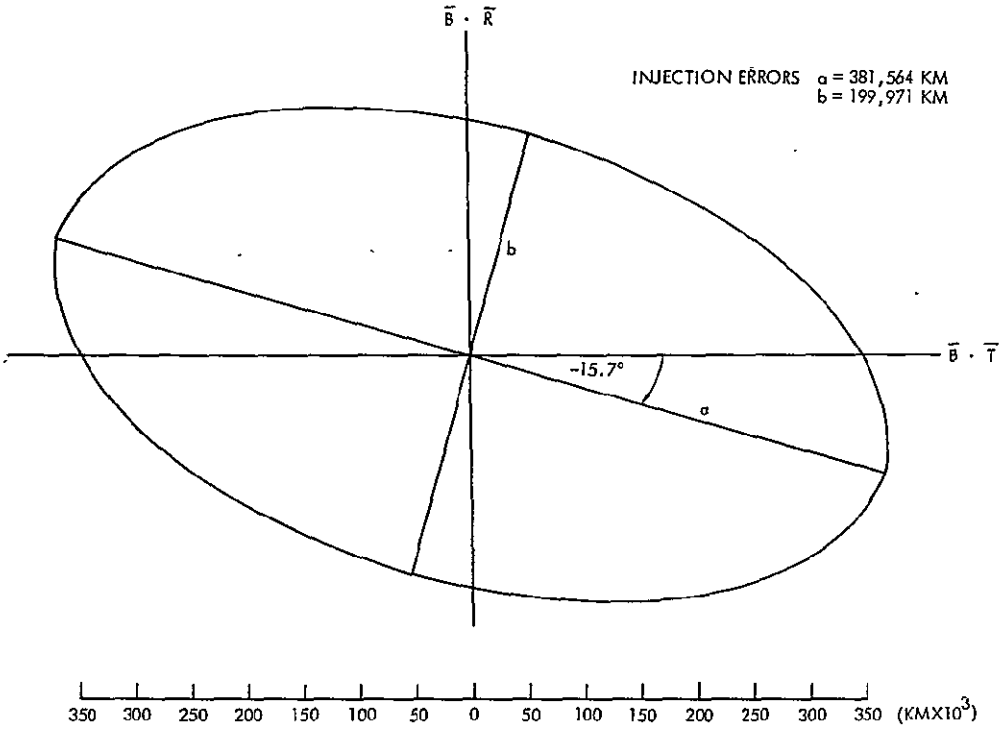

Figure 4-9. Jupiter, Solar Probe Trajectory (Uncorrected Miss Ellipse)

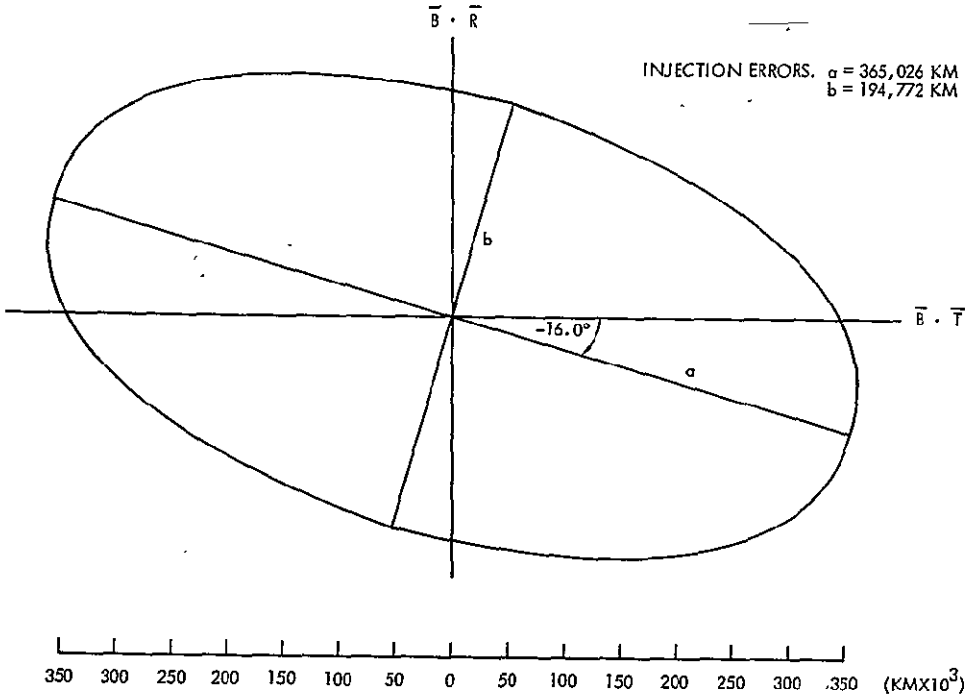

Figure 4-10. Jupiter, Out of Ecliptic Trajectory (Uncorrected Miss Ellipse)

TABLE 4-XI

NINETY-FIVE PERCENT ΔV MIDCOURSE (5 DAYS) REQUIREMENTS FOR THE TWO 1971 JUPITER MISSIONS (TG-266 SYSTEM)

Mission	Correction Type	95% ΔV (m/sec)
Solar Probe	M + T*	10.5
	M**	9.1
Cross Ecliptic Probe	M + T	10.5
	M	9.1

*Miss plus time-of-flight correction.

**Miss correction only.

b) Approach navigation performance was investigated starting from 50 days before encounter, rather than throughout the interplanetary trajectory. (Previous results indicated that significant orbit determination improvements did not occur until about 10 days before encounter.)

c) For the doppler plus onboard optical measurement cases, optical measurements were utilized only in the region where the Mars subtense angle was between 0.2° and 3°. (This corresponds to roughly the time period from 350 hr down to 11 hr prior to encounter for both trajectories, Figure 4-13). See par. 4.6.3 for further discussion.

d) The position and velocity errors as given in the Tasks I and II report were converted to errors in basic approach parameters.

e) The effects of errors in approach trajectory determination and deboost execution errors on total fuel requirements were investigated.

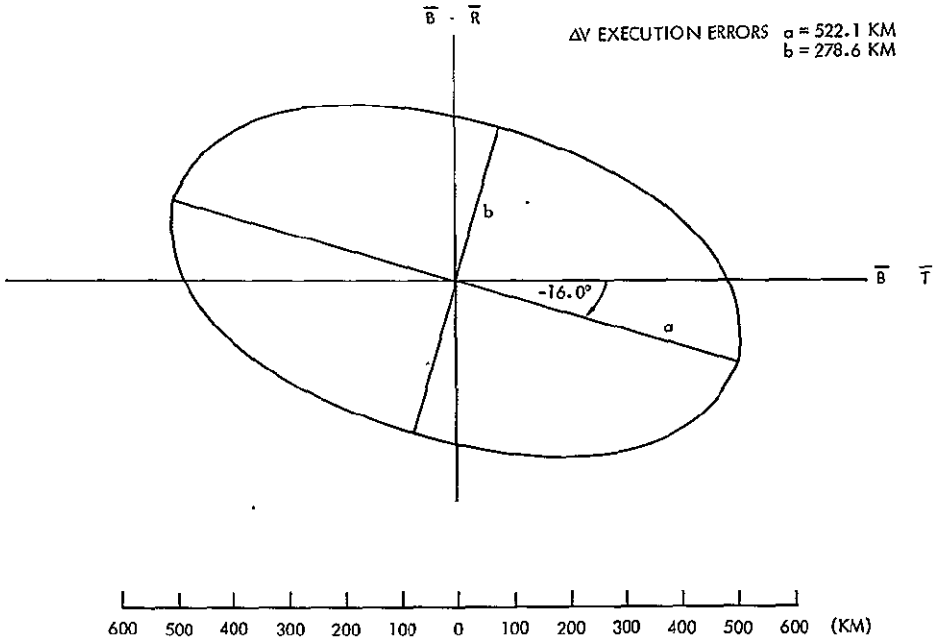

Figure 4-11. Jupiter, Out of Ecliptic Trajectory (Miss Ellipse After First Midcourse)

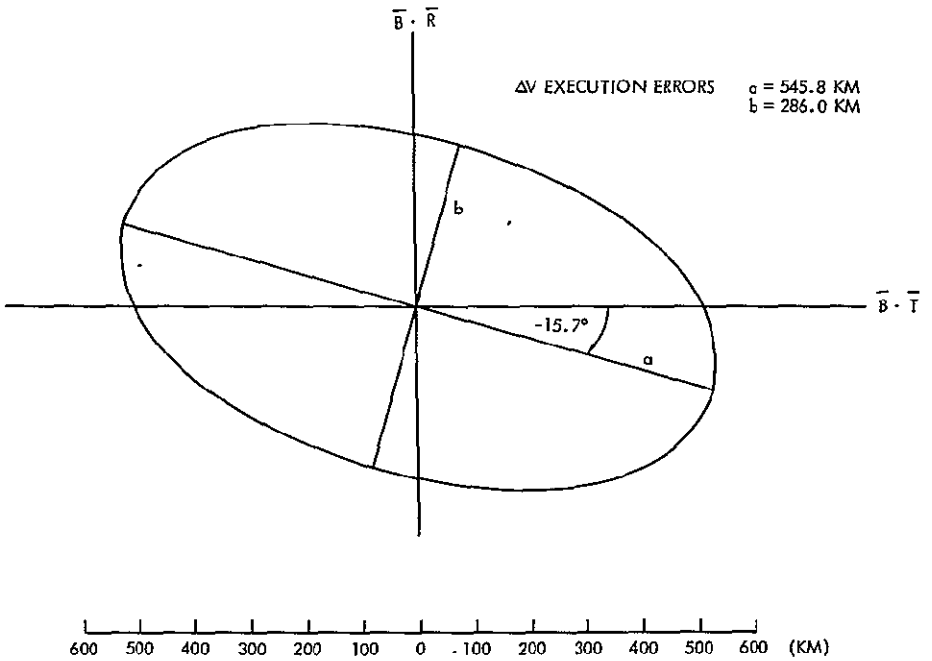

Figure 4-12. Jupiter, Solar Probe Trajectory (Miss Ellipse After First Midcourse)

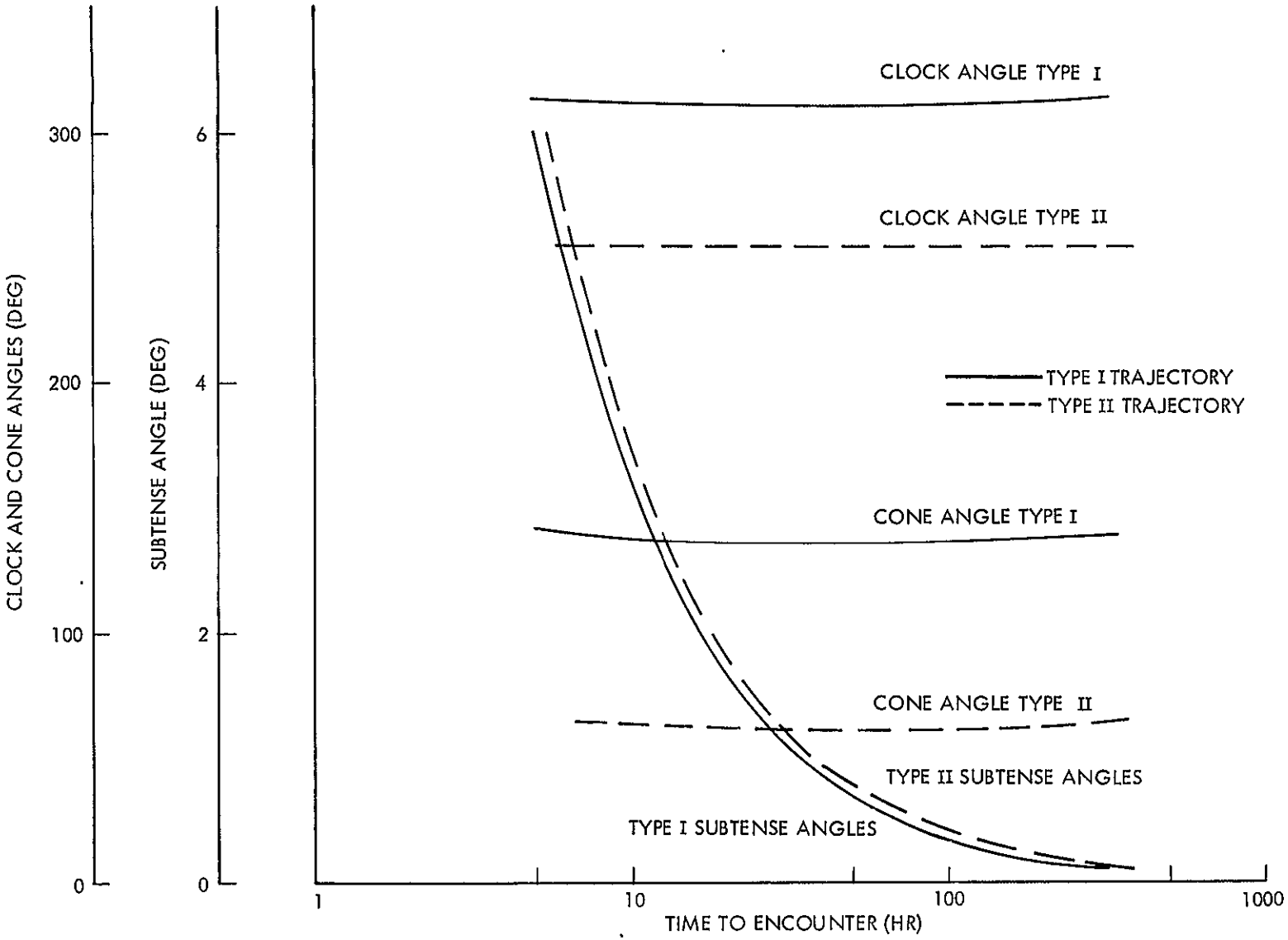

Figure 4-13. Measurement Angles Versus Time to Encounter, 1975 Type I and II Trajectories

For this study, five different configurations were considered:

a) Case 1 — doppler only
b) Case 2 — doppler plus optical Model A*
c) Case 3 — doppler plus optical Model B*
d) Case 4 — doppler plus optical Model C**
e) Case 5 — same as Case 4 less Mars subtense angle measurement

The clock and cone angle measurements used with the optical instruments are illustrated in Figure 4-14. The models are summarized in Tables 4-XII through 4-XV. The nonoptical error model given in Table 4-XII was modified from that used in the previous study to include a more detailed model of the gravitational constant and second zonal harmonic of Mars. These parameters were included in the total error model and switched in when the vehicle approached the sphere of influence of Mars.

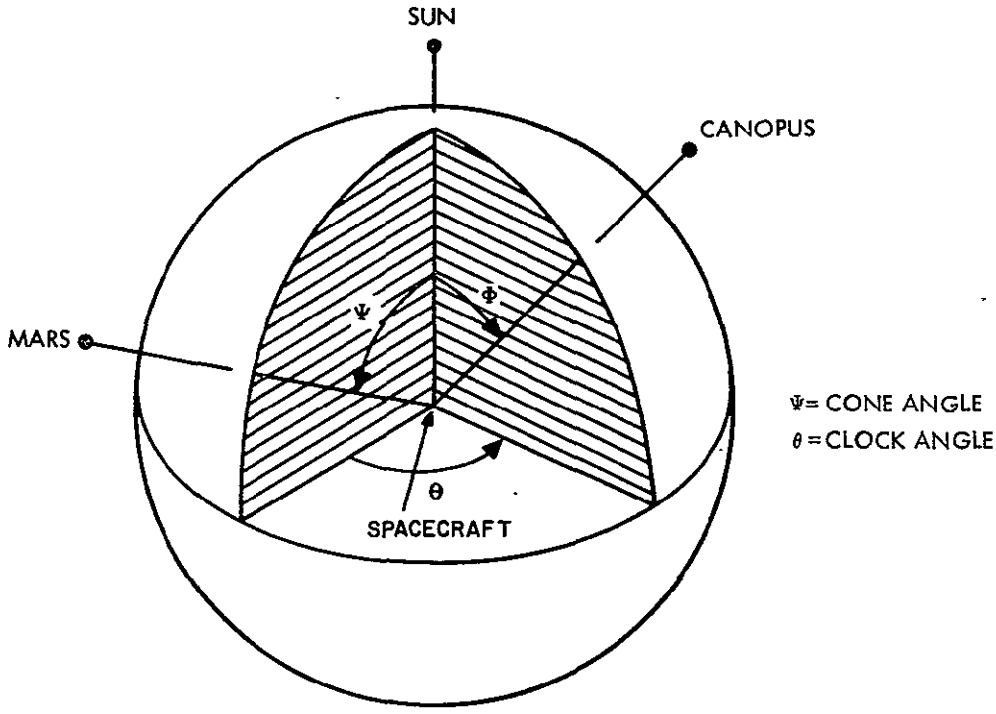

Figure 4-14. Optical Angle Measurements

*Same as that used in Ref. 4-1.

**Model discussed in sec. 5.

TABLE 4-XII

RADIO/OPTICAL/INERTIAL ERROR MODEL MARS MISSION

Error	(Variance)$^{1/2}$	Time Constant
Random acceleration acting on spacecraft* (models uncertainty in the dynamic model of the solar system, i.e., errors in solar pressure forces, gravitational constants, etc.)	0.531×10^{-8} m/sec^2 (0.174×10^{-7} ft/sec^2) (causes a 200-km position error in 176 days)	1 week
Tracking system errors		
• Range rate bias	10^{-2} m/sec (0.0328 ft/sec)	1/3 day
• Uncorrelated noise on doppler rate	0.732×10^{-2} m/sec (0.024 ft/sec) (equivalent to 0.12 ft/sec per 1-sec sample, 25 meas. averaged)	
Vehicle errors at injection (3 hr)		
• Position	2 km (6560 ft)	
• Velocity	2 m/sec (6.56 ft/sec)	
Mars ephemeris error (relative to Earth)		
• Position	220 km (7.22×10^5 ft)	
• Velocity	0.05 m/sec (0.164 ft/sec)	
Radius of Mars	20 km (6.56×10^4 ft)	1 day
Uncertainty in gravitational constant of Mars	8.59556 km^3/sec^2	
Uncertainty in second zonal harmonic of Mars	0.48×10^{-3}	

*Equivalent error averaged over 25 measurements.

TABLE 4-XIII

OPTICAL ERROR MODEL A

Error	(Variance)$^{1/2}$		Time Constant
Sun sensor bias	1.746×10^{-3} rad	(6 arc min)	1/2 week
Sun sensor uncorrelated noise	0.349×10^{-4} rad* (0.1746×10^{-3} rad)**	(0.12 arc min)	
Mars sensor bias	1.92×10^{-3} rad	(6.6 arc min)	1/2 week
Canopus sensor bias	0.873×10^{-3} rad	(3 arc min)	1/2 week
Mars sensor uncorrelated noise	0.349×10^{-4} rad* (0.1746×10^{-3} rad)**		
Canopus sensor uncorrelated noise	0.1746×10^{-4} rad* (0.873×10^{-4} rad)**		
Mars subtense measurement			
Lower limit on (variance)$^{1/2}$ of bias	0.873×10^{-3} rad	(3 arc min)	1/2 week
Error proportional to subtense angle***	1%		1/2 week
Uncorrelated noise	0.1746×10^{-4} rad* (0.873×10^{-4} rad)**	0.06 arc min* (0.3 arc min)**	

*Equivalent error of 25 measurements averaged. This value was used in the error analysis.

**Single measurement error.

***Percent of subtense angle (α) contributing to the standard deviation of the bias error adding to subtense angle, i.e., $\sigma_\alpha^2 = (0.873 \times 10^{-3})^2 + (0.01\alpha)^2$.

TABLE 4-XIV

OPTICAL ERROR MODEL B

Error	(Variance)$^{1/2}$		Time Constant
Sun sensor bias	0.407×10^{-3} rad	(1.4 arc min)	1/2 week
Sun sensor uncorrelated noise	0.349×10^{-4} rad* (0.1746×10^{-3} rad)**	(0.12 arc min)	
Mars sensor bias	0.391×10^{-3} rad	(1.35 arc min)	1/2 week
Canopus sensor bias	0.391×10^{-3} rad	(1.35 arc min)	1/2 week
Mars sensor uncorrelated noise	0.349×10^{-4} rad* (0.1746×10^{-3} rad)**		
Canopus sensor uncorrelated noise	0.1746×10^{-4} rad* (0.873×10^{-4} rad)**		
Mars subtense measurement			
Lower limit on (variance)$^{1/2}$ of bias	0.485×10^{-4} rad	(0.17 arc min)	1/2 week
Error proportional to subtense angle***	0%		
Uncorrelated noise	0.1745×10^{-4} rad* (0.873×10^{-4} rad)**	0.06 arc min** (0.3 arc min)**	

*Equivalent error of 25 measurements averaged. This value was used in the error analysis.

**Single measurement error.

***Percent of subtense angle (α) contributing to the standard deviation of the bias error adding to subtense angle, i.e., $\sigma_\alpha^2 = (0.873 \times 10^{-3})^2 + (0.01\alpha)^2$.

TABLE 4-XV

OPTICAL ERROR MODEL C

Error	(Variance)$^{1/2}$		Time Constant
Sun sensor bias	0.407×10^{-3} rad	(1.4 arc min)	1/2 week
Sun sensor uncorrelated noise	0.349×10^{-4} rad*	(0.12 arc min)	
	(0.1746×10^{-3} rad)**		
Mars sensor bias	0.153×10^{-4} rad	33 arc sec	1/2 week
Canopus sensor bias	0.727×10^{-4} rad	15 arc sec	1/2 week
Mars sensor uncorrelated noise	0.349×10^{-4} rad*		
	(0.1746×10^{-3} rad)**		
Canopus sensor uncorrelated noise	0.1746×10^{-4} rad*		
	(0.873×10^{-4} rad)**		
Mars subtense measurement			
Lower limit on (variance)$^{1/2}$ of bias	0.485×10^{-4} rad	(0.17 arc min)	1/2 week
Error proportional to subtense angle	0%		
Uncorrelated noise	0.1745×10^{-4} rad*	0.06 arc min**	
	(0.873×10^{-4} rad)**	(0.3 arc min)	

*Equivalent error of 25 measurements averaged. This value was used in the error analysis.

**Single measurement error.

4.6.1 Summary of SVEAD Results

The position and velocity error covariance matrices generated by the SVEAD program are expressed in ECI coordinates, with Z along the earth's spin axis and X along the vernal equinox. The 1-σ values of the position and velocity components for the last 10 days of the mission are shown in Figures 4-15 through 4-20 for both the Type I and II trajectories.

One immediate conclusion from these plots is that the results for Cases 4 and 5 are almost identical for all components, i.e., angle subtense measurement, at least with the accuracies quoted, does not improve overall navigation accuracy. Also, except for the X component, there is no apparent significant difference in results for Type I versus Type II trajectories.

4.6.2 Conversion of SVEAD Results to Approach Condition Errors

For purposes of further error analysis, it is convenient to express the SVEAD error quantities in terms of the orbital approach parameters. The pertinent equations are summarized below.

The transformation from ECI to MCI coordinates is (see Ref. 4-2):

$$\underline{x}_{MCI} = [T]\,\underline{x}_{ECI}$$

where

the MCI coordinate system is chosen with Z along the Martian spin axis and X along the Martian vernal equinox, $\underline{x}$ denotes any vector, and [T] is the coordinate transformation matrix, which for 1975 is numerically equal to

$$[T] = \begin{bmatrix} 0.8941\text{E-}3 & 0.9028834 & 0.4297079 \\ -0.9037406 & -0.1847545 & 0.3860002 \\ 0.4279037 & -0.3879994 & 0.8161376 \end{bmatrix} \quad \text{(Ref. 4-2)}$$

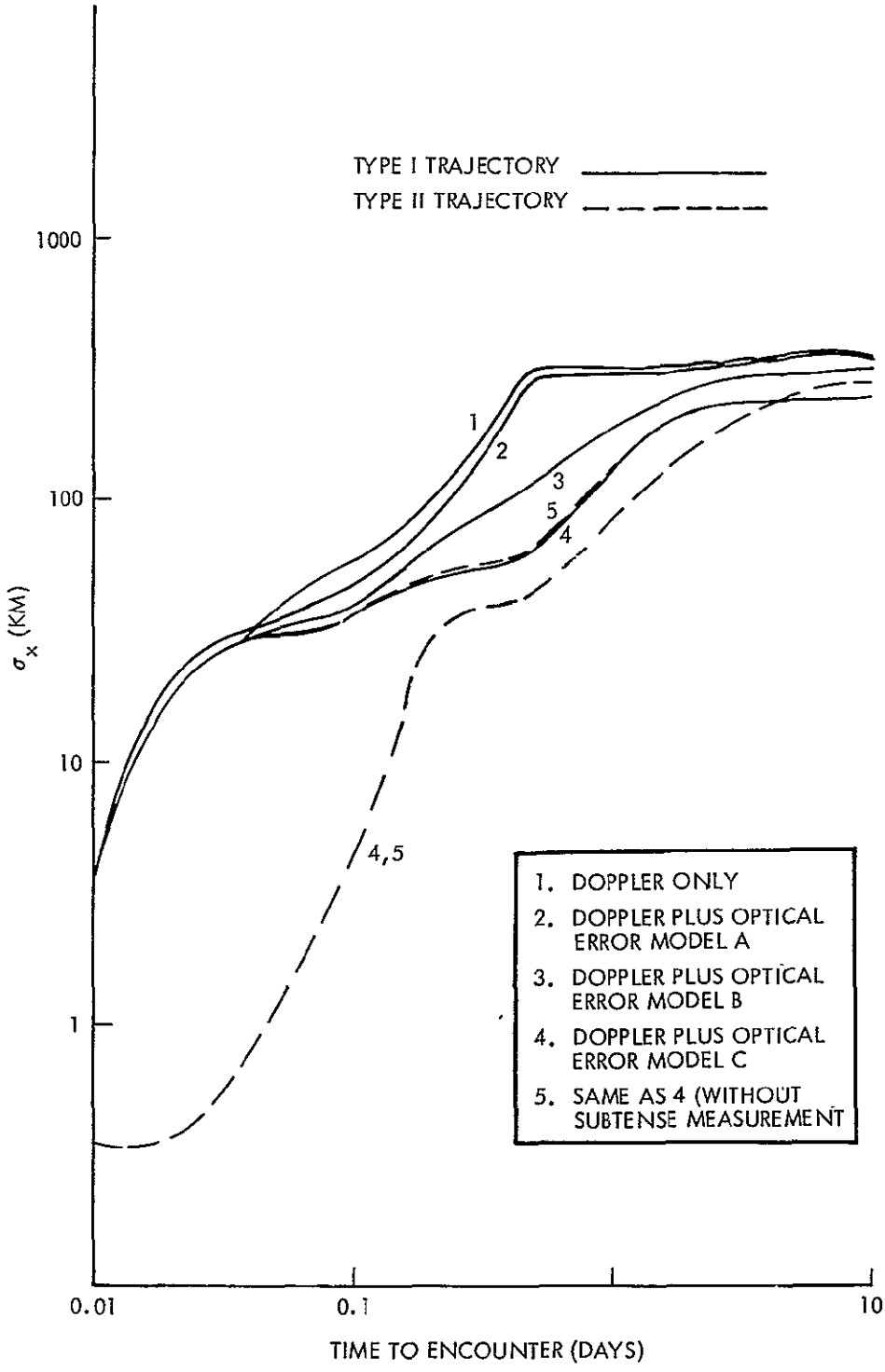

Figure 4-15. Position Uncertainty Versus Time to Encounter (Type I and II Trajectories)

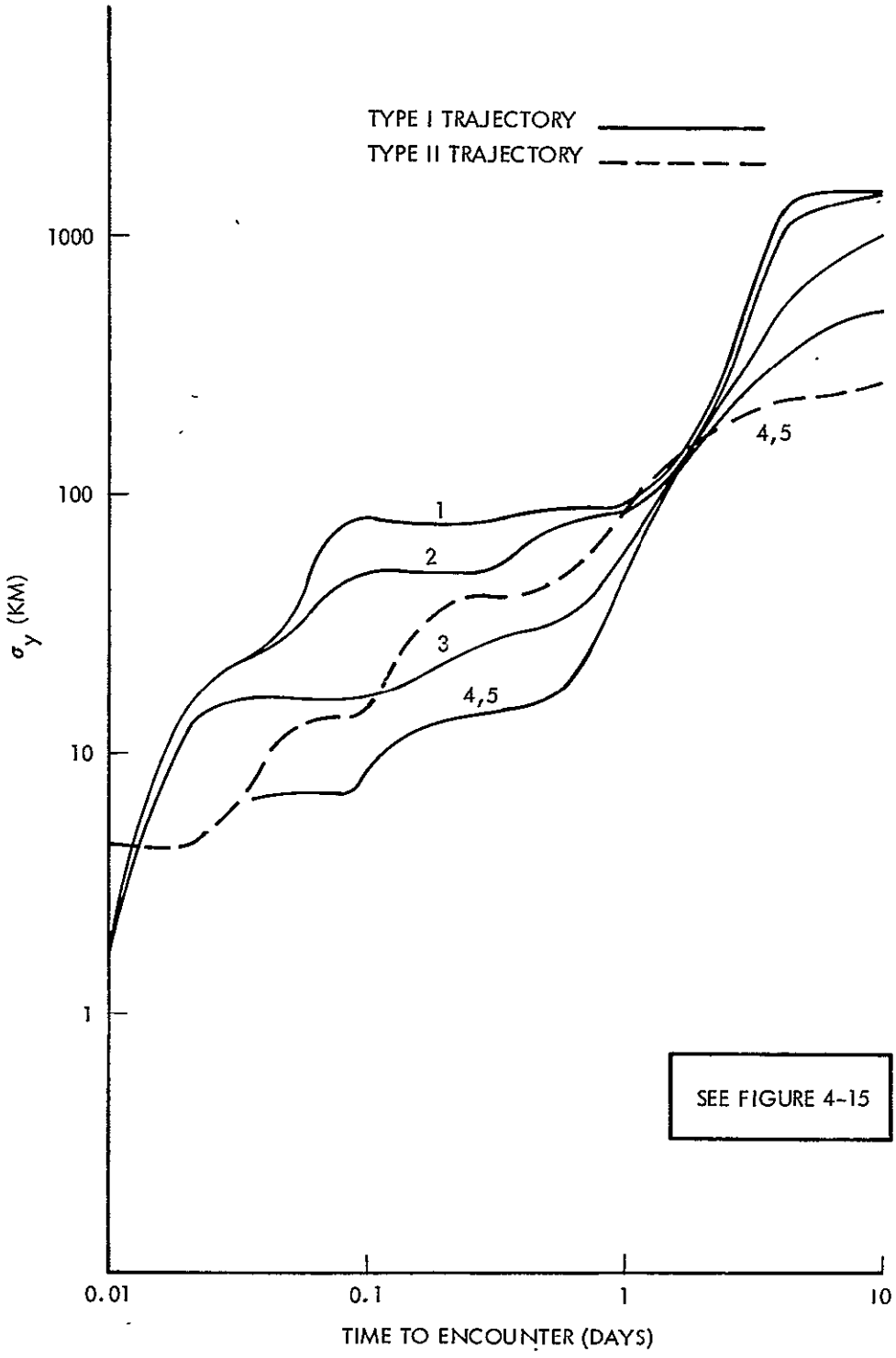

Figure 4-16. Position Uncertainty Versus Time to Encounter (Type I and II Trajectories)

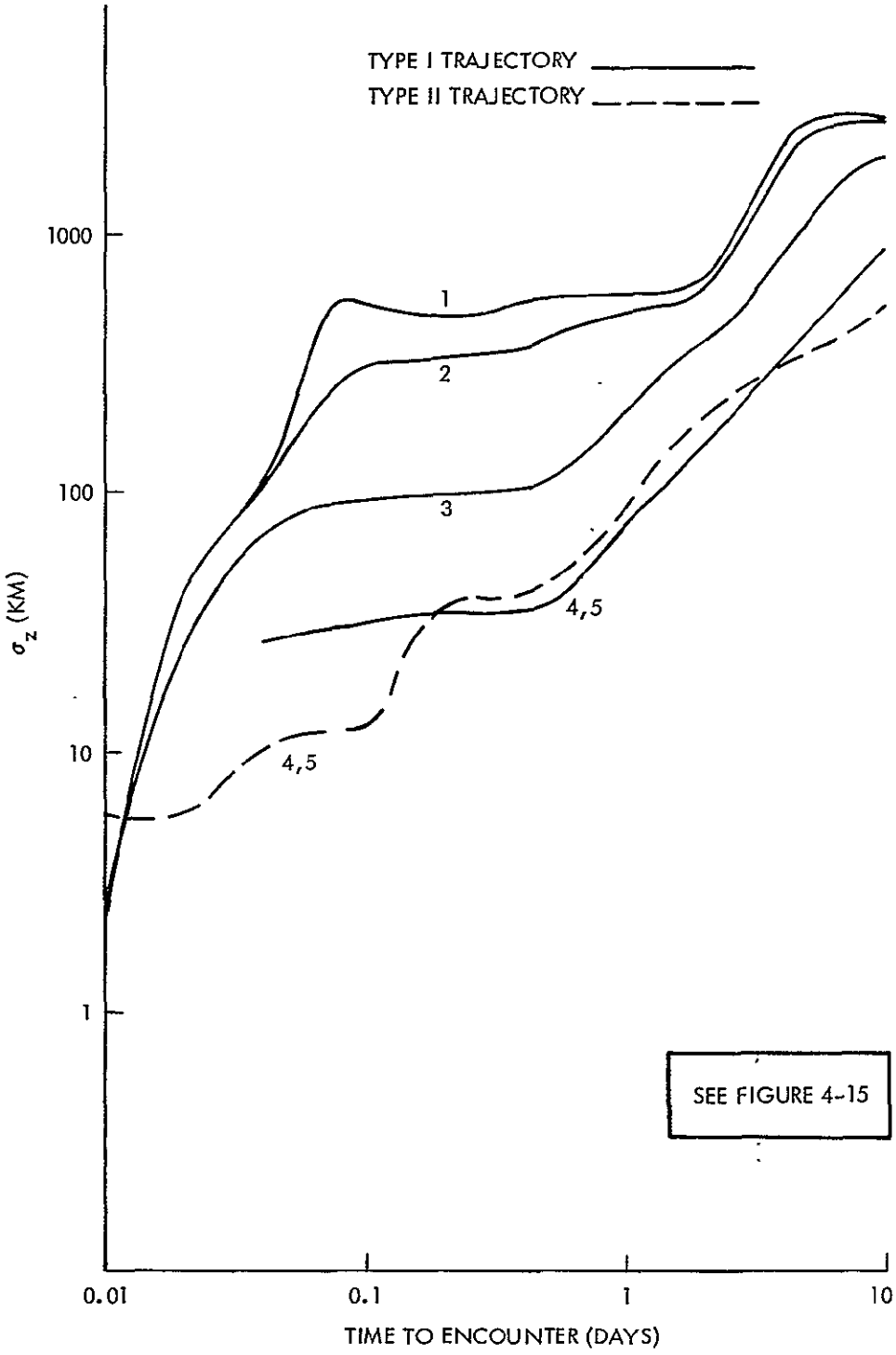

Figure 4-17. Position Uncertainty Versus Time to Encounter (Type I and II Trajectories)

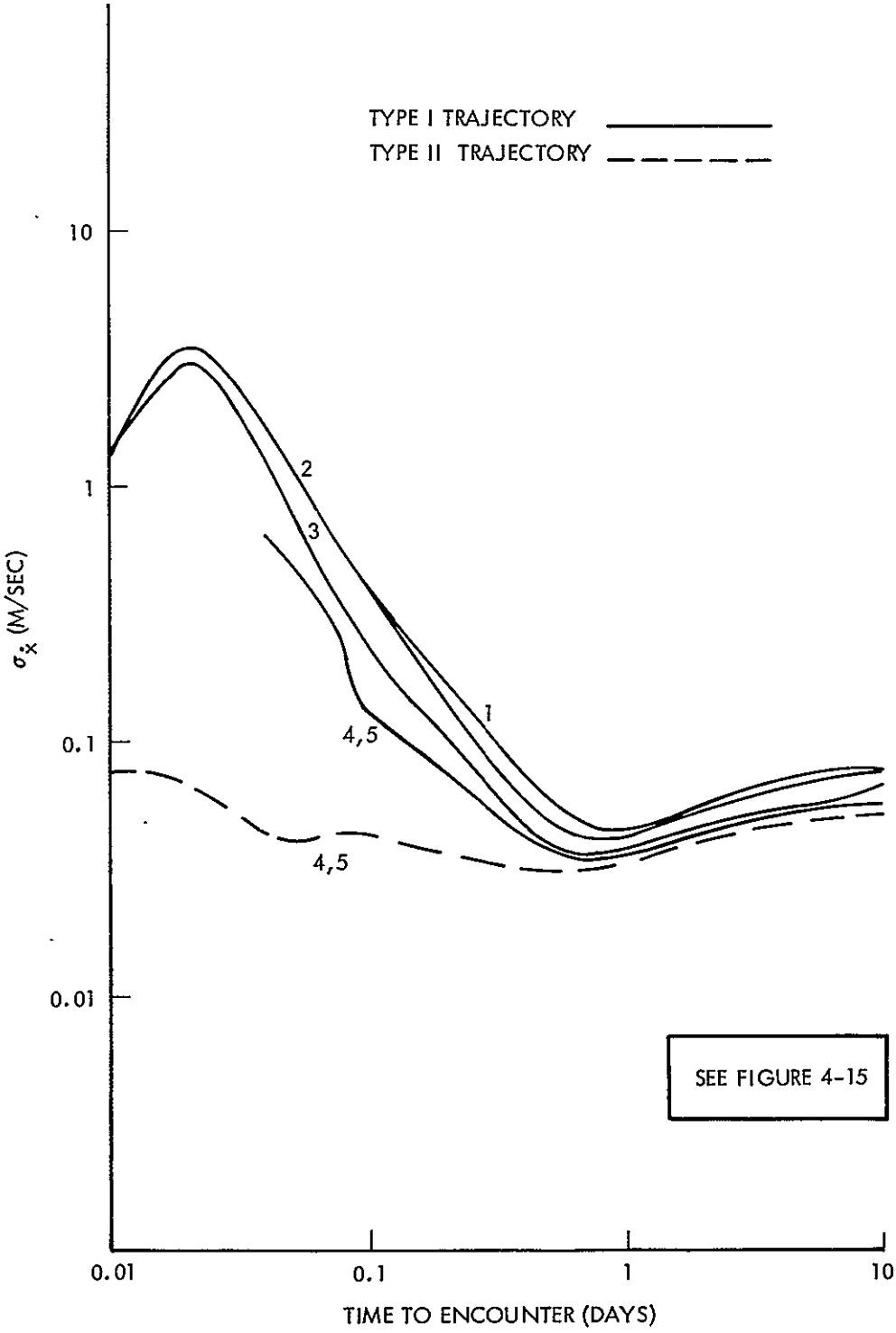

Figure 4-18. Velocity Uncertainty Versus Time to Encounter (Type I and II Trajectories)

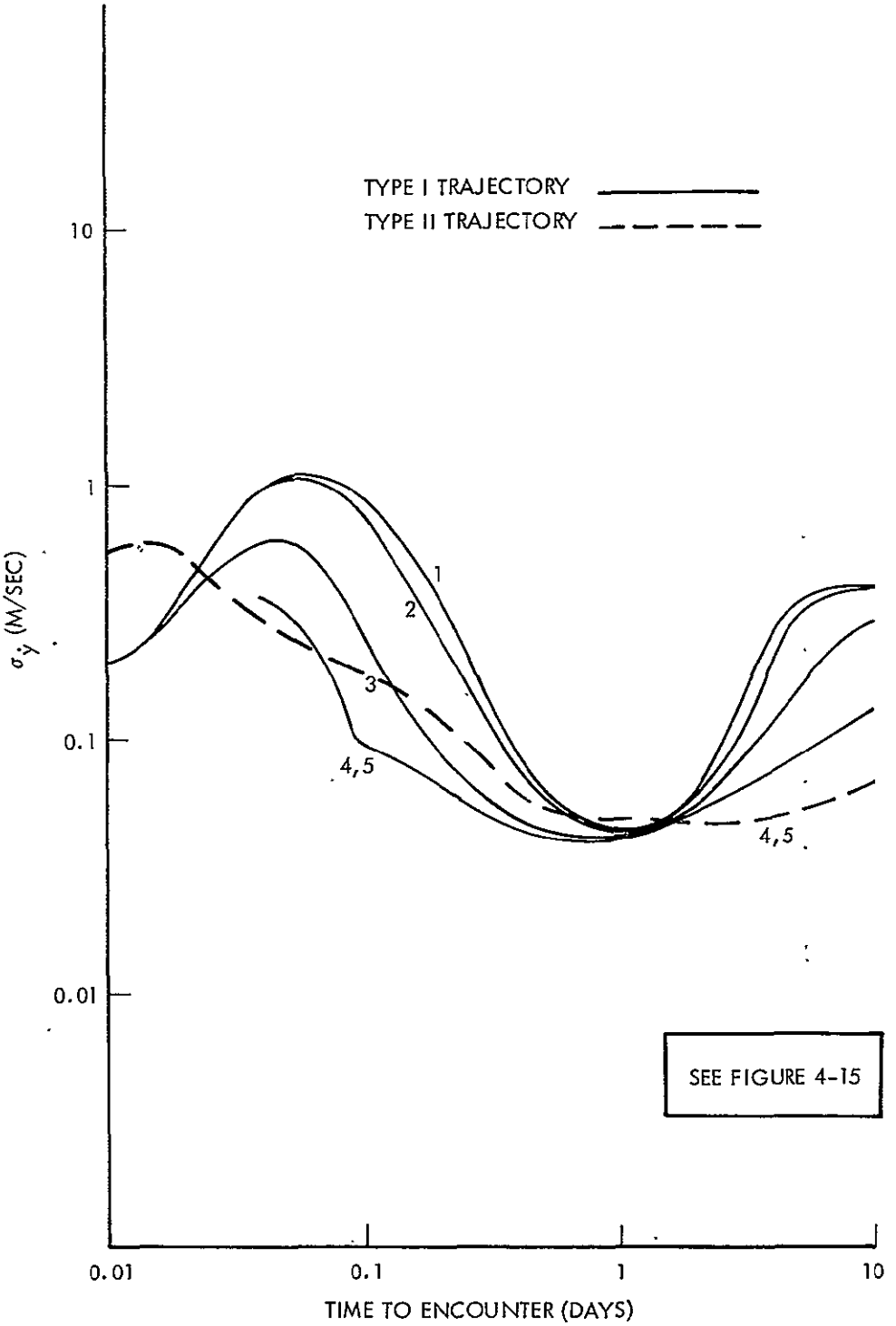

Figure 4-19. Velocity Uncertainty Versus Time to Encounter (Type I and II Trajectories)

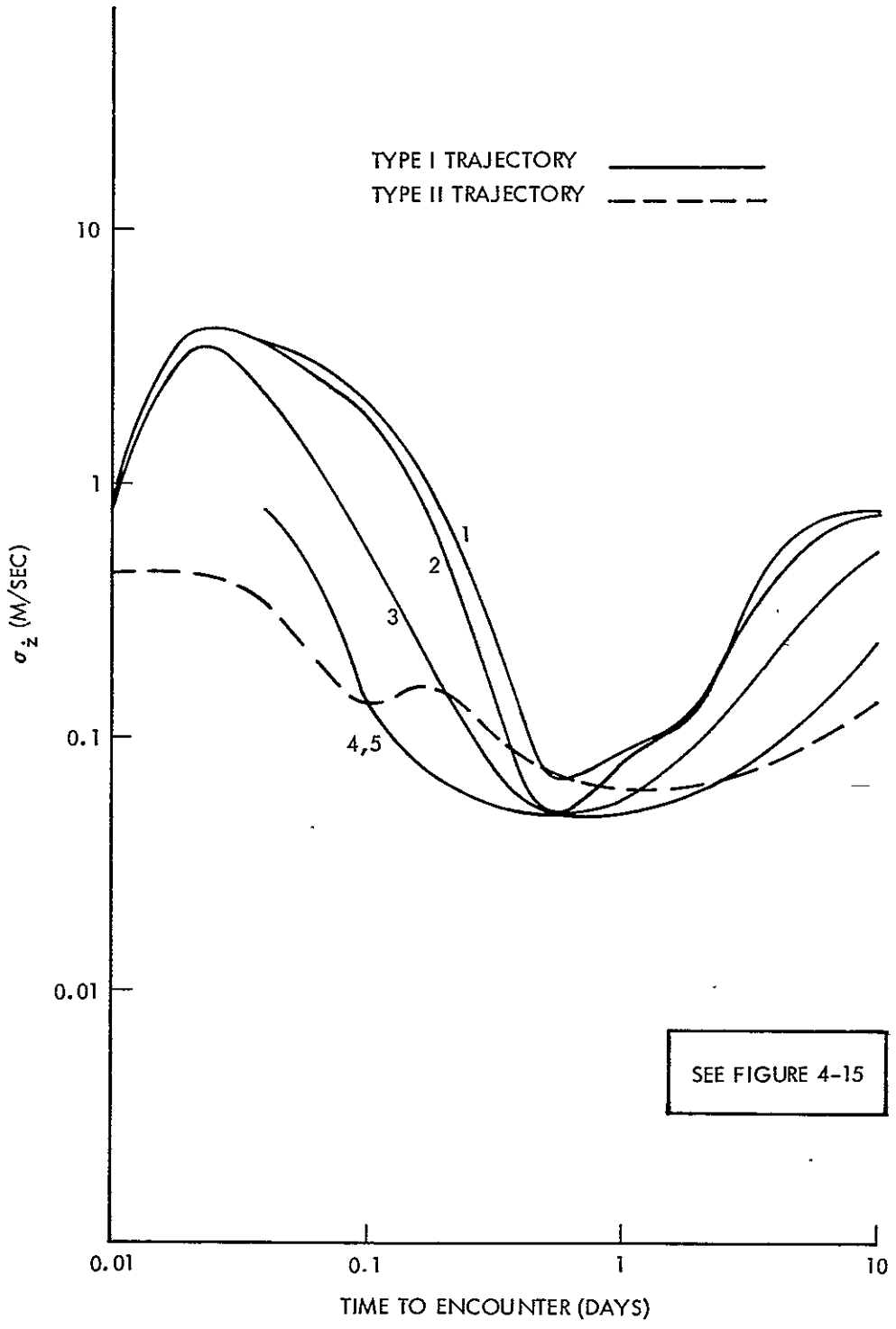

Figure 4-20. Velocity Uncertainty Versus Time to Encounter (Type I and II Trajectories)

Present radial distance:

$$R^2 = X^2 + Y^2 + Z^2$$

where

X, Y, Z are obtained from the SVEAD trajectory printout.

Velocity magnitude at R:

$$V^2 = \dot{X}^2 + \dot{Y}^2 + \dot{Z}^2$$

where

$\dot{X}$, $\dot{Y}$, $\dot{Z}$ are obtained from the SVEAD trajectory printout.

Velocity direction relative to R:

$$\cos \gamma = \frac{X\dot{X} + Y\dot{Y} + Z\dot{Z}}{RV}$$

Hyperbolic approach velocity:

$$V_\infty^2 = V^2 - 2\frac{\mu}{R}$$

where

μ = Mars' gravitational constant.

Impact parameter:

$$B = R\, V \sin \gamma / V_\infty$$

Semimajor axis, approach angle, and eccentricity of the approach hyperbola:

$$a = -\mu / V_\infty^2$$

$$\tan \nu = a/B$$

$$e = \csc \nu$$

Present hyperbolic and true anomaly:

$$\cosh H = (1 - R/a)/e$$

$$\tan f = B \sinh H / a(e - \cosh H)$$

Present longitude, latitude, and azimuth in the MCI coordinates:

$$\tan \alpha = (Y/X)_{MCI}$$

$$\sin \varphi = (Z/R)_{MCI}$$

$$\tan A = \left(\frac{R(X\dot{Y} - Y\dot{X})}{Y(\dot{Y}Z - \dot{Z}Y) - X(\dot{Z}X - \dot{X}Z)} \right)_{MCI}$$

Orbit inclination to the Martian equator:

$$\cos i = \sin A \cos \varphi$$

Longitude of the ascending node and argument of periares:

$$\Omega = \alpha - \lambda$$

$$\omega = u + f$$

where

$$\tan \lambda = \tan A \sin \varphi$$

$$\tan u = \tan \varphi \sec A$$

Time to periares:

$$\Delta T = a(e \sinh H - H)/V$$

The first-order differentials of the above equations yield the error expressions for the usual orbital elements (a, e, i, Ω, ω, ΔT), or equivalently, (B, V_∞, i, Ω, ω, ΔT):

$$\begin{bmatrix} \delta B \\ \delta V_\infty \\ \delta i \\ \delta \Omega \\ \delta \omega \\ \delta(\Delta T) \end{bmatrix} = [A] \begin{bmatrix} \delta X \\ \delta Y \\ \delta Z \\ \delta \dot{X} \\ \delta \dot{Y} \\ \delta \dot{Z} \end{bmatrix}_{MCI} = [A] \cdot [T] \begin{bmatrix} \delta X \\ \delta Y \\ \delta Z \\ \delta \dot{X} \\ \delta \dot{Y} \\ \delta \dot{Z} \end{bmatrix}_{ECI}$$

The approach orbit determination error covariance matrix is then

$$\Sigma_{OD} = [A][T] \Sigma_{P,V} [T]^T [A]^T \qquad (4\text{-}18)$$

where

$\Sigma_{P,V}$ is the error covariance matrix from SVEAD expressed in ECI coordinates.

4.6.3 Conclusions from Approach Navigation Performance Analyses

The results of the conversion indicated in Eq. (4-18) are plotted in Figures 4-21 through 4-26 for Cases 1 and 4 (Type I) and Case 4 (Type II). Between 50 and 2 hr before encounter, the 1-σ values of hyperbolic approach velocity estimation error are essentially identical for the two Type I cases, i.e., the optical angle measurements, although improving the quality of component velocity estimation (see Figures 4-18, 4-19 and 4-20), do not improve the overall approach velocity estimation. This behavior is attributable to the different manner in which the errors are correlated in the doppler-only and doppler-plus-optical cases. In the former, all errors are highly correlated as indicated in the normalized $\Sigma_{P,V}$ covariance matrixes 2 hr before encounter (Table 4-XVI).

In general, there are no significant differences in the result for Type I and Type II trajectories. The choice of the type of trajectory is then dictated by mission considerations other than accuracy.

Another important conclusion to be made from this analysis is that in the time span from about 5 hr down to 2 hr prior to encounter, the position uncertainty as given by σ_B (Figure 4-21) is not significantly improved by the addition of optical measurements to doppler measurements. That is, the added complexity of a planetary approach sensor to the ROI guidance system may not be warranted if only the size of the orbits to be established about Mars is of concern (see also par. 4.6.3). However, if it is desired to accurately establish cross plane parameters, viz, orbital inclination and longitude of the ascending node for the approach phase, the planetary approach sensor can be useful (see Figures 4-23 and 4-24 and par. 4.6.4).

Additional onboard optical measurements during the last 11 hr would result in only minor improvement in knowledge of the approach trajectory characteristics as indicated by Figures 4-21 through 4-26. Tracking was thus terminated at this point to simplify the design of the planet tracker (see subsec. 9.7) and to provide the necessary time for ground computation and transmission of corrections to the orbit insertion maneuver based on the doppler tracking data and telemetered onboard optical measurements.

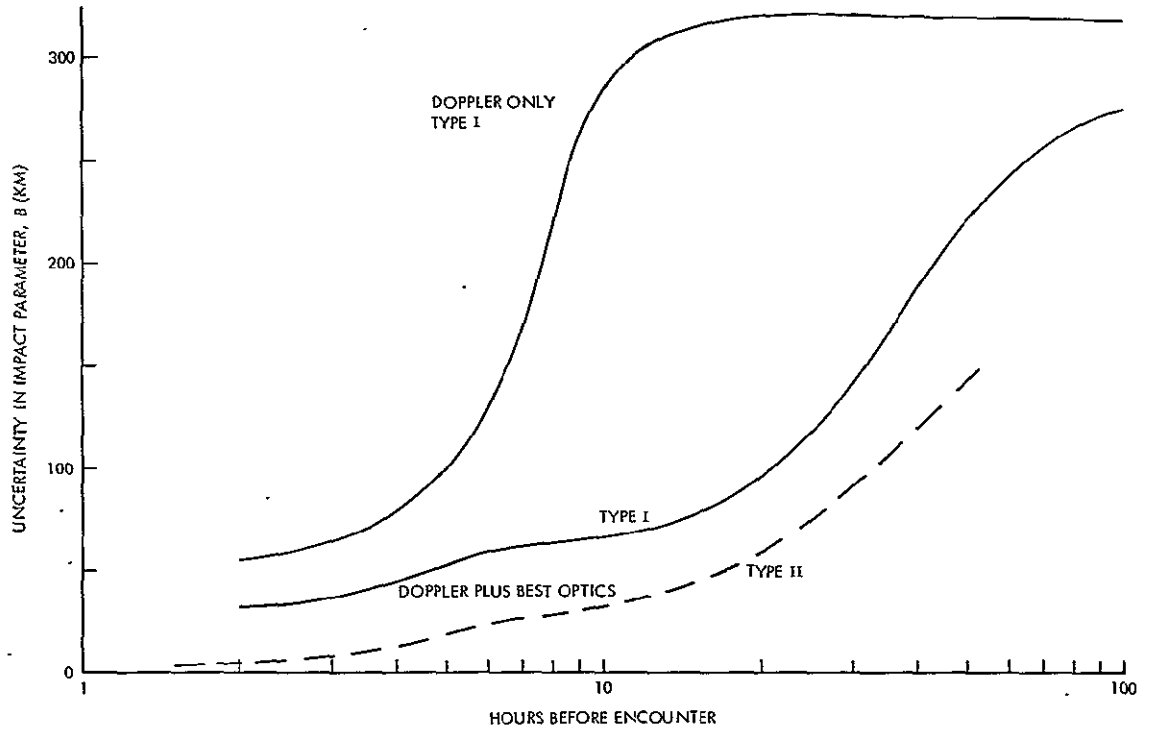

Figure 4-21. Impact Parameter Standard Deviation, 1975 Type I and II Trajectories

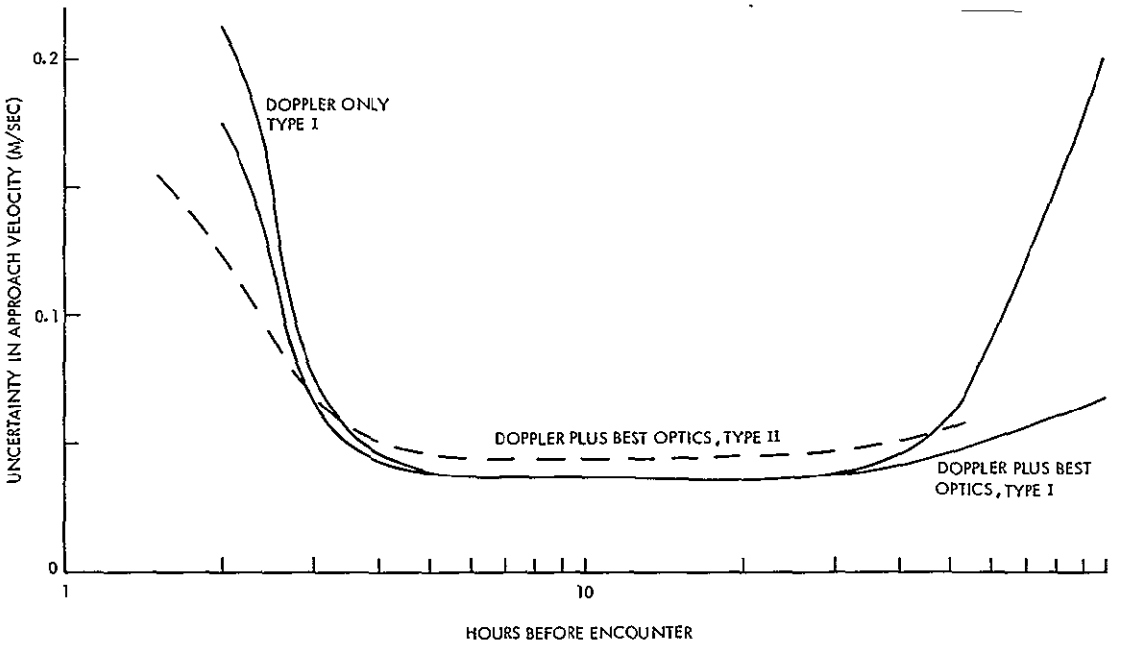

Figure 4-22. Approach Velocity Standard Deviation, 1975 Type I and II Trajectories

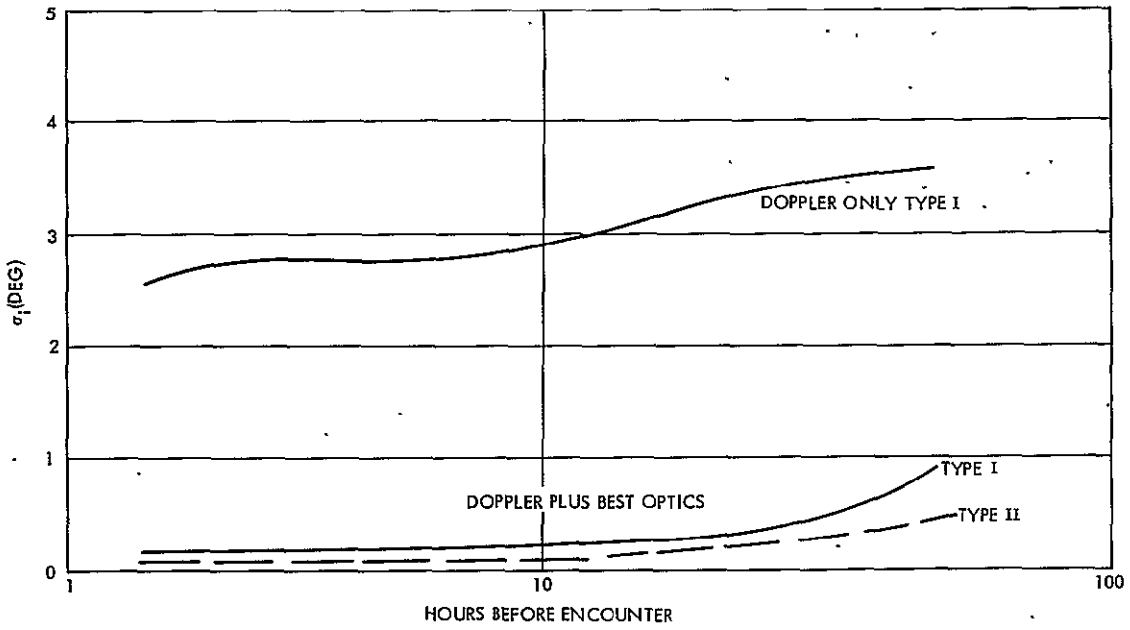

Figure 4-23. Orbital Inclination Standard Deviation, 1975 Type I and II Trajectories

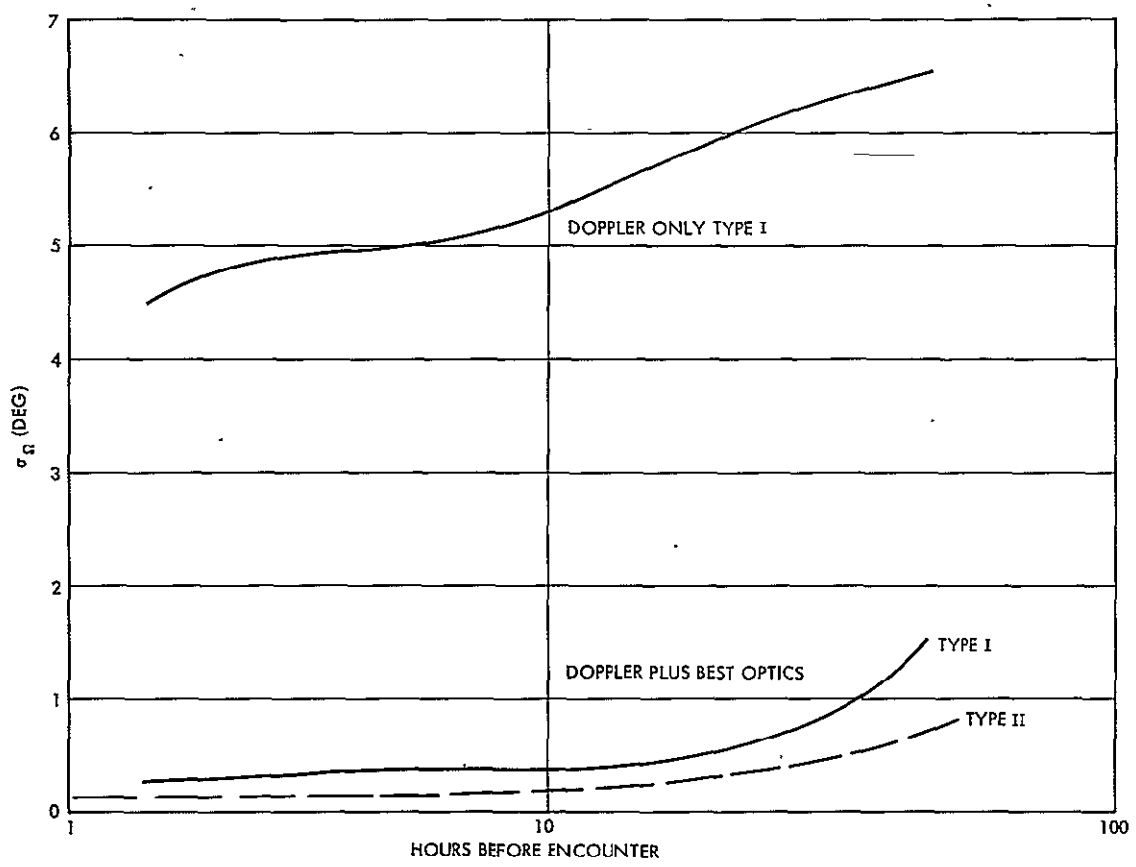

Figure 4-24. Ascending Node Longitude Standard Deviation, 1975 Type I and II Trajectories

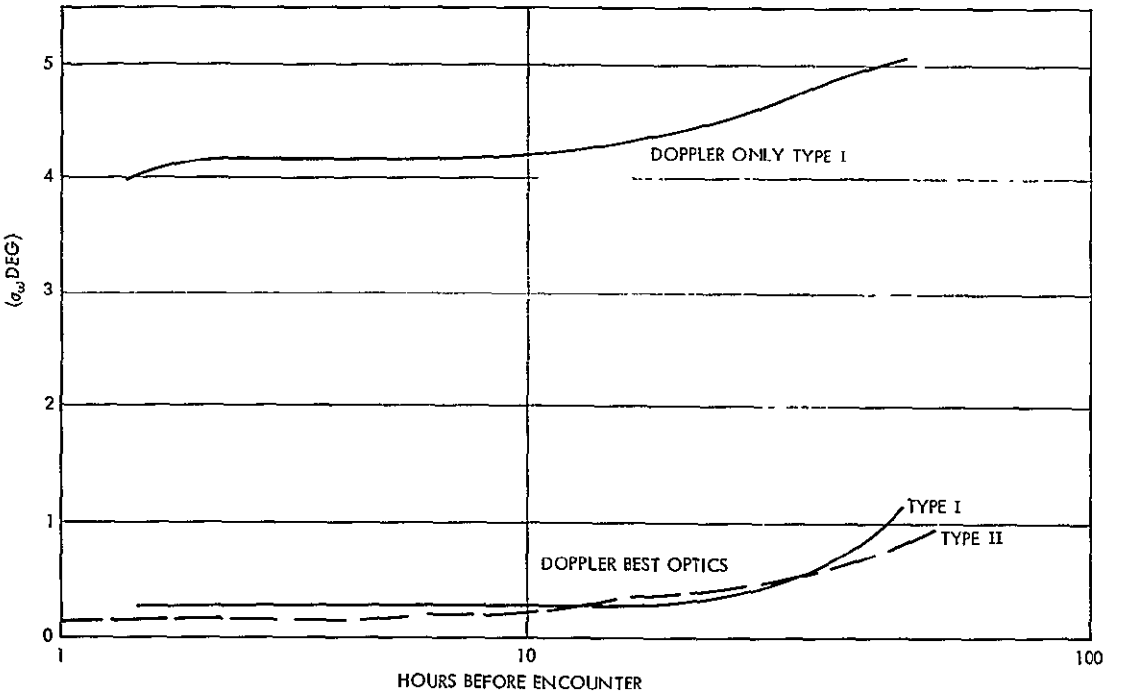

Figure 4-25. Argument of Periapsis Standard Deviation, 1975 Type I and II Trajectories

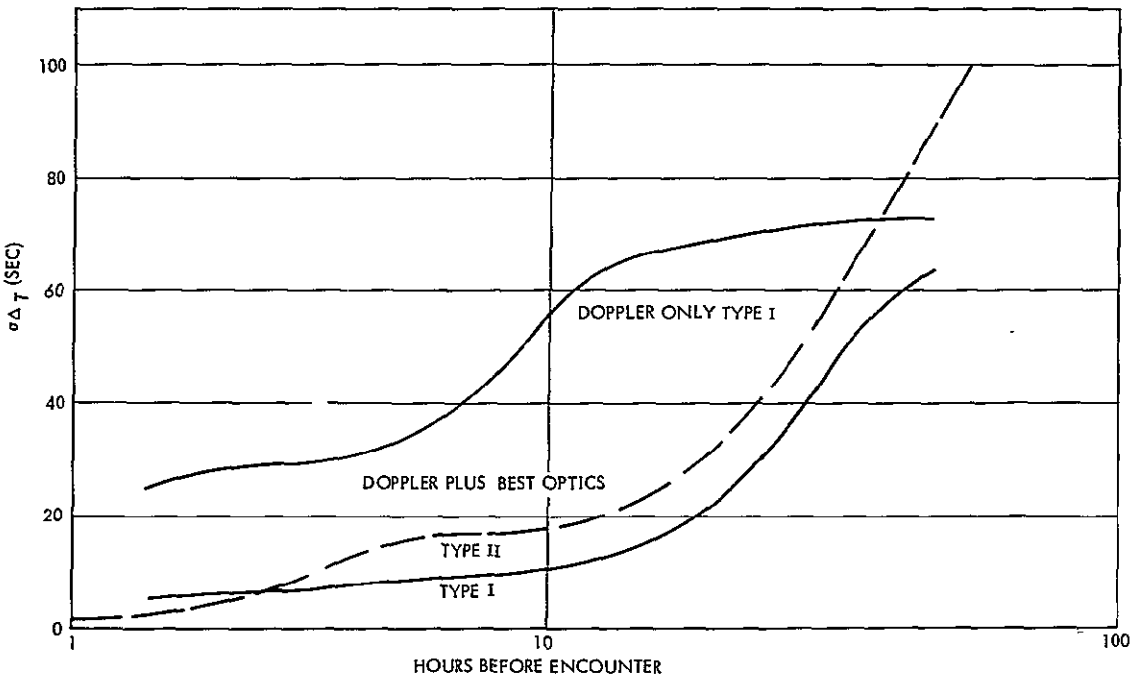

Figure 4-26. Time-to-Encounter Standard Deviation, 1975 Type I and II Trajectories

TABLE 4-XVI.

NORMALIZED COVARIANCE MATRICES AND 1-σ COMPONENT VALUES AT 2 HR BEFORE ENCOUNTER

Doppler only (Case 1):

$\sigma_X = 56.04$, $\sigma_Y = 72.78$, $\sigma_Z = 455.4$ km

$\sigma_{\dot{X}} = 0.801$, $\sigma_{\dot{Y}} = 1.603$, $\sigma_{\dot{Z}} = 3.962$ msec

1	-0.605	-0.687	0.327	-0.749	0.687
	1	0.994	-0.949	0.980	-0.994
		1	-0.911	0.996	-1
	Symmetric		1	-0.870	0.910
				1	-0.996
					1

Doppler + best optics (Case 4)

$\sigma_X = 34.59$, $\sigma_Y = 7.12$, $\sigma_Z = 31.39$ km

$\sigma_{\dot{X}} = 0.264$, $\sigma_{\dot{Y}} = 0.187$, $\sigma_{\dot{Z}} = 0.275$ msec

1	0.647	-0.356	-0.957	-0.846	0.366
	1	0.436	-0.805	-0.165	-0.428
		1	0.107	0.768	-0.981
	Symmetric		1	0.688	-0.12
				1	-0.775
					1

4.6.4 Effects of Approach Orbit Determination and Execution Errors on In-Plane Performance

On the basis of the nominal values of the impact parameter B and hyperbolic approach velocity V_∞ determined during the approach phase, the velocity increment $\Delta V_{deboost}$, required to establish the 1100 x 10,000 km (periares and apoares altitudes) orbit, can be determined from the following* (refer to Figure 4-27):

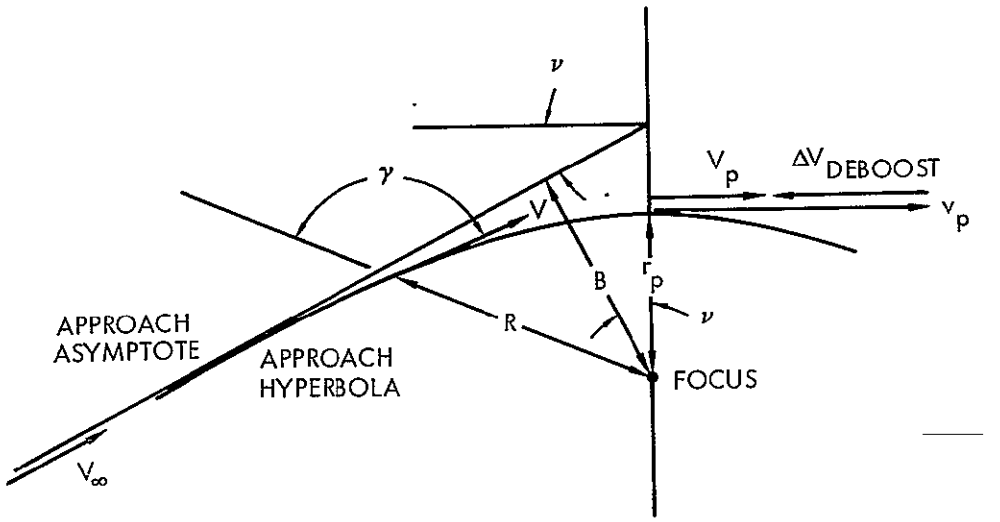

NOTES:
1. ν_p AND r_p ARE PREDICTED APPROACH PERIARES, DISTANCE AND VELOCITY.
2. V_p IS VELOCITY REQUIRED AT r_p TO REACH DESIRED APOARES R_a
3. $\Delta V_{DEBOOST} = v_p - V_p$ APPLIED ANTIPARALLEL TO v_p

Figure 4-27. Approach Parameters

*It is assumed that the desired orbits about Mars are in the same plane as the approach orbit plane.

Semimajor axis of approach hyperbola:

$$a = \mu/V_\infty^2$$

Approach angle:

$$\tan \nu = a/B$$

Eccentricity of approach hyperbola:

$$e = \csc \nu$$

Periares distance:

$$r_p = a(e - 1)$$

Velocity at periares:

$$v_p = B V_\infty / r_p$$

Velocity at periares required to attain desired apoares R_a:

$$V_p^2 = 2\mu \frac{R_a/r_p}{R_a + r_p}$$

Required deboost velocity:

$$\Delta V_{deboost} = v_p - V_p$$

The time from some reference point until $\Delta V_{deboost}$ is to be applied can be obtained from

$$T = \frac{a}{V_\infty} (e \sinh H_o - H_o)$$

where

$$\cosh H_o = (1 + r_o/a)/e$$

r_o = reference distance.

It is apparent from the above that errors in the determination of B and V_∞ will propagate to an error in the magnitude of $\Delta V_{deboost}$ and nontangential application of $\Delta V_{deboost}$ as illustrated in Figure 4-28.

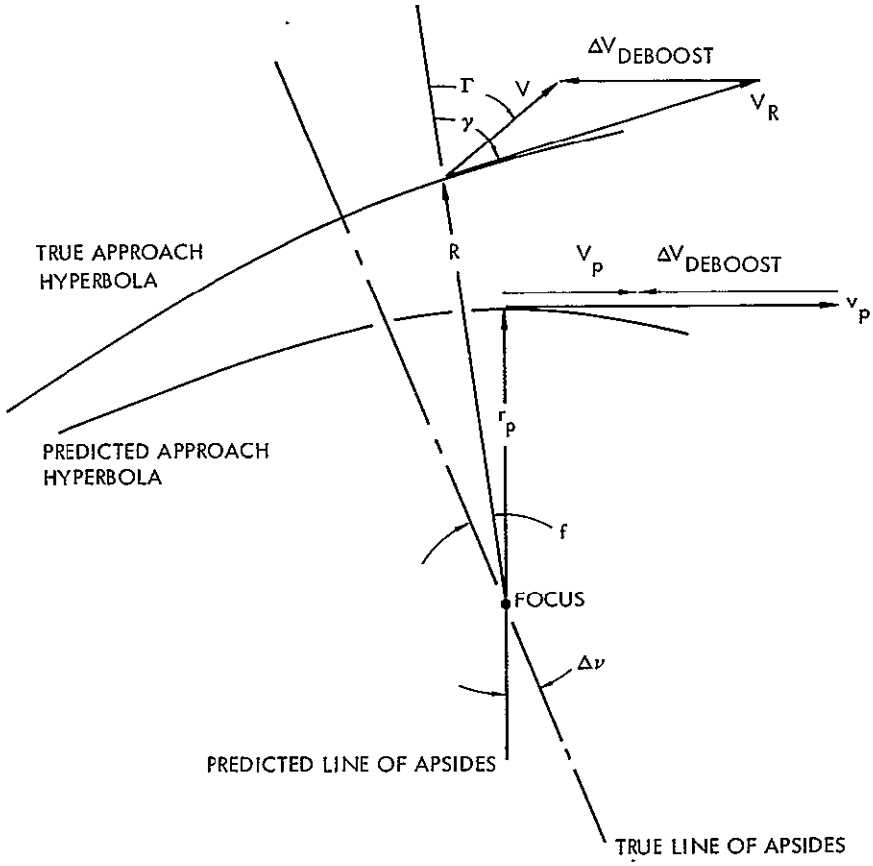

NOTES: 1. R, V_R ARE ACTUAL DISTANCE AND VELOCITY PREVAILING AT PREDICTED TIME OF $V_{DEBOOST}$ APPLICATION
2. V IS RESULTING VELOCITY AT R

Figure 4-28. $\Delta V_{Deboost}$ Application Error Geometry

In Figure 4-28, the angles of interest are

$\Delta\nu$ — rotation of the line of apsides of the approach hyperbola

f — true anomaly angle at which $\Delta V_{deboost}$ application is applied

γ, Γ — flight path angles before and after $\Delta V_{deboost}$ application at (R, f)

The rotation of the line of apsides of the approach hyperbola due to errors in estimation of B and V_∞ is

$$\Delta\nu = -\sin\nu\cos\nu\frac{\Delta B}{B} - 2\sin\nu\cos\nu\frac{\Delta V_\infty}{V_\infty}$$

For the nominal approach conditions of

$$B = 7829 \text{ km},$$

$$V_\infty = 3.0922 \text{ km/sec, and}$$

$$\nu = 29^\circ 50',$$

$|\Delta\nu|$ is less than 1° for $|\Delta B| < 200$ km and $|\Delta V_\infty| < 2$ msec.

The true anomaly angle measured from the true line of apsides is given by

$$\tan f = \frac{\sqrt{(e+\Delta e)^2 - 1}\sinh H}{(e+\Delta e) - \cosh H}$$

where

$$(e+\Delta e)\sinh H - H = \delta(\Delta T)\frac{(V_\infty + \Delta V_\infty)}{(a+\Delta a)}$$

H = hyperbolic anomaly on the true trajectory at the time of predicted perifocus passage on the assumed trajectory

$\delta(\Delta T)$ = difference in perifocus passage time for the true and assumed approach trajectories

Δe, Δa = the error in predicted approach hyperbola eccentricity and semimajor axis due to ΔB and ΔV_∞.

The flight path angle prior to $\Delta V_{deboost}$ application is

$$\sin\gamma = \frac{(B+\Delta B)(V_\infty + \Delta V_\infty)}{RV}$$

where

$$V^2 = (V_\infty + \Delta V_\infty)^2 + \frac{2\mu}{R}$$

$$R = p/[1 + (e + \Delta e) \cos f]$$

$$p = (e + \Delta e + 1)(r_p + \Delta r_p)$$

Following $\Delta V_{deboost}$ application,

$$V \sin \Gamma = V_R \sin \gamma - (\Delta V_{deboost} + \delta V) \cos (\Delta \nu + f + \eta)$$

$$V \cos \Gamma = V_R \cos \gamma - (\Delta V_{deboost} + \delta V) \sin (\Delta \nu + f + \eta)$$

where

δV = magnitude of execution error

η = execution direction error

The various parameters of the resulting elliptic orbit include the following:

Semimajor axis:

$$a_o = R/(2 - V_R^2 R/\mu)$$

Eccentricity:

$$e_o^2 = 1 - R^2 V_R^2 \sin^2 \Gamma / a_o \mu$$

Periares and apoares:

$$r'_p = a_o(1 - e_o)$$

$$r_a = a_o(1 + e_o)$$

Rotation of line of apsides:

$$\cos(\Delta\psi) = ((r'_p r_a / a_o) - R)/e_o R$$

Thus the orbit established by the application of $\Delta V_{deboost}$ has the following errors from the desired:

Periares error:

$$\delta r_p = r'_p - R_p = r'_p - (1100 + 3410) \text{ km}$$

Apoares error:

$$\delta r_a = r_a - R_a = r_a - (10,000 + 3410) \text{ km}$$

Rotation of the line of apsides:

$$\Delta\psi = \cos^{-1} (((r_p r_a/a_o) - R)/e_o R)$$

For this study, it was assumed desirable to correct to the nominally desired 1,100 x 10,000-km orbit with the desired direction of the line of apsides. From par. 2.4.4 of the Tasks I and II report, the following velocity increments are required to make these corrections:

Apoares correction:

$$\Delta V_a \cong \sqrt{2\mu \frac{R_a/R_p}{R_a + R_p}} \left(\frac{|\delta r_a|}{2R_a} \right)$$

Periares correction:

$$\Delta V_b \cong \sqrt{2\mu \frac{R_a/R_p}{R_a + R_p}} \frac{|\delta r_p|}{2(R_a + R_p)}$$

Rotation correction:

$$\Delta V_c \cong \sqrt{2\mu \frac{R_a/R_p}{R_a + R_p}} (1 - R_p/R_a) \sin \frac{|\Delta\psi|}{2}$$

Substituting the desired numerical values,

$$\Delta V_a = 0.14 \quad |\delta r_a| \text{ m/sec}$$

$$\Delta V_b = 0.105 \quad |\delta r_p| \text{ m/sec}$$

where

δr_a and δr_p are expressed in km, and

$$\Delta V_c = 2490 \sin \frac{|\Delta\psi|}{2} \text{ m/sec}$$

A Monte Carlo simulation was run to determine the effects of ΔB, ΔV_∞, $\delta\nu$, and η on δr_a, δr_p, $\Delta\psi$, and $\delta(\Delta V)$, where $\delta(\Delta V)$ is the difference in total velocity increment requirements from the ideal nominal case. For this case, the total ΔV is that required to deboost into the 1100 x 10,000-km orbit and subsequently transfer down to and circularize at the 500-km altitude circular orbit. ΔV_{TOTAL} is

$$\Delta V_{TOTAL} = (v_p - V_p) + \left(\sqrt{2\mu \frac{R_p/R_a}{R_p + R_a}} - \sqrt{2\mu \frac{R_c/R_a}{R_c + R_a}}\right)$$

$$+ \left(\sqrt{2\mu \frac{R_a/R_c}{R_c + R_a}} - \sqrt{\frac{\mu}{R_c}}\right)$$

where

R_c = desired circular orbit radial distance.

For the parameters of interest,

$$\Delta V_{TOTAL} = 1.577 + 0.07 + 0.80 = 2.45 \text{ km/sec}$$

The Monte Carlo runs were made not only for the nominal approach impact parameter value of B = 7829 km, but also for high- and low-approach cases of B = 8029 and 7629 km, respectively. For these cases, $\delta(\Delta V)$ is affected further by the fact that $\Delta V_{deboost}$ are 1.599 and 1.554 km/sec, respectively, as compared to 1.577 km/sec.

The results from the Monte Carlo runs are shown in Figures 4-29 and 4-30. The 1-σ values used for the runs were

$$10 < \sigma_B < 100 \text{ km}$$

$$\sigma_{V_\infty} = 0.1 \text{ m/sec}$$

$$\sigma_{\delta V} = \sigma_s = 0.043\% \text{ of applied } \Delta V$$

$$\sigma_\eta = \sigma_p = 0.001 \text{ rad}$$

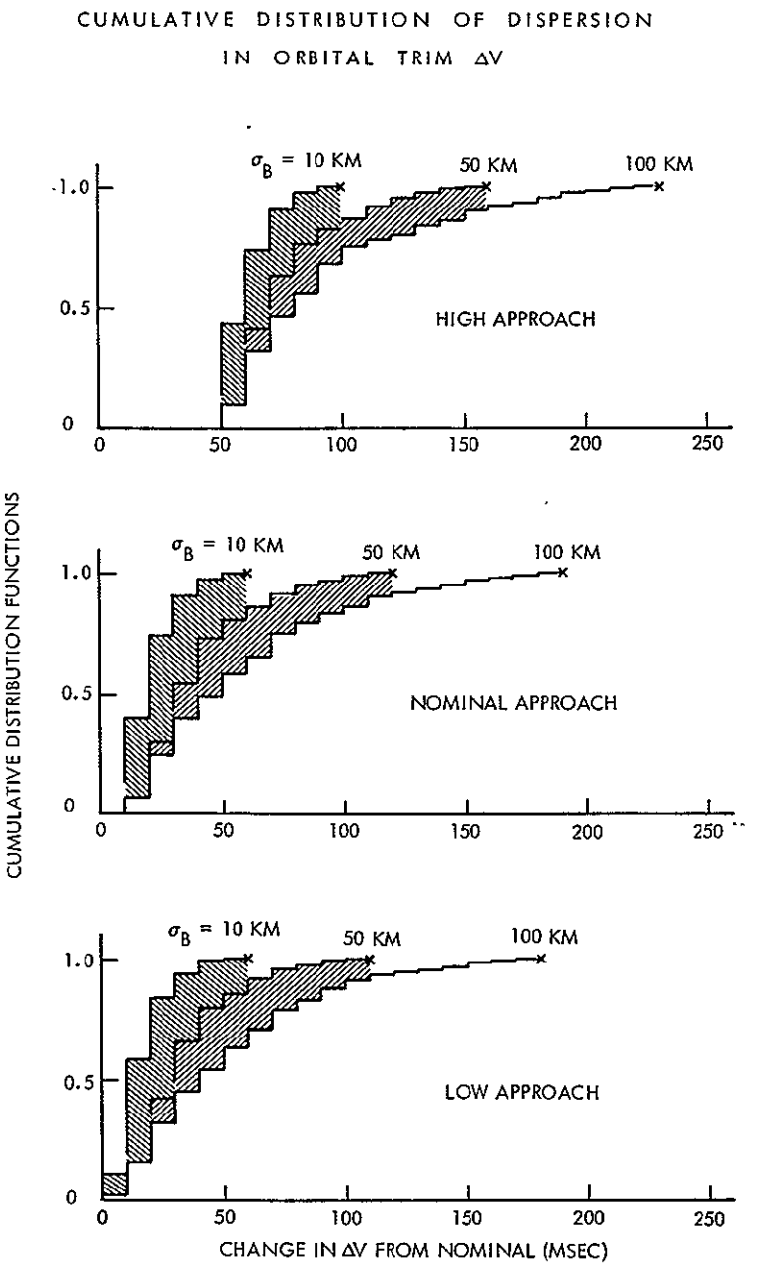

Figure 4-29. Cumulative Distribution of Dispersion in Orbital Trim ΔV

The effects of these errors on the change in total ΔV requirements, i.e., the ΔV required for trimming the deboosted elliptic orbit to the desired 1,100 x 10,000-km orbit, are illustrated in Figure 4-29 in the form of cumulative distributions. The 95% ΔV requirements are summarized in Table 4-XVII.

TABLE 4-XVII.

NINETY-FIVE PERCENT ORBIT TRIM ΔV REQUIREMENTS (M/SEC)

Approach	σ_B = 10 km	50 km	100 km
High	85	125	185
Nominal	45	85	145
Low	45	75	135

If the final approach orbit estimation is delayed until approximately 2 hr before encounter, then $\sigma_B \cong 55$ km for the doppler-only case and 35 km for the doppler-plus-best-optics case (Type I trajectory). Interpolation of data in Table 4-XVII indicates that the reduction in orbital trim requirements afforded by the use of the optical measurements would be slight and would not warrant the added complexity of the onboard planetary approach sensor.

Furthermore, examination of Figure 4-30 indicates that the parameters of the deboosted orbit do not differ significantly from those nominally desired. For $\sigma_B = 50$ km, the maximum differences are shown in Table 4-XVIII. For these magnitude errors, orbital trim would most likely not be applied. The only change in ΔV requirements would be caused by transfer from the non-nominal elliptic orbit to the 500-km circular orbit. In this event, the maximum change in ΔV would be less than ±50 msec (out of 2.45 km/sec) for any case.

Thus, if only in-plane orbital parameters are of concern, the use of a planetary approach sensor would be difficult to justify. Consideration of cross-plane characteristics shows that the approach sensor might possibly be a valuable adjunct to doppler tracking orbit determination in certain missions.

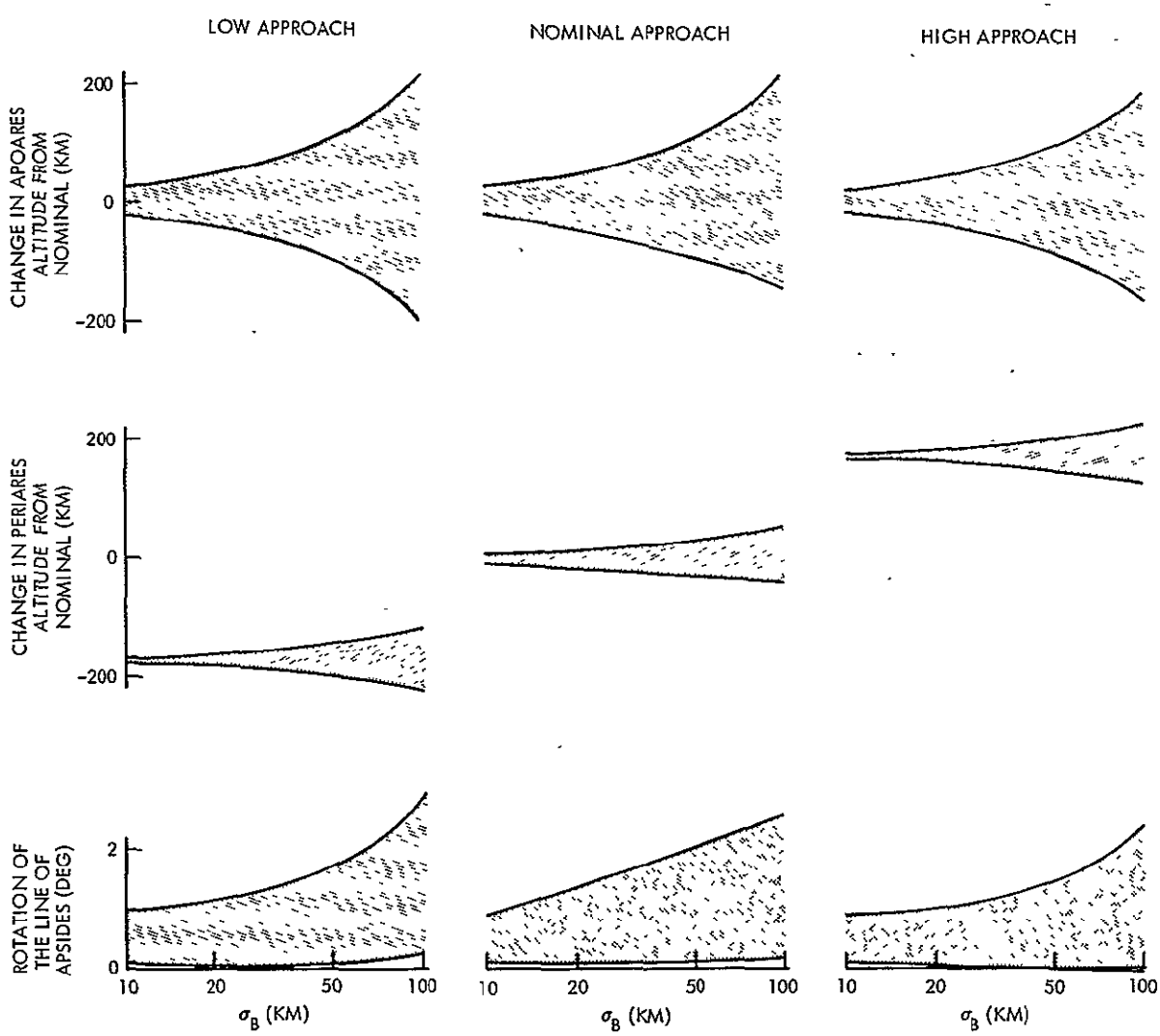

Figure 4-30. ±1σ Spread in Parameters of Deboosted Orbit Due to Uncertainty in Approach Impact Parameter, B

TABLE 4-XVIII

MAXIMUM ERRORS IN DEBOOSTED ORBIT PARAMETERS

Approach	Apoares (km from 10,000)	Periares (km from 1100)	Rotation (deg)
High	-100 to +200	+150 to +230	3.8
Nominal	-100 to +200	-35 to +34	3.8
Low	-100 to +200	-130 to -210	3.8

4.6.5 Effect of Approach Orbit Determination Errors on Out-of-Plane Performance

Referring to Figure 4-23, the uncertainty in the inclination of the approach orbit at 2 hr before encounter is seen to be about 2.5° and 0.25° for the doppler-only and doppler-plus-approach-sensor cases, respectively. If an inclination correction is attempted simultaneously with the deboost ΔV application, subsequent tracking in orbit would reveal the inclination error of the approach orbit determination. The corrective ΔV required to adjust the inclination error is

$$\Delta V_i \cong \sqrt{2\mu \frac{R_a/R_p}{R_a + R_p}} \sqrt{1 - \cos \Delta i} \quad \text{(Ref. 4-1, par. 2.4.4)}$$

$$\cong \Delta i \sqrt{\mu \frac{R_a/R_p}{R_a + R_p}}$$

$$\cong 2665\ \Delta i \text{ m/sec}$$

where

Δi is the negative of the inclination uncertainty of the approach determination function.

For the two cases considered, the ΔV_i penalties are

$$\Delta V_i = \begin{cases} 116 \text{ m/sec; doppler only} \\ 11.6 \text{ m/sec; doppler + approach sensor} \end{cases}$$

Thus the approach sensor can provide significant benefits if either

a) precise inclination information is desired very early, or

b) approach inclination corrections are to be applied simultaneously with the deboost ΔV.

However, if neither of the above is a requirement, then it would be better to doppler track while the payload is in orbit about Mars and forego the approach sensor.

4.7 MARS AND LUNAR ORBIT DETERMINATION

4.7.1 Mars Orbit Determination from DSIF Tracking Data

The accuracy of orbit determination while the spacecraft is in an areocentric orbit was obtained using the SVEAD computer program (see Ref. 4-1, app. D) for the nominal 1,100 x 10,000-km orbit obtained from the Type I heliocentric transfer orbit. The orbital characteristics are shown in Table 4-XIX.

TABLE 4-XIX

ORBITAL PARAMETERS FOR MARS ORBIT
(MARTIAN EQUATORIAL COORDINATE SYSTEM)

Parameter	Value
Semimajor axis (a)	8960 km
Eccentricity (e)	0.496
Inclination (i)	36.6°
Longitude of ascending node (Ω)	143.1°
Argument of perigee (ω)	-12.3°
Period (T)	7.15 hr

For the 1,100 x 10,000-km orbit obtained, the spacecraft goes behind Mars 9 min after periapsis and is visible again 33 min later.

The initial state vector errors used in the analysis were those obtained at the end of the approach orbit determination phase (doppler tracking only). All other error models were the same as those used in the approach orbit determination phase (refer to Table 4-XII).

The resulting behavior of the uncertainties in the spacecraft position and velocity in RTN coordinates are illustrated in Figures 4-31 and 4-32 for slightly more than one complete orbit. The corresponding orbital elements are illustrated in Figures 4-33 and 4-34.

This analysis assumes an uncertainty of 8.6 km^3/sec^2 in the gravitational constant of Mars and an uncertainty of 0.48×10^{-3} in the second zonal harmonic, as indicated in Table 4-XII. The results shown in Figures 4-31 through 4-34 indicate approximately an order of magnitude reduction in the initial errors over a period of one orbit. These results are valid only if no significant local gravity anomalies or other unknown disturbing accelerations are present. The only method of validating this assumption is by analysis of actual tracking data obtained for a spacecraft in Mars orbit.

The maximum allowable 3σ orbit determination errors, specified at orbit insertion plus four returns to periapsis are (from Table 3-VII, vol 1):

Semimajor axis	$3\sigma_a = 10$ km
Eccentricity	$3\sigma_e = 10^{-4}$
Uncertainty in time of periapsis in passage	$3\sigma_t = 5$ sec

Comparison of the orbital determination errors given in Figure 4-33 with these values shows that the errors have been reduced to approximately one-third of the desired values after one orbit. Although the specific analysis was not carried out, it is expected that the desired accuracies would be achieved after four orbits.

4.7.2 Lunar Orbit Determination From MSFN Tracking Data

It has recently become clear that the orbit-determination errors for low trajectories around the moon deviate significantly from previous predictions (Ref. 4-4). A recent report published by JPL (Ref. 4-5) concluded that the moon is gravitationally rougher than anticipated in the sense that comparatively high-degree terms in the spherical harmonic expansion would be required for effective representation of the lunar gravity field. This conclusion is based upon an extensive investigation of the radio tracking data for the Lunar Orbiter Missions received by the NASA Deep Space Network.

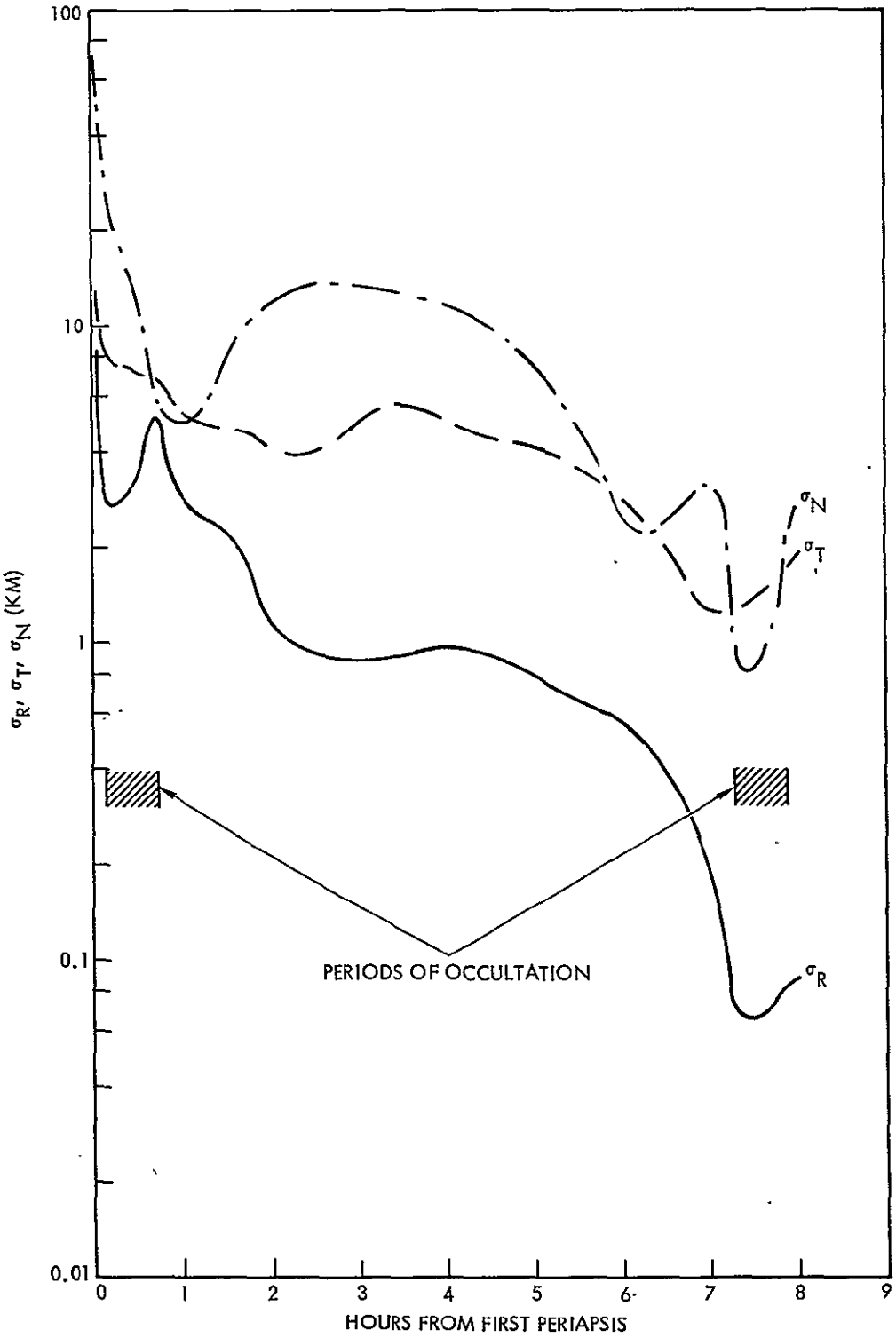

Figure 4-31. Position Uncertainties Versus Time for Spacecraft in Mars Orbit (DSIF Tracking)

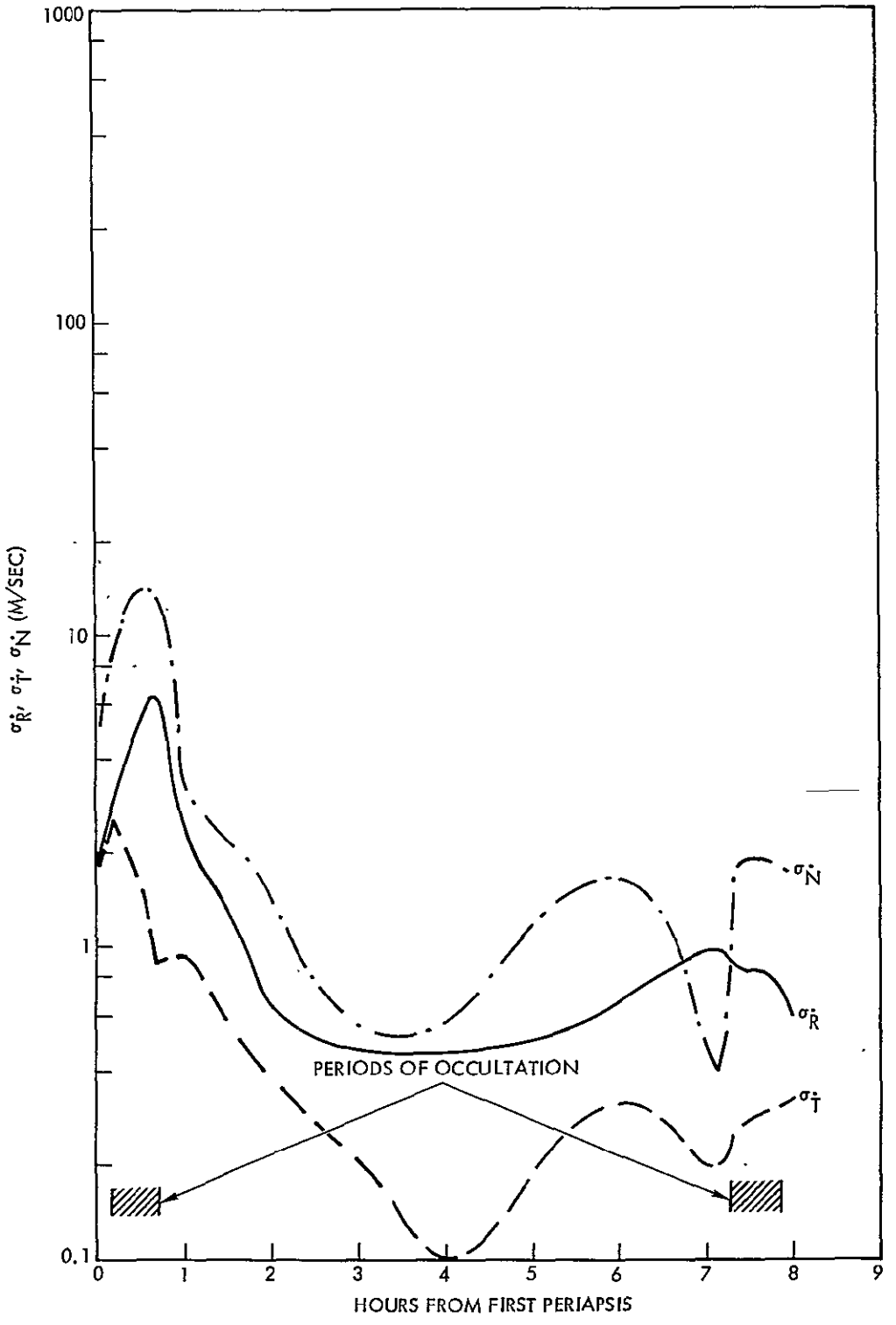

Figure 4-32. Velocity Uncertainties Versus Time for Spacecraft in Mars Orbit (DSIF Tracking)

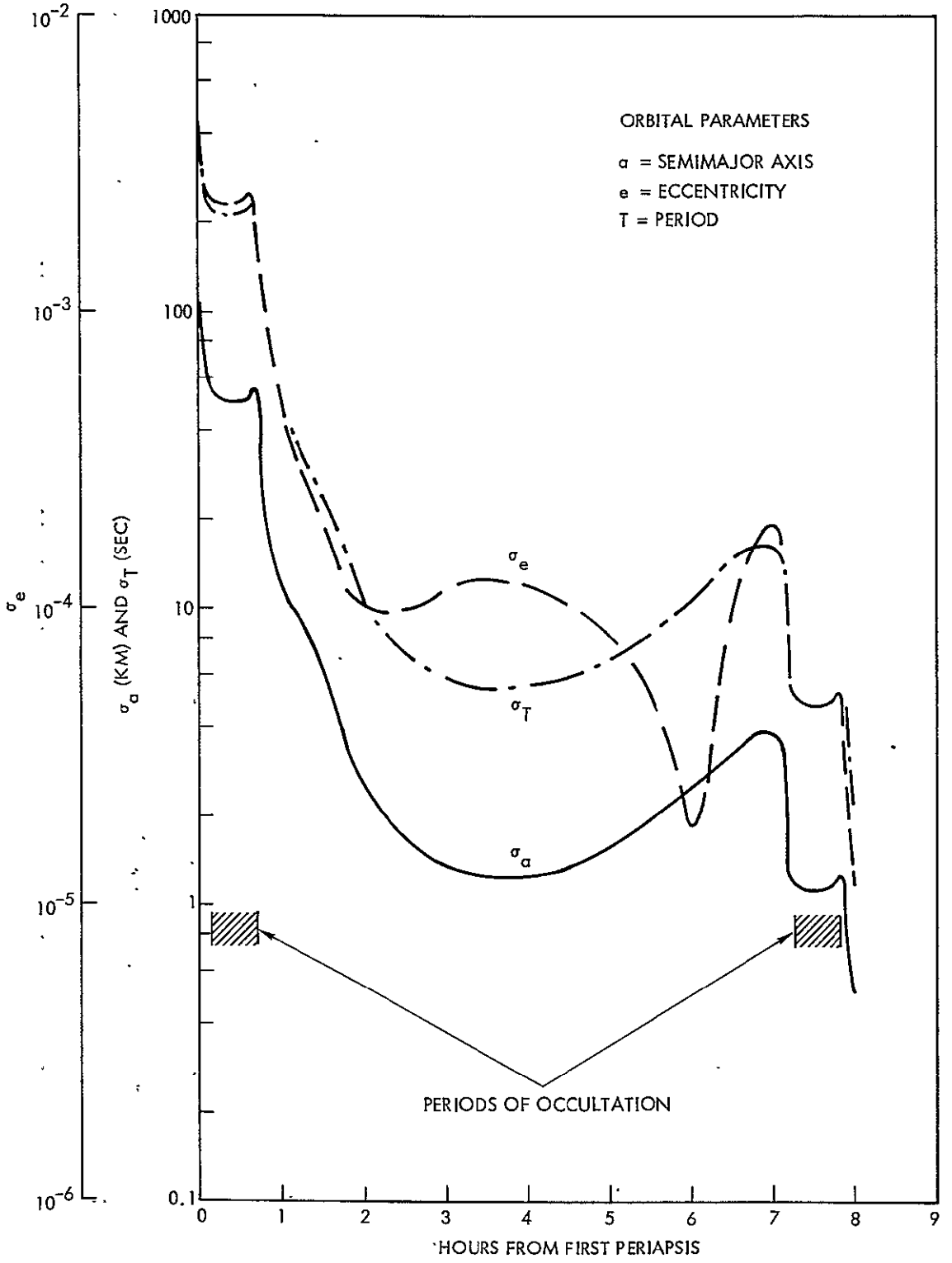

Figure 4-33. Uncertainties in Orbital Parameters Versus Time for Spacecraft in Mars Orbit (DSIF Tracking)

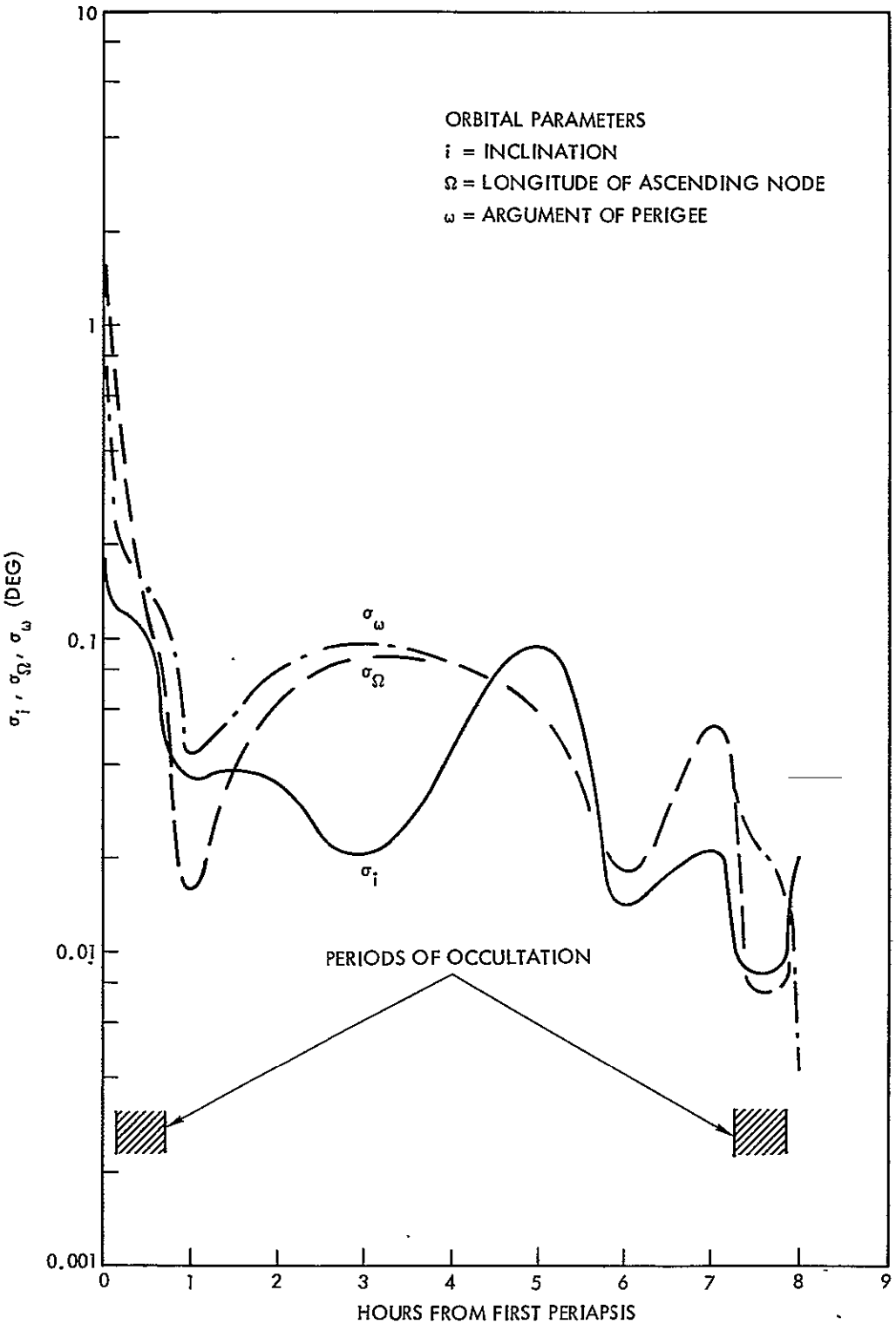

Figure 4-34. Uncertainties in Orbital Orientation Parameters Versus Time for Spacecraft in Mars Orbit (DSIF Tracking)

The effect of the observed gravitational anomalies on orbit-determination accuracies is under intensive investigation at the present time in support of the Apollo program. The results of studies completed to date, while preliminary, give a reasonably good estimate of the orbit-determination capabilities under various circumstances.

Table 4-XX shows the estimated navigation uncertainties based on the Lunar Orbiter ground tracking data postflight analysis for one pass of tracking data (from Ref: 4-6).

Table 4-XX indicates that the uncertainties in the position components of the spacecraft state vector grow rapidly with time after tracking is terminated.

TABLE 4-XX

LUNAR ORBIT NAVIGATION UNCERTAINTIES

	At Time of Tracking	Rate of Growth	Propagated for Two Orbits (no tracking)
σ_R	1000 ft	1200 ft/rev	2600
σ_T	3000	4000 ft/rev	8544
σ_N	300	500 ft/rev	1044
σ_θ	0.1°	0.005°/rev	0.11°
σ_λ	0.02°	0	0.02°
$\sigma_{\dot{R}}$	7.3 ft/sec	-	7.3 ft/sec
$\sigma_{\dot{T}}$	2.2 ft/sec	-	2.2 ft/sec
$\sigma_{\dot{N}}$	9.2 ft/sec	-	9.3 ft/sec

Note:

σ_λ = error in flight path angle

σ_θ = error in direction of angular momentum vector. (See par.1.3.4 for definition of RTN coordinate system)

Figure 4-35 (from Ref. 4-7) compares a trajectory calculation using a triaxial gravity model with a Lunar Orbiter 3 (LO3) trajectory. The LO3 trajectory was generated by processing the nondestruct doppler measurement data by the modified Apollo Powered Flight Data Processing Program (APOP) (Ref. 4-8). The data were obtained at Goldstone, Woomera and Guam. Since the modified APOP can model a large random uncertainty in the gravity model by treating it as a system noise, the trajectory generated by the modified APOP is free to deviate from that predicted by the triaxial gravity model and thus closely approximates the actual trajectory.

Comparison of the results shown in Figure 4-35 with the uncertainties given in Table 4-XX shows reasonable agreement for the inplane components. Figure 4-35 also shows somewhat larger out-of-plane position errors.

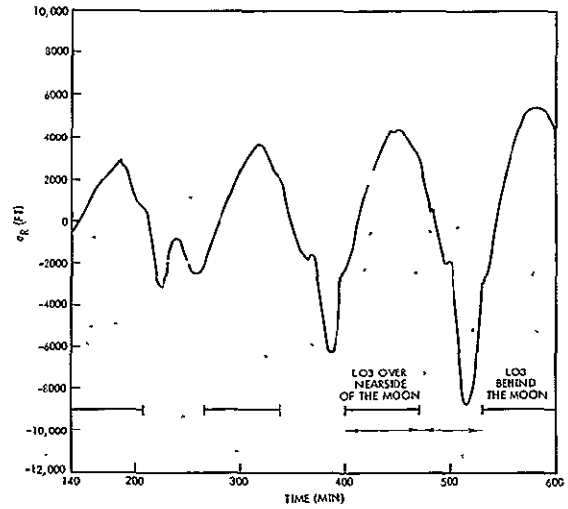

(a) Vertical Position Error Versus Time

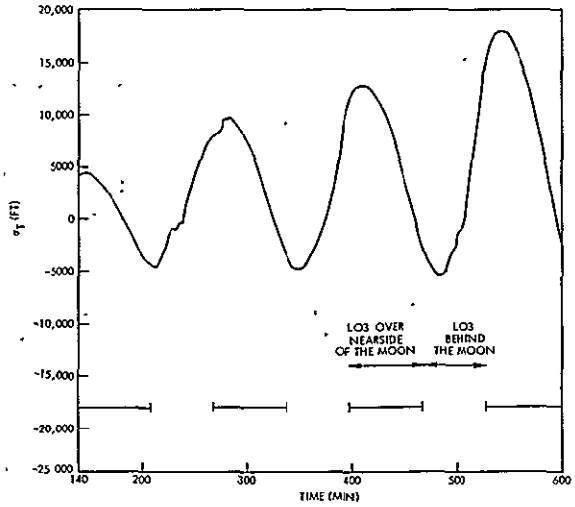

(b) Downrange Position Error Versus Time

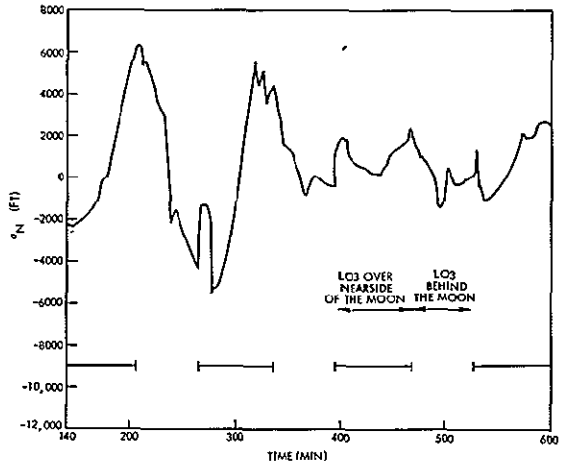

(c) Crossrange Position Error Versus Time

Figure 4-35. Comparison of LO3 Trajectory Data with Trajectory Computed Using Triaxial Gravity Model

REFERENCES

4-1 "Radio/Optical/Strapdown Inertial Guidance Study for Advanced Kick Stage Applications, Vol. II: Detailed Study Results", TRW Final Report 07398-6017-R000, 30 June 1967.

4-2 Pedro Ramon Escobal: Methods of Orbit Determination. John Wiley & Sons, Inc., New York, 1965.

4-3 "Voyager Spacecraft Phase B, Task D, Vol. II: Spacecraft Design and Performance", TRW Final Report October 1967.

4-4 "Apollo Navigation, Ground and Onboard Capabilities," MSC-GSFC Apollo Navigation Working Group Technical Report No. 65-AN-2.0, 1 September 1965.

4-5 P. M. Muller and W. G. Sjogren: "MASCONS: Lunar Mass Concentrations," Jet Propulsion Laboratory, Science, Vol. 161, No. 3842, 16 August 1968.

4-6 Emil R. Schiesser: "Navigation Uncertainties for Descent Dispersion Analysis," NASA/MSC Memorandum 68-FM47-427, 28 October 1968.

4-7 A. T. Monuki: "Analysis of Apollo Navigation Accuracy Utilizing a Triaxial Gravity Model in the Lunar Environment," TRW Systems Report No. 05952-6233-R000, 30 December 1968.

4-8 W. M. Lear: "S-Band, Powered Flight Tracking Programs," TRW Report No. 05952-6131-R000, 22 February 1967.

5. CONTROL SYSTEM PERFORMANCE ANALYSES

5.1 INTRODUCTION AND SUMMARY

Control system analyses made in support of the conceptual and modular design of the Radio/Optical/Strapdown Inertial Guidance and Control system are presented in this section. Several vehicle configurations were evaluated in terms of their bending transmissibility in addition to performance of detailed stability analyses. On the basis of these studies, suitable locations of the rate gyro packages in the launch vehicles have been determined. Filtering requirements for stability compensation also have been determined and used to formulate the general digital control equations presented in sec. 8 for the modular guidance and control system design. Control system stability criteria followed in this study are given in Appendix A.

Gain-phase stability plots, control system gains, and relative stability margins are given for alternate rate gyro locations and compensation filters for the Atlas/Centaur, Saturn 1B/Centaur, launch vehicles and for the Voyager Spacecraft during midcourse and Mars orbit insertion burns. In addition, a spacecraft thrust vector pointing error analysis was performed for the Voyager spacecraft to estimate the TVC pointing errors and crossrange velocity errors incurred during the powered burns.

5.2 CONTROL SYSTEM STABILITY AND BENDING MODE TRANSMISSIBILITY COEFFICIENTS

In the design of the boost vehicle first stage, minimum gains for control system stability are dictated primarily by the aerodynamic moment acting on the vehicle and the control moment available to counteract it. Given a vehicle configuration, its trajectory, and the desired aerodynamic stability margin, the control gains are constrained by a determinable lower limit.

Similarly, an upper constraint on the control gains exists dictated primarily by the effects of vehicle structural resonance modes. When the structural bending sensed by the control system sensors becomes excessive, the control system gains may be over-constrained such that vehicle stability with conventional control systems or, for that matter, any control system becomes impossible.

An illustration of the stability problem is given by Figures 5-1 and 5-2. In the first figure, a typical gain-phase plot is shown in which the control system frequency response and stability margins are indicated. The desired operating point is defined by the intersection of the dashed nominal gain line and the gain axis. The response of the control system to increasing frequencies, indicated by the arrows, is shown to encircle the operating point, producing an island of stability. The associated stability margins are termed: aerodynamic or low-frequency rigid body gain margin (A), rigid body phase margin (C), high-frequency rigid body gain margin (B), and the first bending mode phase margin (D).

As the first bending mode transmissibility increases, an erosion of the high-frequency rigid body gain margin ensues as shown in Figure 5-2. The increase in bending transmissibility is shown to dissolve the island of stability to a point where even the addition of stability compensation networks would be of no avail. It is estimated that a desirable transmissibility would be less than 10 and certainly no greater than 30, this latter case requiring compensation networks which include notch filters.

A notch filter could be designed at the high-frequency rigid body frequency thereby producing attenuation and increased gain margin; however,

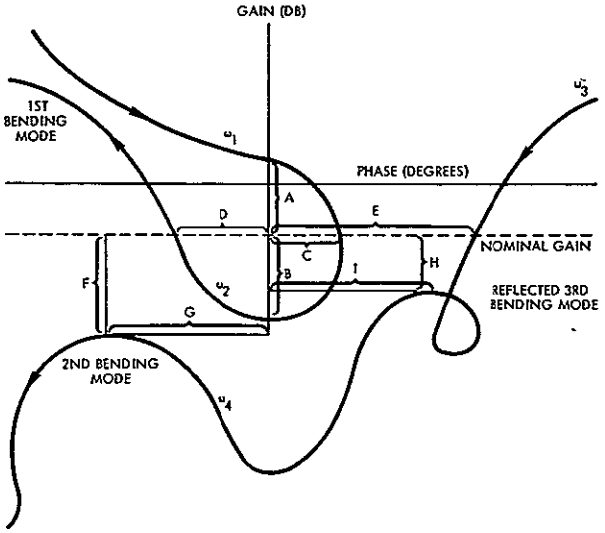

A LOW FREQUENCY AERODYNAMIC GAIN MARGIN
B HIGH FREQUENCY RIGID BODY GAIN MARGIN
C RIGID BODY PHASE MARGIN
D 1ST BENDING MODE PHASE MARGIN (LOW FREQUENCY)
E 1ST BENDING MODE PHASE MARGIN (HIGH FREQUENCY)
F 2ND BENDING MODE GAIN MARGIN (IRRESPECTIVE OF PHASE)
G PHASE TO THE PEAK OF 2ND BENDING MODE RESPONSE
H 3RD BENDING MODE GAIN MARGIN (IRRESPECTIVE OF PHASE)
I PHASE TO THE PEAK OF 3RD BENDING MODE RESPONSE

Figure 5-1. Typical Gain-Phase Diagram With Margins

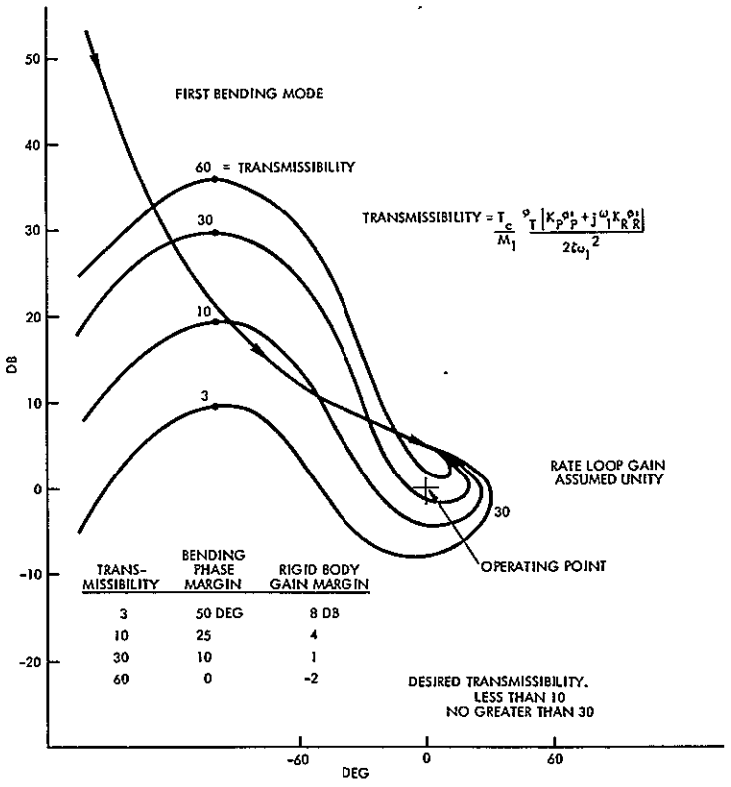

Figure 5-2. Effects of Bending Mode Transmissibility Upon Stability Margins Without Compensation

its use is constrained by its associated phase shifting effects in which increased phase lag and phase lead are accrued about the design frequency. This produces an erosion of both ridid body and first mode bending phase margins, an erosion which may not be tolerable.

An effective and normally used method to maintain low transmissibility coefficients, thereby easing the control compensation problem, is the location of control system sensors on the vehicle such that structural bending effects are minimized. Location of the rate gyro package on or near the first bending mode antinode to accomplish this minimization is a common practice. Location of the angular position sensors is less critical since a smaller contribution to bending transmissibility is usually associated with this feedback loop. In concurrence with the purposes of this design study, the angular position sensors were assumed located in the spacecraft atop the boost vehicle.

Several vehicle configurations were evaluated in terms of their bending transmissibility in addition to the performance of detailed stability analyses. Figure 5-3 shows bending transmissibility time histories of three vehicle configurations. The gains assumed were those employed on present vehicle programs. Gain changes were not included although typically for these liquid propellant boosters, a decrease in gain by a factor of two or three is usually executed at approximately 110 sec after liftoff. In the figure, the effects of locating the rate gyro package at three separate vehicle stations are shown for the Saturn V and Atlas/Centaur vehicle and at two stations for the Saturn IB/Centaur vehicle.

The unusual drop in transmissibility at mid first stage flight for the Atlas/Centaur vehicle results from the abrupt change in the structural damping values which were obtained from past design study reports. In actuality, a representative smooth curve is to be expected. For the Atlas/Centaur vehicle, a rate gyro located at station 708 appears desirable, a location at station 583 (possibly the present location) appears tolerable, and location within the spacecraft appears intolerable.

For the Saturn V/Apollo vehicle, location of the rate gyro package in the aft compartment of the S-IVB stage appears desirable, location in the instrument unit appears tolerable, and location in the spacecraft appears intolerable.

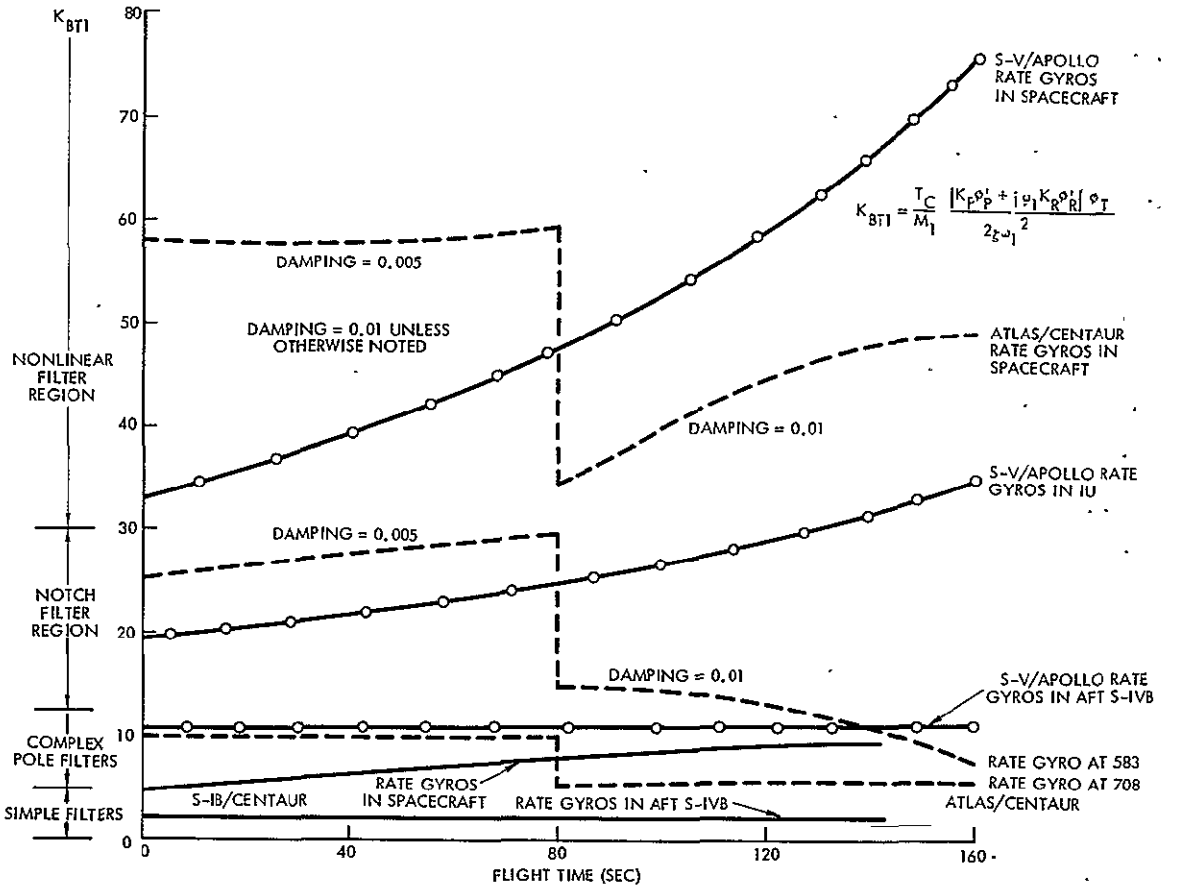

Figure 5-3. First Stage Booster Bending Transmissibility Coefficients (Position Sensors in Spacecraft)

For the Saturn IB/Centaur vehicle, location of the rate gyro package in the spacecraft, IU, or aft S-IVB compartment appears satisfactory with preference given to the aft S-IVB location.

Approximate filtering regions associated with transmissibility coefficient values are indicated on the left side of Figure 5-3. The lower part of each region may require use of only one filter whereas, for the upper part of each region, a filter change during the flight may be required. In the notch filter design, additional complex pole filters are assumed included for attenuation of higher bending modes. The nonlinear filtering region, shown unbounded, also has limits above which stability

is impossible. Indications are that this limit may occur at a transmissibility less than sixty.

The significance of the structural damping value and its influence on control system compensation is evident, and precise values from ground tests are preferable to the use of assumed values. A value of 1% was employed (with the exceptions noted) following the procedure that has been used in the past.

The transmissibility coefficients for the Atlas/Centaur higher modes are shown in Figure 5-4. Stabilization of the higher modes is more readily achieved as indicated by the lower coefficients. Satisfactory second mode stability margins for the design using spacecraft rate gyros will be more difficult to achieve as is shown in subsequent discussions. No attempt was made to relate higher order transmissibility values to filtering requirements although probably such a relationship can be formulated.

The first and second mode transmissibility coefficients for the Saturn V/Voyager vehicle are given in Figures 5-5 and 5-6, respectively.

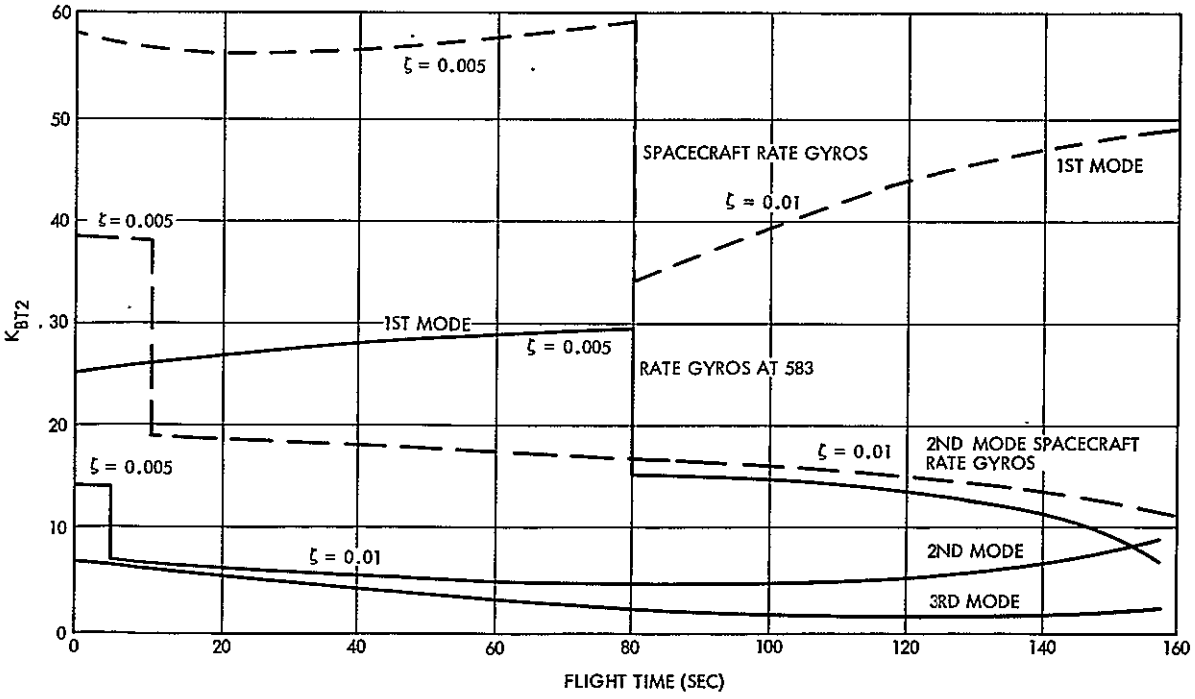

Figure 5-4. Atlas/Centaur Higher Mode Transmissibility Coefficients

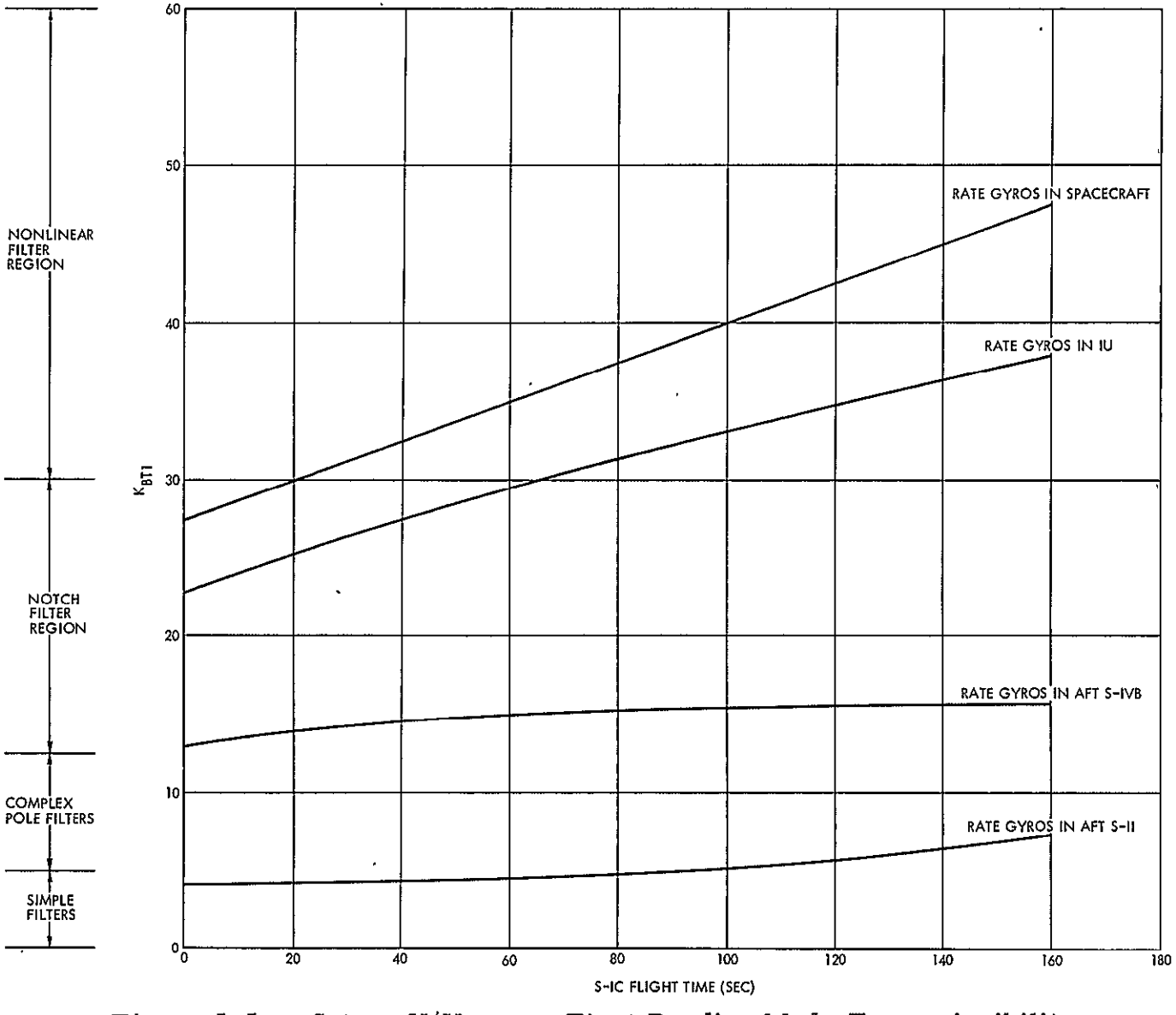

Figure 5-5. Saturn V/Voyager First Bending Mode Transmissibility Coefficients Without Filtering

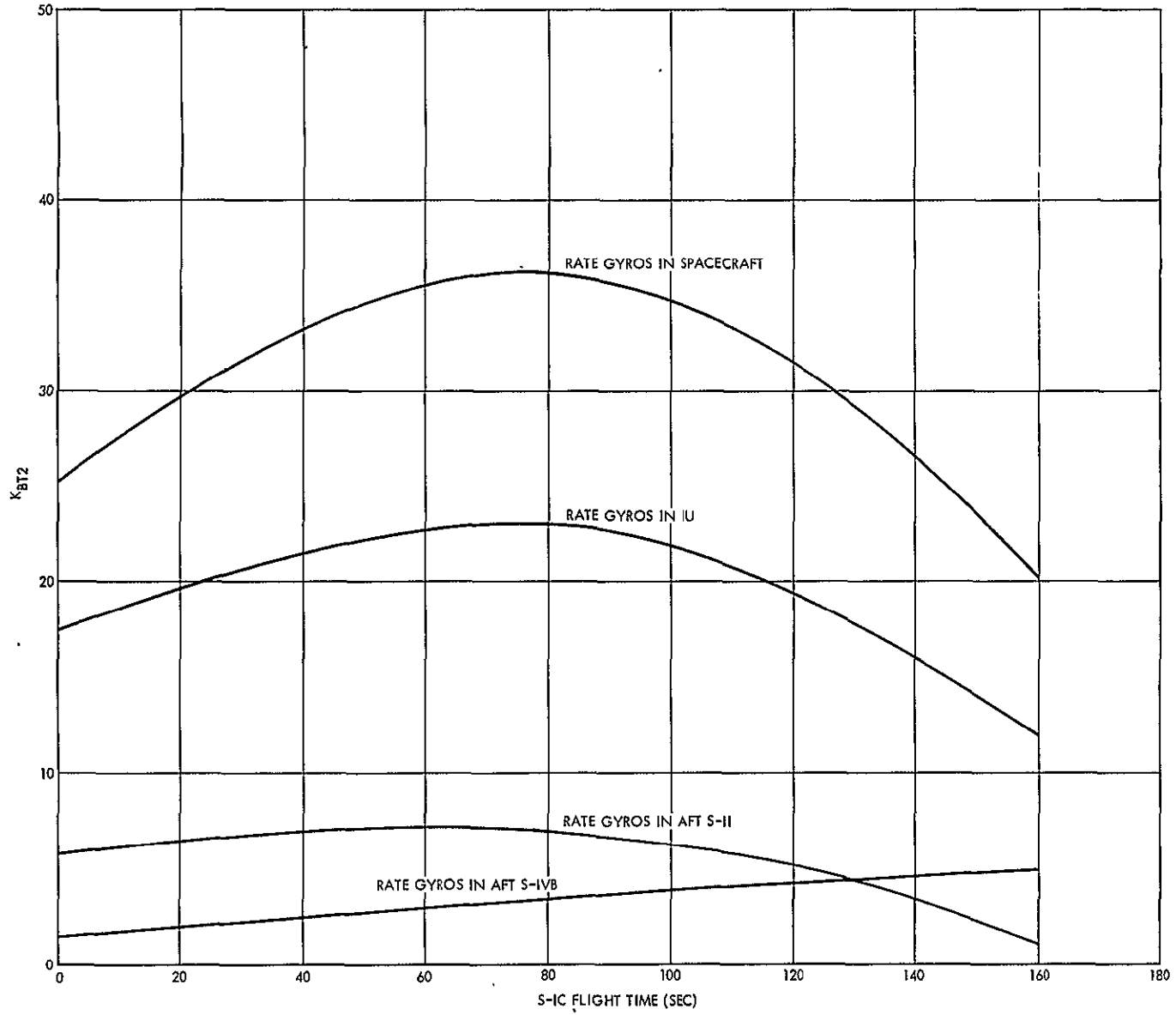

Figure 5-6. Saturn V/Voyager Second Bending Mode Transmissibility Coefficients Without Filtering

Location of the rate gyros in the aft S-II compartment is near ideal; in the aft S-IVB compartment acceptable; in the IU marginal; and in the spacecraft intolerable. Location in the IU is considered marginal rather than unacceptable in view of the gain change that would occur near 110 sec of S-IC flight time. This design condition will, however, pose a considerable filtering challenge. The stabilization of the second mode will also prove to be difficult if the rate gyros are located within the IU.

Two other vehicle configuration transmissibility coefficients are shown in Figure 5-7 for the Saturn IB/Apollo CSM and in Figure 5-8 for the Atlas S LV3/Burner 2. The sharp contrast in transmissibility coefficient between the rigid 9-tank-clustered Saturn IB vehicle and the highly elastic balloon-designed Atlas vehicle is clearly evident.

5.3 STABILITY ANALYSIS OF THE ATLAS/CENTAUR VEHICLE

The equations employed in the booster stability analyses are given in app. B. The analysis data employed are given in app. C for the Atlas/Centaur AC-13 vehicle configuration.

The first step of the AC-13 vehicle design study was to obtain a baseline for design comparison purposes by investigating the stability margins of the existing design. The available data placed the rate gyro location at station 583, the position gyros within the booster stage command, and the control pod at station 991. Since an autopilot design for this new vehicle configuration was not available, the AC-5 vehicle autopilot parameters, consisting of complex poles at 15.5 rad/sec with pole damping of 0.5 and a position gain of 1.8, were employed. The analog control system gain-phase plots at five booster flight times (0, 40, 80, 112, and 154 sec) are given in Figures 5-9 through 5-13. In the first figure, no stability margins for the first bending mode exist and stable slosh modes are shown. In the 40-sec case, a small first mode bending margin exists and an Atlas LOX-slosh instability occurs, which is typical for the Atlas/Centaur vehicle. (This instability exists over a brief duration and is not usually of importance.) In the 80-sec case, the bending margins are considerably improved and the Atlas LOX-slosh mode is stable. In the 112-sec case, the bending margins continue to improve, and problems with the Centaur LOX-slosh mode loom. In the booster engine cutoff (BECO) case at 154 sec, the bending stability

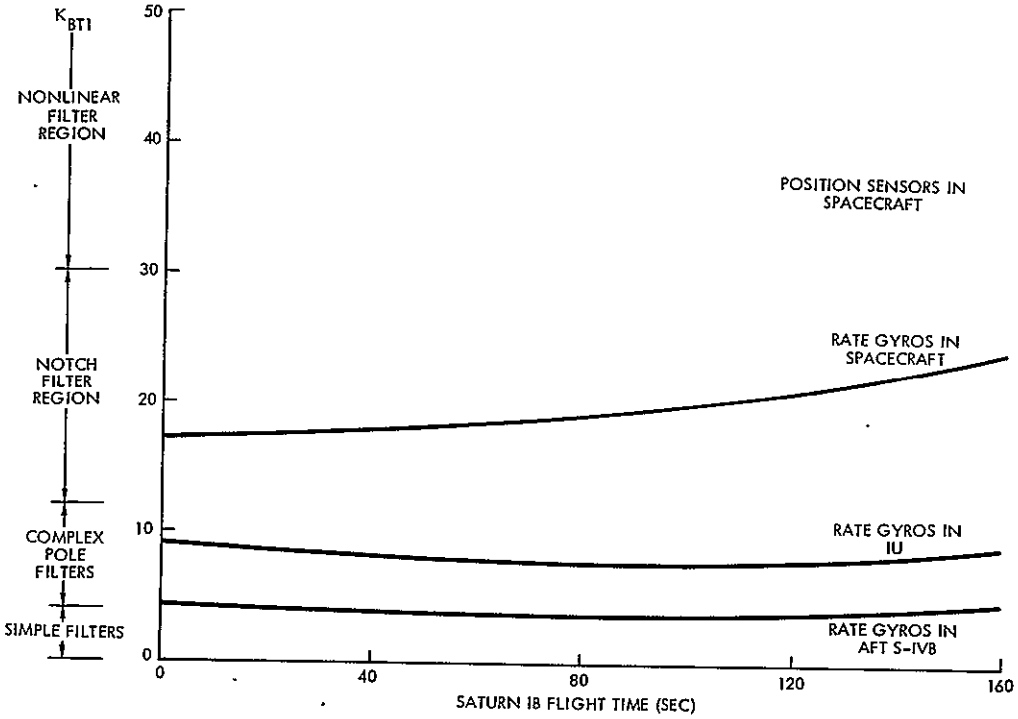

Figure 5-7. Saturn IB/Apollo CSM First-Stage Booster Bending Transmissibility Coefficients

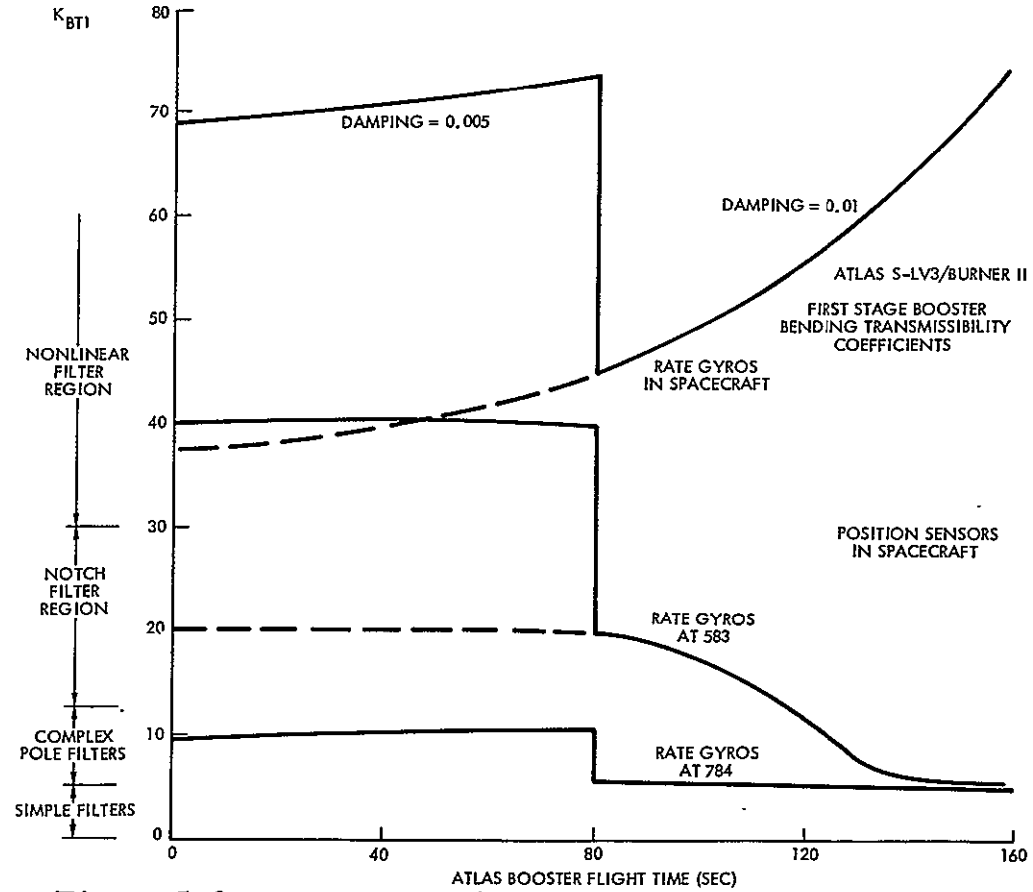

Figure 5-8. Atlas S-LV3/Burner First-Stage Booster Bending Transmissibility Coefficients

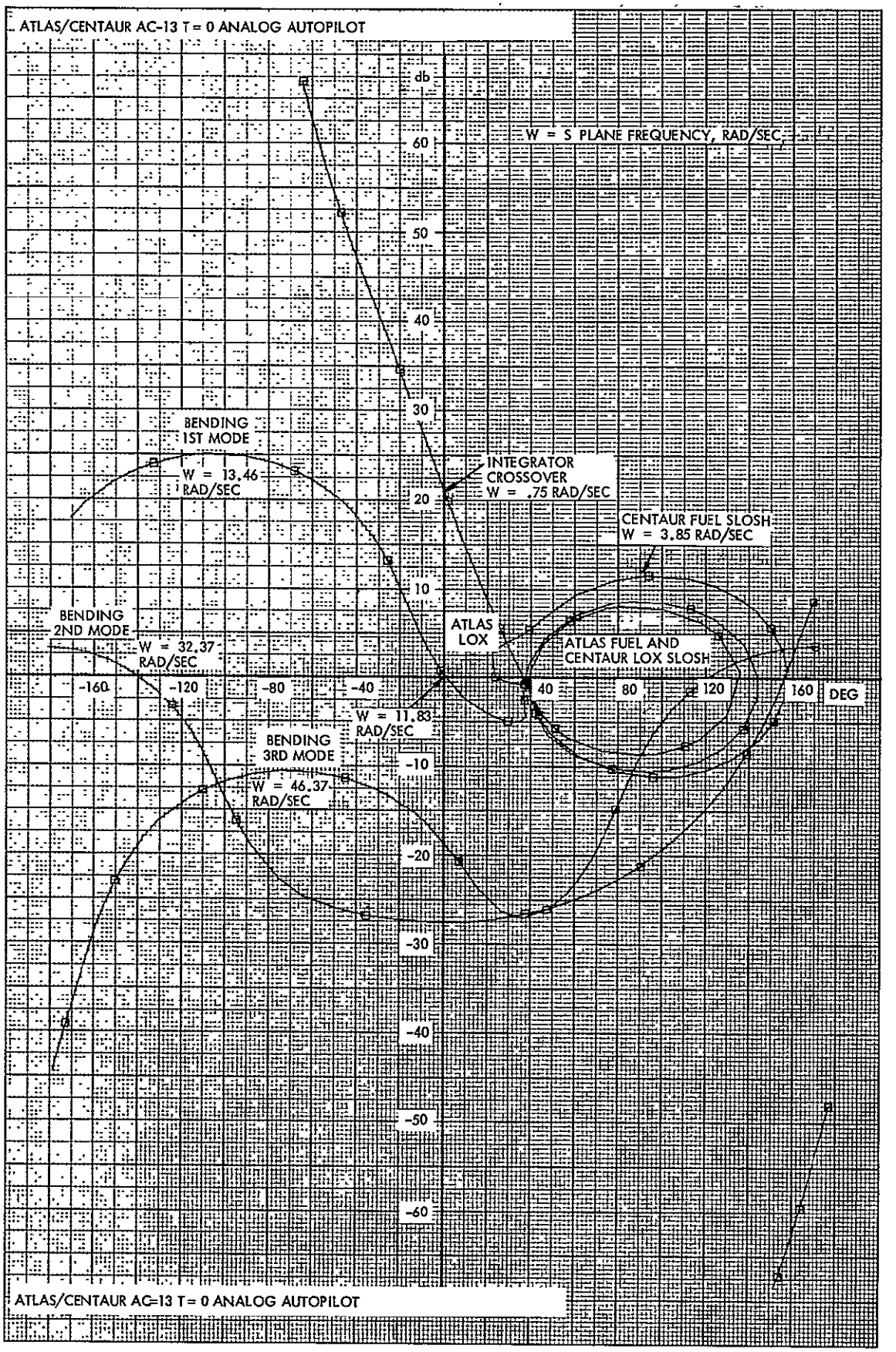

Figure 5-9. Gain-Phase Plot Atlas/Centaur AC=13 T=0 Analog Autopilot

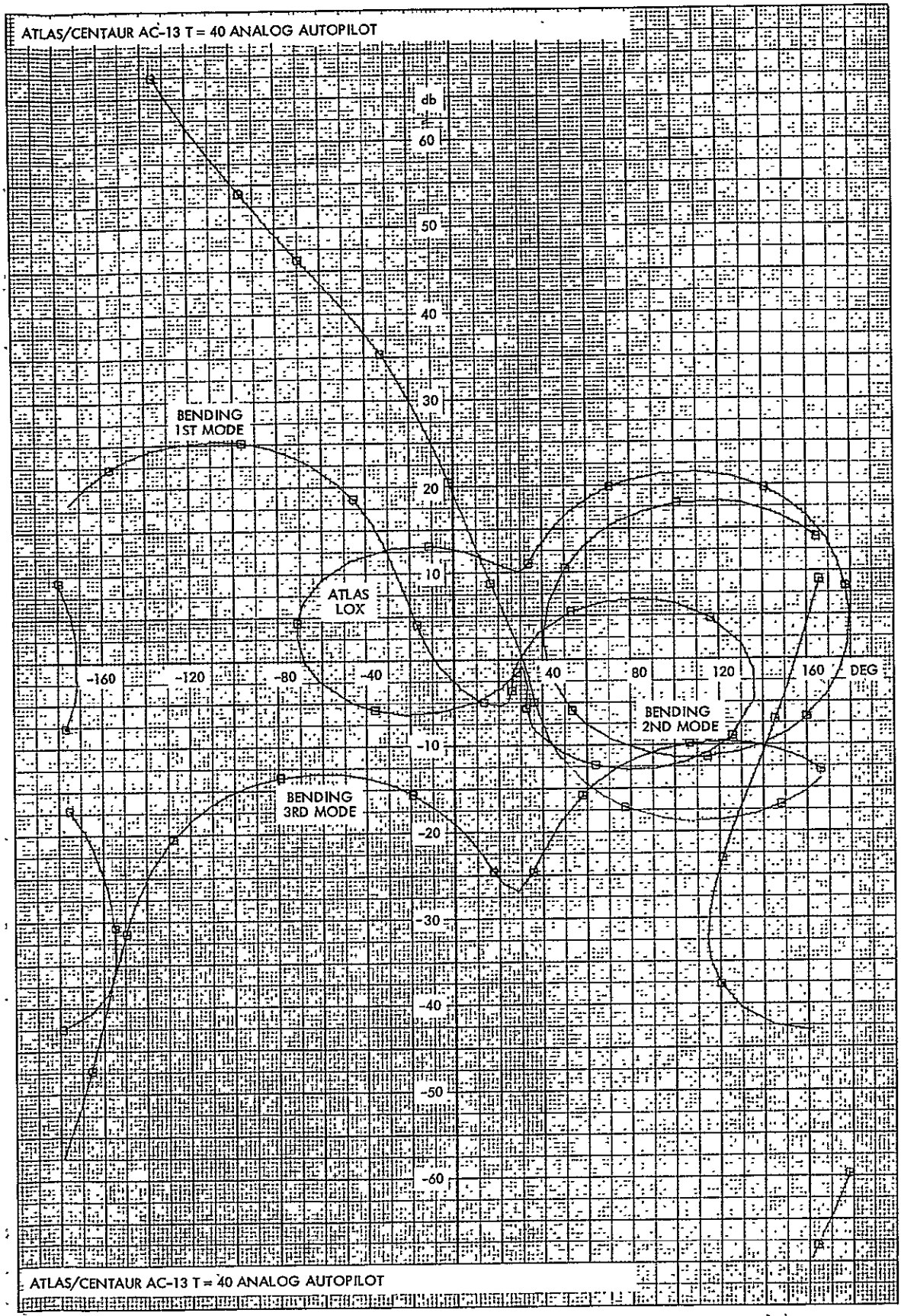

Figure 5-10. Gain-Phase Plot Atlas/Centaur AC-13 T=40 Analog Autopilot

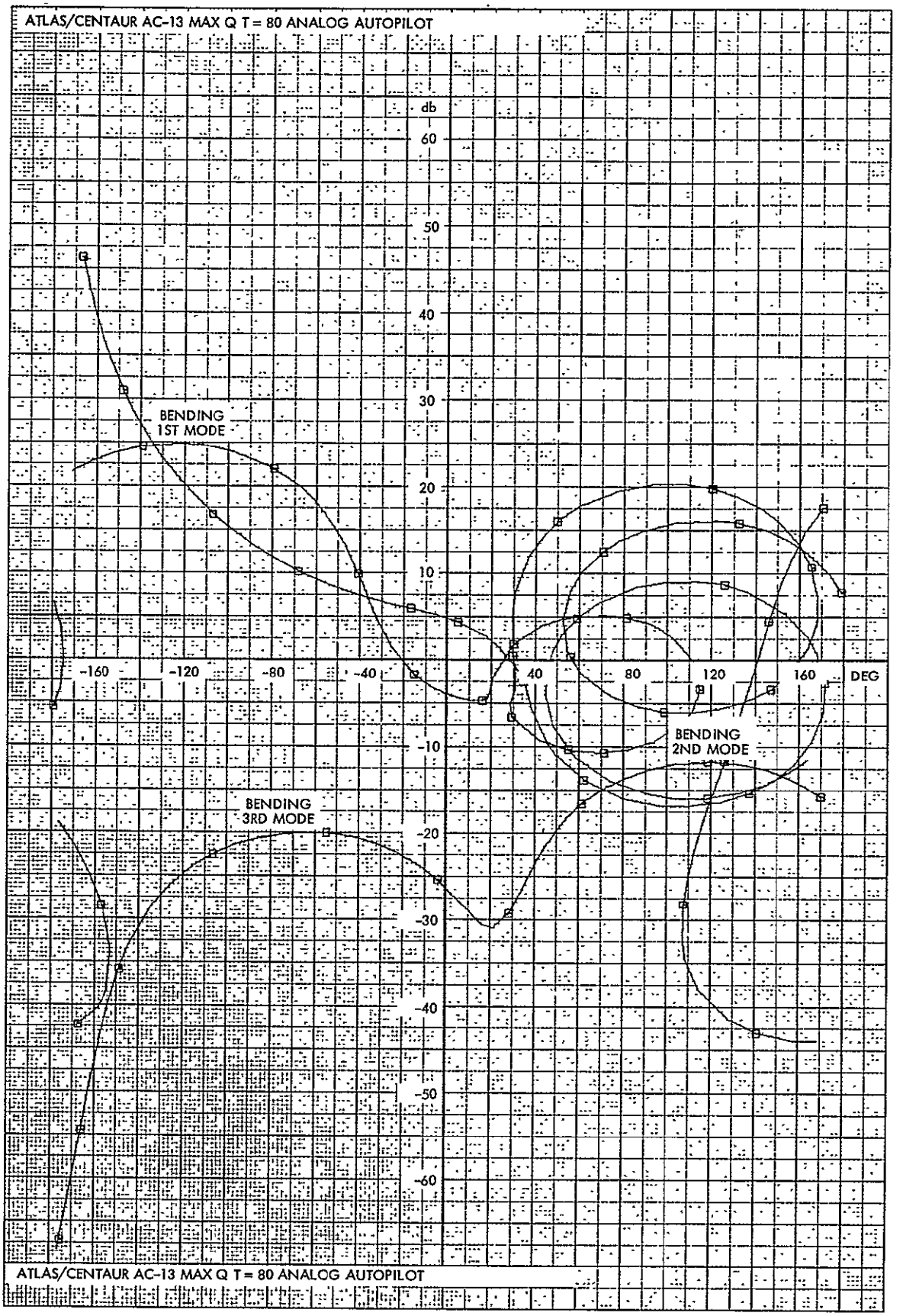

Figure 5-11. Gain-Phase Plot Atlas/Centaur AC-13 Max Q T=80 Analog Autopilot

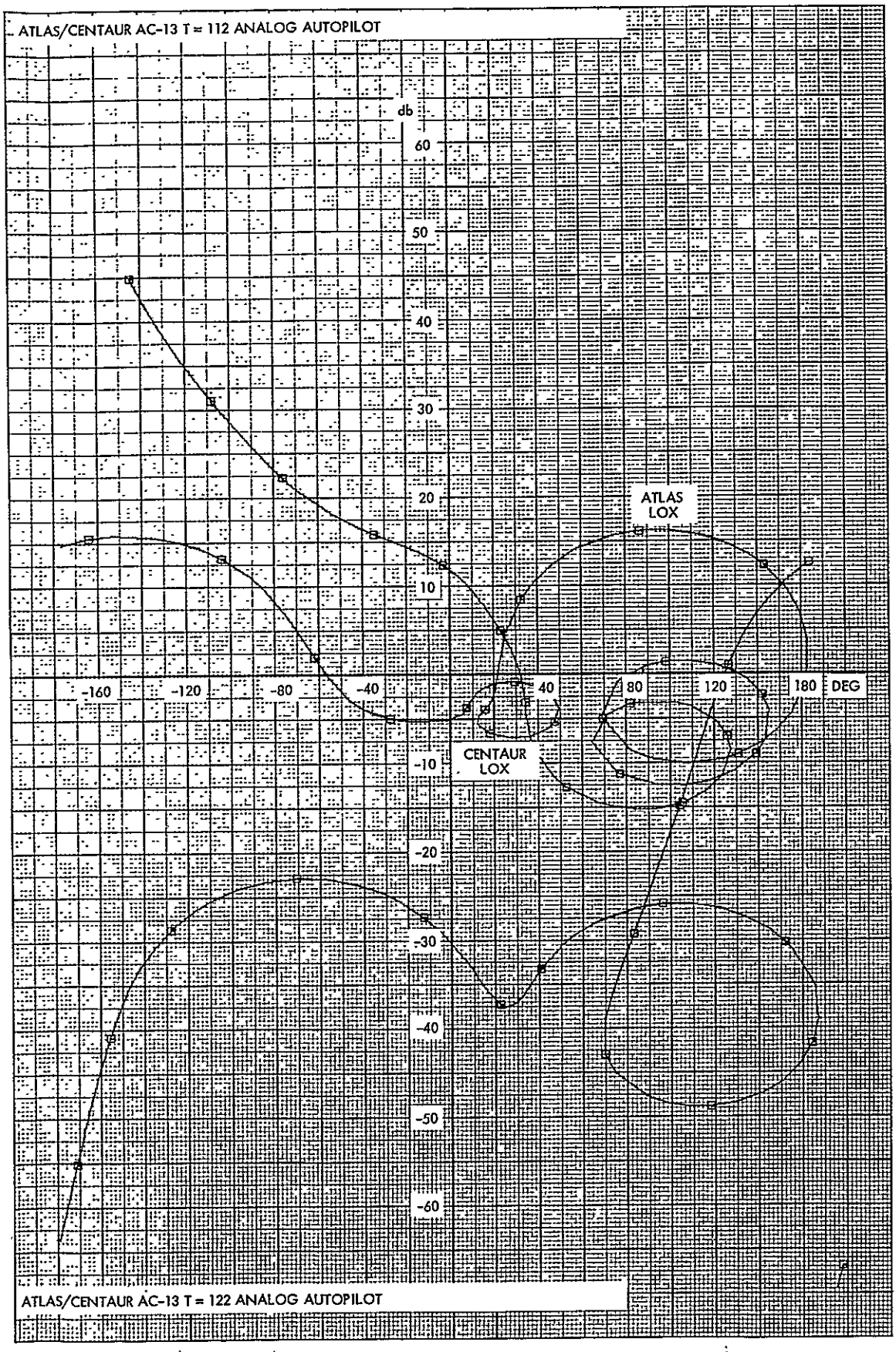

Figure 5-12. Gain-Phase Plot Atlas/Centaur AC-13 T=122 Analog Autopilot

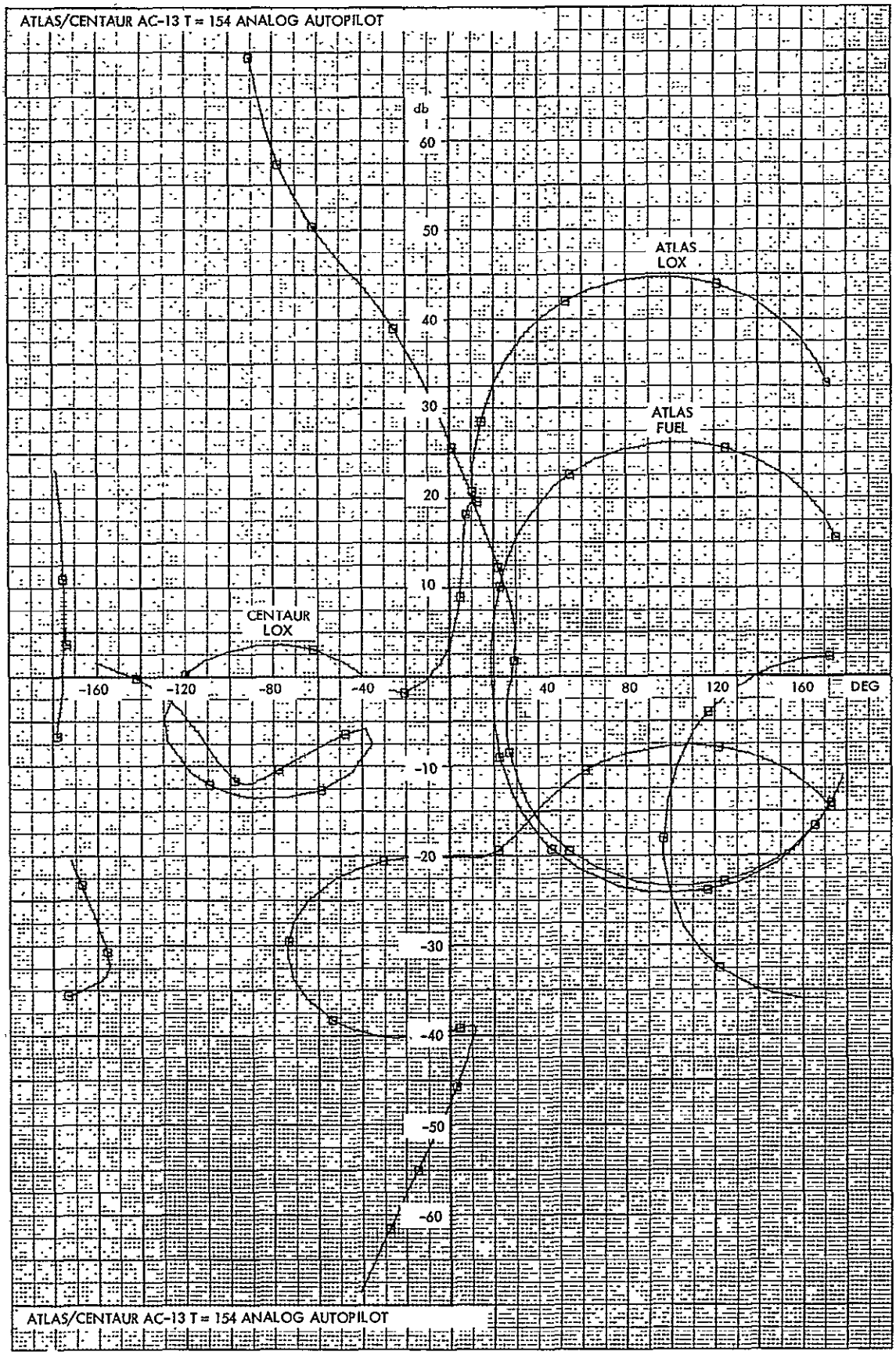

Figure 5-13. Gain-Phase Plot Atlas/Centaur AC-13 T=154 Analog Autopilot

margins are ample and the interaction between the Atlas and Centaur LOX-slosh modes are heightened; therefore resulting in slosh margin reductions. A reduction in control gain to produce some slosh margin appears desirable. Figure 5-14 shows the rigid body gain axis crossover points plotted as a function of time. The desirable gain schedule is shown to involve linear gain variations with time, which will require a rather complex implementation compared with the simple gain changes normally used.

Instead of employing linear gain variations, a filter change used during the first stage of flight would be a simpler design implementation. The effects of changing the complex pole filter frequency to 11 rad/sec, with the filter pole damping maintained at 0.5, are shown in Figures 5-15 through 5-17 for the liftoff, maximum q, and BECO cases, respectively. Bending stability at liftoff is obtained at the expense of slosh instabilities later in flight. Combining these results with the original filter margins produces the composite gain axis crossover curves shown in Figure 5-18. A filter change at 70 sec of flight appears desirable, and a single gain change at 110 sec appears to produce compromising gain margins. Margins in excess of 6 dB are desired and the 4 to 5 dB level of high-frequency crossover margins is considered rather skimpy, but tolerable, for flight-proven vehicles. Certainly, improvements in the design margins are needed.

The location of the rate gyros for the AC-13 vehicle is not optimum for control stability, but the possible movement of this package is discussed subsequently. After evaluation of the analog AC-13 control system, which is employed as a baseline design, the effects of substituting a digital control system were investigated. The ROI guidance system was located in the spacecraft on top of the Centaur and three distinct rate-sensing configurations were studied: 1) use of the present Atlas rate gyros at station 583, 2) use of the ROI rate gyros in the spacecraft, and 3) use of the Atlas rate gyros at station 708 (the optimum first mode stability location). The effects of a 25-samples/sec computer sampling rate and a 10-msec computational delay were included in all of the analyses performed. The roots of the equation matrix given in app. A were

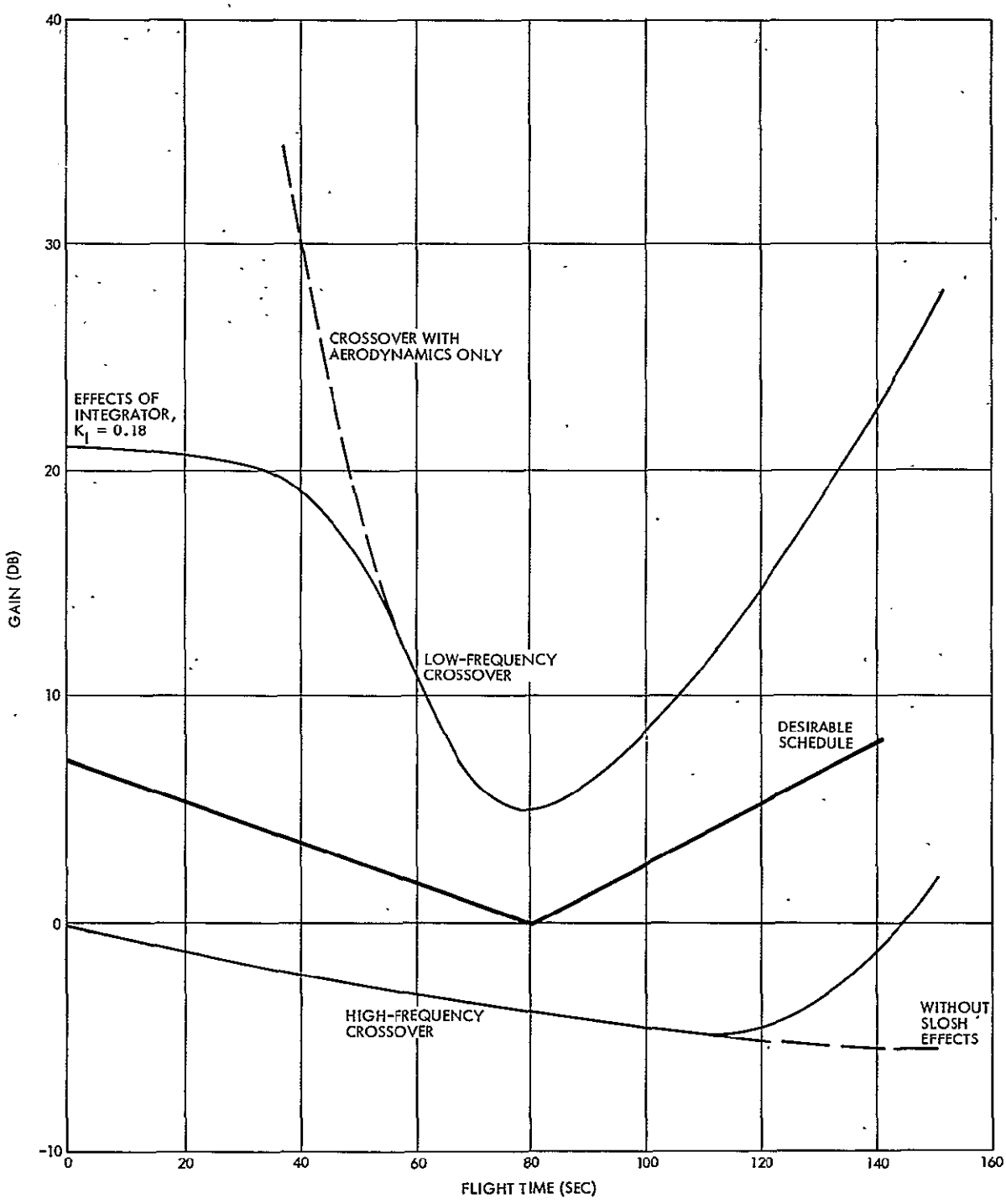

Figure 5-14. Atlas/Centaur AC-13 Rigid Body Gain Margins, Analog Autopilot, and Complex Poles at 15.5 Rad/Sec

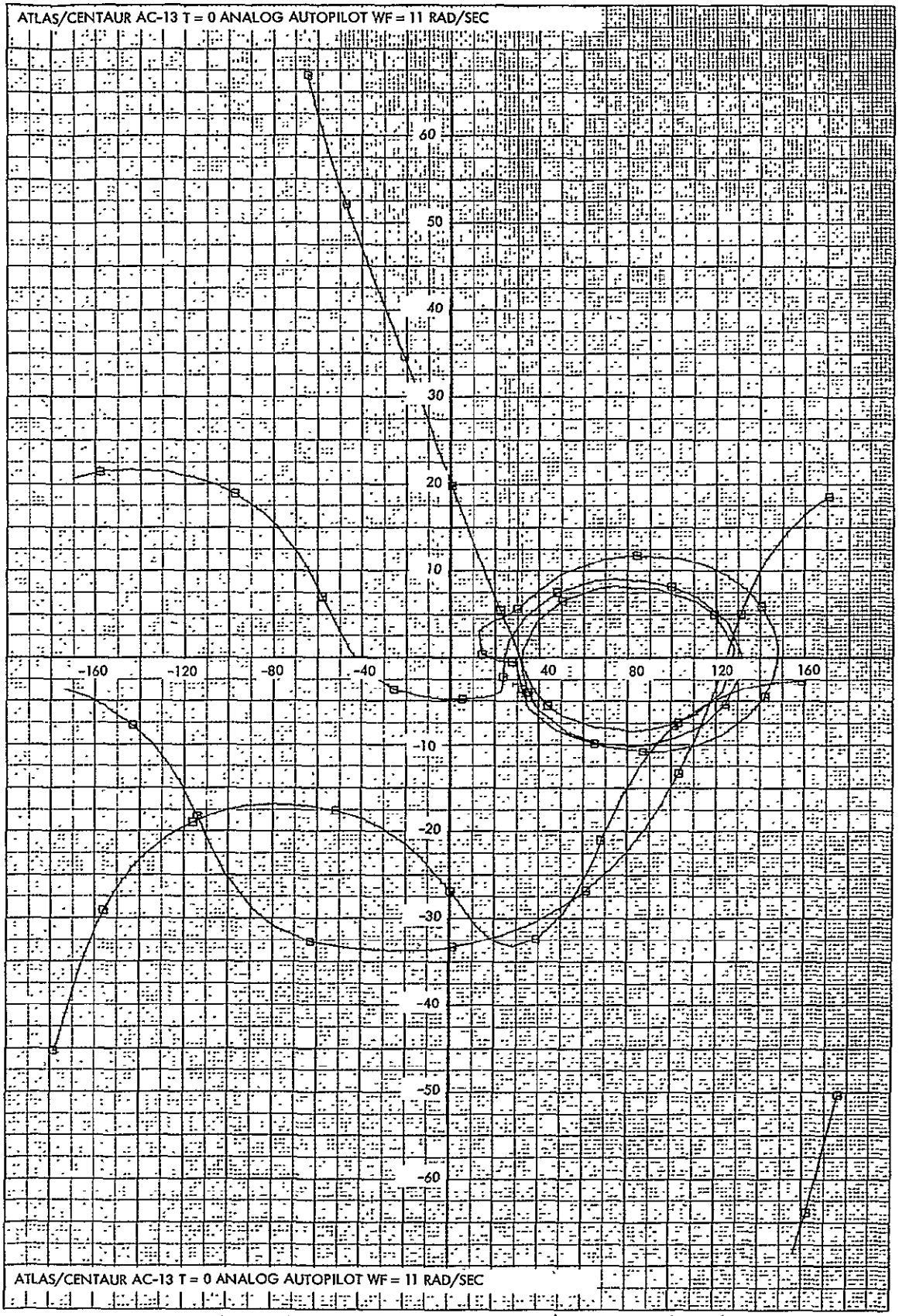

Figure 5-15. Gain-Phase Plot Atlas/Centaur AC-13 T=0 Analog Autopilot WF = 11 Rad/Sec

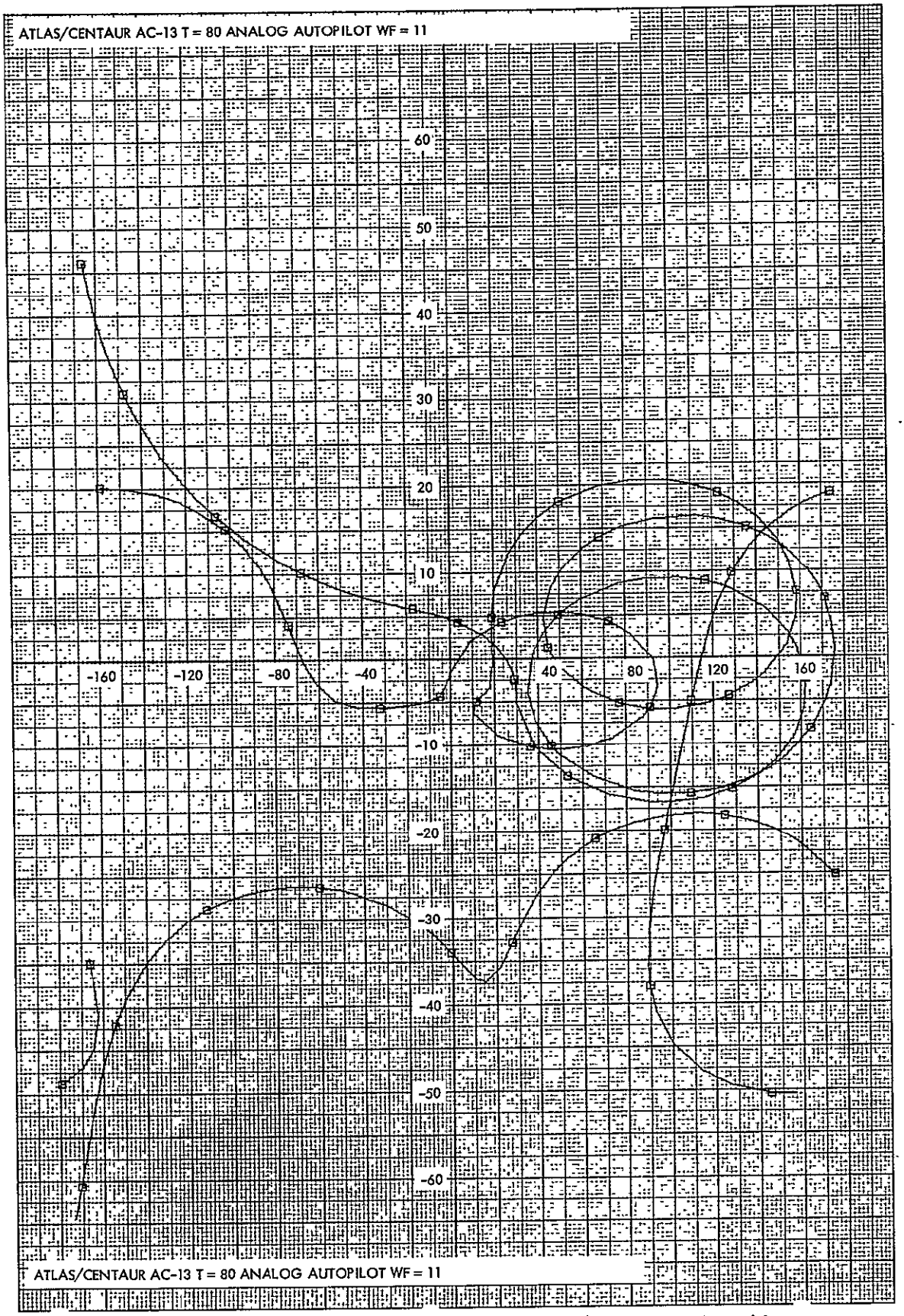

Figure 5-16. Gain-Phase Plot Atlas/Centaur AC-13 T=80 Analog Autopilot WF = 11 Rad/Sec

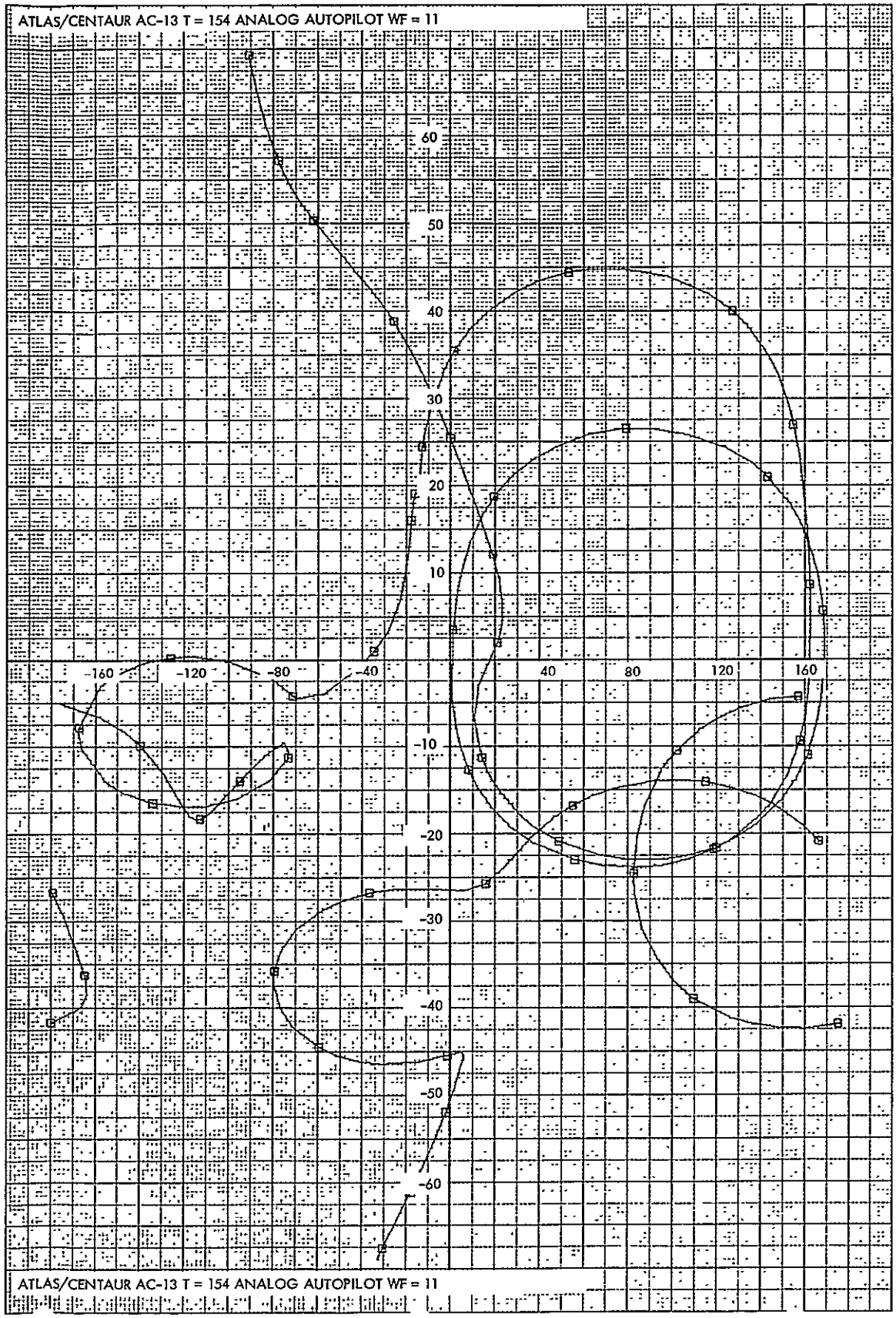

Figure 5-17. Gain-Phase Plot Atlas/Centaur AC-13 T=154 Analog Autopilot WF = 11 Rad/Sec

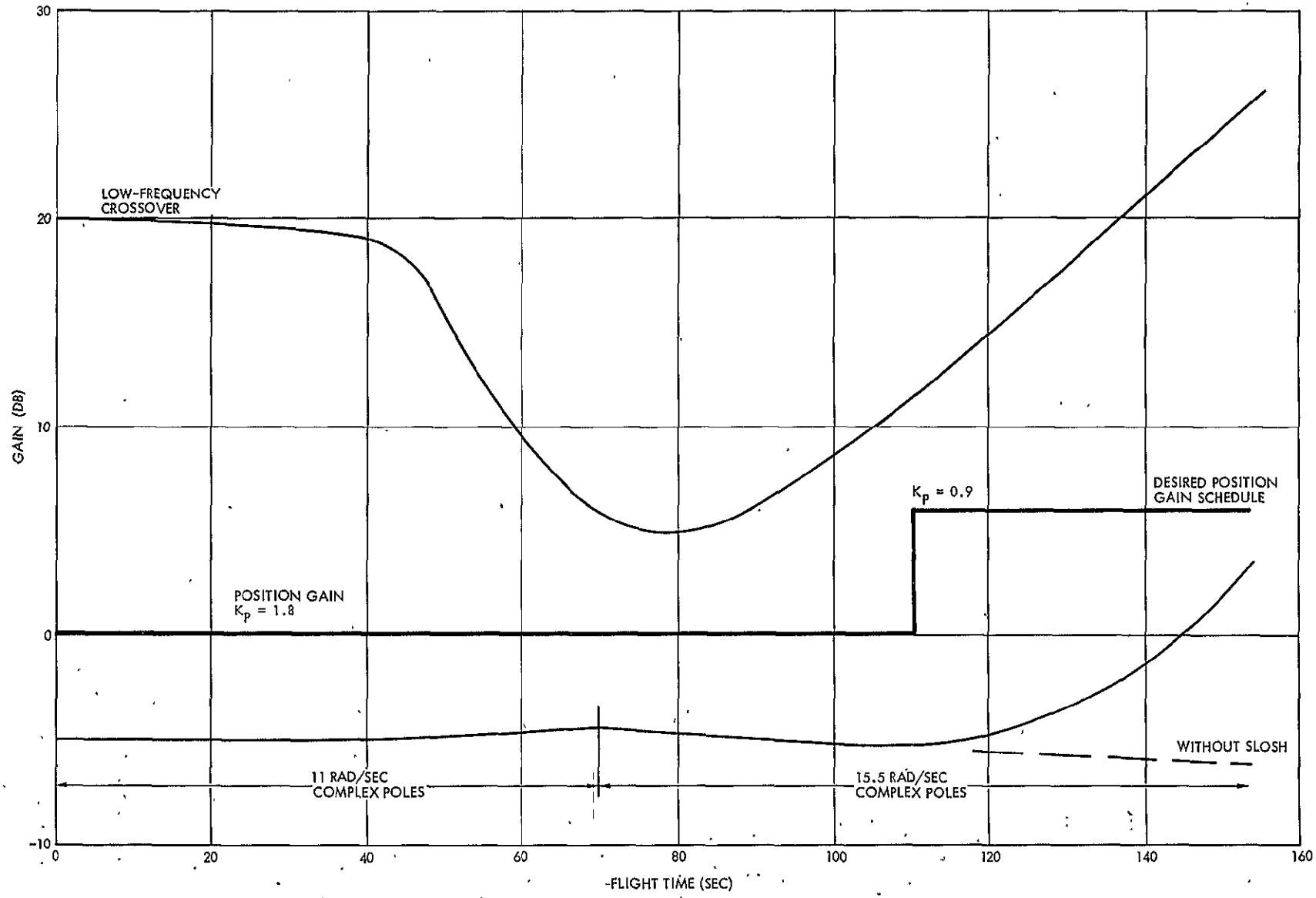

Figure 5-18. Atlas/Centaur AC-13 Rigid Body Gain Margins, Analog Autopilot, and Complex Poles changed at T = 70

transformed first into the Z-plane and then into the W-plane in which control compensation was added. Gain-phase plots of the open-loop frequency response were obtained in the W-plane and appear similar to those for the analog system.

With the rate gyros located at station 583, the output signals routed upstage to the ROI guidance system, and the use of a digital complex pole filter equivalent to the analog filter, the corresponding gain-phase plots for five times of flight are given in Figures 5-19 through 5-23. Compared to the analog counterpart of the first bending mode shown in Figure 5-9, more phase stabilization is obtained because of the relocation of the position sensors from aft to forward of the antinode of the first bending mode. This trend persists through the other four plots, though the slosh mode responses remain unaffected by the design change.

The rigid body gain margin plot of the desirable position gain schedule is shown in Figure 5-24. To maintain gain margins above 4 dB, a two-step gain schedule is required. The use of a digital notch filter in addition to the complex pole filter was next investigated. Two notch filter designs at $V = 0.216$ rad/sec and $V = 0.174$ rad/sec corresponding to S-plane frequencies of 11 rad/sec and 8.8 rad/sec were included in the respective gain-phase plots of Figures 5-25 and 5-26 for the maximum q condition. Damping of the zeros was selected to be 0.2, and 0.3 for the poles. Additional lead also was included to counteract the phase lag effects of the notch, resulting in a net 3 dB of attenuation at the notch frequency. The first of the two designs is more desirable since the notch lies nearer the gain axis, and with the use of the added notch filter, a single gain change may suffice. The other flight times were not investigated since good stability margins are to be expected from employing a filter change which can be readily implemented within the digital computer.

The second ROI guidance design investigated discarded the Atlas rate gyros and used the strapdown rate gyro information for the control process. The placement of the control rate sensors at the top of the vehicle is probably the worst location because the bending transmissibility is increased by two to three fold over the already marginal baseline design.

The liftoff and maximum q (T = 80) cases are shown in Figures 5-27 and 5-28, respectively. A complex pole filter at $V = 0.216$ rad/sec

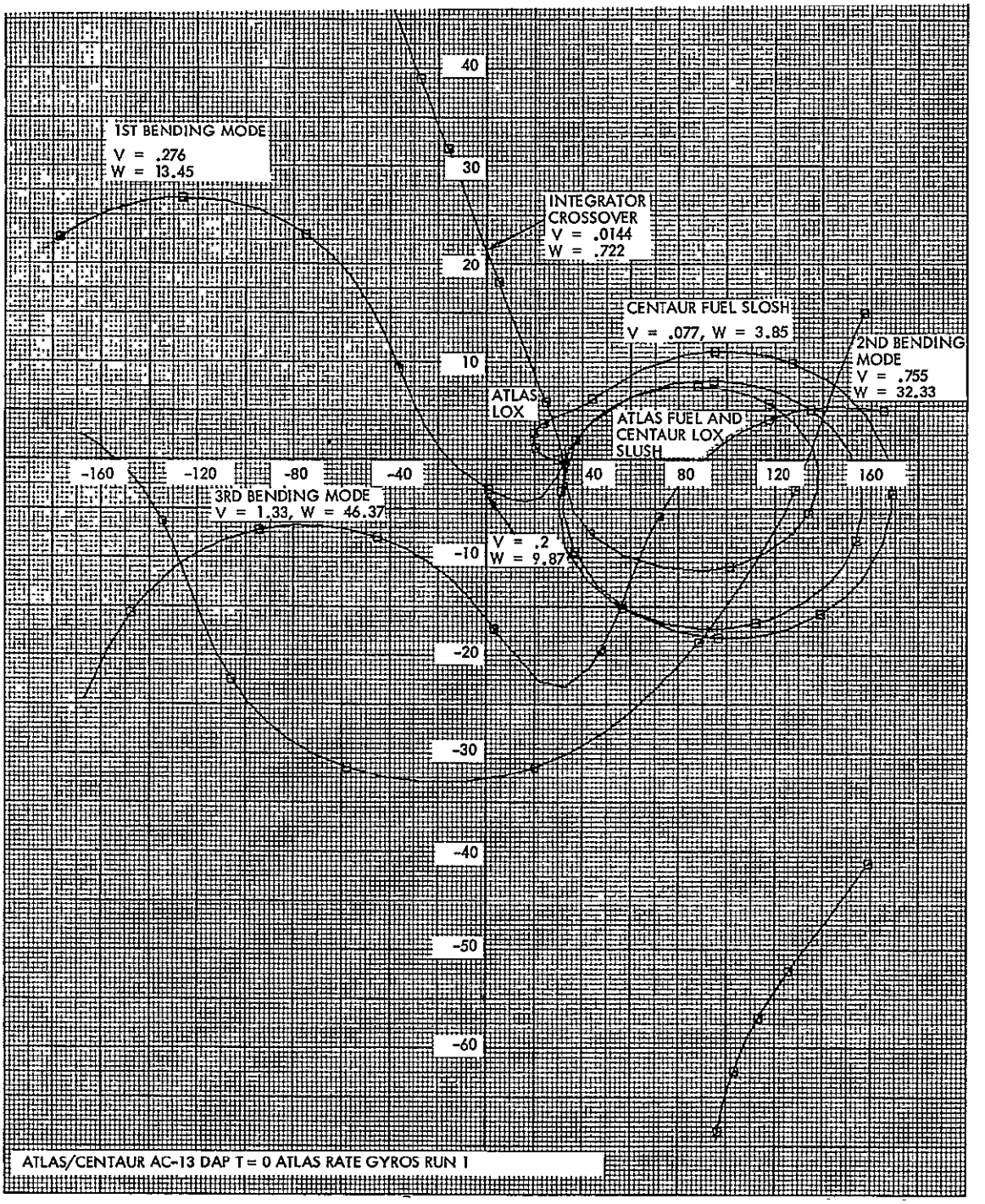

Figure 5-19. Gain-Phase Plot Atlas/Centaur AC-13 Digital Autopilot T=0 Atlas Rate Gyros Run 1

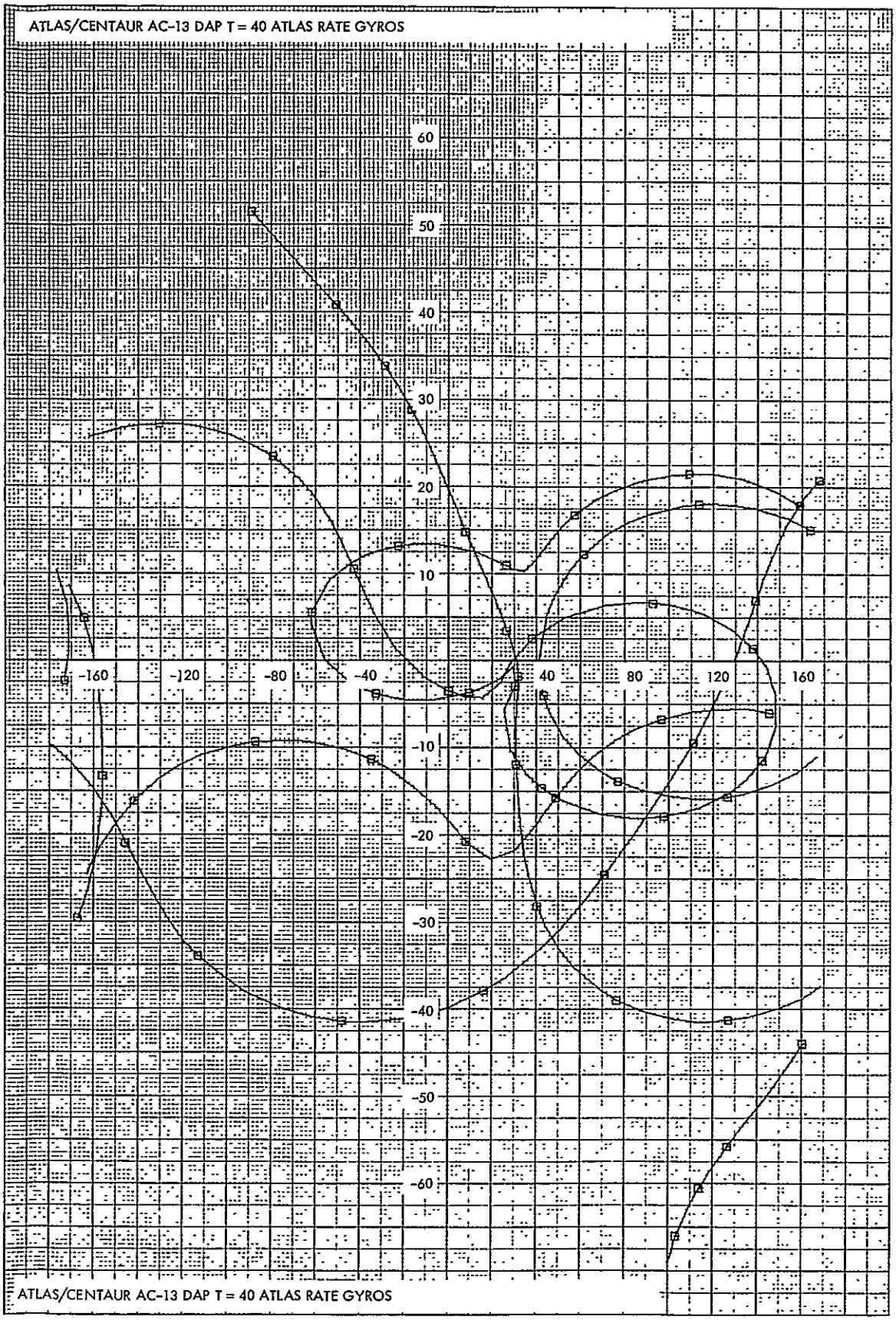

Figure 5-20. Gain-Phase Plot Atlas/Centaur AC-13 Digital Autopilot T=40 Atlas Rate Gyros

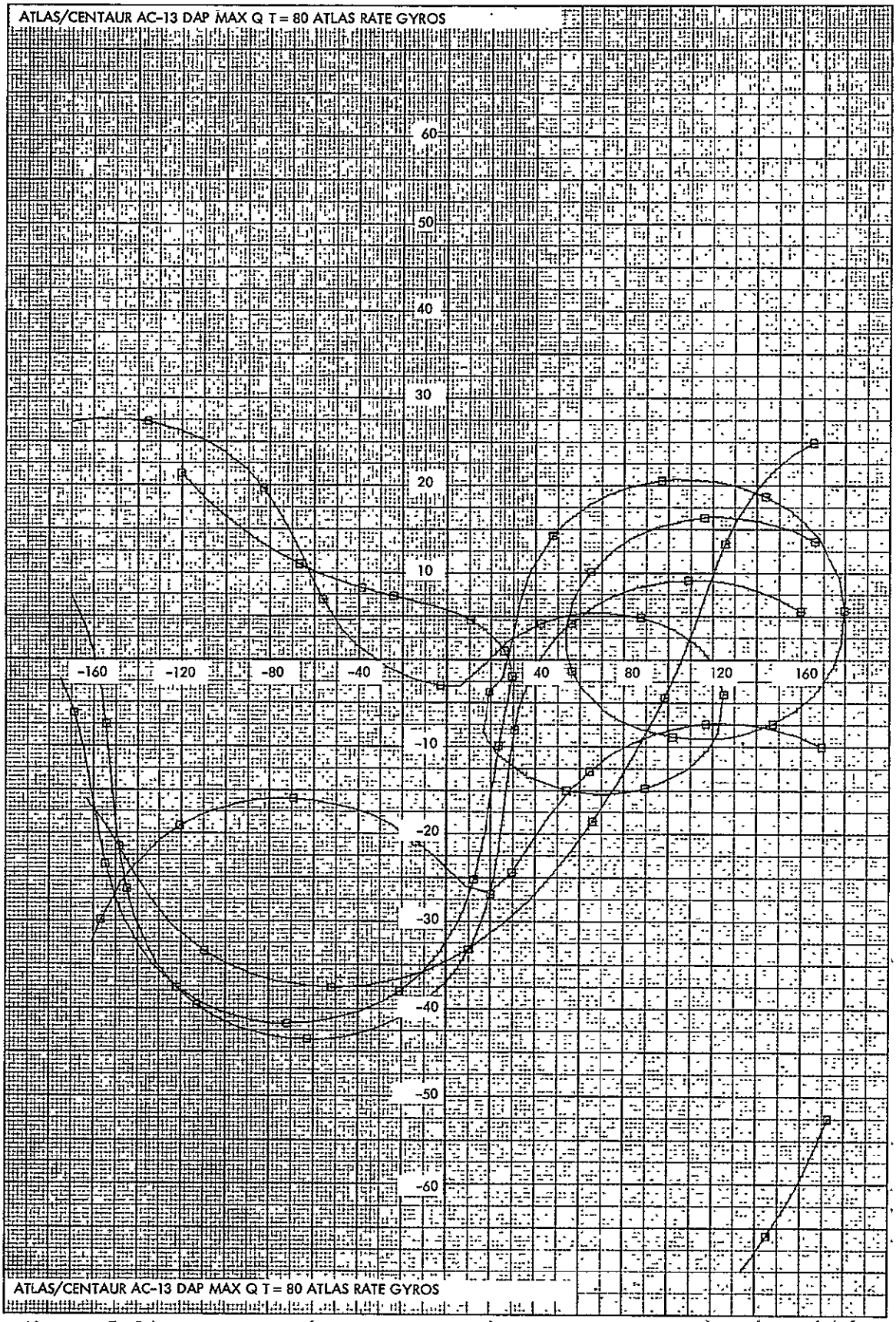

Figure 5-21. Gain-Phase Plot Atlas/Centaur AC-13 Digital Autopilot Max Q T=80 Atlas Rate Gyros

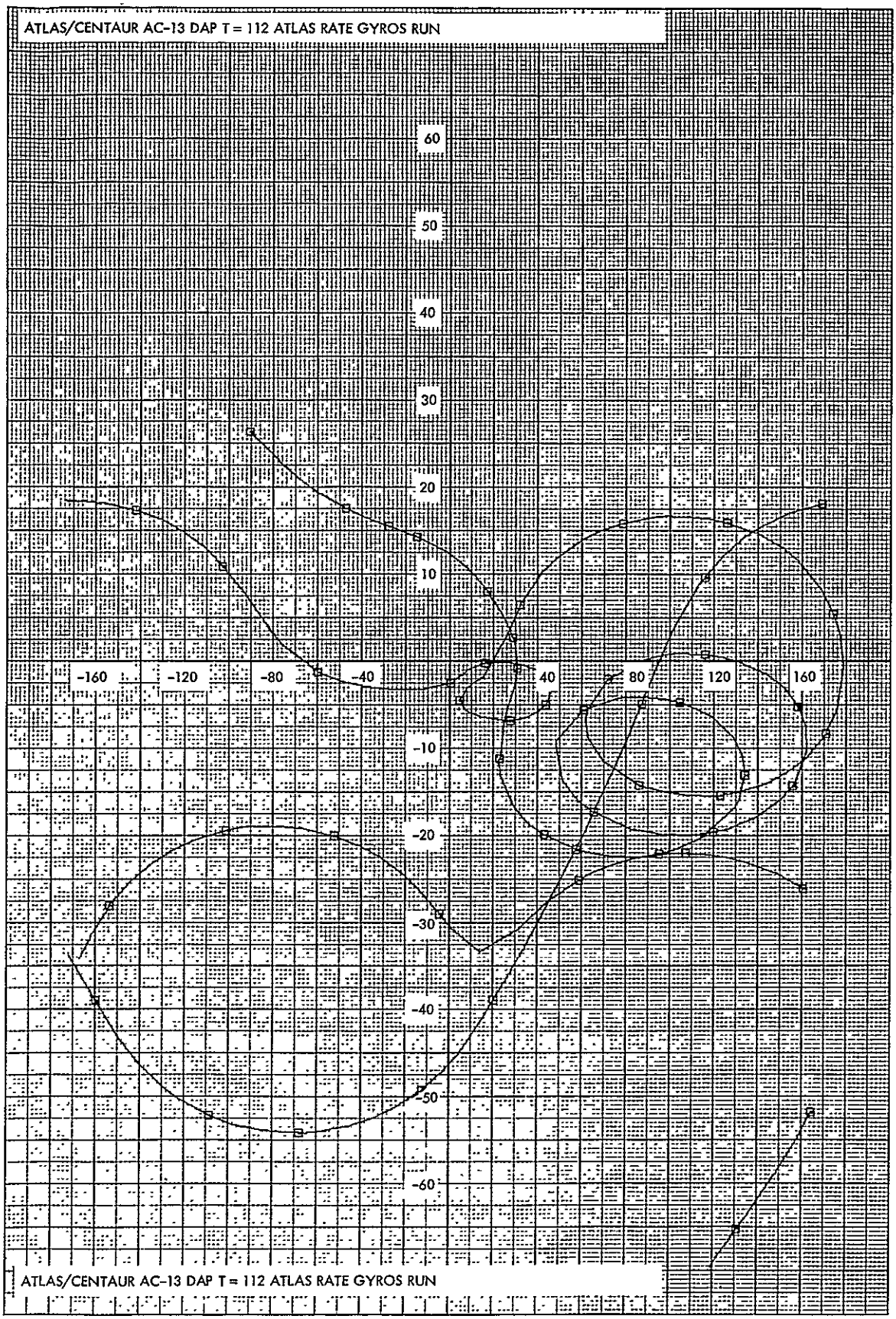

Figure 5-22. Gain-Phase Plot Atlas/Centaur AC-13 Digital Autopilot T=112 Atlas Rate Gyros Run

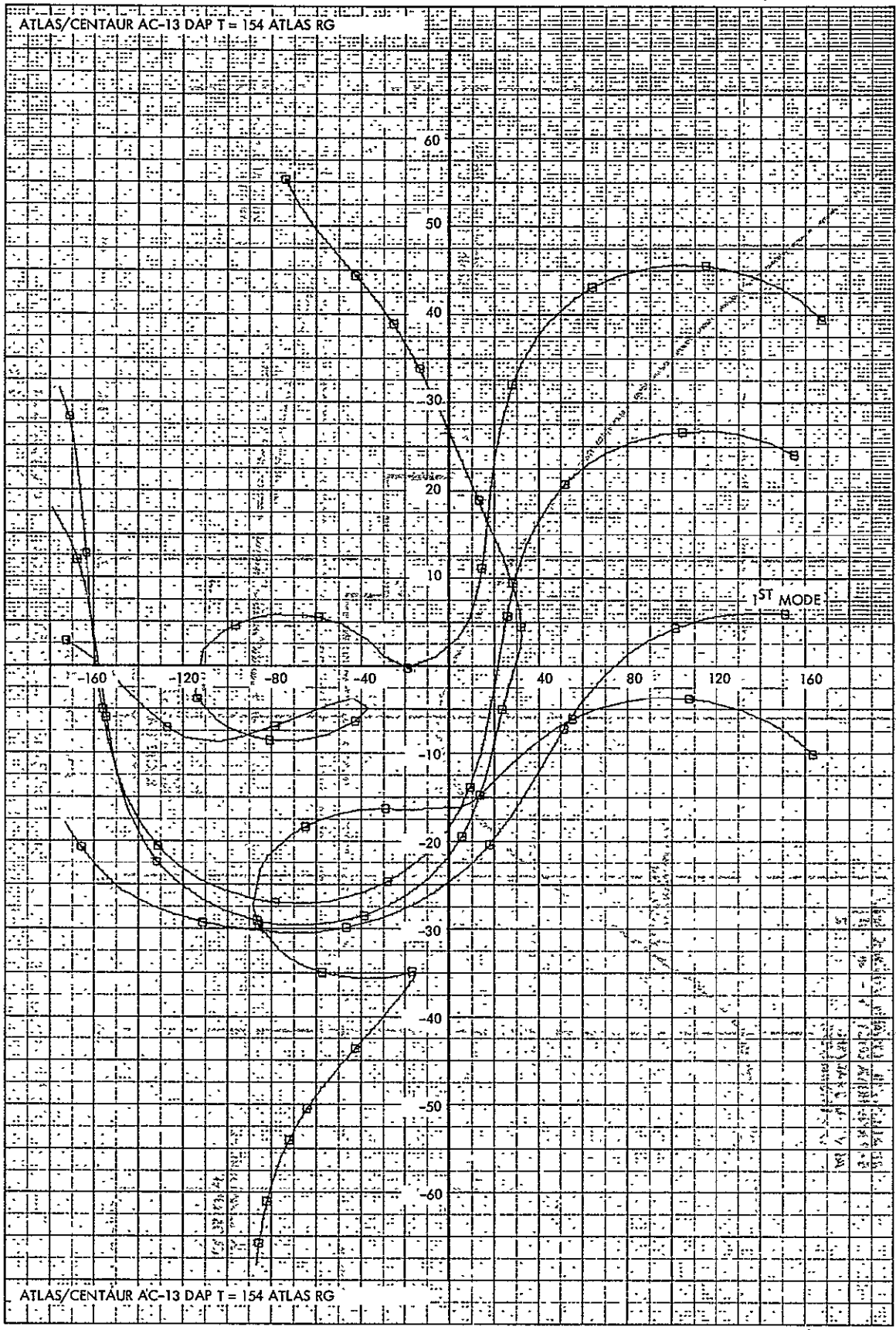

Figure 5-23. Gain-Phase Plot Atlas/Centaur AC-13 Digital Autopilot T=154 Atlas Rate Gyros

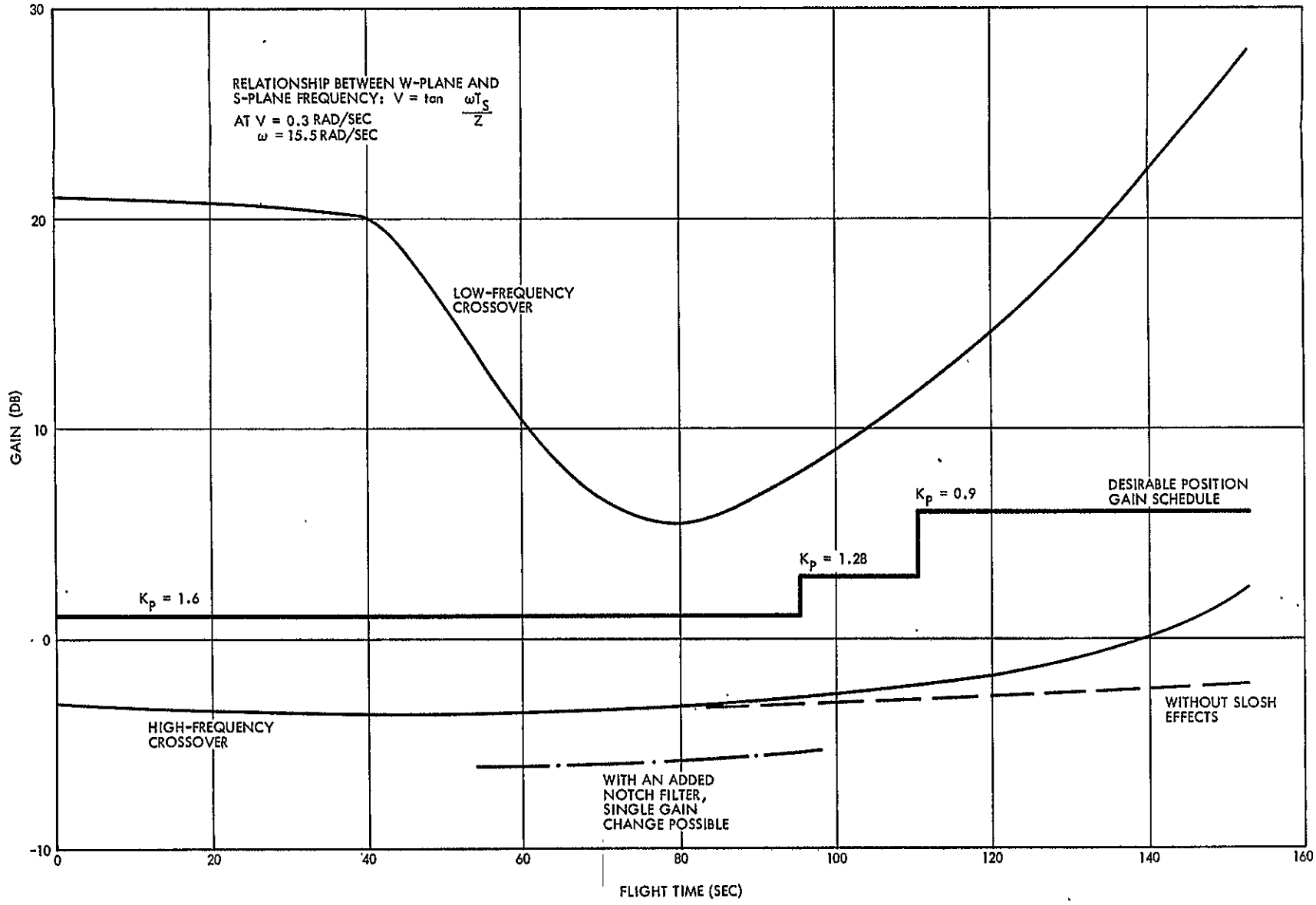

Figure 5-24. Atlas/Centaur AC-13 Body Gain Margins, ROI Guidance System With Atlas Rate Gyros, and Complex Poles at V = 0.3 Rad/Sec

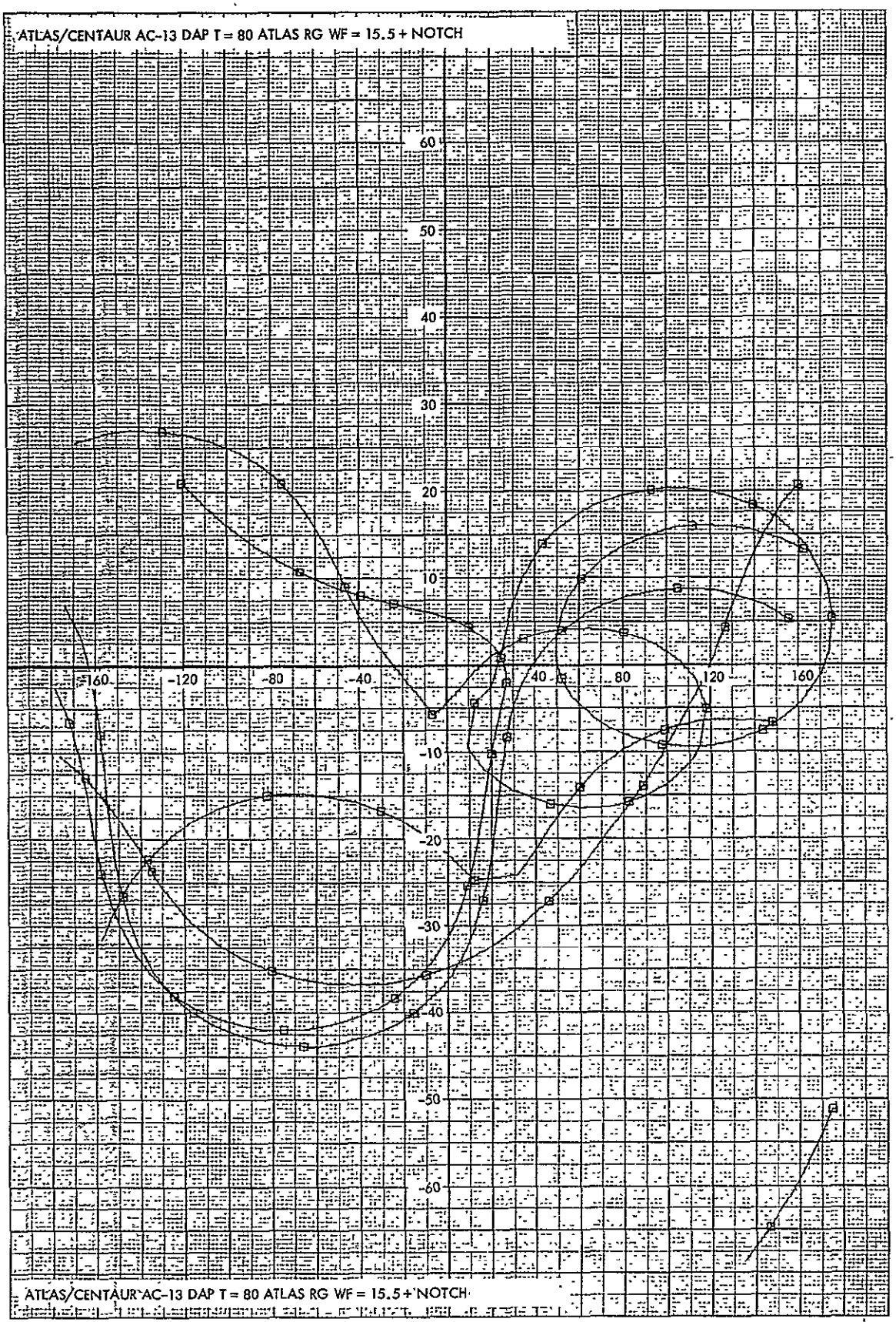

Figure 5-25. Gain-Phase Plot Atlas/Centaur AC-13 Digital Autopilot T=80 Atlas Rate Gyros WF = 15.5 + Notch

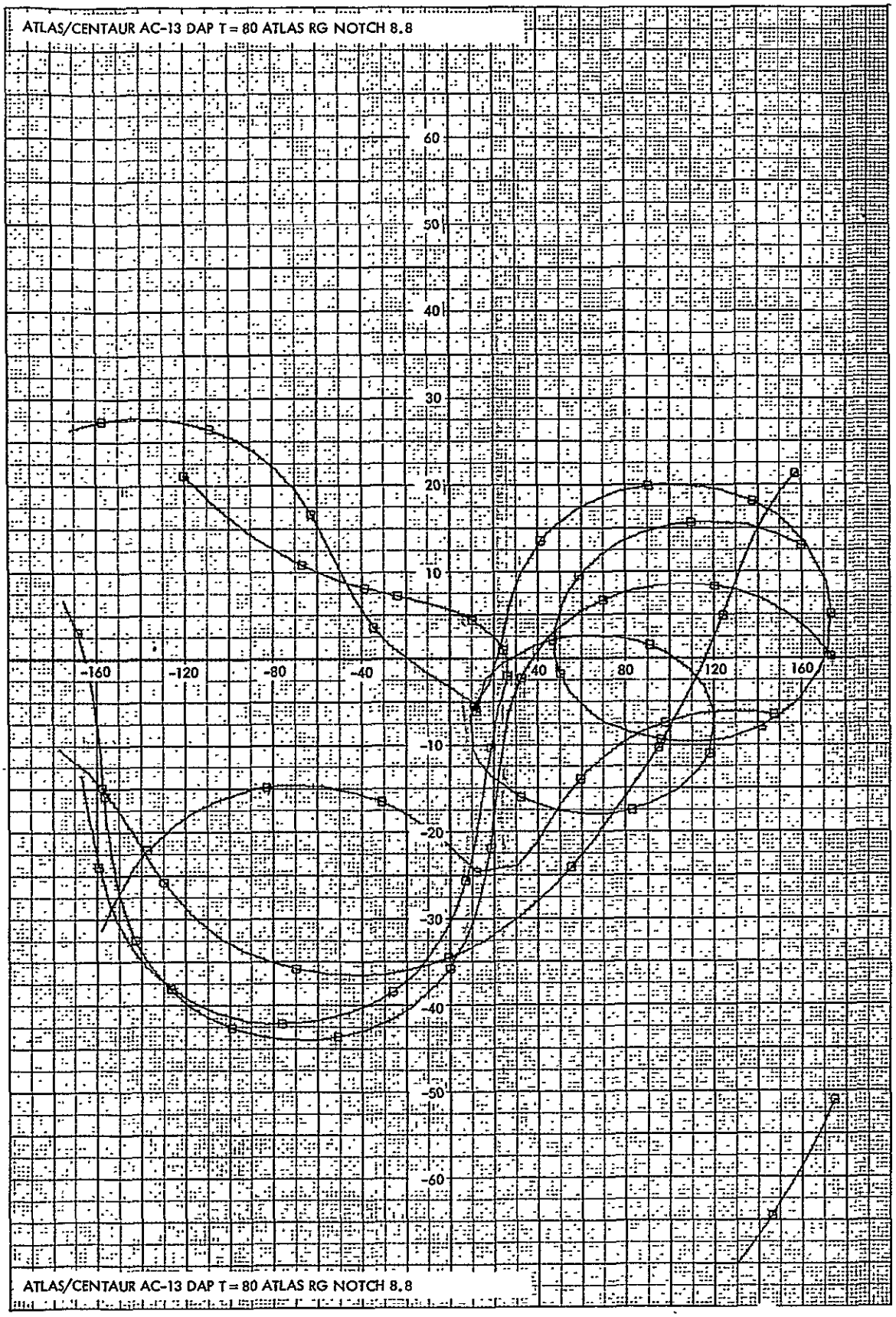

Figure 5-26. Gain-Phase Plot Atlas/Centaur AC-13 Digital Autopilot T=80 Atlas Rate Gyros Notch 8.8

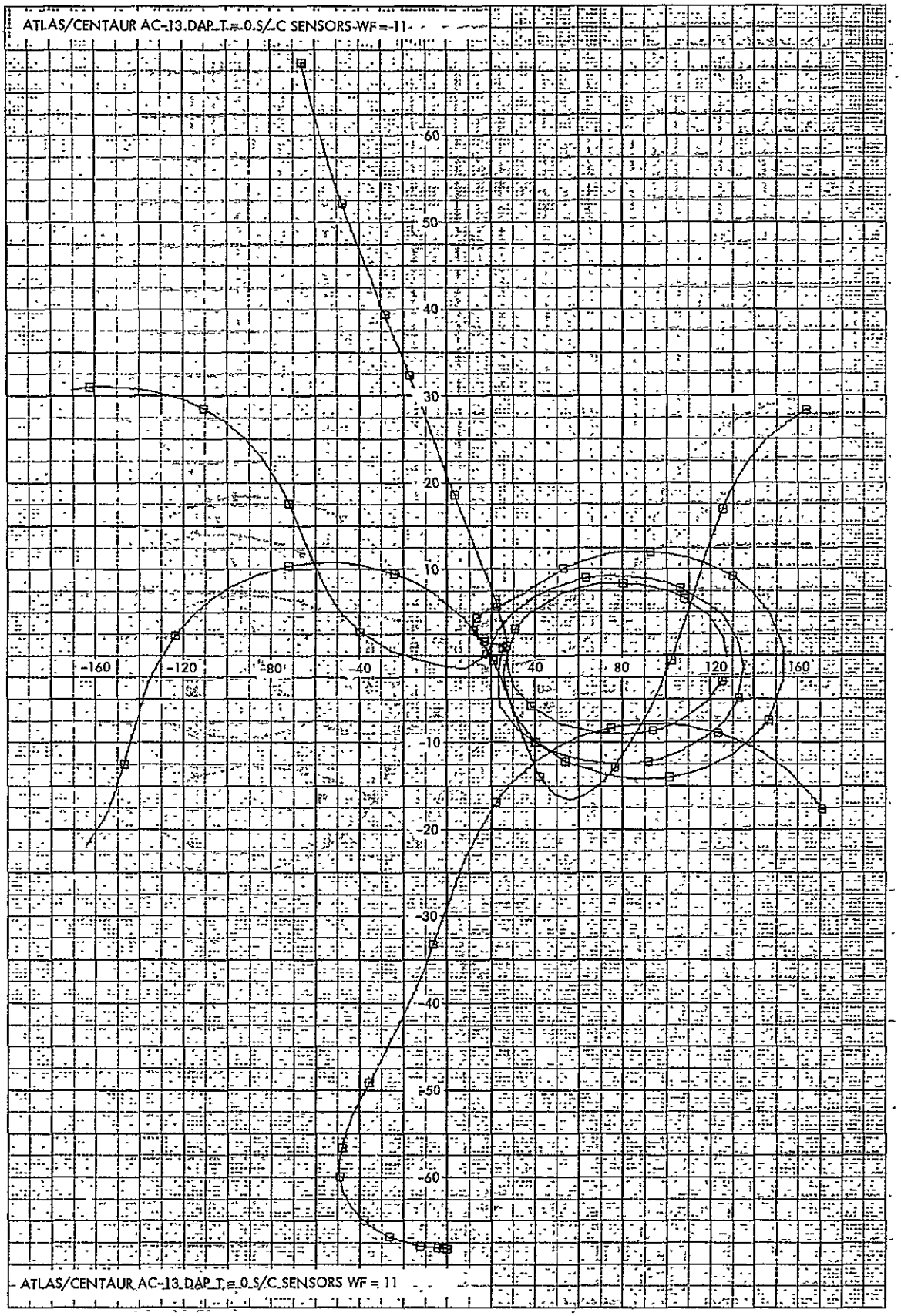

Figure 5-27. Gain-Phase Plot Atlas/Centaur AC-13 Digital Autopilot T=0 Spacecraft Sensors WF = 11

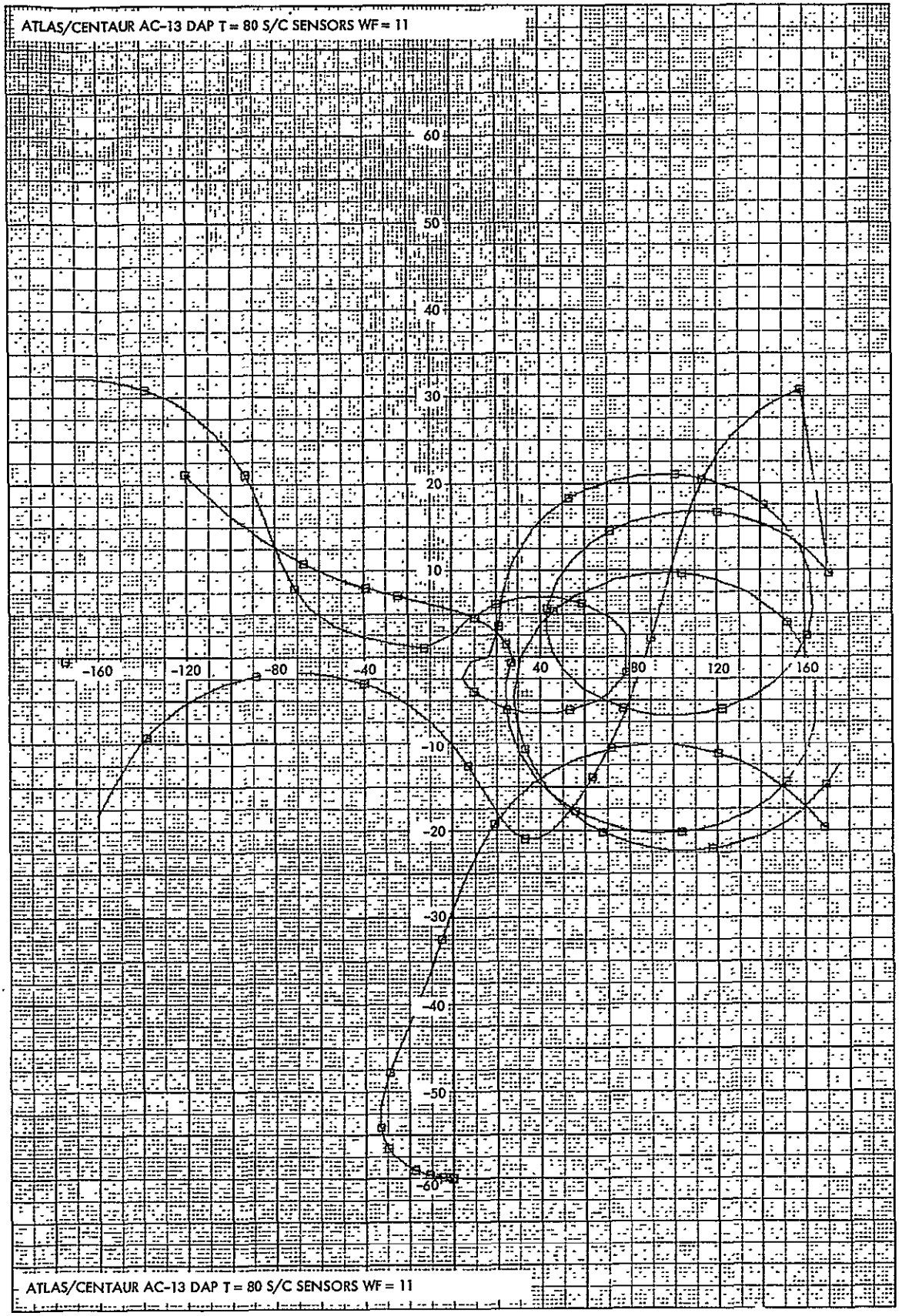

Figure 5-28. Gain-Phase Plot Atlas/Centaur AC-13 Digital Autopilot T=80 Spacecraft Sensors WF = 11

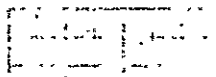

(equivalent to S-plane 11 rad/sec) with 0. 5 damping is included in these responses. The high-frequency rigid body gain margin is shown to be negative or nonexistent for the maximum q condition, and, as shown in Figures 5-29 and 5-30, the added notch filters do not improve this severe condition. The notch pole damping was maintained at 0. 5, while the damping of the zeros was 0. 1 and 0. 2, respectively. The frequency of both notches was kept at V = 0. 174 rad/sec (S-plane frequency of 8. 8 rad/sec).

The third ROI guidance system design utilized Atlas rate gyros that were relocated to station 708. This location was selected to give more weight to the bending stability problem over the first two-thirds of the flight. A plot of the first mode antinode movement with flight time is shown in Figure 5-31, where, at approximately t = 110 sec, the antinode moves past station 708. Assuming that the relocation is acceptable from installation considerations, the corresponding gain-phase plots for the liftoff, maximum q, and BECO conditions are given in Figures 5-32 through 5-34, and a complex pole filter at V = 0. 3 rad/sec (15. 5 rad/sec in the S-plane) is also included. Considerable improvement in the stability portrait is evident for the liftoff and maximum q cases. For the BECO condition, phase stability of the first mode is removed when the antinode passes the rate gyro station. To regain phase stability as well as to obtain gain stability at the time of gain change (T = 110 sec), a second complex pole filter can be added to produce a good control system design.

The use of filter changes has been avoided in past Atlas designs because of the electronic complications. This may explain the selected location of the AC-13 rate gyros. However, use of the digital computer as part of the control system permits filtering changes to be made with ease. This advantage may be used to improve the control system performance margins over those existing in the current Atlas design. Relocation of the rate gyros to station 708 may not be practical, but placement of this gyro package at station 675, as in previous designs, will undoubtedly be acceptable. The rather ample stability margins earlier in flight will be reduced slightly while easing the phase shifting effects later in flight.

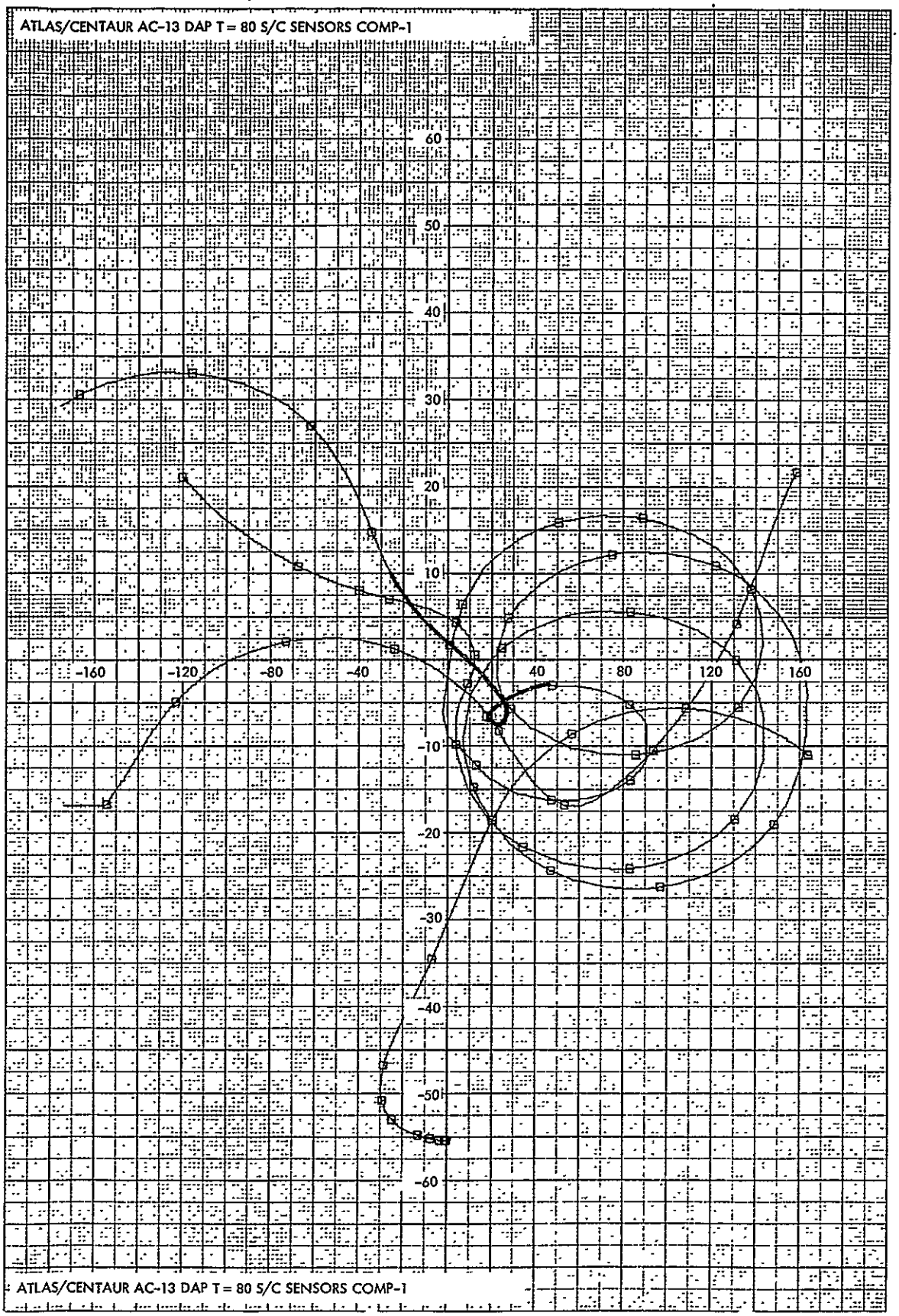

Figure 5-29. Gain-Phase Plot Atlas/Centaur AC-13 Digital Autopilot T=80 Spacecraft Sensors Compensation 1

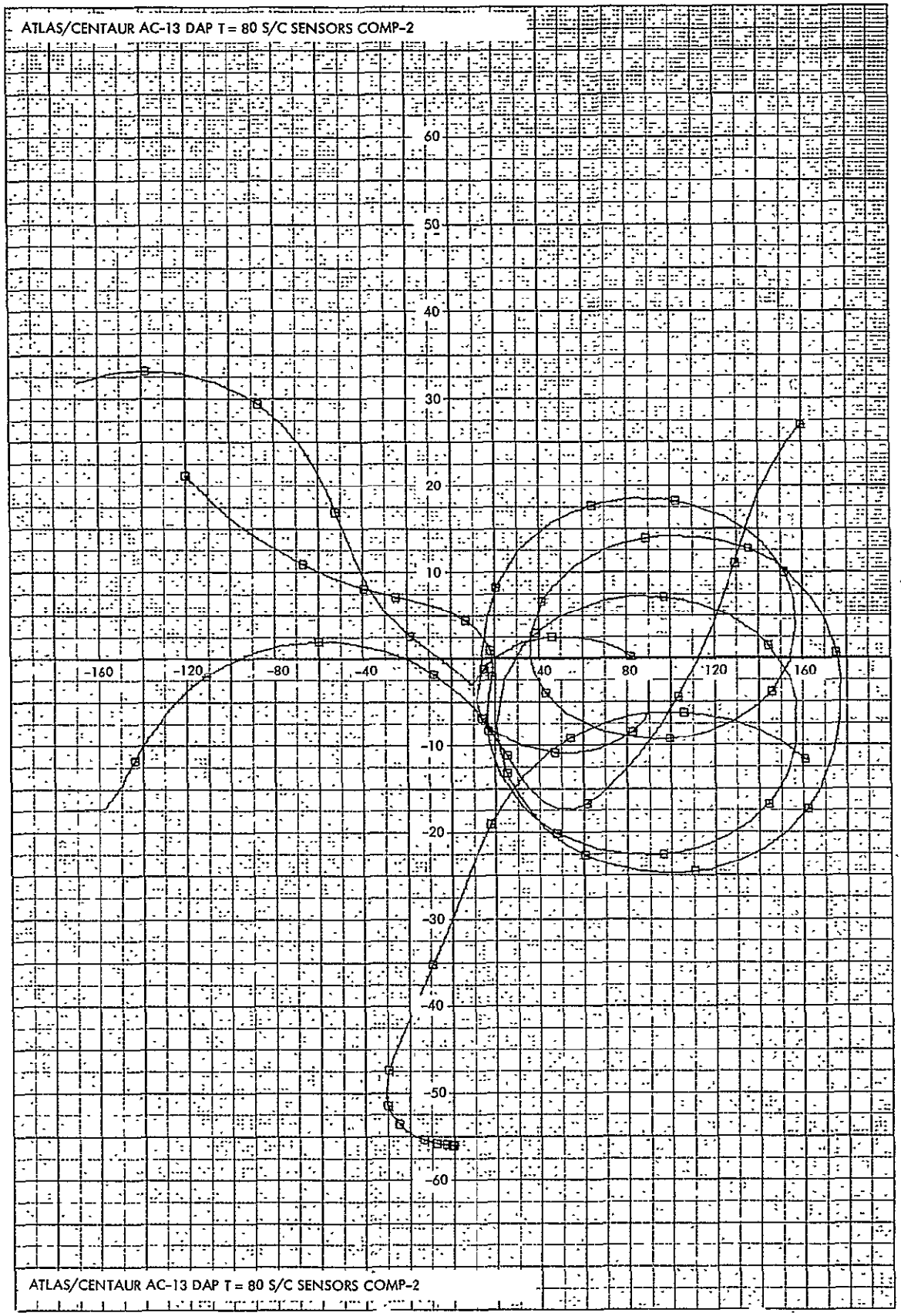

Figure 5-30. Gain-Phase Plot Atlas/Centaur AC-13 Digital Autopilot T=80 Spacecraft Sensors Compensation 2

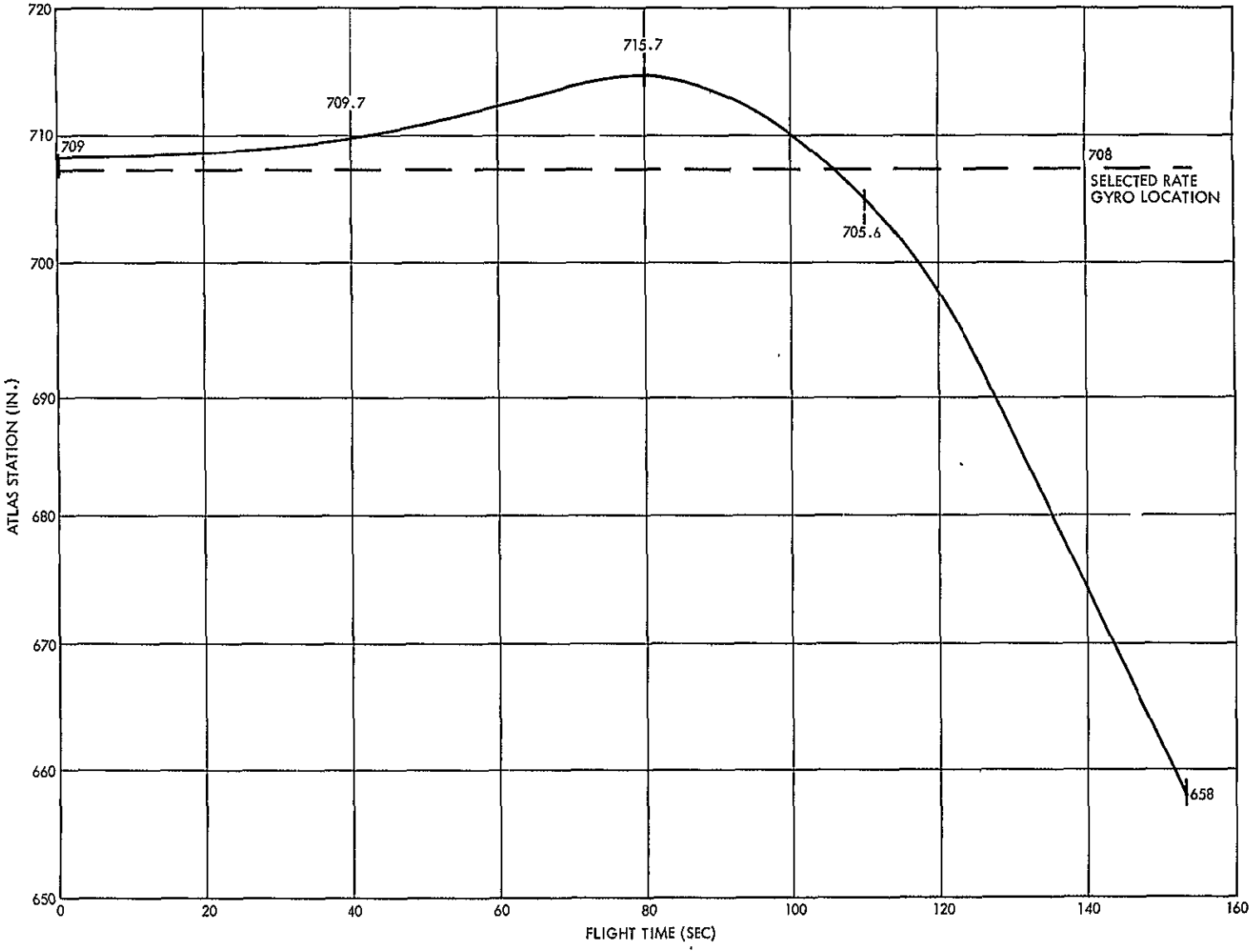

Figure 5-31. Atlas/Centaur AC-13 First Mode Antinode Location versus Flight Time

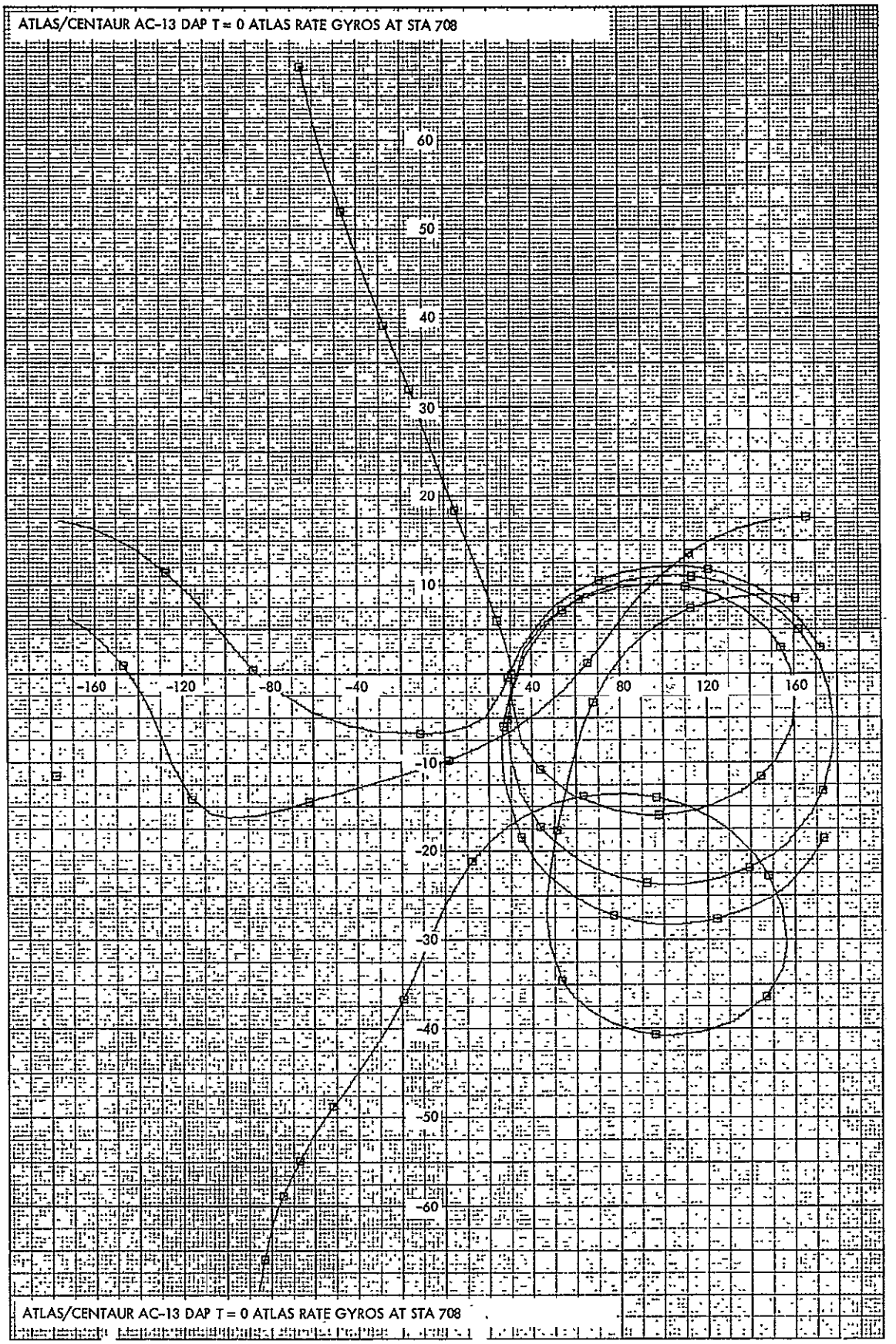

Figure 5-32. Gain-Phase Plot Atlas/Centaur AC-13 Digital Autopilot T=0 Atlas Rate Gyros at Station 708

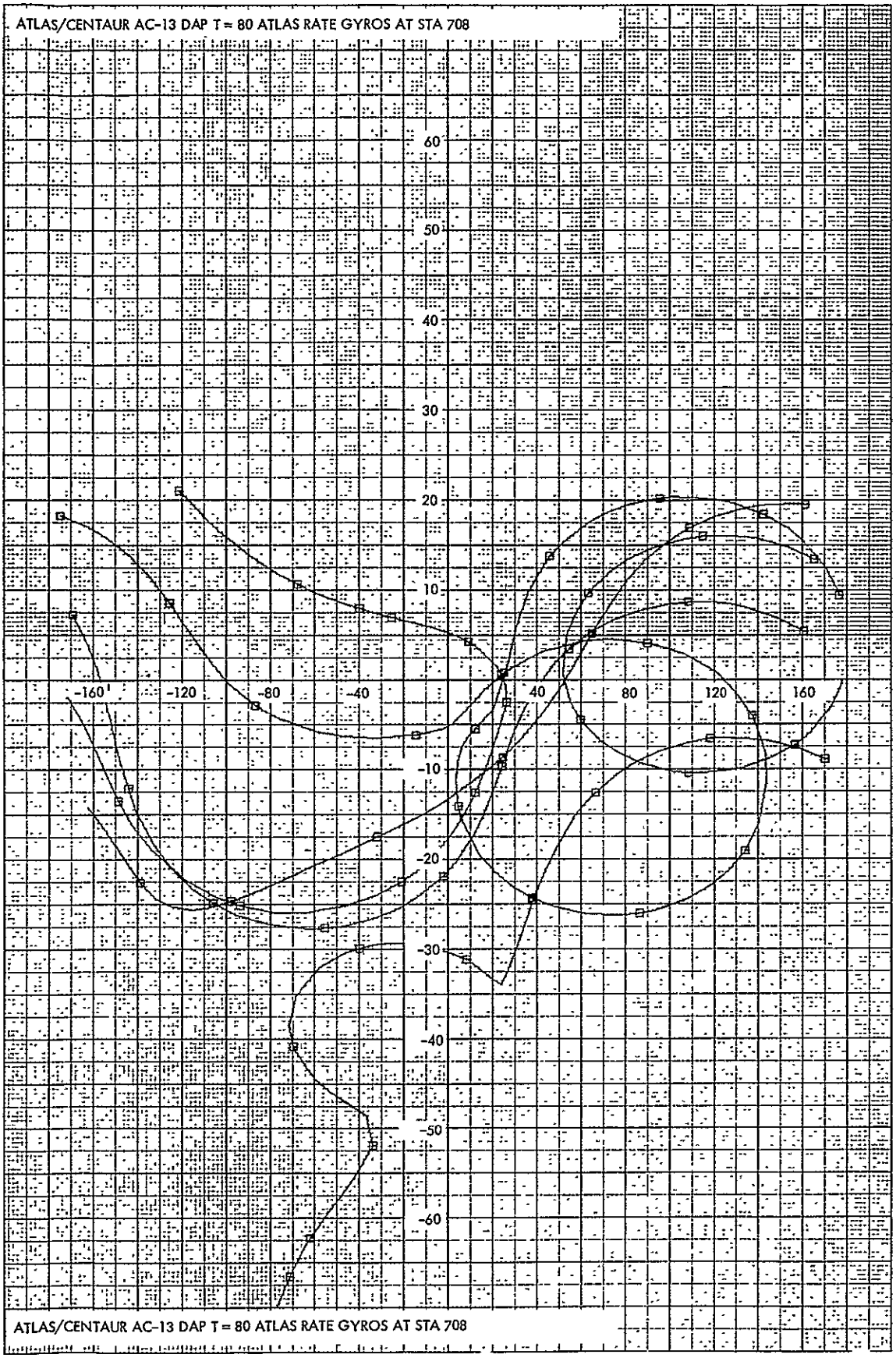

Figure 5-33. Gain-Phase Plot Atlas/Centaur AC-13 Digital Autopilot T=80 Atlas Rate Gyros at Station 708

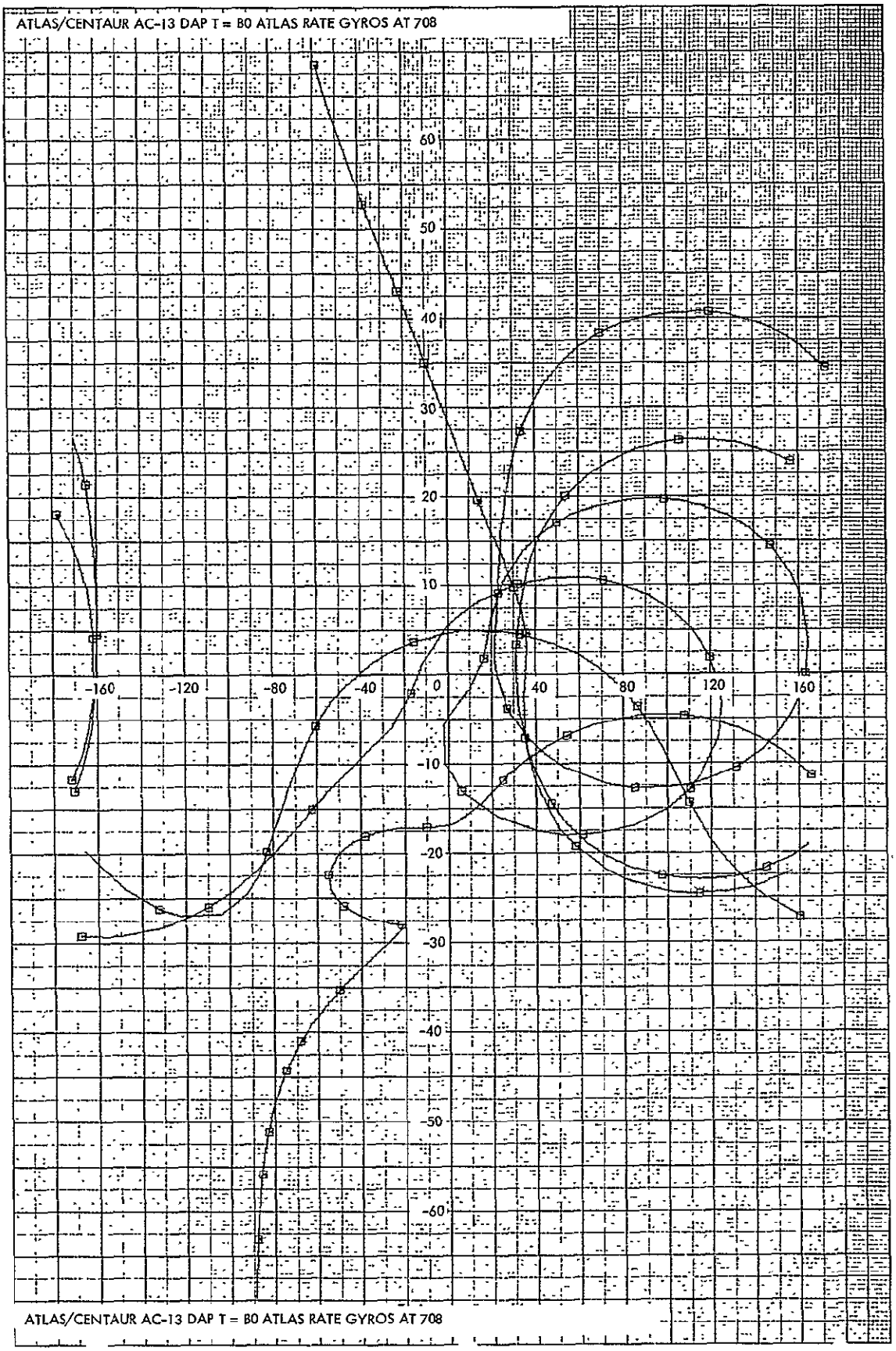

Figure 5-34. Gain-Phase Plot Atlas/Centaur AC-13 Digital Autopilot T=B0 Atlas Rate Gyros at Station 708

5.4 STABILITY ANALYSIS OF THE SATURN IB/CENTAUR VEHICLE

The first stage stability of a Saturn IB/Centaur vehicle carrying a 4100-lb Jupiter probe was examined. Since the S-IB first stage consists of eight 70-in. diameter tanks clustered about a 105-in. diameter center tank, considerable structural rigidity of this stage results. Bending stability is easily achieved and location of the rate sensors either in the aft S-IVB compartment, instrument unit, or spacecraft is acceptable although the aft S-IVB location produces the largest stability margins.

The data employed in the analysis is given in app. D. The forward-loop integrators previously included in the Atlas/Centaur control system are not used on the Saturn vehicles since they employ dynamic pressure feedback servovalves that have zero static leakage, and, hence do not induce attitude errors required to compensate for the hydraulic leakage flow. For the design with rate gyros located in the aft S-IVB compartment, the gain-phase stability for liftoff, maximum q, and burnout conditions of the S-IB stage are given in Figures 5-35 through 5-37, respectively. The compensation filter used consisted of double real poles at a W-plane frequency equivalent to 12.5 rad/sec in the S-plane. Ample stability margins are shown in the figures and listed in Table 5-I. Similarly, the stability margins, with the spacecraft rate sensors used corresponding to Figures 5-38 through 5-40 are listed in Table 5-II. The rigid-body gain margins for both designs are shown in Figure 5-41a, with the desired position gain schedule indicated.

The corresponding rigid-body phase margins are shown in Figure 5-41b as a function of flight time. The rigid-body phase margin is shown dropping briefly to 0.22° as a result of the gain change; however, this is considered acceptable based on previous vehicle design experience. The closed-loop propellant slosh roots listed in Table 5-III indicate an unstable mode due to the slosh masses in the S-IB 70-in. LOX tanks. The slosh instability is small as indicated by the real part of the root, the inverse of which produces a 700-sec divergence time constant. Because of the large magnitude of the time constant and since a similar condition undoubtedly exists and is acceptable on Saturn IB/Apollo flights, it must be assumed to be acceptable for the Saturn IB/Centaur vehicle. However, further evaluation of the propellant slosh oscillations resulting from the instability would be warranted.

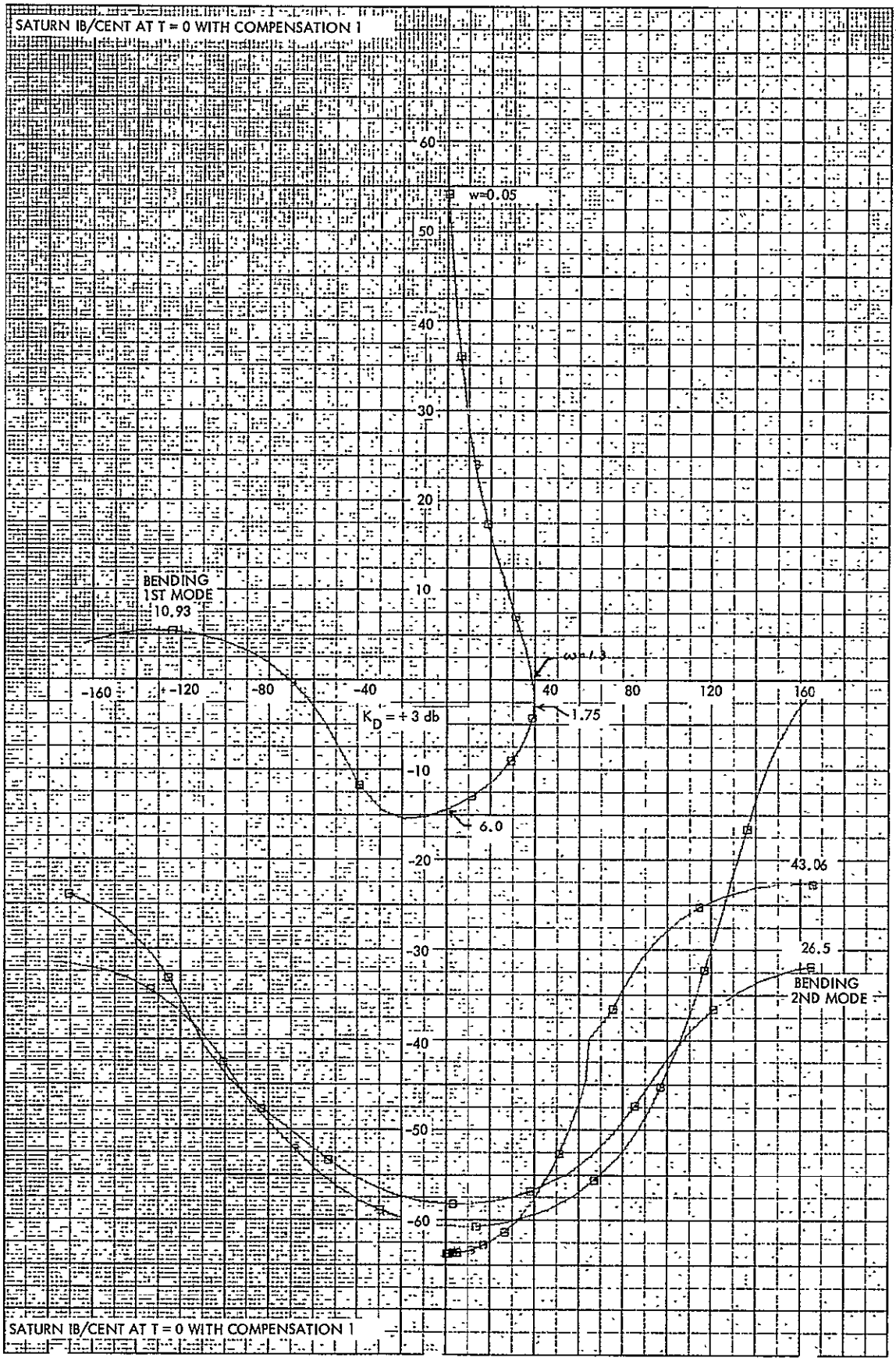

Figure 5-35. Gain-Phase Plot Saturn IB/Centaur at T=0 With Compensation 1

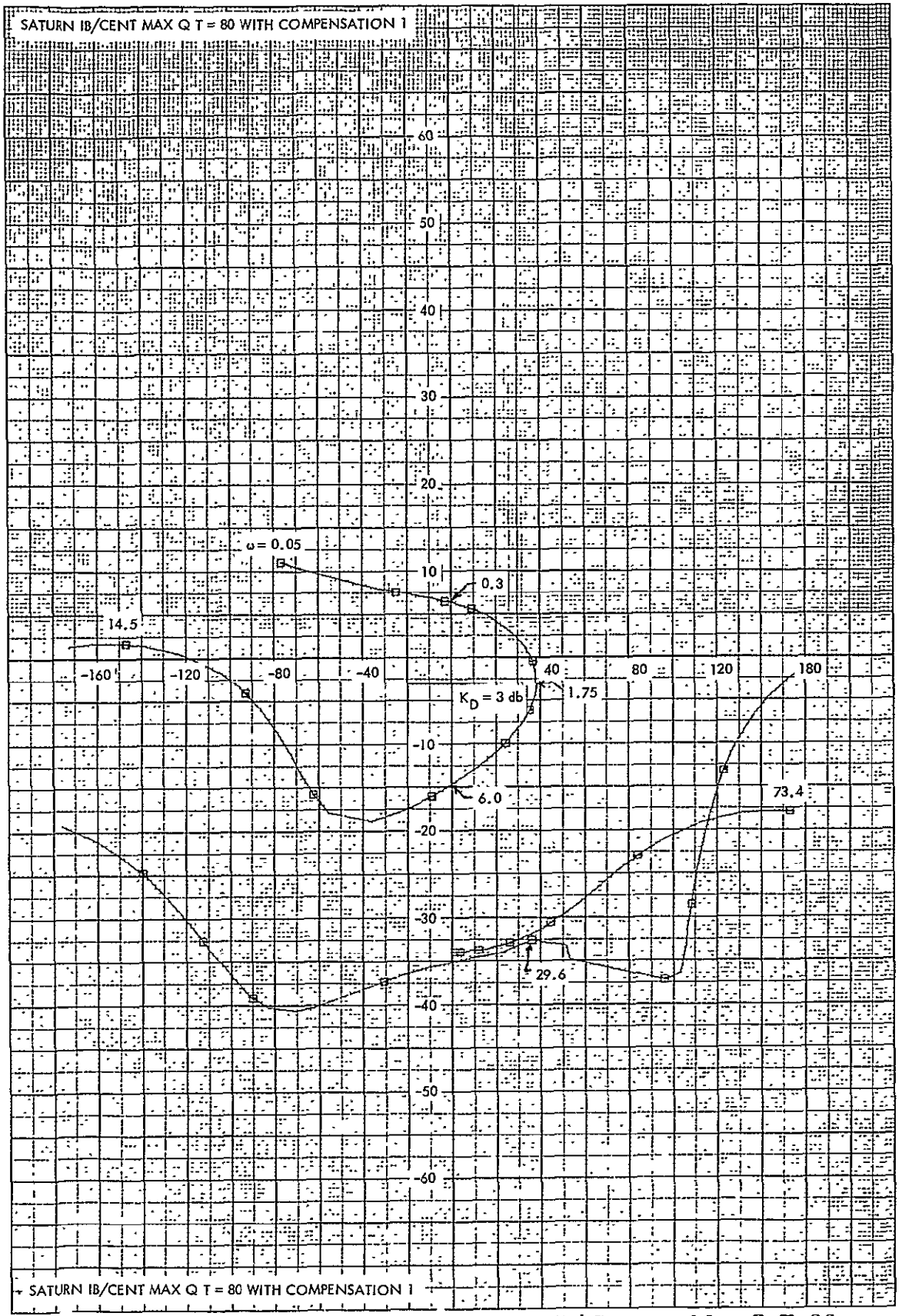

Figure 5-36. Gain-Phase Plot Saturn IB/Centaur Max Q T=80 With Compensation 1

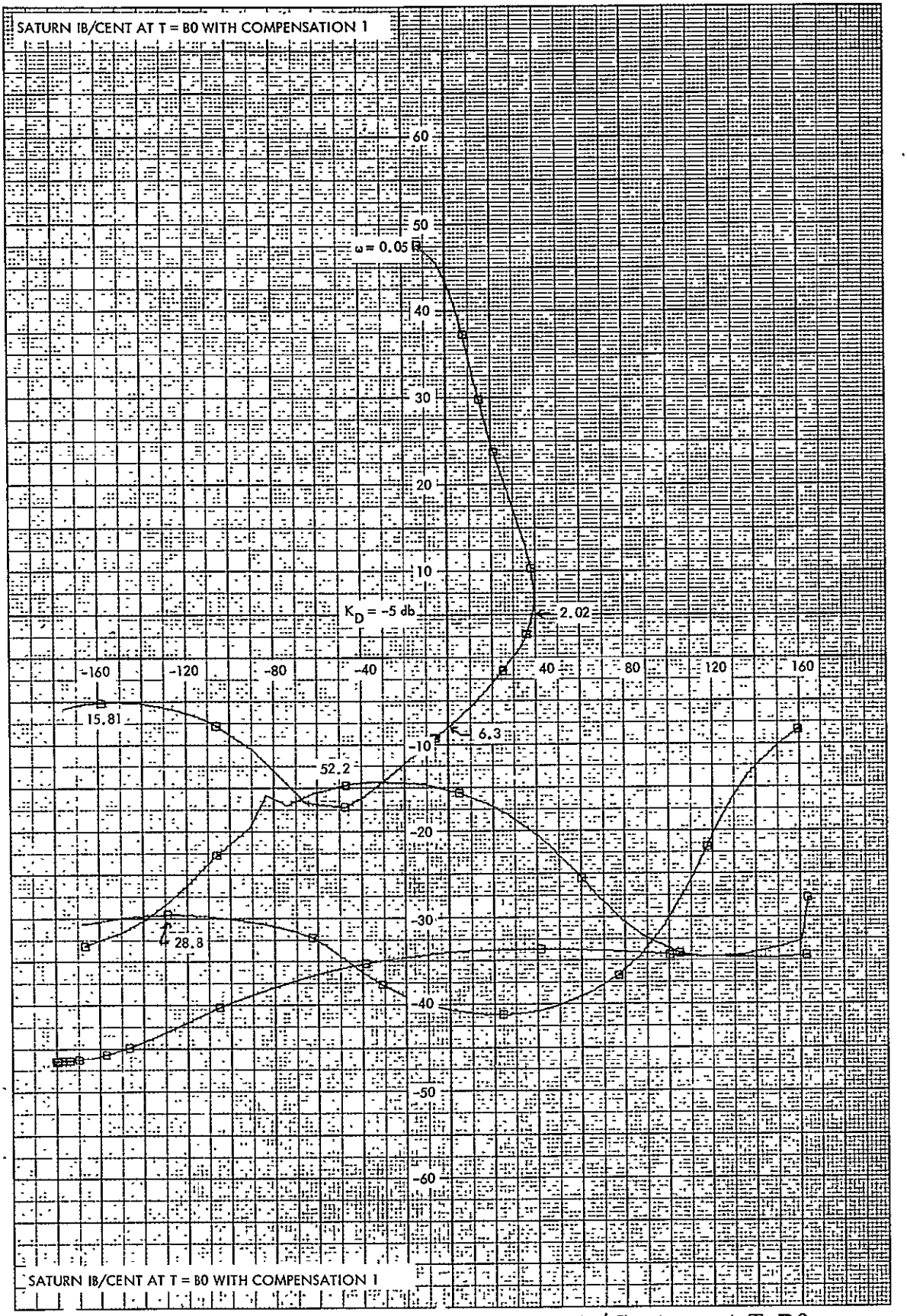

Figure 5-37. Gain-Phase Plot Saturn IB/Centaur at T=B0 With Compensation 1

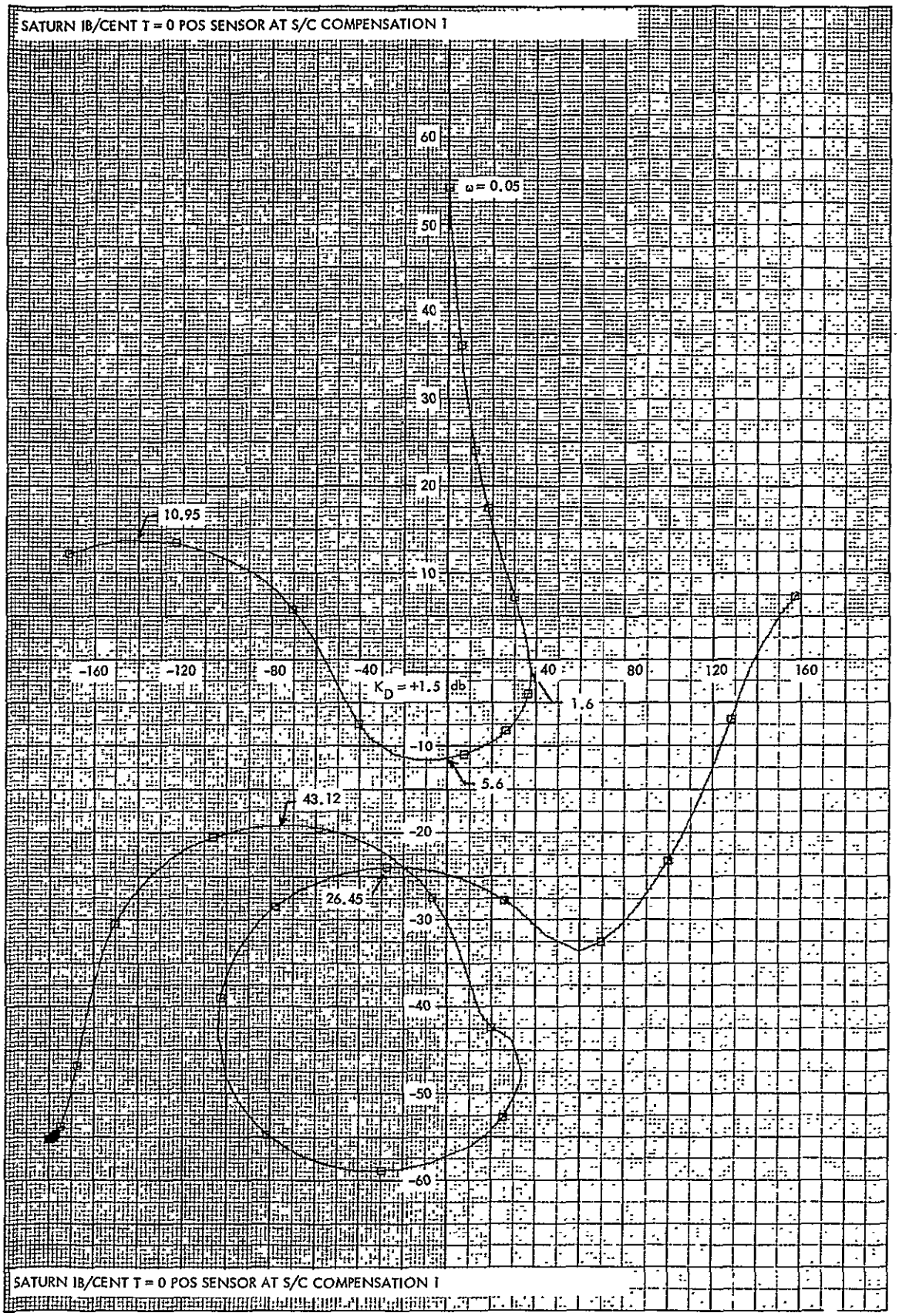

Figure 5-38. Gain-Phase Plot Saturn IB/Centaur T=0 Position Sensor at Spacecraft Compensation 1

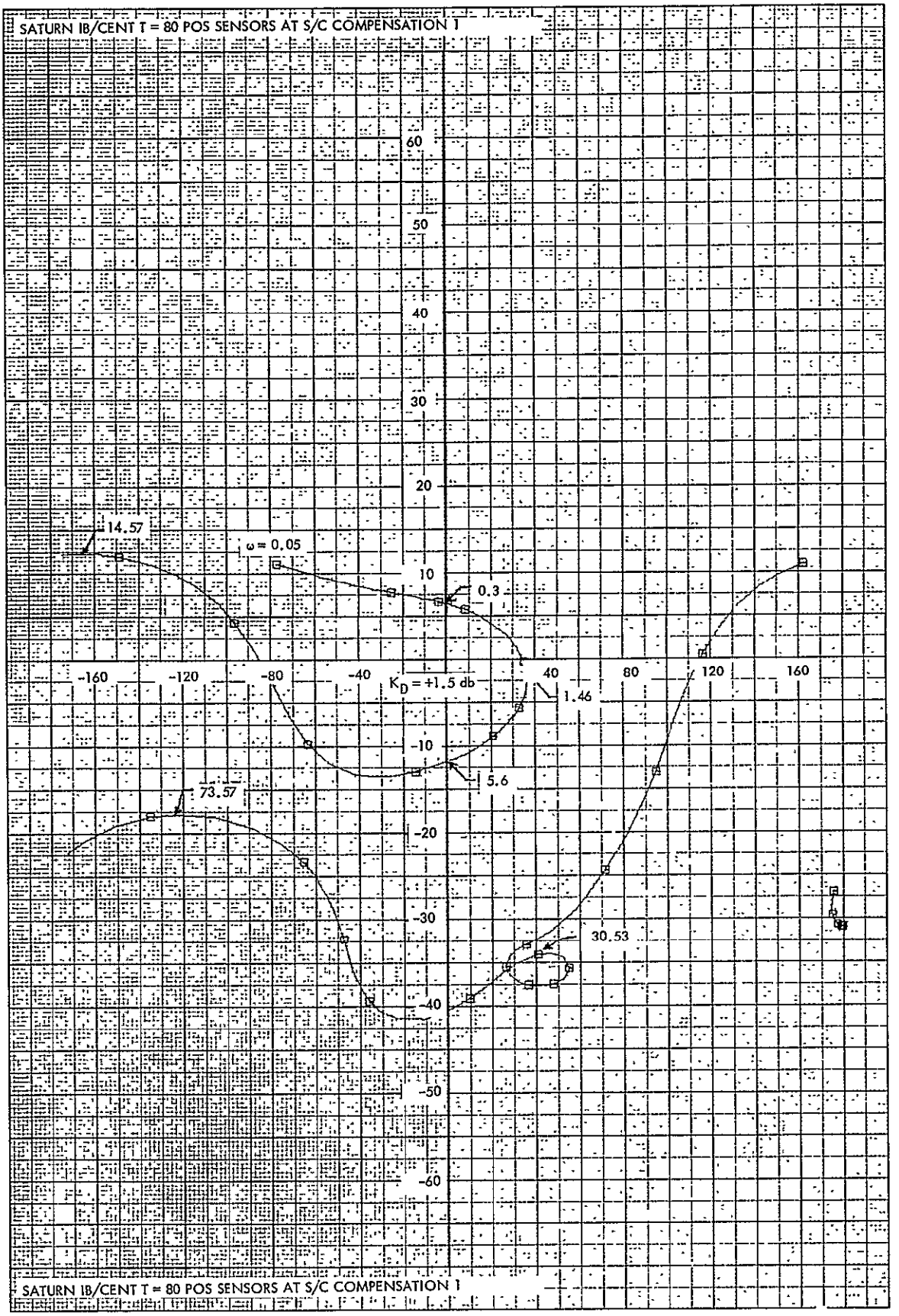

Figure 5-39. Gain-Phase Plot Saturn IB/Centaur T=80 Position Sensors at Spacecraft Compensation 1

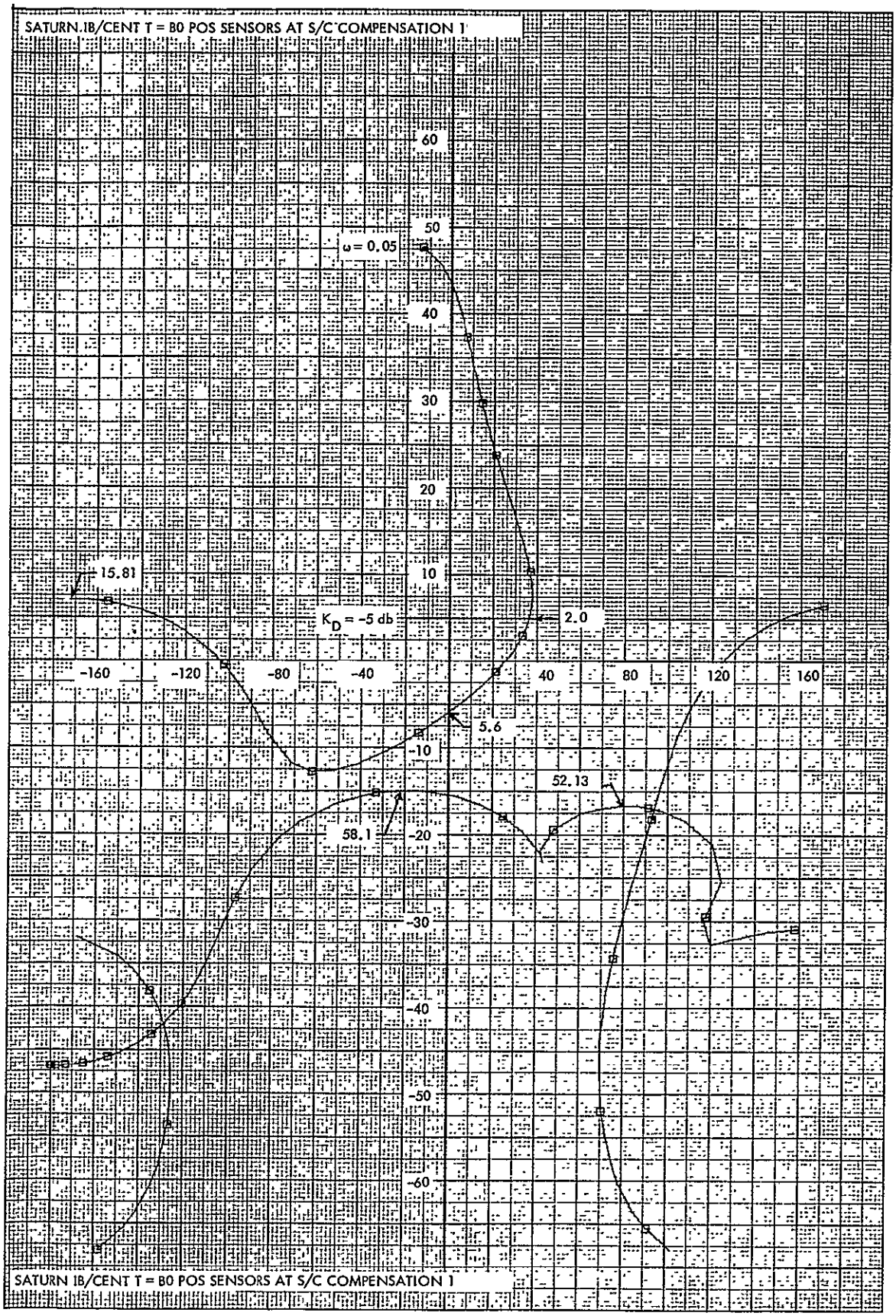

Figure 5-40. Gain-Phase Plot Saturn IB/Centaur T=B0 Position Sensors at Spacecraft Compensation 1

TABLE 5-I

SATURN IB/CENTAUR CONTROL SYSTEM GAINS AND RELATIVE STABILITY MARGINS – AFT S-IVB RATE GYROS

Flight Time	K_R/K_D (sec)	K_D	Rigid Body Phase Margin (deg)	1st Bend Phase Margin (deg)	1st Bend Amplitude above Nominal Gain (dB)	Digital Filter D(Z) and Comment
0	1.2	1.413	40	-60	8.5	$\frac{1}{9}\frac{1}{(1-1.2Z^{-1}+0.36Z^{-2})}$
80	1.2	1.413	38	-98	5	S-plane equivalent:
110	Gain change from K_D = 1.413 to K_D = 0.562					$\frac{(12.5)^2}{(s+12.5)^2}$
153	1.2	0.562	38		-10	

TABLE 5-II

SATURN IB/CENTAUR CONTROL SYSTEM GAINS AND RELATIVE STABILITY MARGINS – SPACECRAFT SENSORS

Flight Time	K_D	Rigid Body Phase Margin (deg)	1st Bend Phase Margin (deg)	1st Bend Amplitude above Nominal Gain (dB)	Digital Filter D(Z) and Comment
0	1.189	38	-53	15	$\frac{61}{18}\frac{\left(1-\frac{59}{61}Z^{-1}\right)}{\left(1-\frac{4}{3}Z^{-1}+\frac{4}{9}Z\right)^{-2}}$
80	1.189	36	-82	14	Equivalent K_R/K_D S term is incorporated in D(Z).
110	Gain change from K_D = 1.189 to K_D = 0.562				S-plane equivalent:
153	0.562	36	-130	2	$\frac{100\ (1.2\ s+1)}{(s+10)^2}$

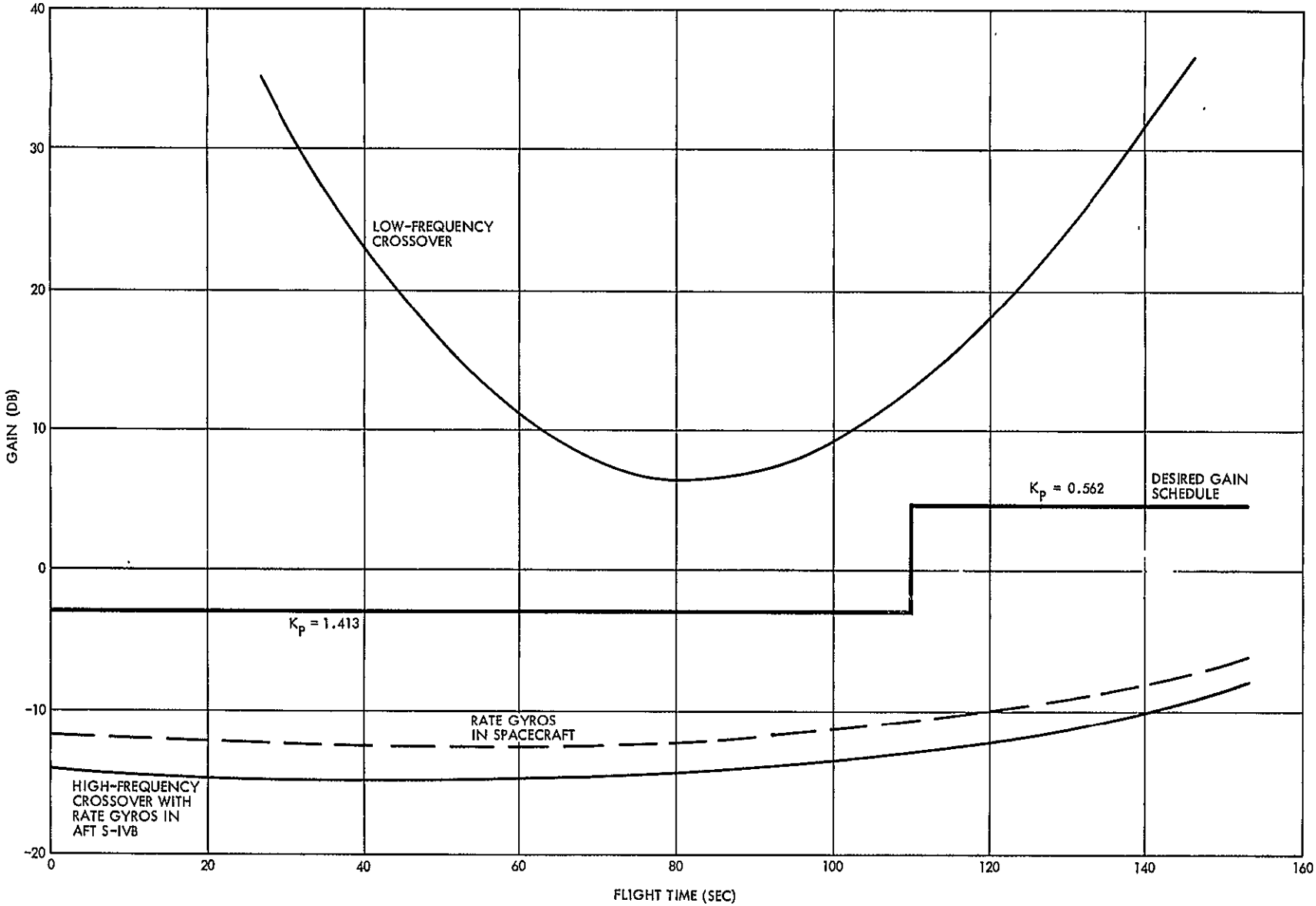

Figure 5-41a. Saturn IB/Centaur Rigid-Body Gain Margins

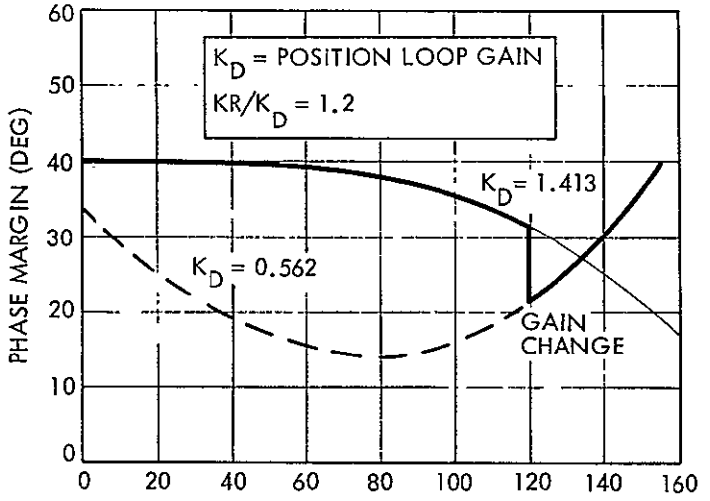

(a) Booster Rate Gyros at Station 950 (AFT S-IVB)

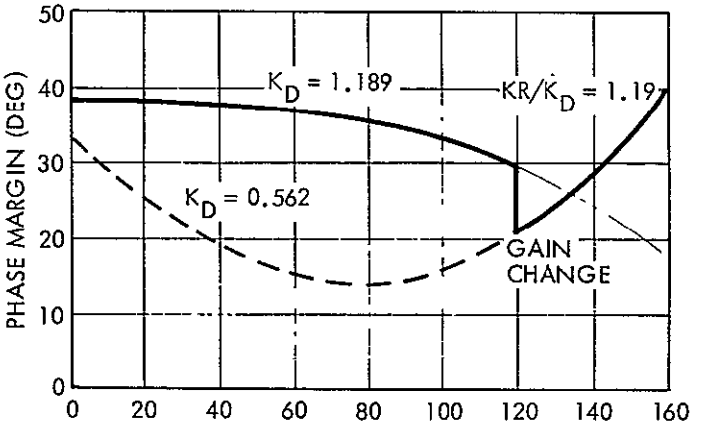

(b) Spacecraft Sensors

Figure 5-41b. Rigid-Body Phase Margin versus Flight Time With Position Gain as a Parameter for the Saturn IB/Centaur Stage I Digital Control System

5.5 ANALYSIS OF THE VOYAGER SPACECRAFT

5.5.1 Powered Flight Stability Analysis

The Voyager spacecraft design consists of two vehicles: 1) the bus which performs midcourse corrections and Martian orbit deboost firings, and 2) the capsule which subsequently separates from the bus and lands on the Martian surface.

TABLE 5-III

SATURN IB/CENTAUR CLOSED LOOP SLOSH POLES, S-IB PHASE

t	0	80	153
S-IB Fuel	0 ± j4.838	0 ± j6.032	-0.003 ± j3.288
S-IB 70-in. LOX	+0.0015 ± j4.863	+0.0004 ± j6.112	-
S-IB 105-in. LOX	-0.0005 ± j3.973	-0.0003 ± j4.931	-
S-IVB LOX	-0.069 ± j3.174	-0.075 ± j3.948	-0.088 ± j4.316
S-IVB LH2	-0.0669 ± j2.544	-0.075 ± j3.184	-0.0713 ± j3.496
Centaur LOX	-0.158 ± j3.631	-0.128 ± j4.157	-0.105 ± j4.839
Centaur LH2	-0.099 ± j3.860	-0.107 ± j4.821	-0.106 ± j5.246

The LM Descent Stage Engine is employed at two thrust levels, that is, a high level for the Mars Orbit Insertion (MOI) firings; and a throttled level for Midcourse Correction (MCC) and Mars Orbit Trim (MOT) firings. The engine is gimbaled and controlled by electromechanical actuators for pitch and yaw axis stability while pulsing of jets are employed for roll control.

The powered flight stability analysis performed on the Voyager spacecraft used the data given in app. E and included the propellant slosh effects for both the bus and capsule modes. The primary body bending modes were those caused by coupling of the bus with various appendage resonances, the bus essentially acting as a rigid beam with little deformation. The major appendage modes were those caused by an aft equipment module, a high-gain antenna, the cantilevered capsule, and a platform (PSP) employed for scanning the planet surface. The true bus bending modes were of much higher frequency and safely ignored.

The analysis was previously performed for an analog control system design; however, very little difference with a digital control system is obtained if the high sampling rate of 25 samples/sec employed for booster control is also maintained during the spacecraft powered phases.

The use of forward loop integrators to reduce trajectory errors because of thrust vector misalignments was found desirable and is discussed in par. 5.4.2.

Gain-phase stability portraits for the four mission phases studied are given in Figures 5-42 through 5-45. The low-frequency crossover due to inclusion of an attitude integrator (gain of 0.125) is indicated. A large but stable bus slosh loop and a smaller capsule slosh loop are visible followed by the aft equipment module mode, high gain antenna mode, capsule, and PSP modes. The desired position gain for the low-thrust midcourse correction and Mars orbit trim firings is shown to be $K_p = 4$, while the desired gain during the Mars orbit-insertion phase is kept constant at $K_p = 0.5$. No compensation filters were included in the design; however, use of some filtering would be desirable to further increase stability margins and furnish added noise attenuation.

5.5.2 Voyager Spacecraft Thrust Vector Pointing Error Analysis

To estimate the thrust vector control (TVC) pointing errors and crossrange velocity errors incurred during midcourse correction (MCC), Mars orbit insertion (MOI), and Mars orbit trim (MOT), the pointing errors introduced by the gyros, the attitude control system, vehicle limit cycles, and attitude reference misalignments were combined with thrust vector pointing errors due to cg offsets, and thrust vector misalignments to obtain the total powered flight thrust vector pointing error. The effects of three control system designs on the thrust-vector-induced pointing error were evaluated. Following are the three control system designs studied:

a) Without integrators

b) With attitude feedback integration

c) With attitude and engine angle feedback integration

The larger cg uncertainty and the small distance between the engine and cg locations at MOT produce a large offset angle. Attitude and engine angle feedback integration reduce the steady-state pointing error for these effects to zero. The addition of an outer guidance loop (closed-loop guidance steering) will significantly reduce these errors.

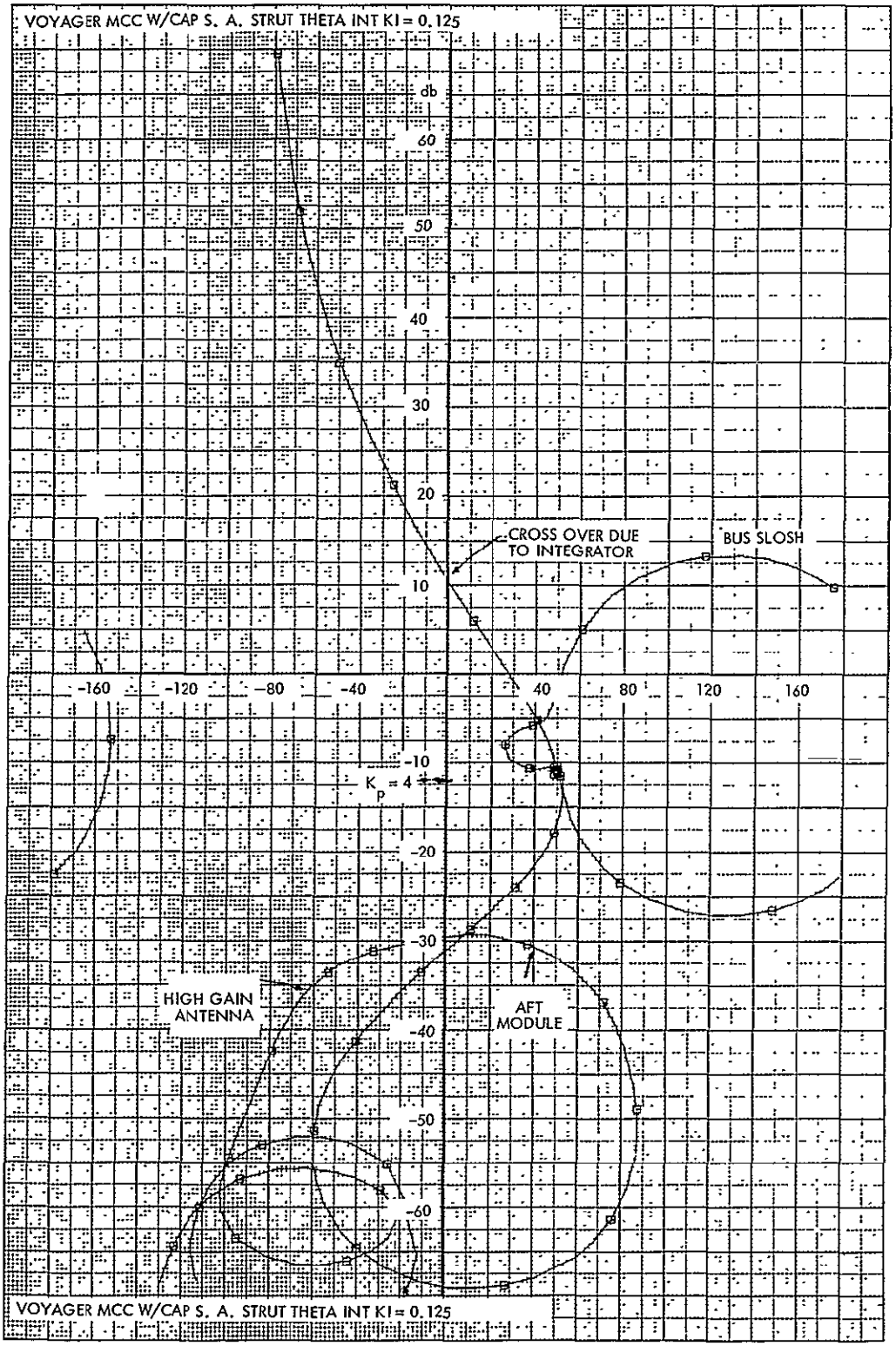

Figure 5-42. Gain-Phase Plot, MCC, with Capsule, Integral Attitude Feedback, $K_I = 0.125$

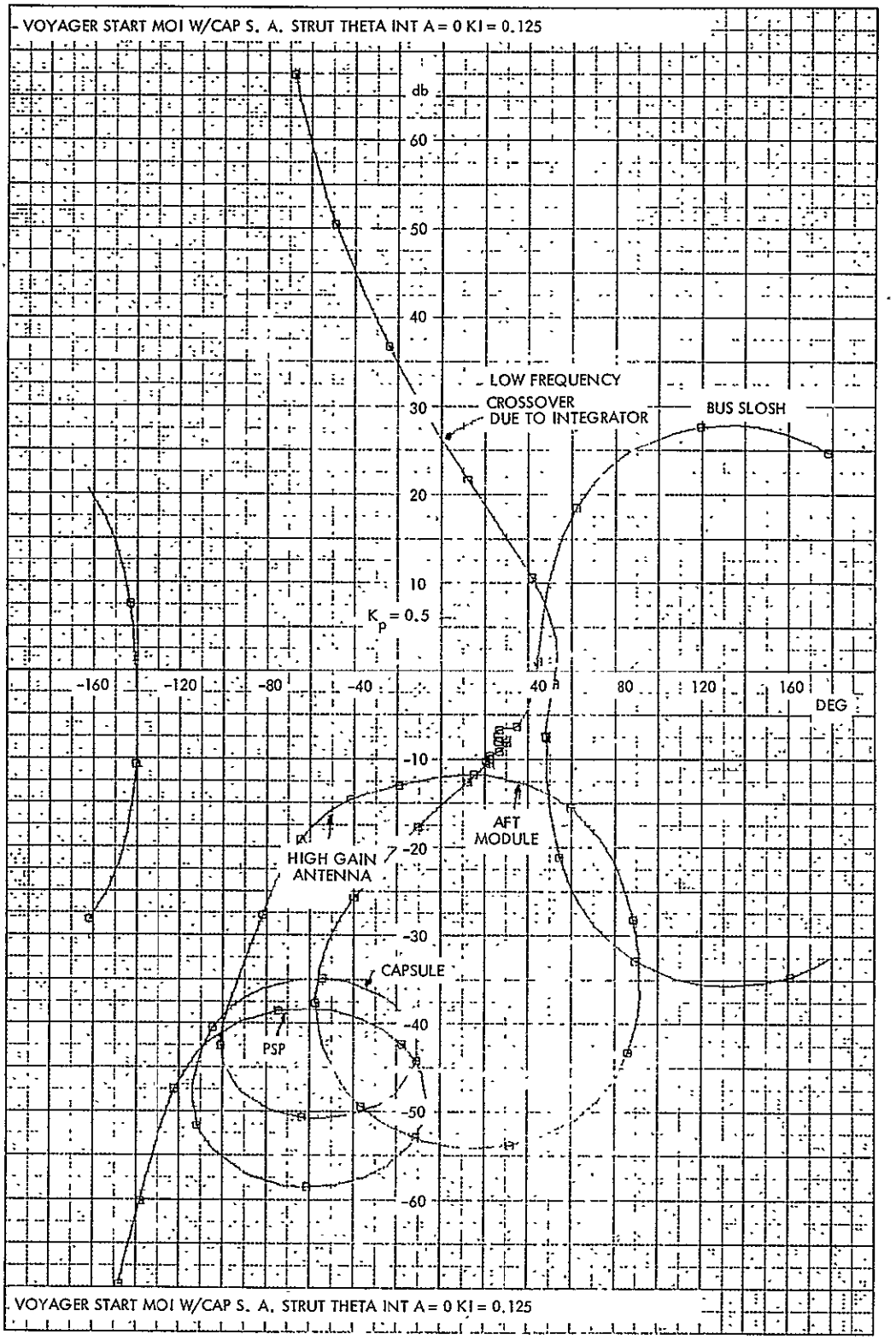

Figure 5-43. Gain-Phase Plot, Start MOI, With Capsule, Integral Attitude Feedback, K_I = 0.125

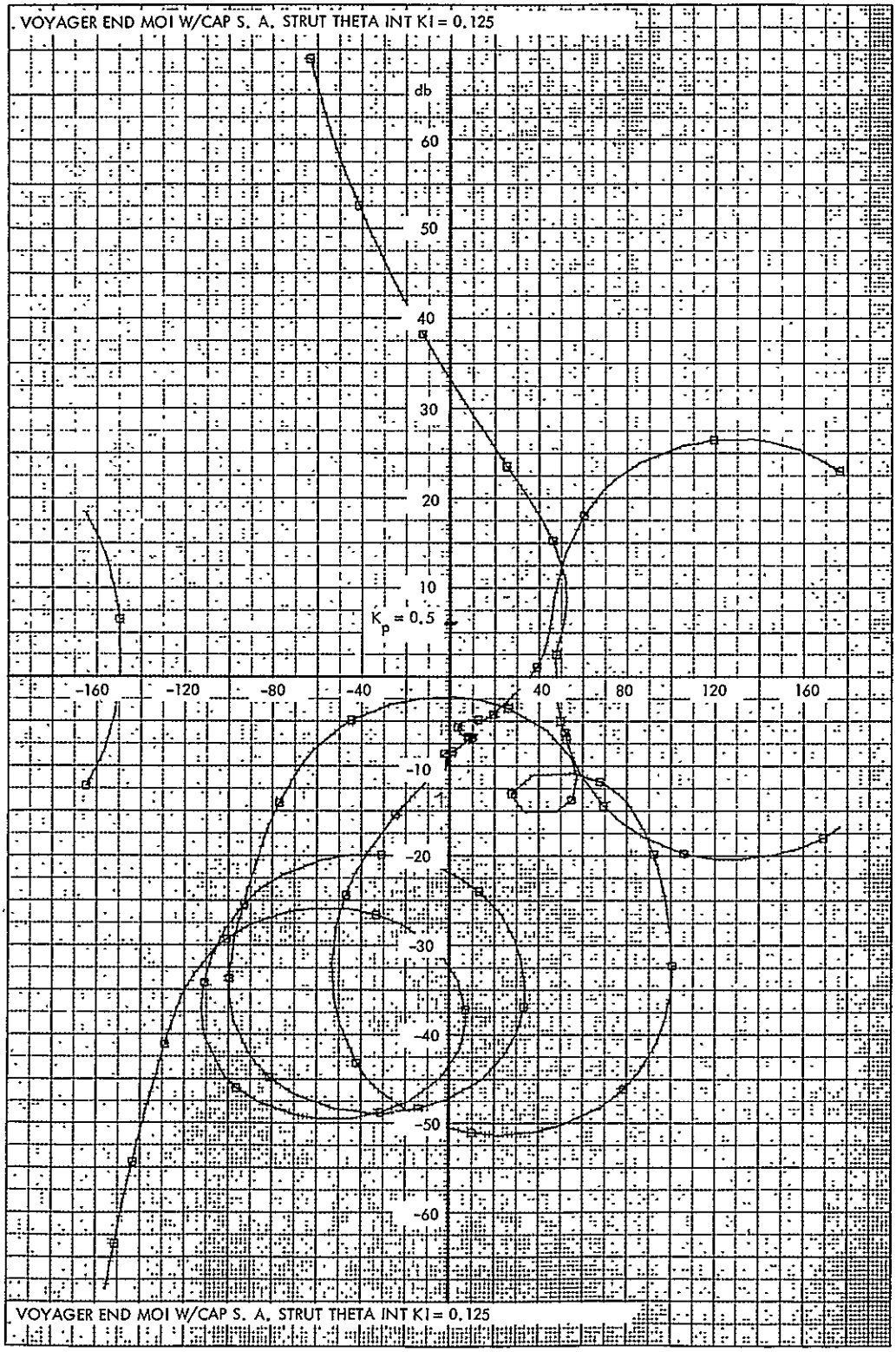

Figure 5-44. Gain-Phase Plot, End MOI, With Capsule, Integral Attitude Feedback, K_I = 0.125

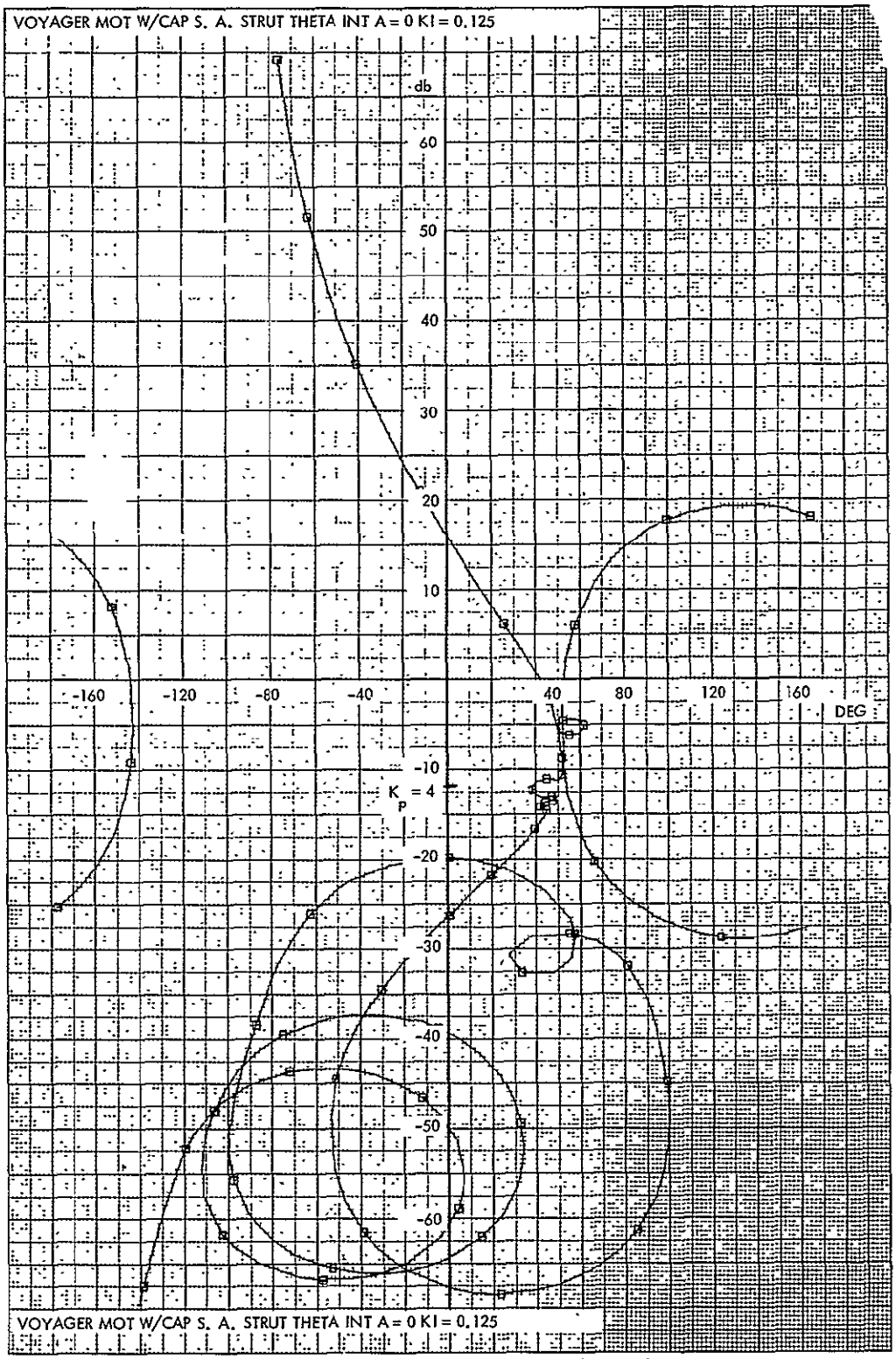

Figure 5-45. Gain-Phase Plot, MOT, With Capsule, Integral Attitude Feedback, $K_I = 0.125$

Time histories of the unguided control system instantaneous pointing error, ϵ_T, and velocity error, V_T, for a 1° thrust vector misalignment or a 1° thrust vector offset angle are shown in Figures 5-46 through 5-51 for the three integrator cases. For constant thrust levels, the velocity error curve can be obtained from the pointing error curve by multiplying the thrust by the integral of ϵ_T.

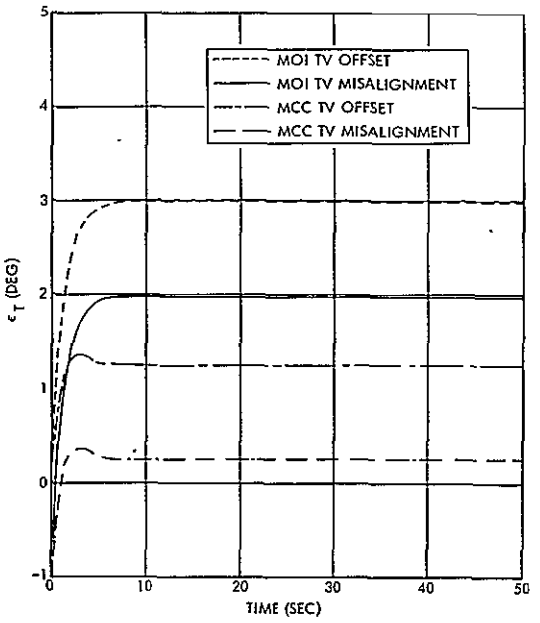

Figures 5-46. ϵ_T Without Integrators

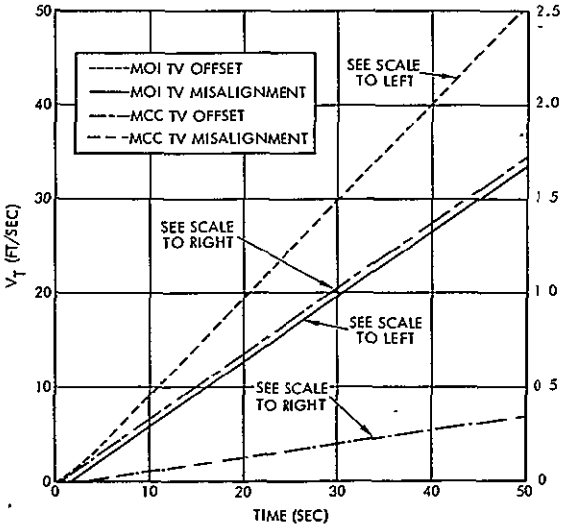

Figures 5-47. V_T Without Integrators

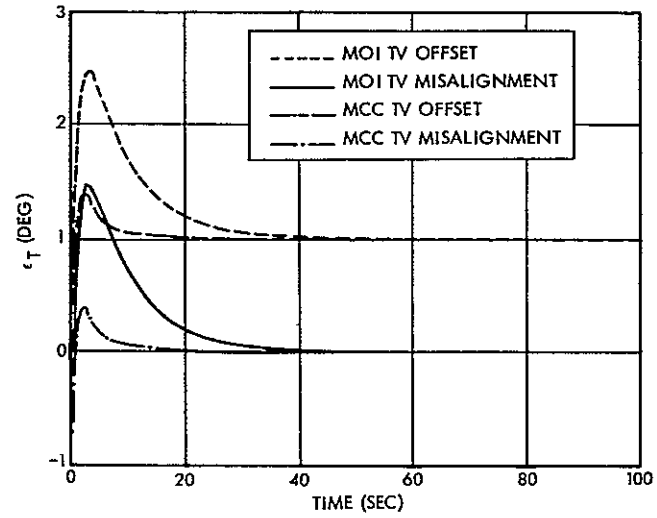

Figures 5-48. ϵ_T With Attitude Feedback Integration

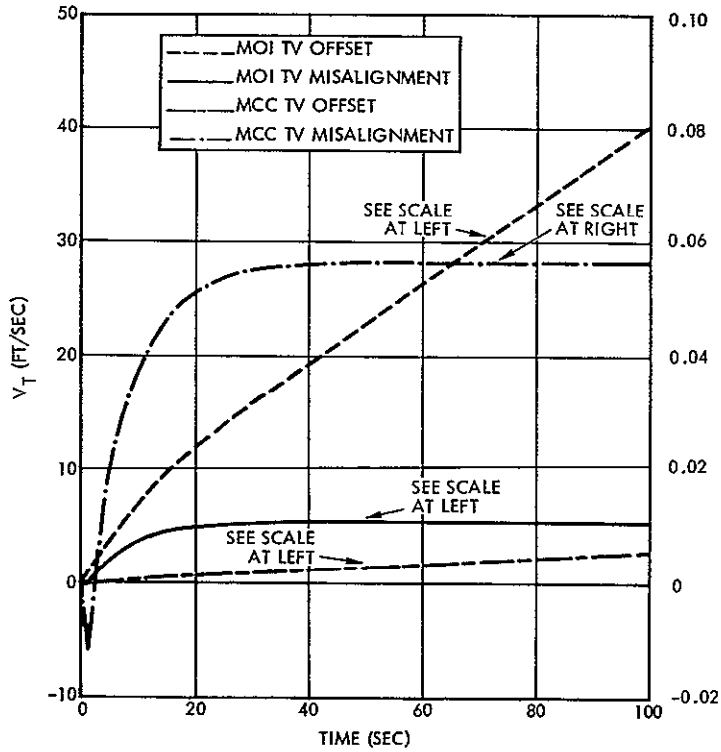

Figures 5-49. V_T With Attitude Feedback Integration

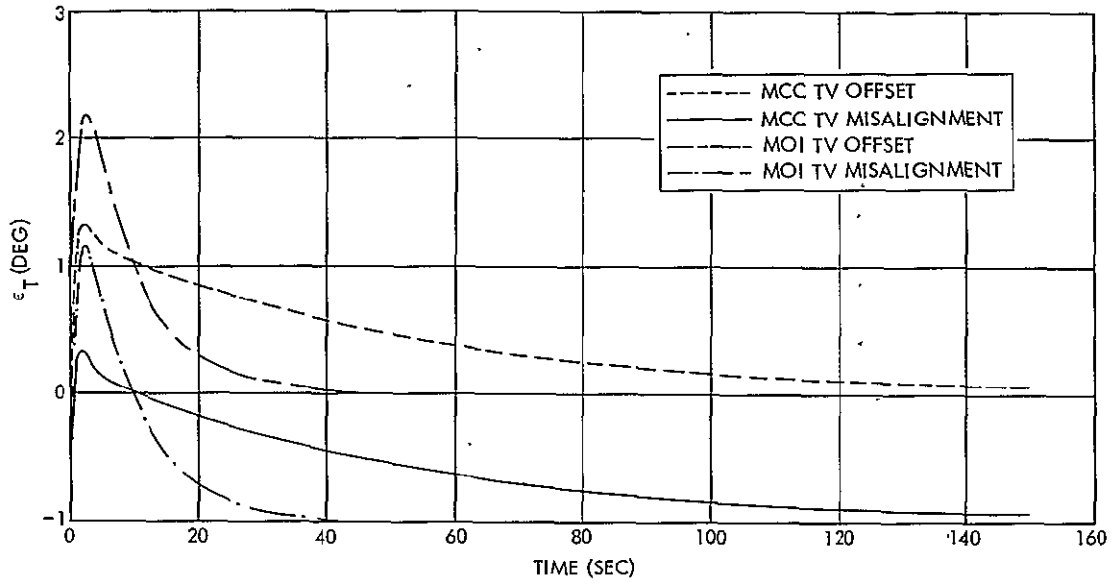

Figures 5-50. ϵ_T With Attitude and Engine Angle Feedback Integration

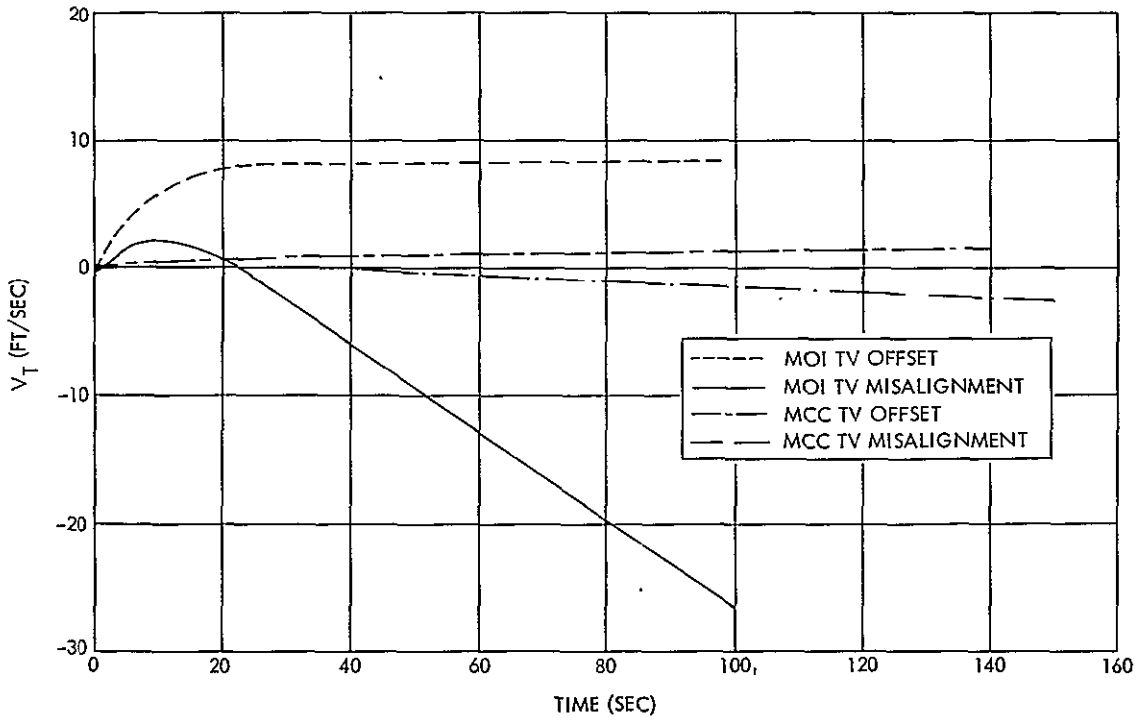

Figures 5-51. V_T With Attitude and Engine Angle Feedback Integration

The use of attitude feedback integration with biases for mean cg offsets is considered more desirable than the use of attitude plus engine angle feedback integration. Although the latter design removes the effects of cg offsets and thrust vector offsets, it does so rather slowly, thereby compromising its usefulness for this purpose. Also, difficulties in its implementation result since the engine feedback loop is unstable without main engine thrusting. The attitude feedback integration design does not exhibit this instability; hence, the feedback loop can be closed prior to engine startup.

A 380-sec main engine firing (ΔV = m/sec) was assumed for MCC and a 330-sec firing (ΔV = 2 km/sec) for MOI. The total pointing error angle and the cross velocity error at the end of engine firing are provided for each of the control systems. The results are based on a constant coefficient simulation. Since the mass and inertia properties change radically from the start to the end of MOI, these results are considered preliminary.

It was determined that the use of integrators considerably improved the steady-state total pointing angle and cross-velocity accuracy. For each of the unguided control systems, the total pointing angle errors, after reaching steady state, were as follows:

	Unguided Control Systems Total Steady-State Pointing Angle Error (°)					
	MCC		MOI		MOT	
	Mean	3σ	Mean	3σ	Mean	3σ
Without integrators	0.28	0.87	1.5	1.52	0.5	2.04
With attitude feedback integration, no bias angles	0.22	0.73	0.5	0.67	1.0	1.98
With attitude feedback integration and with bias angles	0	0.73	0	0.67	0	1.98
With attitude and engine angle feedback integration	0	0.76	0	0.76	0	0.76

REFERENCES

5-1. "Voyager Support Study, LM Descent Stage Applications, Final Report, Volume IV, Guidance and Control Studies," TRW Report 04480-6007-R000 prepared for JPL, July 1967.

5-2. "Summary Report of Centaur Analysis for Saturn IB/Centaur/Voyager Launch Vehicle (U)," TRW Report 8448-6001-RC000 prepared for NASA/MSFC, 23 September 1963 (C).

5-3. "Saturn IB/Centaur/Voyager Bending Data (First Stage Burning)," cover letter dated 29 July 1963 from NASA/MSFC.

5-4. "Saturn IB/Centaur/Voyager Bending Data (Second Stage Burning)," cover letter dated 15 August 1963 from NASA/MSFC.

5-5. "Aerodynamic Data ($C_{z\alpha}$, CP)," cover letter dated 9 August 1963 from NASA/MSFC.

5-6. "Aerodynamic Data (C_{D0})," cover letter dated 30 May 1963 from NASA/MSFC.

5-7. "Atlas SLV-3C/Centaur AC-13 Mass Property, Aerodynamic, Trajectory, Slosh, and Bending Data," General Dynamics/Astronautics Report GDC-BTD66-132, July 1967.

5-8. "Flight Dynamics and Control Analysis of the Centaur Vehicle (ATLAS/CENTAUR AC-5)," General Dynamics/Astronautics Report GD/A-DDE65-004, January 1965.

5-9. "Flight Dynamics and Control Analysis, Atlas/Centaur Vehicle AC-2," General Dynamics/Astronautics Report GDA 63-0398, 30 September 1963.

5-10. "Astrionics System Handbook, Saturan Launch Vehicles," NASA/MSFC, 15 August 1966.

5-11. "Saturn V Thrust Vector Control System Data," NASA/MSFC Report R-ASTR-NFS, 25 March 1966.

APPENDIX A

CONTROL SYSTEM STABILITY CRITERIA

The control system stability criteria followed in this study are given in this appendix. In general, the stability margins employing the ROI guidance and control system were required to be equal to or greater than the margins existing with present vehicle designs. In addition, the specific stability requirements given below were employed.

1. RIGID-BODY STABILITY MARGINS

The minimum rigid-body stability margins generally used are 6 dB of gain and 30^{o} of phase. Decreases in margins below these minimums often occur for a short duration because of required gain changes. Some relaxation in the margin requirements based upon the length of this duration may be warranted since deficiencies for a few seconds would be tolerable at rigid-body frequencies. The curves shown in Figure A-1 and A-2 illustrate the rigid-body stability requirements that would be representative of this more flexible approach.

2. PROPELLANT-SLOSH STABILITY MARGINS

Propellant-slosh stability is strongly influenced by the propellant damping available in the propellant tank, particularly through the use of tank baffles. The damping values employed in linear stability analyses are generally based upon acceptable slosh-limit cycles amplitudes. The limit cycle amplitude reaches a steady-state condition when slosh stability margins become zero, hence, zero margins could be considered as being the minimum requirements for linear slosh stability. If these requirements are not met, divergence to a larger slosh limit cycle would be expected. If the divergence is slow and occurs over a short duration, it may still be acceptable; however, a simulation study to determine this would be required. For the purposes of this study, zero slosh margins are considered as minimum requirements.

3. STRUCTURAL BENDING MODE STABILITY MARGINS

Phase stabilization of the first and second structural bending modes is generally accepted, particularly if the mode frequencies are well below

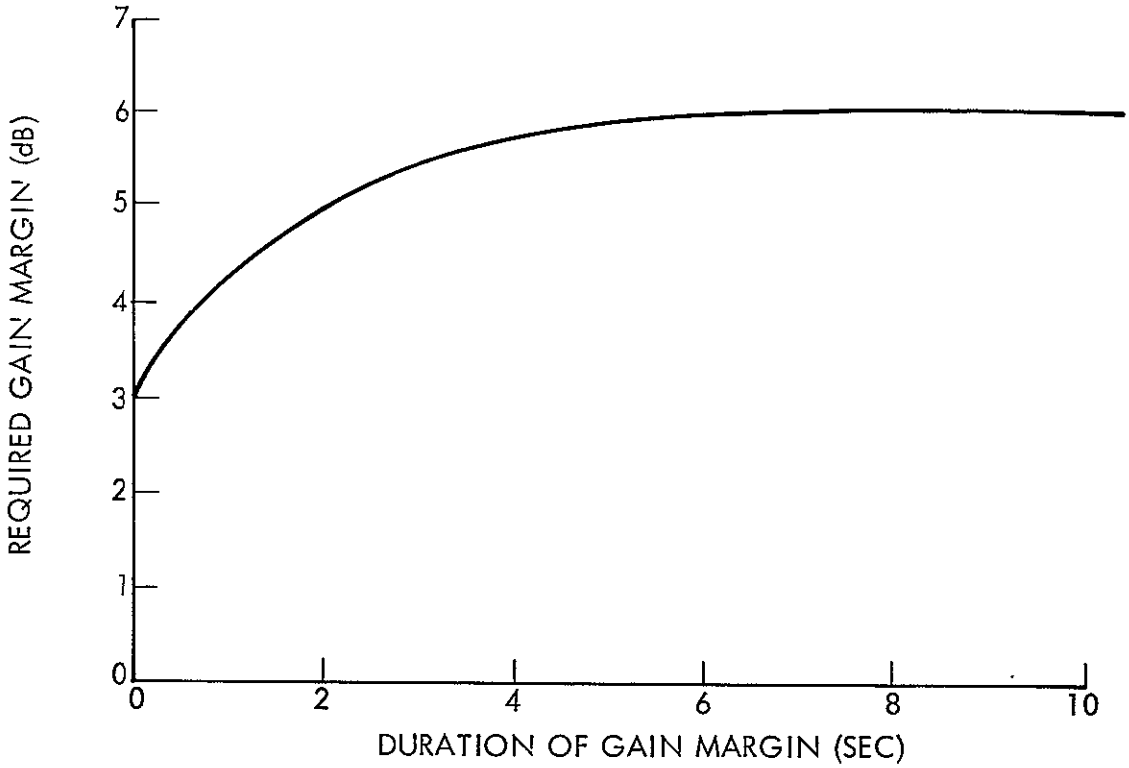

Figure A-1. Relaxation of Rigid-Body Gain Margin Requirements Over Short Durations

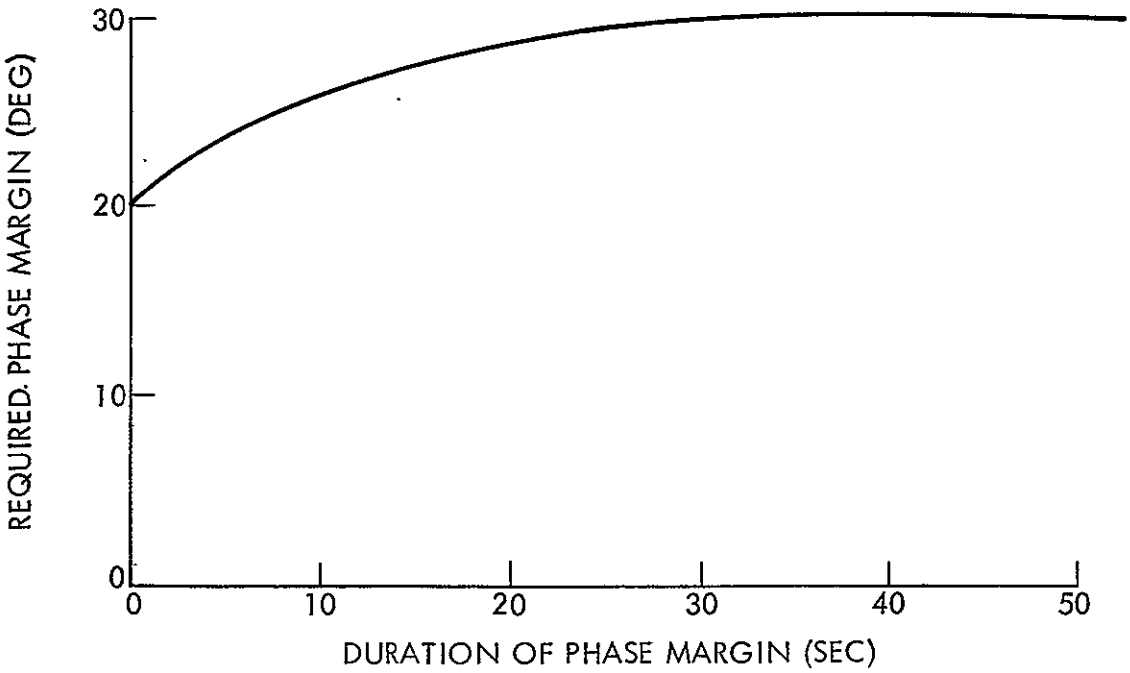

Figure A-2. Relaxation of Rigid-Body Phase Margin Requirements Over Short Durations

(less than one-third) the actuation system frequency. Since nonlinearities within the actuation system produce significant phase uncertainty at high frequencies, phase stabilization at these frequencies is generally avoided. A criteria to be employed for phase stabilization should therefore be based upon the frequency of bending stabilization. An example of such criteria that can be used is given in Figure A-3 in which the allowable phase margin requirements are related to the ratio of bending mode and rigid-body frequencies. For gain stabilized bending modes a gain margin criteria as exemplified in Figure A-4 could be employed.

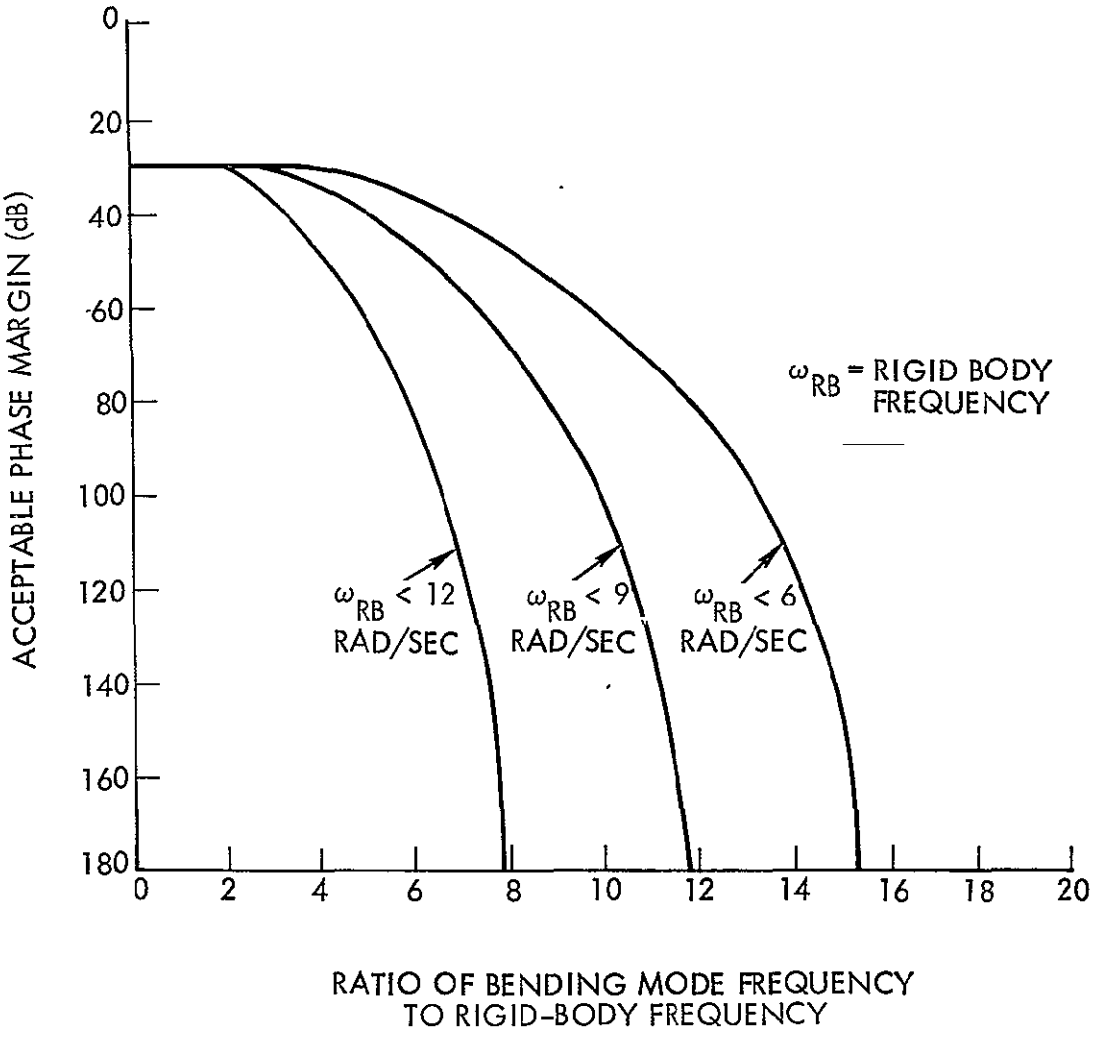

Figure A-3. An Example of Acceptable Phase Margins for Phase Stabilized Bending Modes as a Function of Modal Frequency Ratio

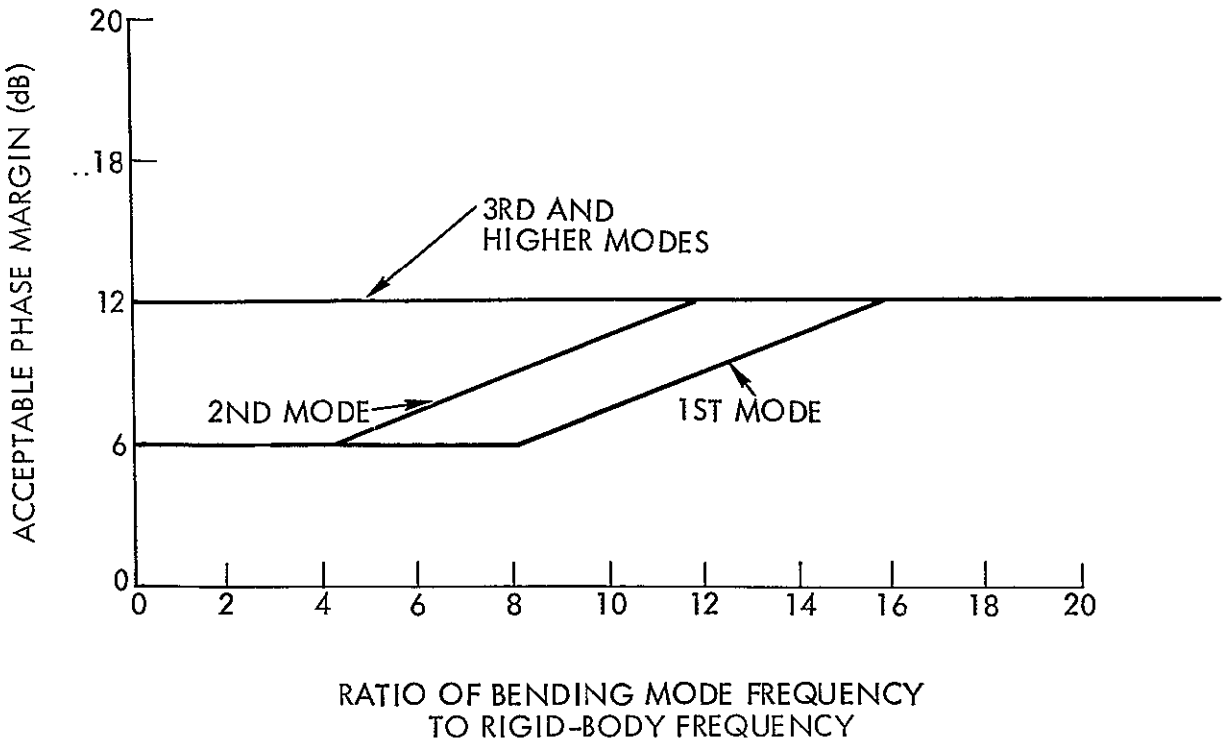

Figure A-4. Acceptable Gain Margins for Gain Stabilized Bending Modes as a Function of Modal Frequency Ratio

For the launch vehicles considered in this study, phase stabilization of all first bending modes and the Saturn V vehicle second bending mode has been employed as criteria in the past. Gain stabilization of all other bending modes was a further requirement in these programs. These criteria are also considered applicable to the vehicle configurations used in this study.

APPENDIX B

VEHICLE DYNAMICS AND CONTROL SYSTEM HOMOGENEOUS EQUATION MATRIX

The generalized homogeneous equation matrix representing the vehicle and control system dynamics used by TRW for linearized control system analyses (see Section 6) is given in this appendix. In addition to the rigid body equations of motion, including aerodynamics, this representation includes fuel sloshing and bending (flexible body) dynamics. Table B-1 and Figure B-1 present the nomenclature used and the definition of vehicle and control system angles used in the analysis. Figure B-2 is a generalized block diagram of the control system. Table B-2 contains the homogeneous equation matrix.

In all propellant slosh data given, a spring-mass model was employed for the propellant slosh modes as indicated by Figure B-1.

Table B-1

Definition of Variables and Coefficients

Variables of the Matrix

S	Laplace Operator
θ	Vehicle attitude angle from reference line
λ_{01}	Displacement of first-stage oxidizer slosh mass
λ_{f1}	Displacement of first-stage fuel slosh mass
λ_{02}	Displacement of second-stage oxidizer slosh mass
λ_{f2}	Displacement of second-stage fuel slosh mass
q_1	Displacement of normalized first-bending mode
q_2	Displacement of normalized second-bending mode
q_3	Displacement of first-stage third-bending mode
q_4	Displacement of normalized fourth-bending mode
δ	Engine displacement angle
α	Vehicle total angle of attack
γ	Vehicle velocity angle from reference line
ψ	Vehicle velocity angle of attack without winds
α_w	Angle of attack due to winds
V_w	Wind velocity
V_a	Vehicle velocity with respect to air
δ_{ci}	Engine command input to the actuation system (control system loop broken at this point to enable open-loop stability analysis and insertion of additional compensation)
θ_g	Total sensed gyro feedback from both position and rate gyros
δ_{co}	Engine command outputs from the autopilot
θ_e	Total autopilot error signal prior to autopilot compensation
θ_c	Command angle (shown with pseudoguidance but need not be used)

Table B-1

Definition of Variables and Coefficients (cont'd)

Coefficients of the Matrix

I	Vehicle moment of inertia	
M_{01}	Slosh mass of first-stage oxidizer	
M_{f1}	Slosh mass of first-stage fuel	
M_{02}	Slosh mass of second-stage oxidizer	
M_{f2}	Slosh mass of second-stage fuel	
K_{01}	Slosh spring constant of first-stage oxidizer	
K_{f1}	Slosh spring constant of first-stage fuel	
K_{o2}	Slosh spring constant of second-stage oxidizer	
K_{f2}	Slosh spring constant of second-stage fuel	
ℓ_{01}	Slosh mass moment arm of first-stage oxidizer	positive values if slosh masses are aft of c.g.
ℓ_{f1}	Slosh mass moment arm of first-stage fuel	
ℓ_{02}	Slosh mass moment arm of second-stage oxidizer	
ℓ_{f2}	Slosh mass moment arm of second-stage fuel	
ζ_{01}	Slosh mode damping of first-stage oxidizer	
ζ_{f1}	Slosh mode damping of first-stage fuel	
ζ_{02}	Slosh mode damping of second oxidizer	
ζ_{f2}	Slosh mode damping of second-stage fuel	
ω_{01}	Slosh mode frequency of first-stage oxidizer	
ω_{f1}	Slosh mode frequency of first-stage fuel	
ω_{02}	Slosh mode frequency of second-stage oxidizer	
ω_{f2}	Slosh mode frequency of second-stage fuel	
T	Total vehicle thrust	
T_c	Vehicle control thrust	

Table B-1

Definition of Variables and Coefficients (cont'd)

N_α	=	Aerodynamic normal force
l_p	=	Aerodynamic normal force moment arm
V	=	Vehicle inertial velocity
M	=	Vehicle mass excluding slosh masses
m_e	=	Total control engine mass
l_e		Effective distance of engine c. g. from engine gimbal
l_x		Distance between engine gimbal and vehicle c. g.
I_h		Total control engine inertia about gimbal
M_1		Normalized mass of the first-bending mode
M_2		Normalized mass of the second-bending mode
M_3		Normalized mass of the third-bending mode
M_4		Normalized mass of the fourth-bending mode
A_T		Total vehicle axial acceleration including aerodynamic drag effects
ω_1		Modal frequency of the first-bending mode
ω_2		Modal frequency of the second-bending mode
ω_3		Modal frequency of the third-bending mode
ω_4		Modal frequency of the fourth-bending mode
ζ_1		Damping of the first-bending mode
ζ_2		Damping of the second-bending mode
ζ_3		Damping of the third-bending mode
ζ_4		Damping of the fourth-bending mode
ϕ_{1T}		Displacement of the engine gimbal for the first-bending mode
ϕ_{2T}		Displacement of the engine gimbal for the second-bending mode
ϕ_{3T}		Displacement of the engine gimbal for the third-bending mode

Table B-1

Definition of Variables and Coefficients (cont'd)

ϕ_{4T}	Displacement of the engine gimbal for the fourth-bending mode
ϕ'_{1T}	Bending slope at the engine gimbal for the first-bending mode
ϕ'_{2T}	Bending slope at the engine gimbal for the second-bending mode
ϕ'_{3T}	Bending slope at the engine gimbal for the third-bending mode
ϕ'_{4T}	Bending slope at the engine gimbal for the fourth-bending mode
ϕ'_{1G}	Bending slope at the position gyro for the first-bending mode
ϕ'_{2G}	Bending slope at the position gyro for the second-bending mode
ϕ'_{3G}	Bending slope at the position gyro for the third-bending mode
ϕ'_{4G}	Bending slope at the position gyro for the fourth-bending mode
ϕ'_{1R}	Bending slope at the rate gyro for the first-bending mode
ϕ'_{2R}	Bending slope at the rate gyro for the second-bending mode
ϕ'_{3R}	Bending slope at the rate gyro for the third-bending mode
ϕ'_{4R}	Bending slope at the rate gyro for the fourth-bending mode
ϕ_{011}	First-bending mode displacement at the first-stage oxidizer slosh station
ϕ_{f11}	First-bending mode displacement at the first-stage fuel slosh station
ϕ_{021}	First-bending mode displacement at the second-stage oxidizer slosh station
ϕ_{f21}	First-bending mode displacement at the second-stage fuel slosh station
ϕ_{012}	Second-bending mode displacement at the first-stage oxidizer slosh station
ϕ_{f12}	Second-bending mode displacement at the first fuel slosh station
ϕ_{022}	Second-bending mode displacement at the second oxidizer slosh station
ϕ_{f22}	Second-bending mode displacement at the second fuel slosh station

Table B-1

Definition of Variables and Coefficients (cont'd)

ϕ_{013} Third-bending mode displacement at the first oxidizer slosh station

ϕ_{f13} Third-bending mode displacement at the first fuel slosh station

ϕ_{023} Third-bending mode displacement at the second oxidizer slosh station

ϕ_{f23} Third-bending mode displacement at the second fuel slosh station

ϕ_{014} Fourth-bending mode displacement at the first oxidizer slosh station

ϕ_{f14} Fourth-bending mode displacement at the first fuel slosh station

ϕ_{024} Fourth-bending mode displacement at the second oxidizer slosh station

ϕ_{f24} Fourth-bending mode displacement at the second fuel slosh station

K_p = Control system autopilot position gain

K_R = Control system autopilot rate-to-position gain

K_G = Guidance loop gain

ϵ = Pseudoguidance pole (need not be used)

c_2, c_1, b_2, b_1, a_2, a_1 = Coefficients for modelling the actuation system and control compensation.

Note: The structural bending mode equations require a positive displacement and slope occurring at the engine gimbal point.

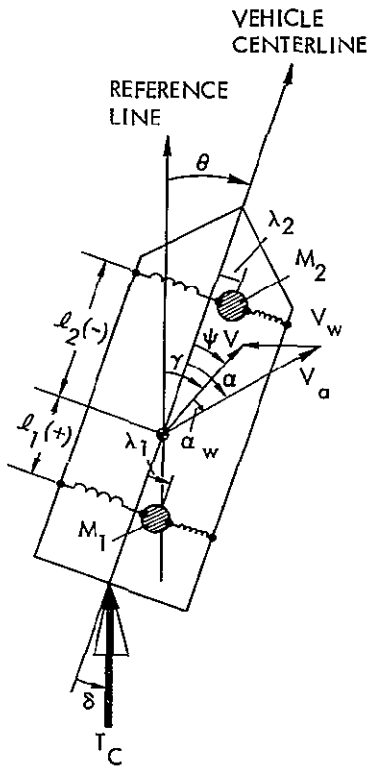

Figure B-1. Definition of Vehicle and Control System Angles

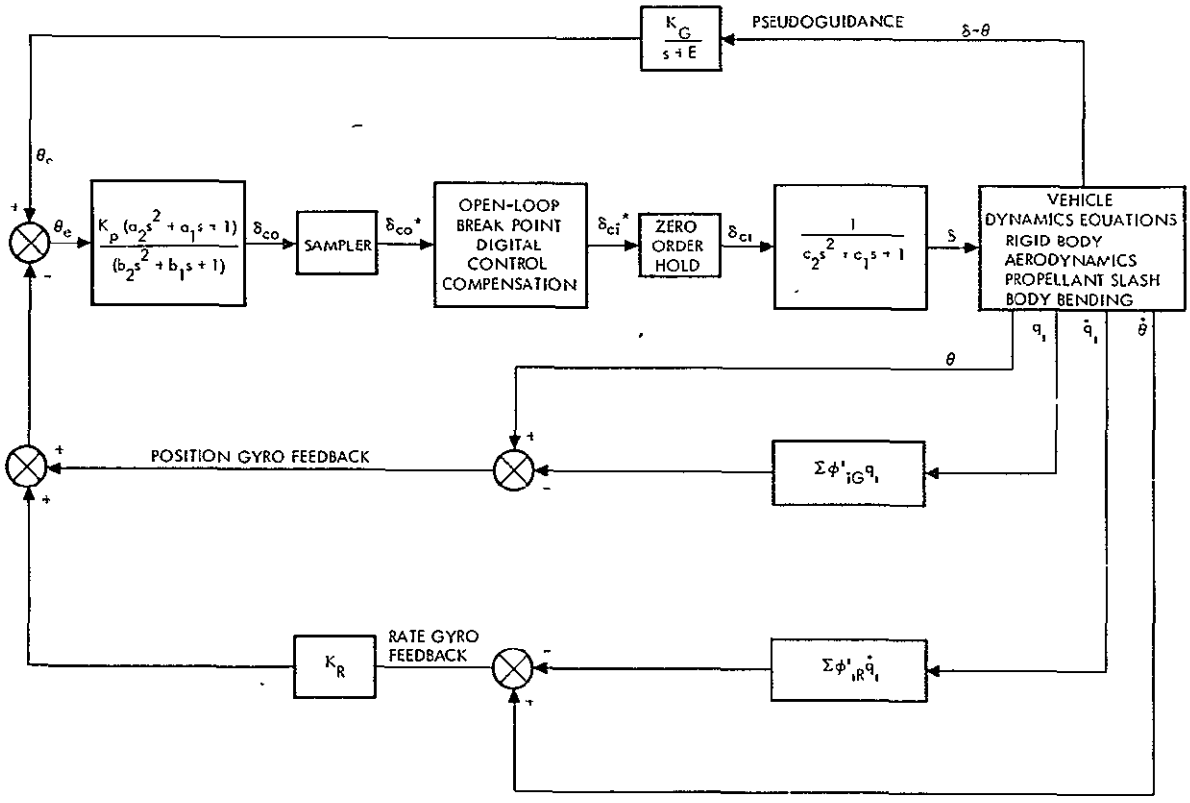

Figure B-2. Control System Block Diagram

Table B-2

Vehicle Dynamics and Control System Homogeneous Equation Matrix

	1	2	3	4	5	6	7	8	9	10	11	12	13	14	15	16	17
	ϕ	λ_{01}	λ_{f1}	λ_{02}	λ_{f2}	q_1	q_2	q_3	q_4	t	α	γ	ϕ_{c1}	ϕ_G	ϕ_{ca}	ϕ_e	ϕ_c
1	Is^2	$K_{01}\ell_{01}-m_{01}A_T$	$K_{f1}\ell_{f1}-m_{f1}A_T$	$K_{02}\ell_{02}-m_{02}A_T$	$K_{f2}\ell_{f2}-m_{f2}A_T$	$T\phi_{1T}-\phi_{1T}'\ell_{x1}$	$T\phi_{2T}-\phi_{2T}'\ell_{x1}$	$T\phi_{3T}-\phi_{3T}'\ell_{x1}$	$T\phi_{4T}-\phi_{4T}'\ell_{x1}$	$-\left[T_c\ell_{t1}\left(1+\frac{m_e\ell_e}{M\ell_x}\right)+s^2\left(I_n+m_e\ell_e\ell_{x1}\right)\right]$	$N_\alpha\ell_p$						
2	$-\ell_{01}s^2$	$s^2+2\zeta_{01}\omega_{01}s+\omega_{01}^2$				$\phi_{011}s^2$	$\phi_{012}s^2$	$\phi_{013}s^2$	$\phi_{014}s^2$			VS					
3	$-\ell_{f1}s^2$		$s^2+2\zeta_{f1}\omega_{f1}s+\omega_{f1}^2$			$\phi_{f11}s^2$	$\phi_{f12}s^2$	$\phi_{f13}s^2$	$\phi_{f14}s^2$			VS					
4	$-\ell_{02}s^2$			$s^2+2\zeta_{02}\omega_{02}s+\omega_{02}^2$		$\phi_{021}s^2$	$\phi_{022}s^2$	$\phi_{023}s^2$	$\phi_{024}s^2$			VS					
5	$-\ell_{f2}s^2$				$s^2+2\zeta_{f2}\omega_{f2}s+\omega_{f2}^2$	$\phi_{f21}s^2$	$\phi_{f22}s^2$	$\phi_{f23}s^2$	$\phi_{f24}s^2$			VS					
6						$M_1\left(s^2+2\zeta_1\omega_1s+\omega_1^2\right)$ $+T\phi_{1T}\phi_{1T}'$	$T\phi_{2T}\phi_{2T}'$	$T\phi_{3T}\phi_{3T}'$	$T\phi_{4T}\phi_{4T}'$	$T_c\phi_{1T}\left(1-\frac{Ih+m_e\ell_e\ell_x}{I}\right)$ $-s^2\left(Ih\phi_{1T}'-m_e\ell_e\phi_{1T}\right)$						
7						$T\phi_{1T}\phi_{1T}'$	$M_2\left(s^2+2\zeta_2\omega_2s+\omega_2^2\right)$ $+T\phi_{2T}\phi_{2T}'$	$T\phi_{3T}\phi_{3T}'$	$T\phi_{4T}\phi_{4T}'$	$T_c\phi_{2T}\left(1-\frac{Ih+m_e\ell_e\ell_x}{I}\right)$ $-s^2\left(Ih\phi_{2T}'-m_e\ell_e\phi_{2T}\right)$						
8						$T\phi_{1T}\phi_{1T}'$	$T\phi_{2T}\phi_{2T}'$	$M_3\left(s^2+2\zeta_3\omega_3s+\omega_3^2\right)$ $+T\phi_{3T}\phi_{3T}'$	$T\phi_{4T}\phi_{4T}'$	$T_c\phi_{3T}\left(1-\frac{Ih+m_e\ell_e\ell_x}{I}\right)$ $-s^2\left(Ih\phi_{3T}'-M_e\ell_e\phi_{3T}\right)$						
9						$T\phi_{1T}\phi_{1T}'$	$T\phi_{2T}\phi_{2T}'$	$T\phi_{3T}\phi_{3T}'$	$M_4\left(s^2+2\zeta_4\omega_4s+\omega_4^2\right)$ $+T\phi_{4T}\phi_{4T}'$	$T_c\phi_{4T}\left(1-\frac{Ih+m_e\ell_e\ell_x}{I}\right)$ $-s^2\left(Ih\phi_{4T}'-m_e\ell_e\phi_{4T}\right)$						
10										$\left(C_2s^2+C_1s+1\right)$			-1				
11		$m_{01}\omega_{01}^2$	$-m_{f1}\omega_{f1}^2$	$-m_{02}\omega_{02}^2$	$m_{f2}\omega_{f2}^2$					$m_e\ell_es^2+T_c$	N_α	MVS					
12	1										1	-1					
13	$-1-k_Rs$					$\phi_{1G}'+\phi_{1R}'K_Rs$	$\phi_{2G}'+\phi_{2R}'K_Rs$	$\phi_{3G}'+\phi_{3R}'K_Rs$	$\phi_{4G}'+\phi_{4R}'K_Rs$					1			
14															$b_2s^2+b_1s+1$	$-K_\gamma(A_2s^2+A_1s+1)$	
15														-1		-1	1
16	$-K_G$									k_G							$(s+\cdots$
17													-1 = closed-loop poles 0 = open-loop zeroes +1 = open-loop poles		-1 = closed-loop poles +1 = open-loop zeroes 0 = open-loop poles		

APPENDIX C

ATLAS/CENTAUR CONTROL SYSTEM DATA

1. INTRODUCTION

Appendix C contains data necessary for the analysis of the Atlas/Centaur control system. Figure C-1 shows the general vehicle configuration, including the location of control-system components. Table C-1 defines the nomenclature used in describing the vehicle dynamics and the Atlas/Centaur control system.

Sections 2, 3, and 4 of this appendix present aerodynamic parameters, fuel-sloshing data, and bending data for this vehicle. Section 5 presents data and linearized models for the Atlas (booster and sustainer stages) and Centaur thrust-vector control (TVC) systems.

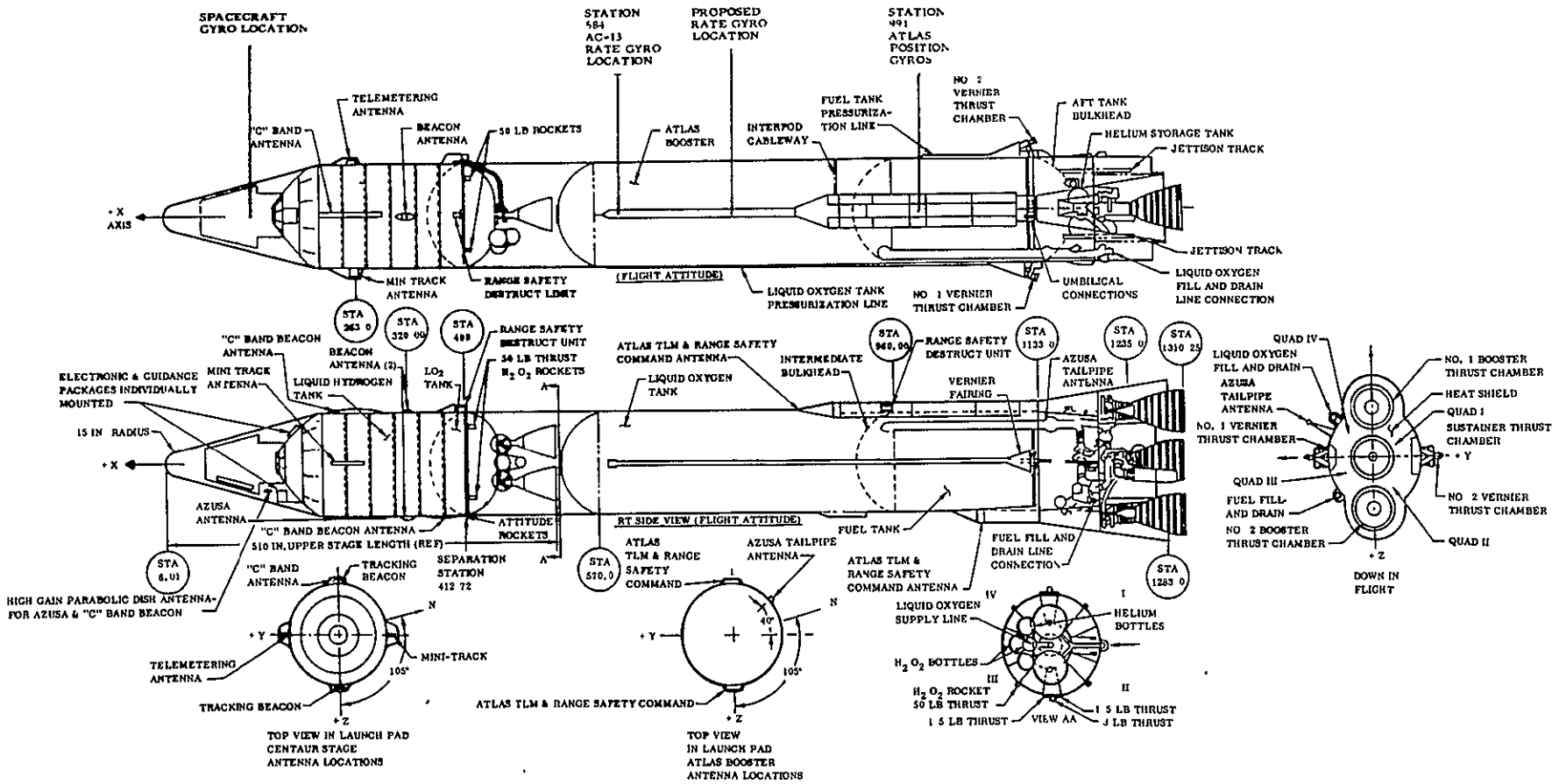

Figure C-1. Atlas/Centaur General Configuration

Table C-1

Atlas/Centaur Nomenclature

M_a	Vehicle mass excluding propellant slosh masses
I	Vehicle moment of inertia
X_{cg}	Vehicle longitudinal c. g. station
T_c	Control thrust
T_t	Total thrust
A_t	Vehicle acceleration
l_c	Control thrust moment arm
μ_c	Control moment coefficient
V	Vehicle velocity
N_α	Aerodynamic normal force
l_p	Aerodynamic moment arm
μ_α	Aerodynamic moment coefficient
l_{ao}	Atlas oxidizer slosh mass moment arm
l_{af}	Atlas fuel slosh mass moment arm
l_{co}	Centaur oxidizer slosh mass moment arm
l_{cf}	Centaur fuel slosh mass moment arm
M_{ao}	Atlas oxidizer slosh mass moment arm
M_{af}	Atlas fuel slosh mass moment arm
M_{co}	Centaur oxidizer slosh mass moment arm
M_{cf}	Centaur fuel slosh mass moment arm
ω_{ao}	Atlass oxidizer slosh frequency
ω_{af}	Atlas fuel slosh frequency
ω_{co}	Centaur oxidizer slosh frequency
ω_{cf}	Centaur fuel slosh frequency

Table C-1

Atlas/Centaur Nomenclature (con't)

ζ_{ao}	Atlas oxidizer slosh mode damping
ζ_{af}	Atlas fuel slosh mode damping
ζ_{co}	Centaur oxidizer slosh mode damping
ζ_{cf}	Centaur fuel slosh mode damping
ω_1	First-bending mode frequency
ω_2	Second-bending mode frequency
ω_3	Third-bending mode frequency
M_1	First-bending mode mass
M_2	Second-bending mode mass
M_3	Third-bending mode mass
ζ_1	First-bending mode damping
ζ_2	Second-bending mode damping
ζ_3	Third-bending mode damping
ϕ_{T1}	First-bending mode deflection at booster engine gimbal station
ϕ_{T2}	Second-bending mode deflection at booster engine gimbal station
ϕ_{T3}	Third-bending mode deflection at booster engine gimbal station
ϕ'_{T1}	First-bending mode slope at booster engine gimbal station
ϕ'_{T2}	Second-bending mode slope at booster engine gimbal station
ϕ'_{T3}	Third-bending mode slope at booster engine gimbal station
ϕ'_{1ap}	First-bending mode slope at Atlas position gyro station
ϕ'_{2ap}	Second-bending mode slope at Atlas position gyro station
ϕ'_{3ap}	Third-bending mode slope at Atlas position gyro station

Table C-1

Atlas/Centaur Nomenclature (con't)

ϕ'_{1sp}	First-bending mode slope at spacecraft gyro station
ϕ'_{2sp}	Second-bending mode slope at spacecraft gyro station
ϕ'_{3sp}	Third-bending mode slope at spacecraft gyro station
ϕ'_{1ar}	First-bending mode slope at Atlas rate gyro station
ϕ'_{2ar}	Second-bending mode slope at Atlas rate gyro station
ϕ'_{3ar}	Third-bending mode slope at Atlas rate gyro station
ϕ'_{1rr}	First-bending mode slope at recommended rate gyro station
ϕ'_{2rr}	Second-bending mode slope at recommended rate gyro station
ϕ'_{3rr}	Third-bending mode slope at recommended rate gyro station
I_h	Booster engine inertia about gimbal
M_e	Booster engine mass
ℓ_e	Booster engine mass moment arm about gimbal
X_h	Booster engine gimbal station
$\omega_{T\omega D}$	Booster engine tail wags dog frequency
$\omega_{D\omega T}$	Booster engine actuator frequency
K_c	Booster engine actuator loop velocity gain
K_c'	Booster engine actuator loop model gain for low-frequency approximation.
δ	Booster engine deflection angle
δ_c	Booster engine command angle
$\dot{\delta}_a$	Booster engine actuation rate

2. AERODYNAMIC, MASS PROPERTIES, AND TRAJECTORY-RELATED CONTROLS DATA

Aerodynamic parameters, mass properties data, and trajectory-related control parameters for the Atlas/Centaur vehicle are given in Table C-2 for the booster portion of flight. Additional trajectory-related data is given in References C-1 and C-2.

Table C-2

Aerodynamic, Mass Properties, and Trajectory-Related Controls Data for Atlas/Centaur

Aerodynamic Parameters

t sec	0	40	80	112	154
N_α lb/rad	2.14	49.2×10^3	300×10^3	134×10^3	11.8×10^3
ℓ_p ft	42.3	42.2	37.9	33.8	13.0
μ_α sec^{-2}	0	0.070	3.55	1.56	0.075
Mach	0	0.41	1.65	3.61	8.07
Q lb/ft^2	0	193	801	320	28

Mass Properties

M_a slugs	9530	7310	5350	3790	1920
I slug ft^2	4.25×10^6	3.60×10^6	3.2×10^6	2.9×10^6	2.05×10^6
X_{cg} in.	766	787	788	762	610

Trajectory and Control Parameters

T_c lb	330×10^3	343×10^3	368×10^3	378×10^3	382×10^3
T_T lb	389×10^3	407×10^3	446×10^3	460×10^3	465×10^3
A_T ft/sec^2	37.5	49.6	66.9	99.2	183
ℓ_c ft	37.2	35.4	35.3	37.5	50.2
μ_c sec^{-2}	2.88	3.38	4.05	4.88	9.33
V ft/sec	3	456	1600	3570	8530

Atlas position gyro station = 991 in.
Atlas rate gyro station = 584 in.
Spacecraft gyro station = 100 in.
Recommended rate gyro station = 708 in.

3. PROPELLANT SLOSHING DATA

Propellant-sloshing data for the Atlas/Centaur vehicle is given in Table C-3 and in Figures C-2 through C-4.

Table C-3

Propellant Slosh Parameters for Atlas/Centaur Vehicle

Propellant Slosh Parameters for Atlas/Centaur Vehicle					
t sec	0	40	80	112	154
ℓ_{ao} ft	-18.8	-13.4	-3.2	4.4	17.5
ℓ_{af} ft	14.0	18.6	24.3	29.0	42.5
ℓ_{co} ft	-28.8	-31.0	-31.0	-28.5	-15.9
ℓ_{cf} ft	-40.5	-42.4	-42.4	-40.1	-27.5
M_{ao} slugs	100	374	374	374	330
M_{af} slugs	75	280	280	280	180
M_{co} slugs	210	210	210	210	210
M_{cf} slugs	18	18	18	18	18
ω_{ao} rad/sec	4.68	4.27	4.96	6.04	7.32
ω_{af} rad/sec	4.68	4.27	4.96	5.96	6.88
ω_{co} rad/sec	5.59	6.43	7.47	9.09	12.40
ω_{cf} rad/sec	3.83	4.41	5.12	6.24	8.48
ζ_{ao} N.D.	0.0009	0.0009	0.0010	0.0080	0.0004
ζ_{af} N.D.	0.0008	0.0008	0.0010	0.0030	0.0008
ζ_{co} N.D.	0.0030	0.0030	0.0030	0.0030	0.0030
ζ_{cf} N.D.	0.0008	0.0008	0.0008	0.0008	0.0008

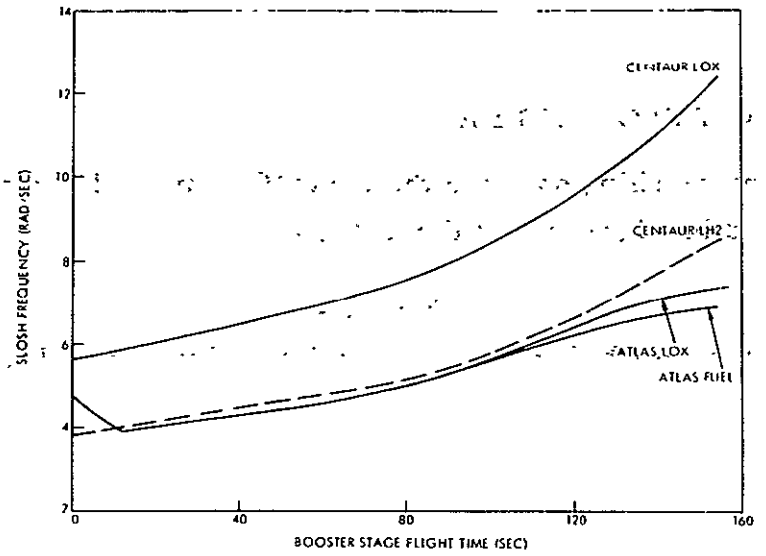

Figure C-2. Slosh Frequencies versus Flight Time

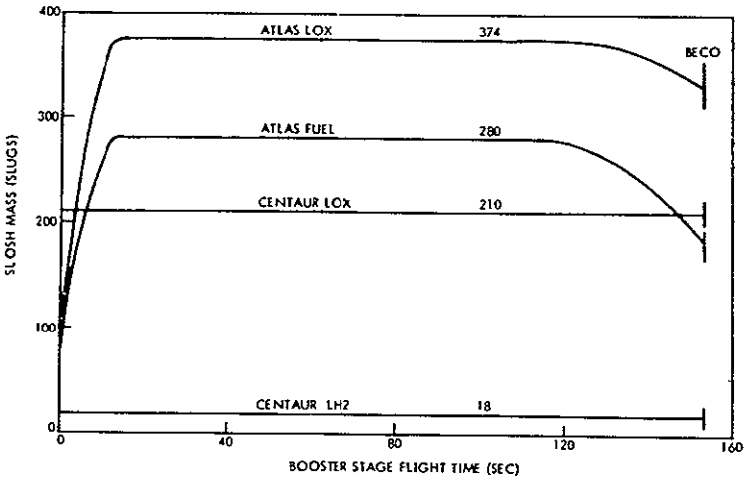

Figure C-3. Slosh Masses versus Flight Time

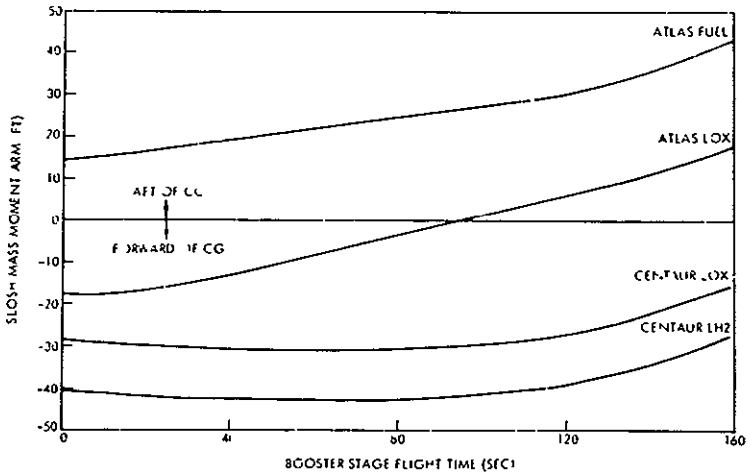

Figure C-4. Slosh Moment Arms versus Flight Time

4. VEHICLE BENDING DATA

Vehicle bending data for the Atlas/Centaur vehicle is given in Table C-4 for three modes at five times of flight during booster flight. Additional data will be found in Reference C-2.

Table C-4
Bending Mode Parameters

Bending Mode Parameters					
t sec	0	40	80	112	154
ω_1 rad/sec	13.46	13.92	15.58	18.52	25.89
ω_2 rad/sec	32.37	37.29	38.45	38.71	45.97
ω_3 rad/sec	46.37	47.07	47.88	48.38	49.53
M_1 slugs	3171	2740	2085	1617	2166
M_2 slugs	3257	5044	10620	8462	3087
M_3 slugs	2122	1989	2360	3249	12015
ζ_1 N. D.	0.005	0.005	0.005	0.010	0.010
ζ_2 N. D.	0.005	0.010	0.010	0.010	0.010
ζ_3 N. D.	0.010	0.010	0.010	0.010	0.010
φ_{T1} ft/ft	1.0	1.0	1.0	1.0	1.0
φ_{T2} ft/ft	1.0	1.0	1.0	1.0	1.0
φ_{T3} ft/ft	1.0	1.0	1.0	1.0	1.0
φ'_{T1} rad/ft	0.052	0.055	0.061	0.071	0.110
φ'_{T2} rad/ft	0.124	0.169	0.181	0.189	0.456
φ'_{T3} rad/ft	0.368	0.413	0.470	0.511	0.403
φ'_{1ap} rad/ft	0.045	0.046	0.049	0.054	0.070
φ'_{2ap} rad/ft	0.051	0.046	0.049	0.051	0.043
φ'_{3ap} rad/ft	0.0017	-0.0078	-0.015	-0.021	-0.056
φ'_{1sp} rad/ft	-0.075	-0.063	-0.061	-0.067	-0.141
φ'_{2sp} rad/ft	0.125	0.200	0.328	0.273	0.084
φ'_{3sp} rad/ft	-0.067	-0.051	-0.036	-0.018	-0.066
φ'_{1ar} rad/ft	-0.033	-0.031	-0.026	-0.023	-0.022
φ'_{2ar} rad/ft	-0.045	-0.062	-0.107	-0.097	-0.064
φ'_{3ar} rad/ft	0.040	0.026	0.0131	0.012	0.063
φ'_{1rr} rad/ft	-0.001	-0.001	-0.003	0.002	0.015
φ'_{2rr} rad/ft	-0.072	-0.1	-0.122	-0.096	-0.059
φ'_{3rr} rad/ft	-0.0139	-0.011	0.001	0.004	0 04

5. THRUST VECTOR CONTROL DATA

Data and linearized models for the Atlas/Centaur TVC system are given in Tables C-5 through C-7 and in Figures C-5 and C-6.

Table C-5

Booster Engine Servoactuator Data

Booster Engine Parameters For One Engine

I_h	slug-ft^2	= 377
M_e	slug	= 30.8
ℓ_e	ft	= 2.52
X_h	in.	= 1212
ω_{TWD}	rad/sec	= 46
ω_{DWT}	rad/sec	= 93
K_c	sec^{-1}	= 36
δ_{max}	deg	= 5
$\dot{\delta}_{a\ max}$	deg/sec	= 28

Engine actuation model for $\delta\omega$ = 2°/sec:

$$\frac{\delta}{\delta_c} = \frac{K_c\ \omega_{DWT}^2}{(S + 27.5)\ (S + 68.35 \pm j81.6)}$$

Low-frequency approximation for $\delta\omega$ = 2°/sec:

$$\frac{\delta}{\delta_c} \approx \frac{K_c'}{S + K_c'} = \frac{18}{S + 18}$$

Engine actuation model for $\delta\omega$ = 1°/sec:

$$\frac{\delta}{\delta_c} = \frac{K_c\ \omega_{DWT}^2}{(S + 14.5)\ (S + 120 \pm j84)}$$

Low-frequency approximation for $\delta\omega$ = 1°/sec:

$$\frac{\delta}{\delta_c} = \frac{K_c'}{S + K_c'} = \frac{12.5}{S + 12.5}$$

Table C-6

Atlas Servoactuator Characteristics

Symbol	Definition	Units	Booster	Sustainer
A	Actuating piston area	ft^2	2.47×10^{-2}	4.1×10^{-2}
B	Bulk modules of hydraulic fluid	lb/ft^2	3.89×10^{7}	3.89×10^{7}
C_B	Coulomb friction coefficient	ft-lb	5.65×10^{2}	5.59×10^{2}
C_L	Discharge coefficient for leakage (bypass) orifice	$\frac{ft^3/sec}{\sqrt{lb/ft^2}}$	4.78×10^{-6}	2.47×10^{-6}
C_V	Viscous friction coefficient	ft-lb-sec/deg	6.3×10	3.76×10
I_R	Moment of inertia, engine-gimbaled "wet" mass about engine gimbal axis	$slug\text{-}ft^2$	3.77×10^{2}	4.20×10^{2}
K_a	Servoamplifier gain	ma/V	2.7	3.42
K_m	Spring constant of actuator-backup structure	lb/ft	1.138×10^{6}	1.441×10^{6}
K_t	Feedback transducer gain	volt/deg	2.2	3.0
K_V	Servovalve discharge coefficient	$\frac{ft^3/sec}{mA\sqrt{lb/ft^2}}$	7.125×10^{-6}	1.68×10^{-6}
ℓ_R	Distance from center of gravity of gimbaled mass to center line of engine gimbal axis	ft	2.52	2.68

Table C-6

Atlas Servoactuator Characteristics (Cont'd)

Symbol	Definition	Units	Booster	Sustainer
M_R	Gimbaled mass, one engine "wet"	slugs	3.08×10	3.19×10
P_R	Hydraulic return pressure from servovalve	lb/ft^2	7.2×10^3	7.2×10^3
P_S	Hydraulic supply pressure to servovalve	lb/ft^2	4.32×10^5	4.32×10^5
R	Distance from center line of actuator mounting to center line of engine at gimbal point	ft	1.769	8.33×10^{-1}
V_T	Total volume of hydraulic fluid in one actuator cylinder	ft^3	7.6×10^{-3}	4.14×10^{-3}
T	Thrust	lb	1.545×10^5	5.7×10^4
K_c	No-load, open-loop actuator velocity gain		36.8	18.06
δ_{max}	Engine displacement limit	deg	5	3
$\dot{\delta}_{max}$	Engine actuation rate limit	deg/sec	28	-

Table C-7

Centaur Servovalve-Actuator-Engine Parameters-
RL-10A-3 Propulsion System

Symbol	Definition	Units	Value
A	Actuating piston area	ft^2	1.06×10^{-2}
B	Bulk modules of hydraulic fluid	lb/ft^2	3.89×10^{7}
C_b	Coulomb friction coefficient	ft/lb	200
C_v	Viscous friction coefficient	ft lb/deg/sec	3.62
I_R	Moment of inertia, engine-gimbaled "wet" mass about engine gimbal axis	$slug\text{-}ft^2$	66.5
M_R	Gimbaled mass, one engine "wet"	slugs	11.0
ℓ_R	Distance from center of gravity of gimbaled mass to center line of engine gimbal axis	ft	2.04
R	Distance from center line of actuator mounting to center line of engine at gimbal point	ft	1.16
K_a	Servoamplifier gain	mA/volt	3.6
K_t	Feedback transducer gain	volt/deg	2.06
K_m	Spring constant of actuator-backup structure	lb/ft	5.1×10^{5}
K_v	Servovalve discharge coefficient	$\frac{(ft^3/sec)}{mA\sqrt{lb/ft^2}}$	1.02×10^{-6}

Table C-7

Centaur Servovalve-Actuator-Engine Parameters-
RL-10A-3 Propulsion System (Cont'd)

Symbol	Definition	Units	Value
P_R	Hydraulic return pressure from servovalve	lb/ft^2	7.2×10^3
P_S	Hydraulic supply pressure to servovalve	lb/ft^2	1.512×10^5
T		lb	1.5×10^4
V_T	Total volume of hydraulic fluid in one actuator cylinder	ft^3	1.33×10^{-3}
K_c	No-load, open-loop actuator velocity gain	1/sec	13.1
A_F	Area of washout piston DPF	ft^2	3.41×10^{-4}
C_F	Discharge coefficient for DPF orifice	$\frac{(ft^3/sec)}{\sqrt{lb/ft^2}}$	1.342×10^{-7}
K_f	Spring constant-washout piston	lb/ft	9.36×10^3
K_s	Pressure feedback gain	$mA/lb/ft^2$	1.218×10^{-4}

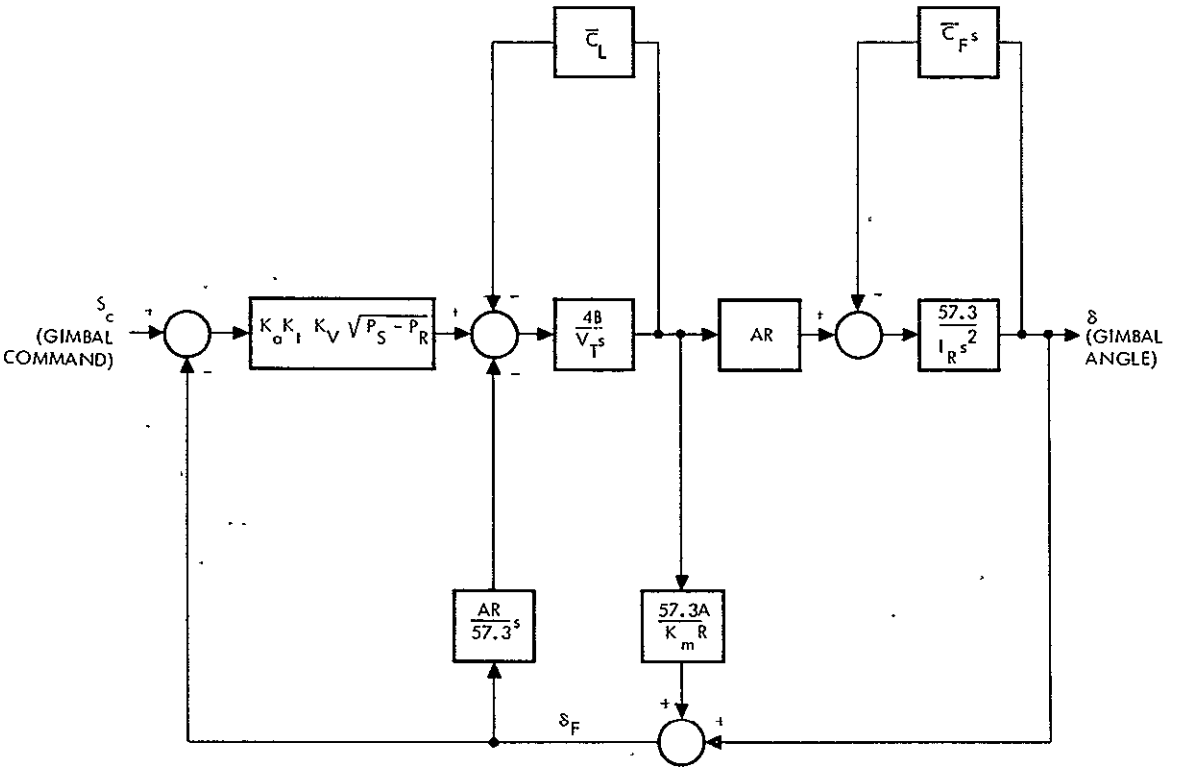

Figure C-5. Linearized Block Diagram of Atlas Booster and Sustainer Servoactuator (load torque assumed negligible)

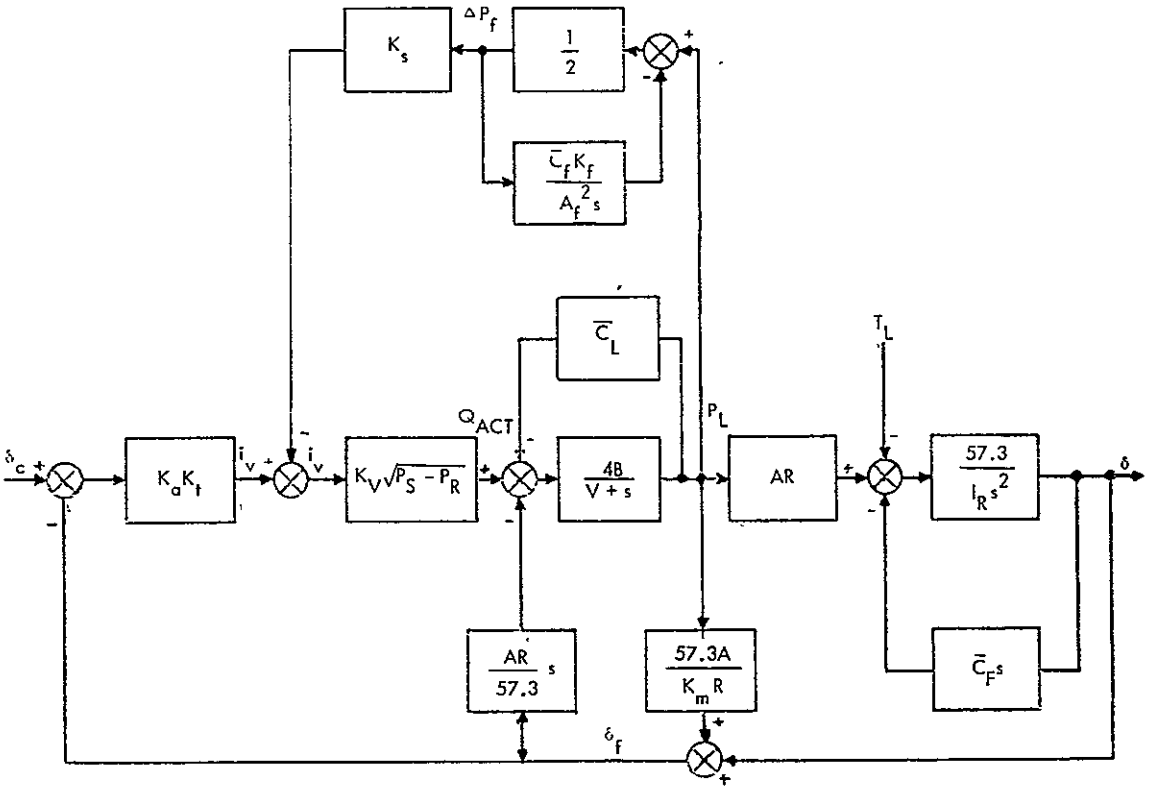

Figure C-6. Linearized Block Diagram Centaur Servoactuator

APPENDIX D

SATURN IB/CENTAUR CONTROL SYSTEM DATA

1. INTRODUCTION

Appendix D contains data necessary for the analysis of the Saturn IB/Centaur control system. Figure D-1 shows the general vehicle configuration, including the location of control-system components. Sections 2, 3, and 4 of this appendix present the aerodynamic parameters, fuel-sloshing data, and bending data for this vehicle. Section 5 presents data and a linearized model for the Saturn IB thrust vector control system. Data for the Centaur TVC system is given in Appendix C.

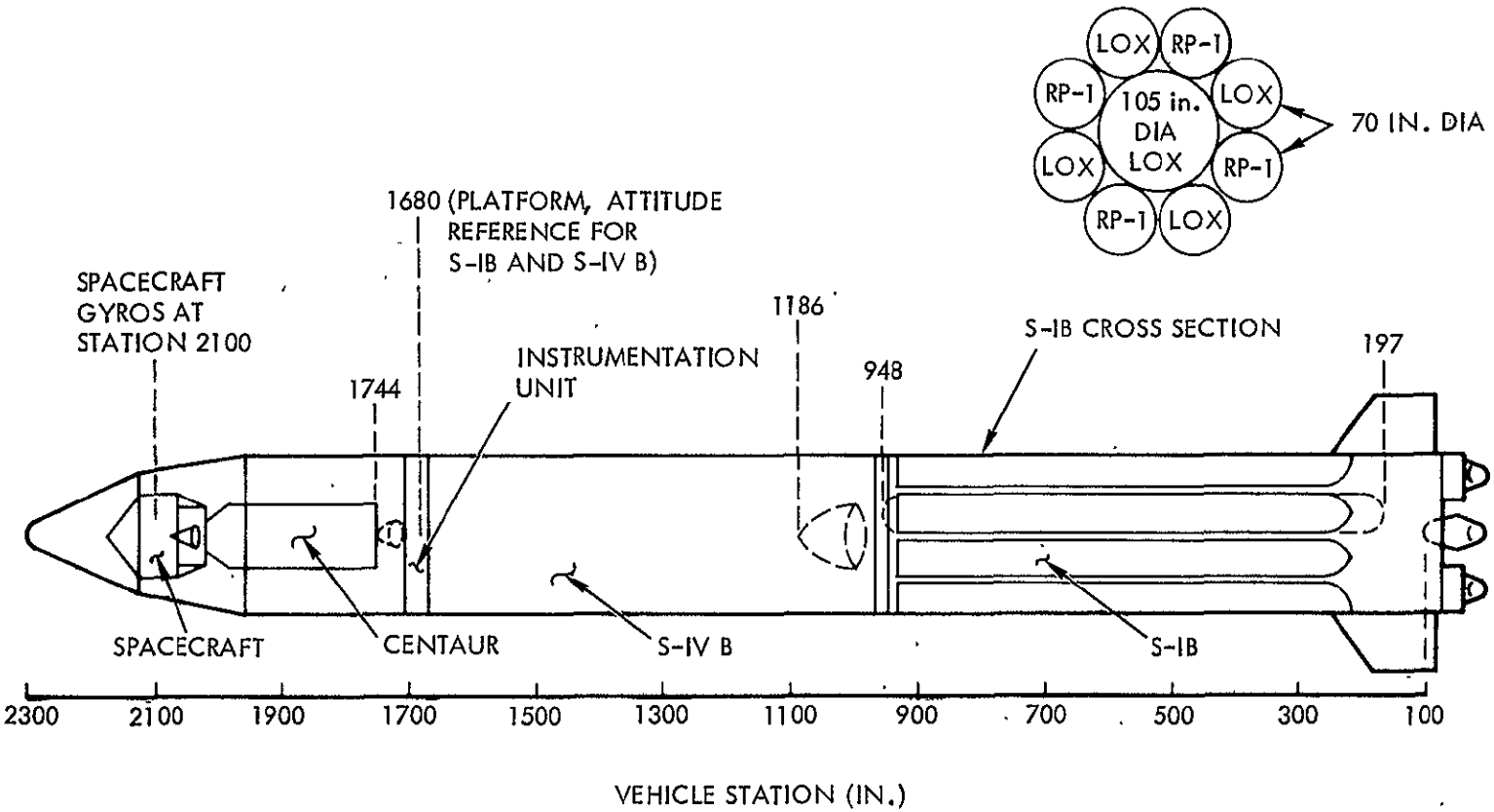

Figure D-1. Saturn IB/Centaur General Configuration

2. AERODYNAMIC, MASS PROPERTIES, AND TRAJECTORY-RELATED CONTROLS DATA

Aerodynamic parameters, mass properties data, and trajectory-related controls parameters are summarized in Table D-1 for the Saturn IB/Centaur vehicle. Additional aerodynamic data (normal force coefficient) is given in Figures D-2 and D-3 for the 260-in. and 154-in. diameter fairings. Mass properties data as a function of vehicle weight and flight time is given in Figures D-4 through D-6. Additional trajectory data may be found in Reference D-1.

3. PROPELLANT SLOSHING DATA

Propellant sloshing data for the Saturn IB/Centaur vehicle is given in Figures D-7 through D-9.

4. VEHICLE BENDING DATA

Vehicle bending data for the Saturn IB/Centaur vehicle is given in Table D-2 at three times of flight during the S-I stage burning and in Table D-3 at three times of flight during the S-IVB stage burning. Additional data is given in Reference D-2.

Table D-1

Saturn IB/Centaur, Summary of Mass Properties, Aerodynamic Parameters, and Trajectory-Related Control Parameters

Parameter	S-IB Flight			S-IVB Flight			
	L. O.	80	153	158.6	200 W/S*	200 WO/S*	625.6
Mass Properties							
M_a (slugs)	39,831	25,202	12,423	8954	8406	8142	1880
I (slug-ft^2)	44.9×10^6	43.6×10^6	22.4×10^6	3.25×10^6	3.22×10^6	2.58×10^6	1.22×10^6
X_{cg} (in.)	718	724	1069	1340	1349	1328	1553
Trajector and Control Parameters							
T_c (lb)	0.74×10^6	0.83×10^6	0.622×10^6	2×10^5	2×10^5	2×10^5	2×10^5
T_τ (lb)	1.47×10^6	1.66×10^6	1.24×10^6	2×10^5	2×10^5	2×10^5	2×10^5
A_τ (ft/sec^2)	36.9	59.0	99.8	22.4	23.8	24.6	106.3
ℓ_c (ft)	51.5	52.0	80.7	103.0	104.0	102.0	121.1
μ_c (1/sec^2)	0.85	0.99	2.78				
V (ft/sec)	1.0	1275.0	5924.0	5817	6036	6036	24197
$g\cos\gamma$ (ft/sec^2)	32.2	29.63	20.08	19.54	15.71	15.71	0
Aerodynamic Parameters							
N_α (lb/rad)	0	1.4×10^6	12.9×10^3	--	--	--	--
ℓ_p (ft)	11.9	15.3	17.8	--	--	--	--
$\mu\alpha$ (1/sec^2)	0	0.48	0.010	--	--	--	--
Q (lb/ft^2)	0	565.0	7.9	--	--	--	--
Mach	0	1.317	5.837	--	--	--	--

*Shroud

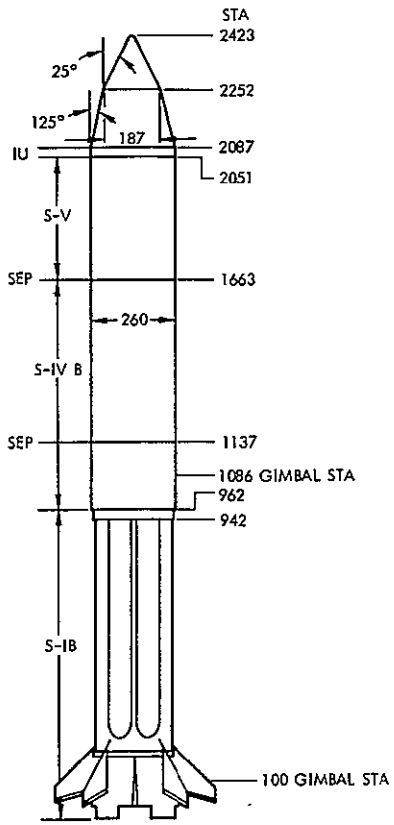

Figure D-2a. Saturn IB/Centaur Three-Stage Vehicle 260" Diameter Fairing

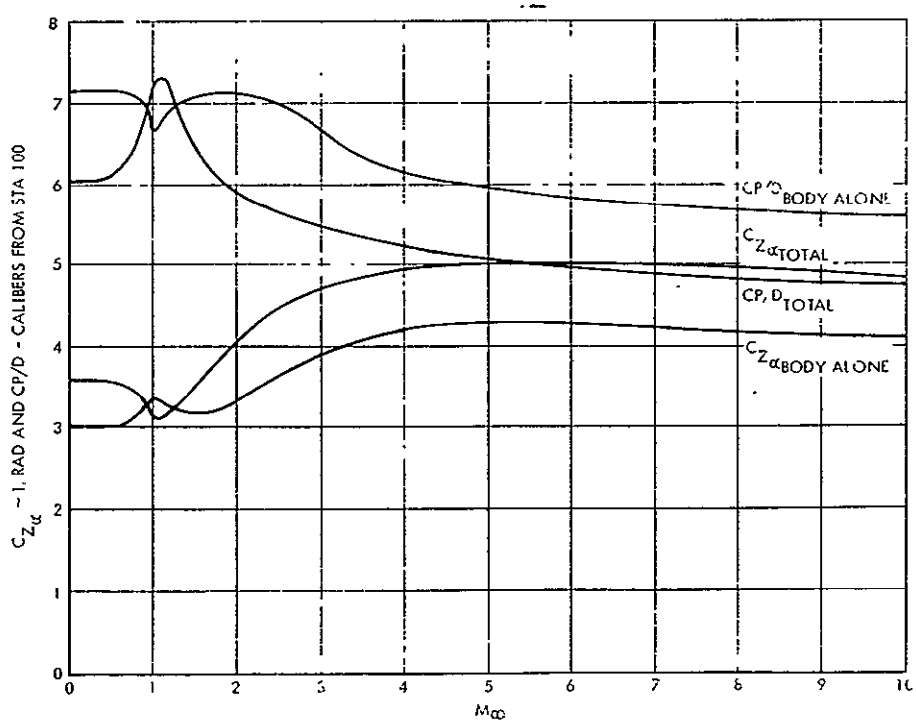

Figure D-2b. Normal Force Coefficient, Saturn IB/Centaur 260" Diameter Fairing

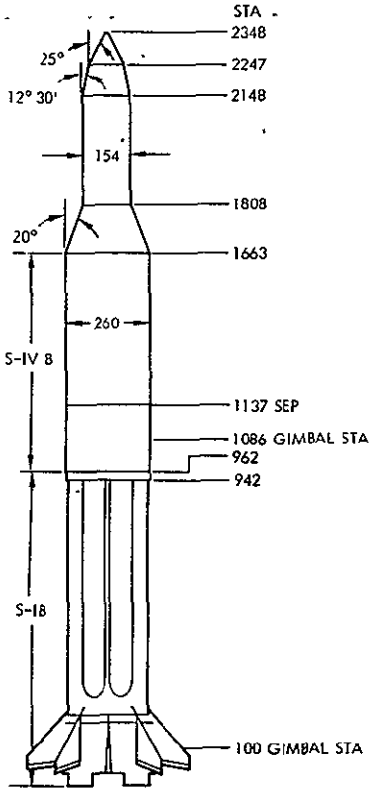

Figure D-3a. Saturn IB Three-Stage Vehicle, 154" Diameter Fairing

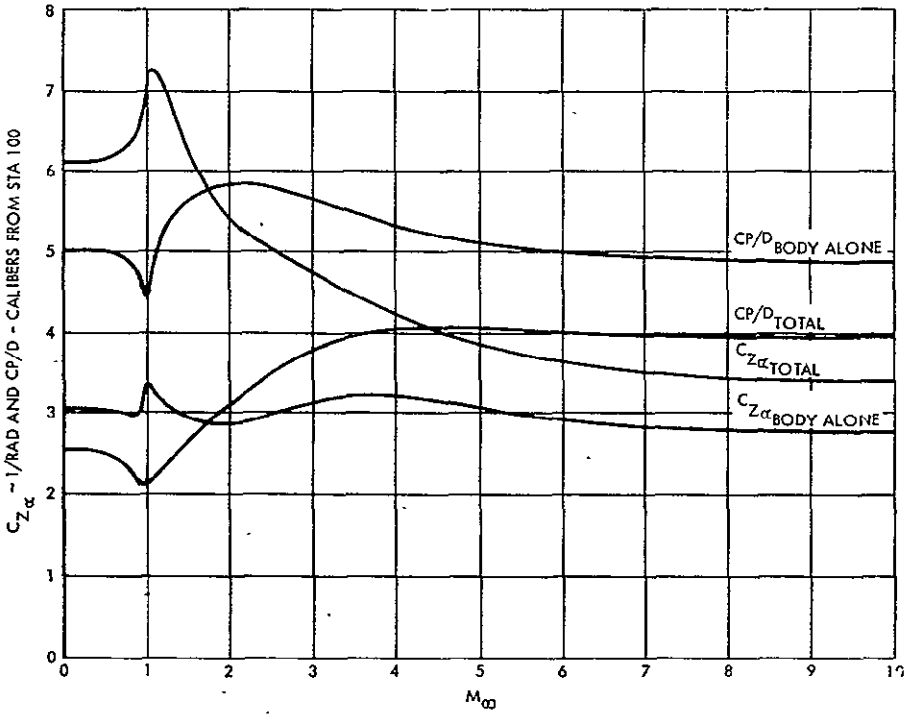

Figure D-3b. Normal Force Coefficient Saturn IB/Centaur 154" Diameter Fairing

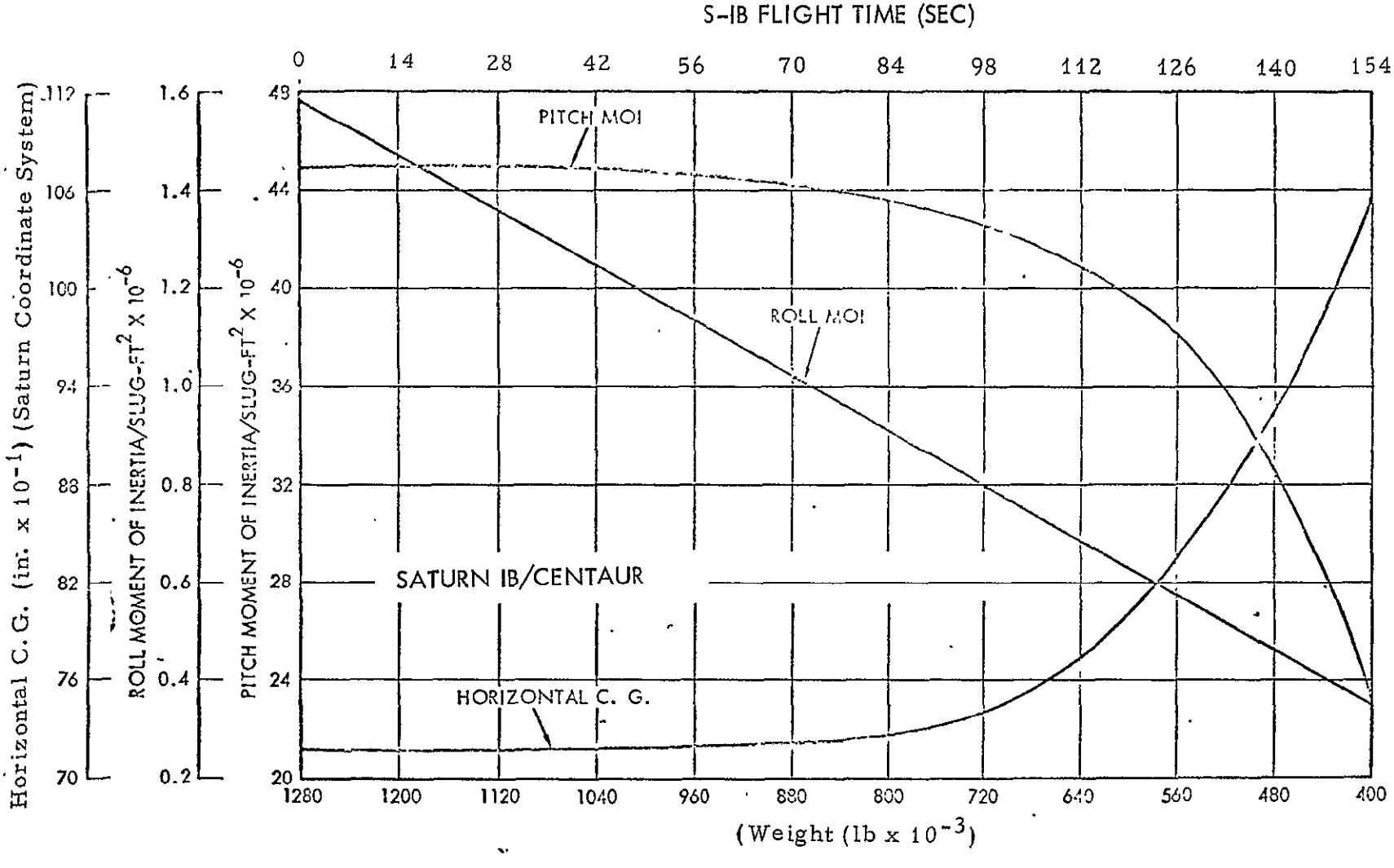

Figure D-4. Moment of Inertia and C. G. Versus Weight, Liftoff to S-I Burnout

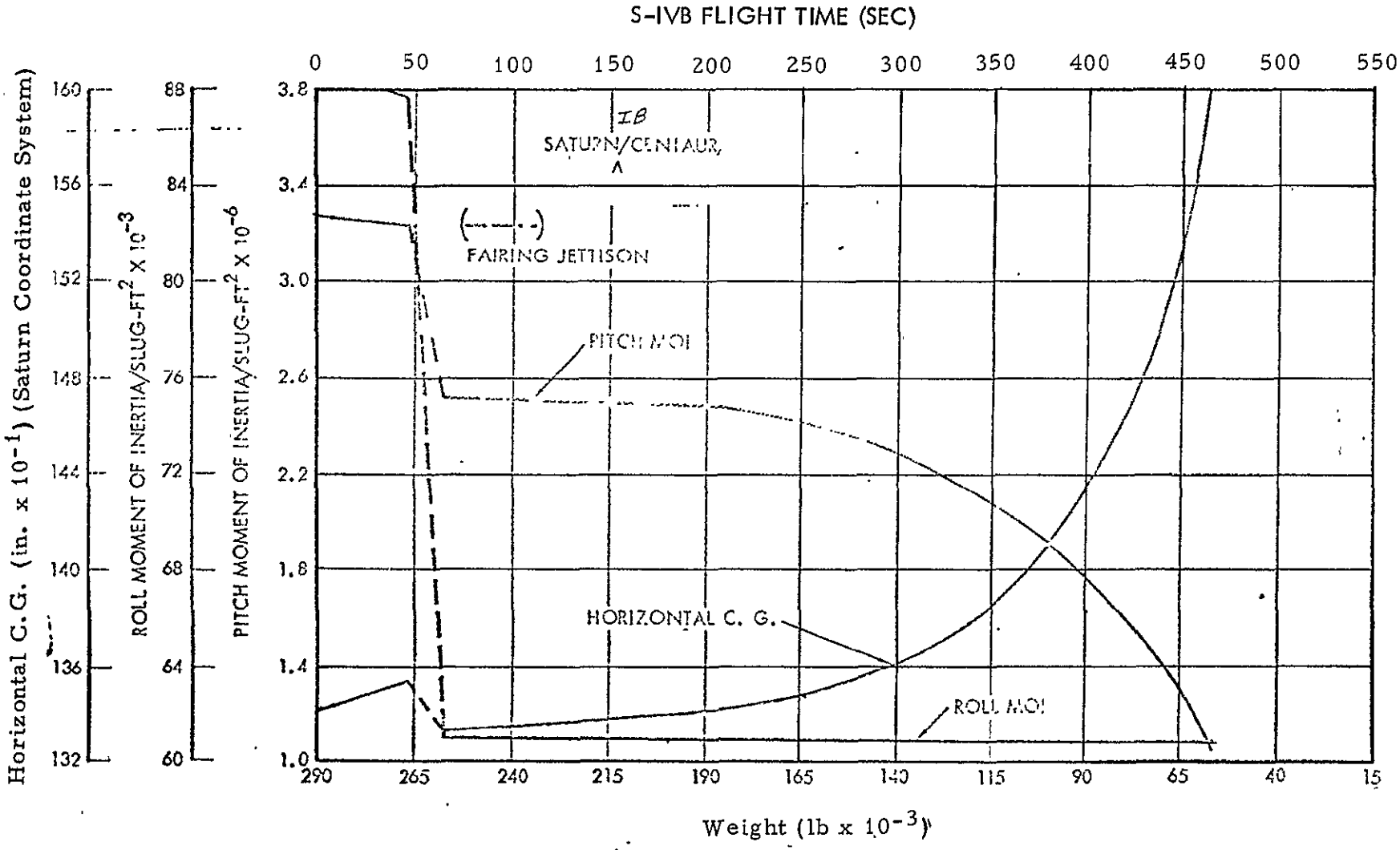

Figure D-5. Moment of Inertia and C.G. Versus Weight, S-IVB Start to S-IVB Burnout

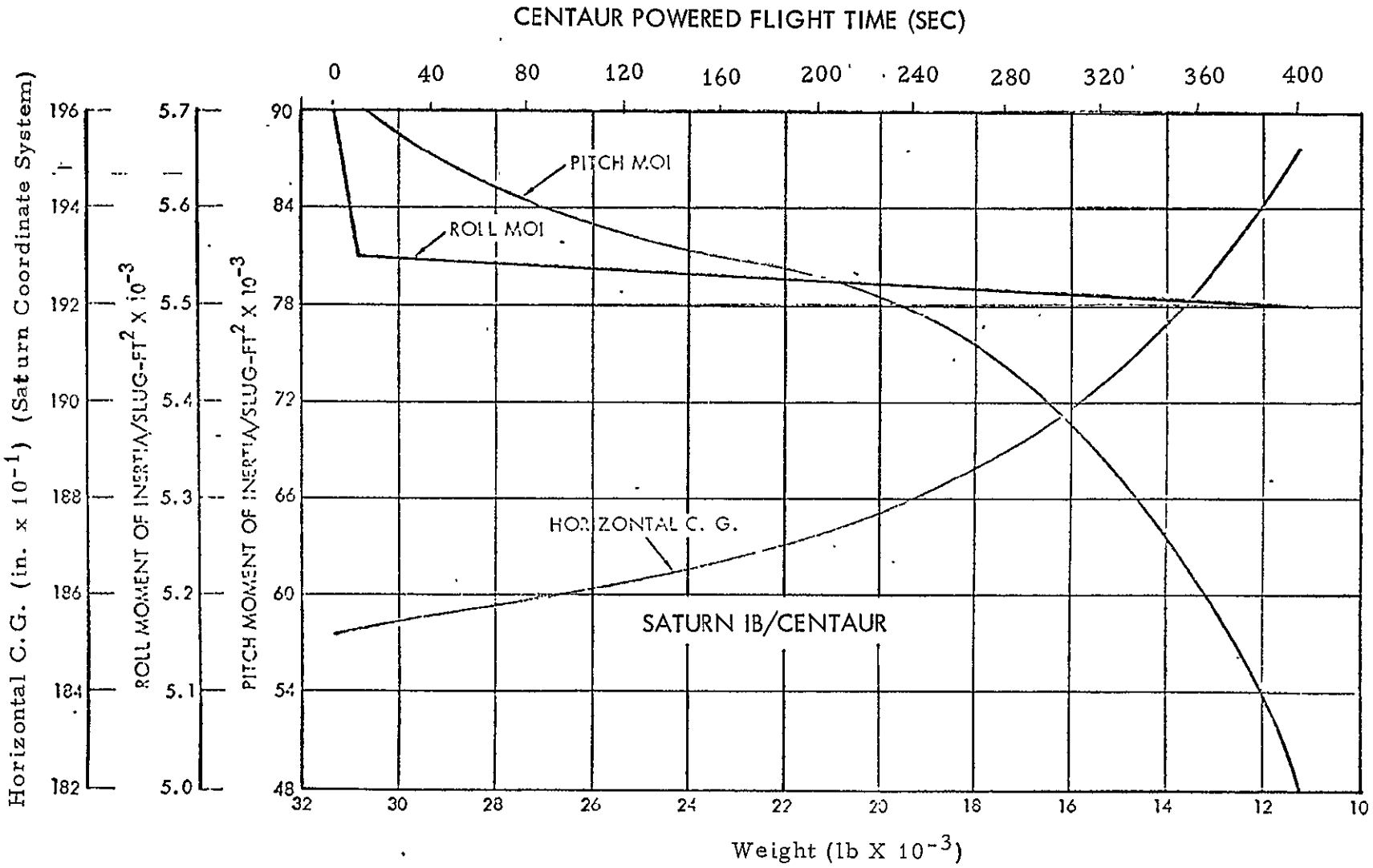

Figure D-6. Moment of Inertia and C.G. Versus Weight, Centaur Separation to Centaur Burnout

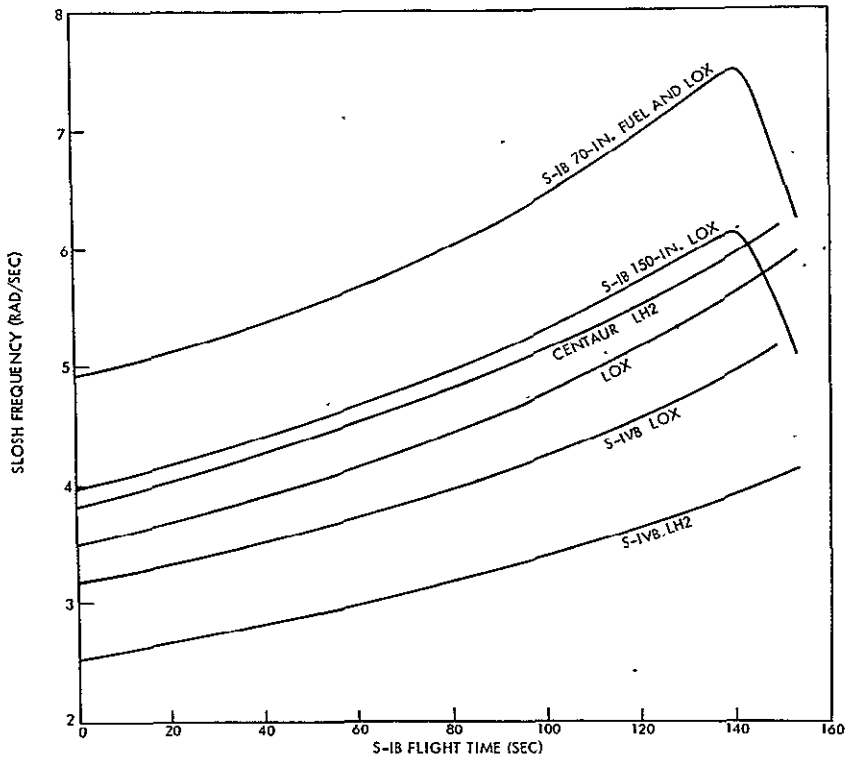

Figure D-7. Slosh Frequencies Versus Flight Time

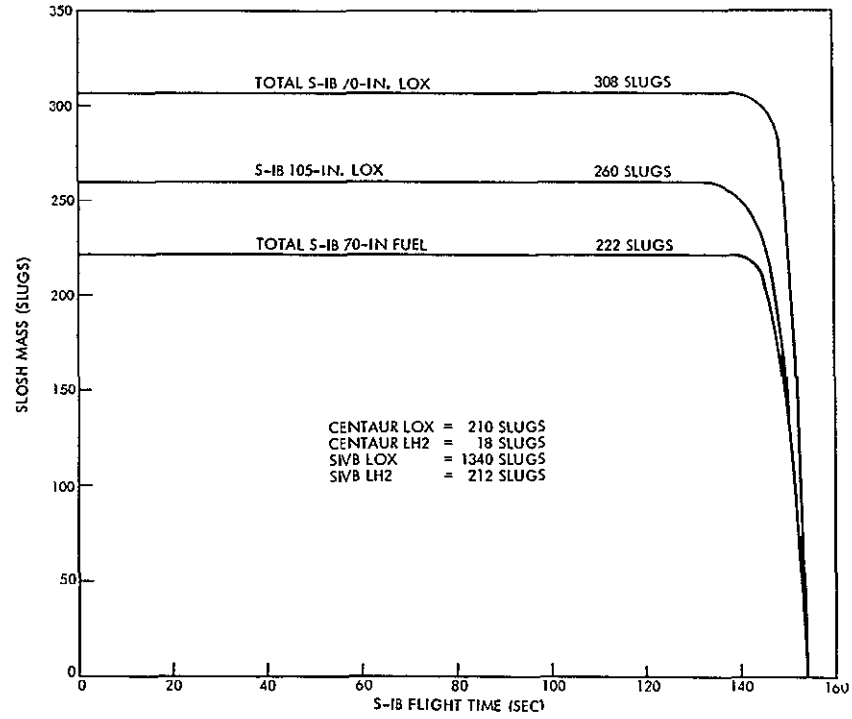

Figure D-8. Slosh Masses Versus Flight Time

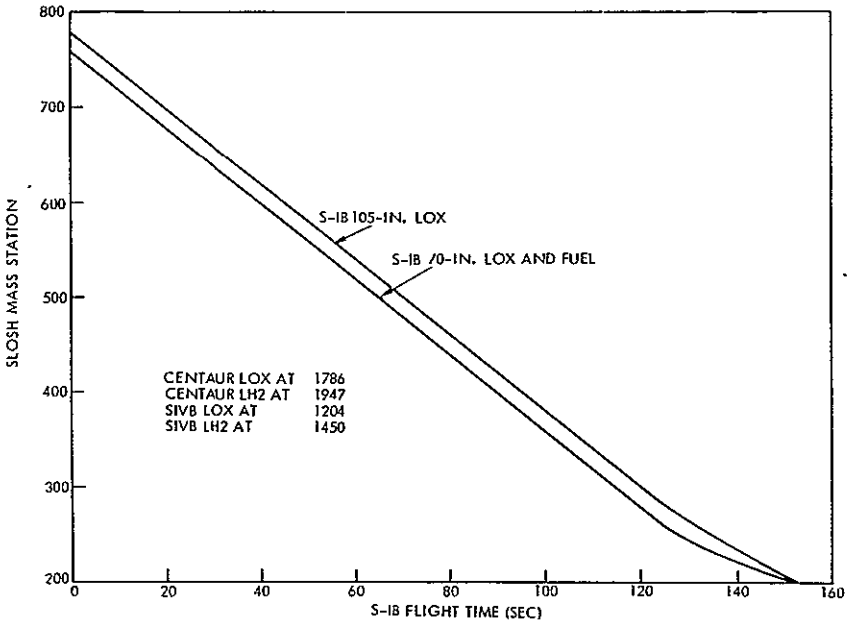

Figure D-9. Slosh Moment Arms Versus Flight Time

Table D-2

Saturn S-I Stage Bending Mode Parameters

Bending Mode Parameters \ Flight Time		0 sec	80 sec	153 sec
Combined Mode Freq.				
ω_1	(rad/sec)	10.93	14.57	15.82
ω_2	(rad/sec)	26.50	29.39	52.05
ω_3	(rad/sec)	43.14	73.52	99.15
Mass (Slugs)				
M_1		39831	25202	12423
M_2		39831	25202	12423
M_3		39831	25202	12423
Damping (N. D.)				
ζ_1		0.01	0.01	0.01
ζ_2		0.01	0.01	0.01
ζ_3		0.01	0.01	0.01
Modal Deflection (ft/ft)				
ϕ_{T1}	At Station	2.3	1.8	1.3
ϕ_{T2}		1.8	2.0	1.0
ϕ_{T3}	X = 100	2.4	1.7	0.6
Bending Slope (1/ft)				
ϕ'_{T1}	At Station	0.0775	0.0815	0.0558
ϕ'_{T2}		0.0917	0.117	0.15
ϕ'_{T3}	X = 100	0.147	0.157	0.13

Table D-2

Saturn S-I Stage Bending Mode Parameters (con't)

Bending Mode Parameters \ Flight Time	0 sec	80 sec	153 sec
Bending Slope (1/ft) (cont)			
ϕ'_{1IU} } At Station	-0.0567	-0.0658	-0.0525
ϕ'_{2IU} } At Station	0.0875	0.0541	0.0317
ϕ'_{3IU} } X = 1680	-0.045	-0.045	-0.055
ϕ'_{1SC} } At Station	-0.060	-0.0683	-0.055
ϕ'_{2SC} } At Station	0.0975	0.0616	0.0467
ϕ'_{3SC} } X = 2100	-0.0575	-0.0716	-0.0983
ϕ'_{1BR} } At Station	-0.022	-0.019	-0.0125
ϕ'_{2BR} } At Station	-0.040	-0.0383	-0.07
ϕ'_{3BR} } X = 950	0.035	0.0558	-0.01

Table D-3

Saturn S-IVB Stage Bending Mode Parameters

Bending Mode Parameters \ Flight Time	158.6 sec	200 sec w/Shroud	200 sec wo/Shroud	625 sec
Combined Mode Bending Freq.				
ω_1 (rad/sec)	92.27	99.60	35.59	41.31
ω_2 (rad/sec)	197.03	238.97	109.89	172.71
ω_3 (rad/sec)	260.92	272.08	181.22	228.97
Mass (Slugs)				
M_1	8954	8406	8142	1880
M_2	8954	8406	8142	1880
M_3	8954	8406	8142	1880
Damping (N. D.)				
ξ_1	0.01	0.01	0.01	0.01
ξ_2	0.01	0.01	0.01	0.01
ξ_3	0.01	0.01	0.01	0.01
Modal Deflection (ft/ft)				
ϕ_{T1} at Station x = 1186	0.90	0.90	0.45	1.2
ϕ_{T2} at Station x = 1186	0.82	0.38	0.535	2.0
ϕ_{T3} at Station x = 1186	0.36	0.22	0.53	2.0

Table D-3

Saturn S-IVB Stage Bending Mode Parameters (cont'd)

Bending Mode Parameters \ Flight Time		158.6 sec	200 sec w/Shroud	200 sec wo/Shroud	625 sec
Bending Slope (1/ft)					
ϕ'_{T1}	At Station x = 1186	0.149	0.163	0.0711	0.0533
ϕ'_{T2}		0.200	0.125	0.156	0.111
ϕ'_{T3}		0.138	0.238	0.2	0.122
ϕ'_{1IU}	At Station x = 1680	-0.0945	-0.0945	0.0522	0.05
ϕ'_{2IU}		0.0133	-0.0511	-0.178	0.0222
ϕ'_{3IU}		0.200	0.200	-0.104	-0.089
ϕ'_{1SC}	At Station x = 2100	-0.0945	-0.105	-0.32	-0.145
ϕ'_{2SC}		0.17	0.23	0.32	0.34
ϕ'_{3SC}		0.425	0.36	-0.70	0.33

5. THRUST VECTOR CONTROL DATA

The linearized TVC Model for the Saturn IB control system is given in Figure D-10 and the associated data for the S-I and S-IVB stages in Table D-4. Table D-5 gives the corresponding TVC transfer functions.

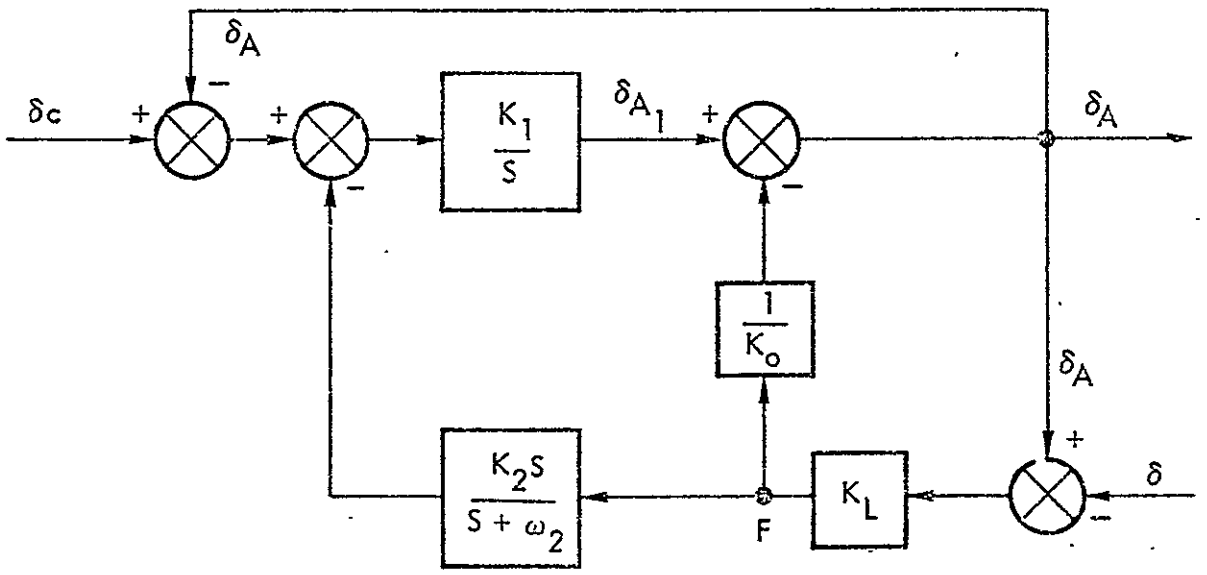

Note: δ is derived from an actuator moment equation.

Figure D-10. Linearized Block Diagram of Saturn 1B Thrust Vector Control System

Table D-4

Parameters for S-IB and S-IVB Stages

Parameter		S-I (H-1 Engines)*	S-IVB (J-2 Engine)
I_n	(slug-ft^2)	1015.0	2660
d	(in.)	27.5	11.625
M_L	$\frac{\text{lb-sec}^2}{\text{in}}$	16.1	117.0
l_n	(ft)	2.657	2.425
K_1	(1/sec)	17.142	18.76
K_2	(in/lb)	0.704437×10^{-5}	0.6573×10^{-5}
K_o	(lb/in)	4.35×10^5	12.889×10^5
K_L	(lb/in)	0.668×10^5	3.9101×10^5
B	(lb-sec/in)	116.0	538
ω_2	(rad/sec)	20.0	12.0

*H-1 Engine data is only for one engine.

Table D-5

Thrust Vector Control System Transfer Function

TVC System	$\frac{\delta}{\delta_c}(s)$	Approximated $\frac{\delta}{\delta_c}(s)$
S-I	$\frac{\left(\frac{s}{20}+1\right)}{\left(\frac{s}{20.674}+1\right)\left(\frac{s}{16.770}+1\right)\left(\frac{s}{5.8073 \pm j\,127.45}+1\right)}$	$\frac{\left(\frac{s}{20}+1\right)}{\left(\frac{s}{20.674}+1\right)\left(\frac{s}{16.770}+1\right)}$
S-IVB	$\frac{\left(\frac{s}{12}+1\right)}{\left(\frac{s}{10.285}+1\right)\left(\frac{s}{35.583}+1\right)\left(\frac{s}{9.050 \pm j\,38.671}+1\right)}$	$\frac{\left(\frac{s}{12}+1\right)}{\left(\frac{s}{10.285}+1\right)\left(\frac{s}{35.583}+1\right)}$

Note: The effect of engine reaction is neglected.

S-IB actuator limit ±8°
actuation rate limit ±24°/sec

S-IVB actuator limit ±7°
actuation rate limit ±8°/sec

APPENDIX E

SATURN V (VOYAGER PAYLOAD) CONTROL SYSTEM DATA

1. INTRODUCTION

Appendix E contains data necessary for the analysis of the Saturn V control system and the Voyager spacecraft. Figure E-1 shows the general Saturn V vehicle configuration with the Voyager payload. Section 3 presents the fuel sloshing data for this vehicle configuration. Vehicle bending data is given in Reference E-1. Section 3 presents data on the Saturn V thrust vector control (TVC) system for the S-IC, S-II and S-IVB stages. Controls data for the Voyager spacecraft is presented in Section 4.

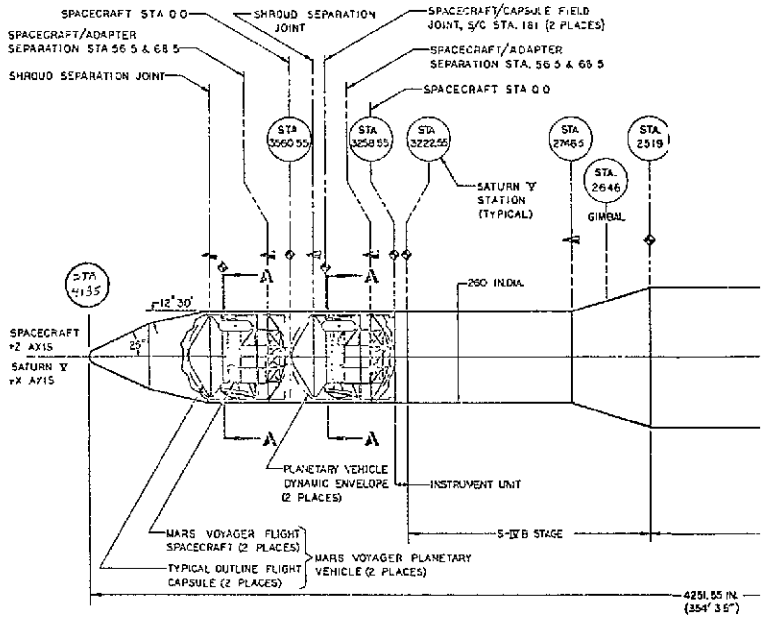

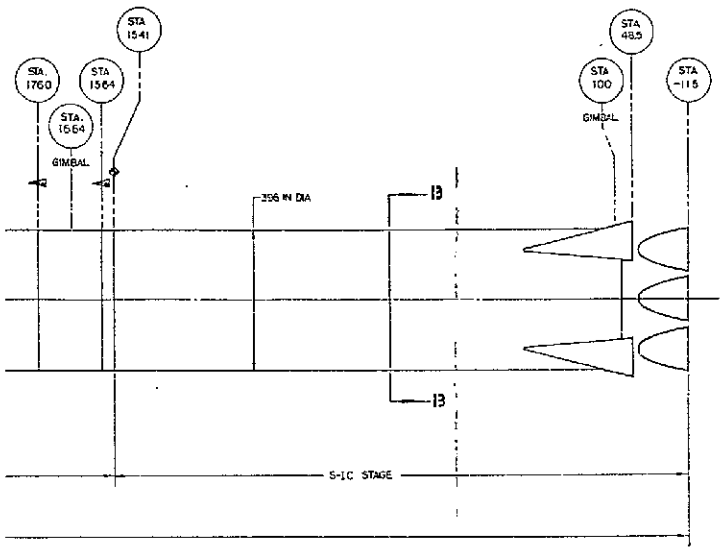

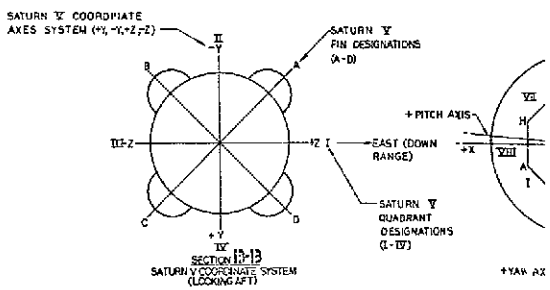

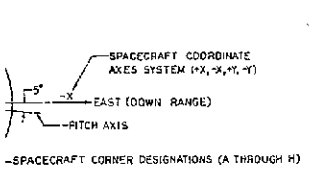

NOTES:
- FIELD SPLICE
- SEPARATION

ALL DIMENSIONS ARE IN INCHES

Figure E-1. Saturn V (Voyager Payload) Vehicle Configuration

FOLDOUT FRAME

2. PROPELLANT SLOSHING DATA

Propellant sloshing data for the Saturn V vehicle is given in Figures E-2 through E-4.

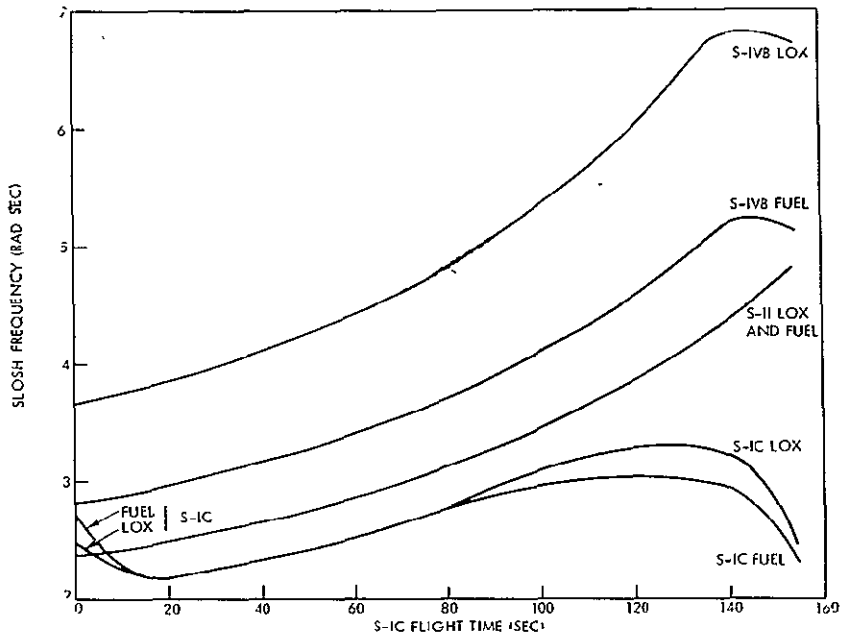

Figure E-2. Slosh Frequencies Versus Flight Time

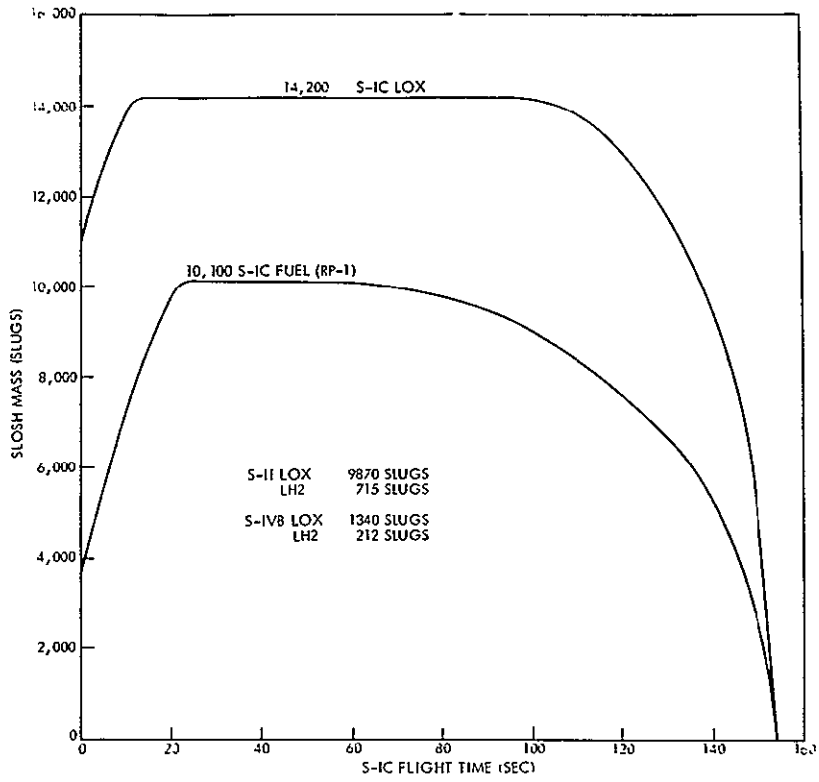

Figure E-3. Slosh Masses Versus Flight Time

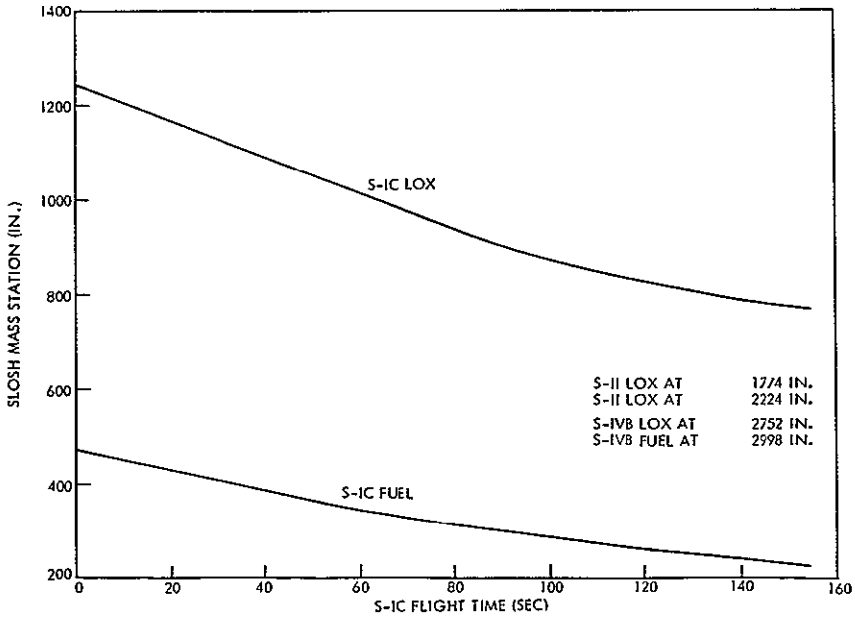

Figure E-4. Slosh Mass Stations Versus Flight Time

3. SATURN V THRUST VECTOR CONTROL SYSTEM DATA

3.1 SATURN V CONTROL COMPUTER FREQUENCY RESPONSE

The Saturn V control computer mixing amplifier has a frequency response as shown in Figure E-5. The linear equation that describes this response is as follows:

$$\frac{I_o}{I_{in.}} = \frac{1666.}{\left[\frac{S^2}{(396)^2} + \frac{1.70}{(396)} S + 1\right]}$$

$I_{in.}$ = Input current in mA

I_o = Servovalve or output current in mA

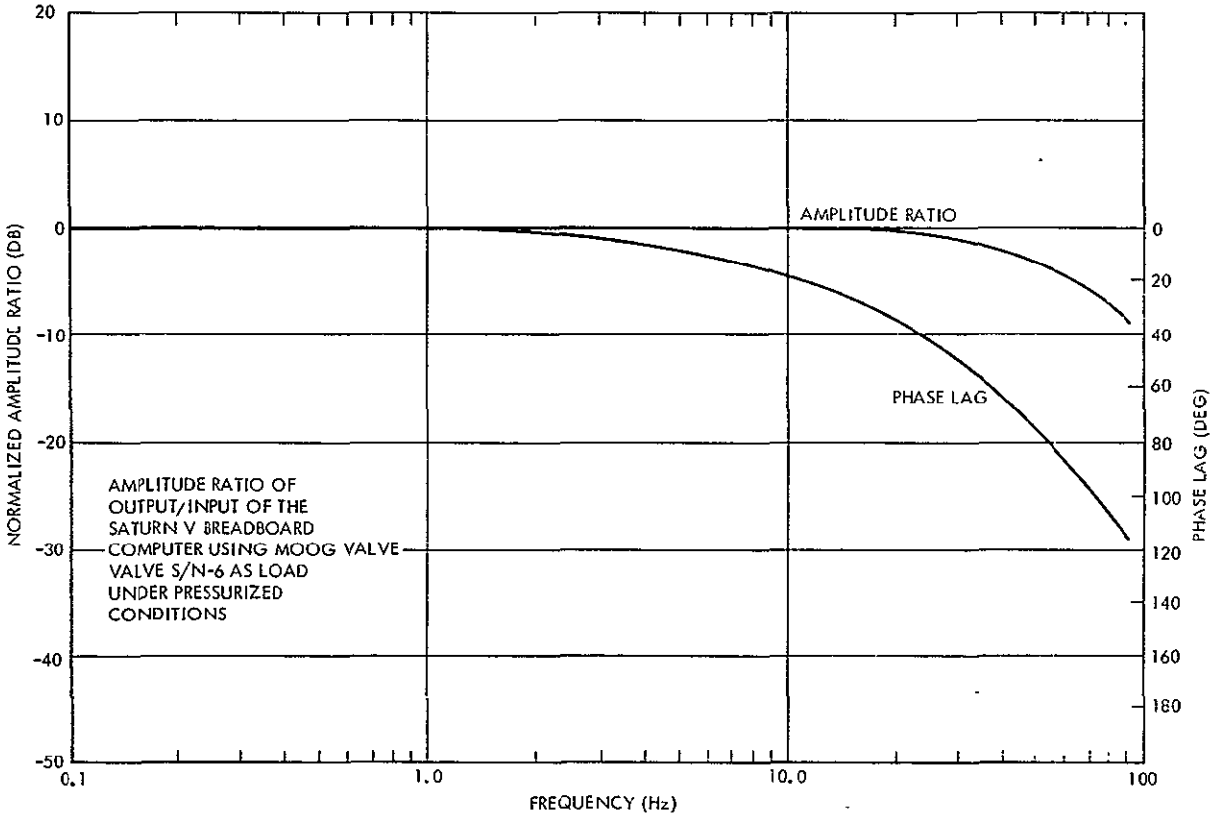

Figure E-5. Saturn V Control Computer Mixing Amplifier Frequency Response

3.2 S-IC STAGE TVC DATA

The linear block diagram for the S-IC stage TVC system is shown in Figure E-6. The nonlinear block diagram and system parameters are shown in Figure E-7 and Table E-1, respectively. The frequency response and time response specifications are shown in Figures E-8, E-9, and E-10.

The linear equation describing the S-IC Stage thrust vector control system is as follows:

$$\frac{\beta_e}{\beta_c} = \left\{ \frac{0.1036\,(0.25\,S + 1)}{\left[\frac{S}{4.023} + 1\right]\left[\frac{S^2}{(34.48)^2} + \frac{2(0.434)S}{34.48} + 1\right]} \right\} \times \left\{ \frac{1}{\left[\frac{S^2}{(84.09)^2} + \frac{2(0.594)S}{84.09} + 1\right]\left[\frac{S^2}{(409.68)^2} + \frac{2(0.946)S}{409.68} + 1\right]} \right\}$$

where:

β_e is in degrees

β_c is in milliamperes

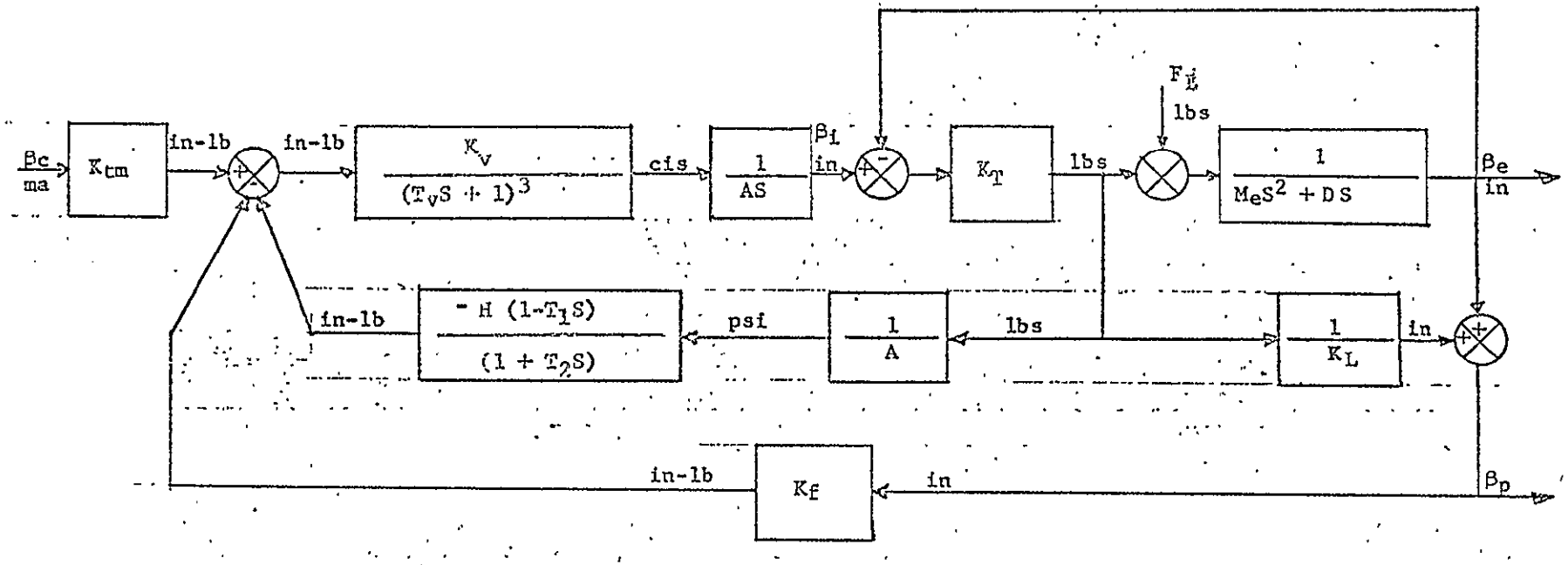

K_{tm}	0.04 in-lb/ma	M_e	94.5 lb-sec^2/in	δe_{max}	= 5.15 deg
K_v	2940 cis/in-lb	D	505 lb-sec/in	$\dot{\delta} e_{max}$	= 7 deg/sec
T_v	3.32×10^{-3} sec	H	6.03688×10^{-5} in-lb/psi	R_n	= 5.31 ft
A	57 in^2	T_i	0.53 sec	I_n	= 56,760 slug ft^2
K_T	205,000 lbs/in	T_2	0.25 sec	$\omega_{DWT} = \omega_n$	= 38 rad/sec
K_L	239,000 lbs/in	K_f	0.3479 in-lb/in	ω_{TWD}	= 24 rad/sec

Figure E-6. S-IC Stage Thrust Vector Control System Block Diagram and System Parameters

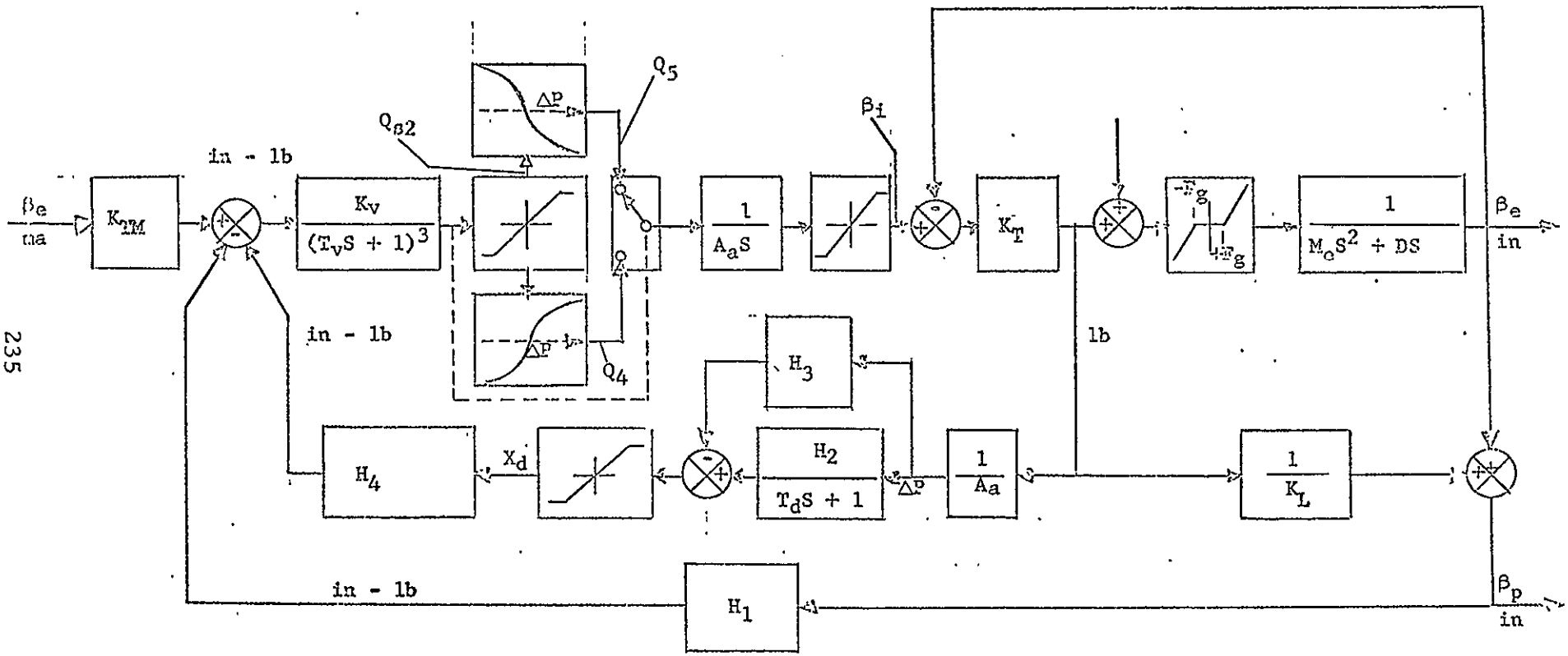

Figure E-7. S-IC Stage Thrust Vector Control System Nonlinear Block Diagram

Table E-1

S-IC Parameters

$K_{TM} = 0.04 \frac{\text{in.-lb}}{\text{ma}}$

$K_v = 2940 \frac{\text{cis}}{\text{in.-lb}}$

$T_v = 3.32 \times 10^{-3}$ sec

$T_d = 0.25$ sec

$H_1 = 0.3479 \frac{\text{in.-lb}}{\text{in.}}$

$H_2 = 3.69 \times 10^{-5} \frac{\text{in.}}{\text{psi}}$

$H_3 = 2.51 \times 10^{-5} \frac{\text{in.}}{\text{psi}}$

$H_4 = 5.116 \frac{\text{in.-lb}}{\text{in.}}$

$A_a = 57 \text{ in.}^2$

$M_e = 94.5 \frac{\text{lb-sec}^2}{\text{in.}}$

$D = 505 \frac{\text{lb-sec}}{\text{in.}}$

$P_S = 1800$ psi (nom)

$K_L = 239,000 \frac{\text{lb}}{\text{in.}}$

$K_T = 205,000 \frac{\text{lb}}{\text{in.}}$

(X_a) max. $= \pm 0.05$ in.

(Q_{s2}) max. $= \pm 740$ cis

(β_i) max. $= \pm 5.74$ in.

$F_g = 12,000$ lb

$F_L = 66,000 + 30,000 \sin (500\ t)$

$$\frac{Q_4}{Q_{s2}} = \frac{-(\Delta P - P_s)}{|\Delta P - P_s|} \left| \frac{\Delta P}{P_s} - 1 \right|^{1/2}$$

$$\frac{Q_5}{Q_{s2}} = \frac{(\Delta P + P_s)}{|\Delta P - P_s|} \left| \frac{\Delta P}{P_s} + 1 \right|^{1/2}$$

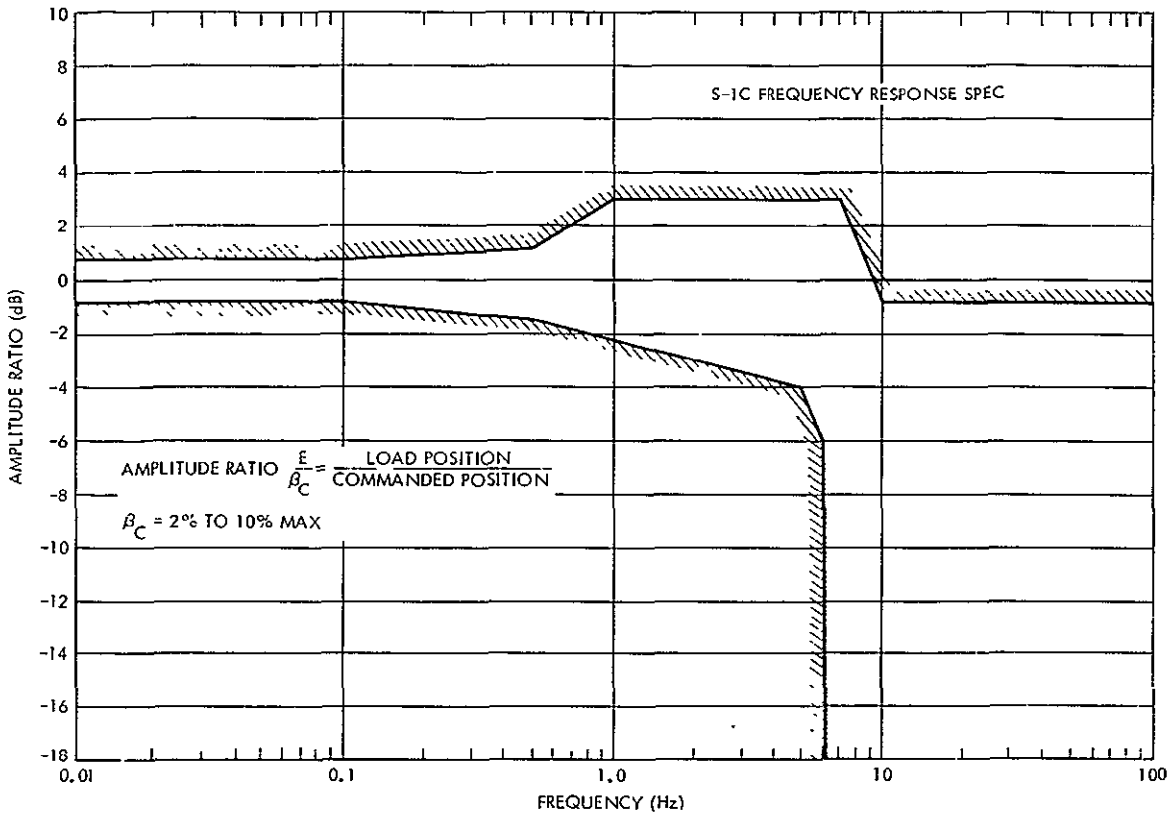

Figure E-8. S-IC Frequency Response Specification (amplitude ratio)

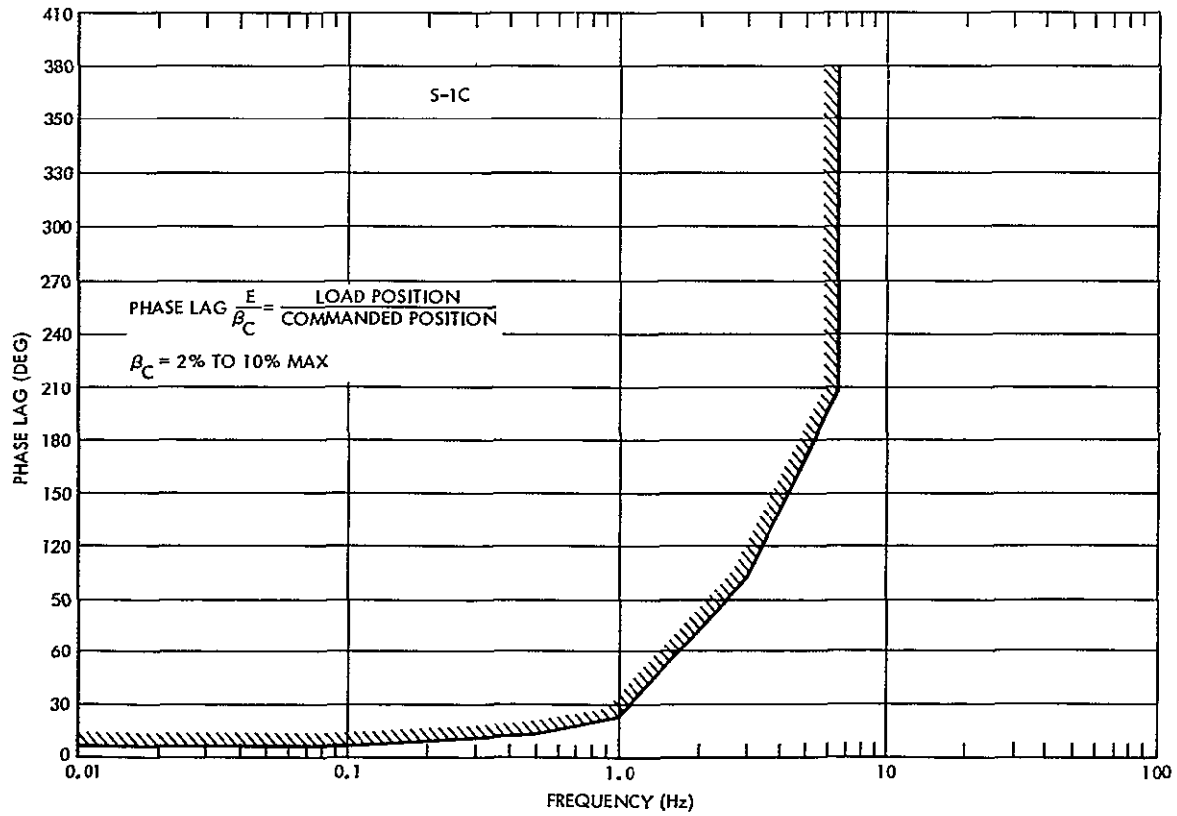

Figure E-9. S-IC Frequency Response Specification (phase lag)

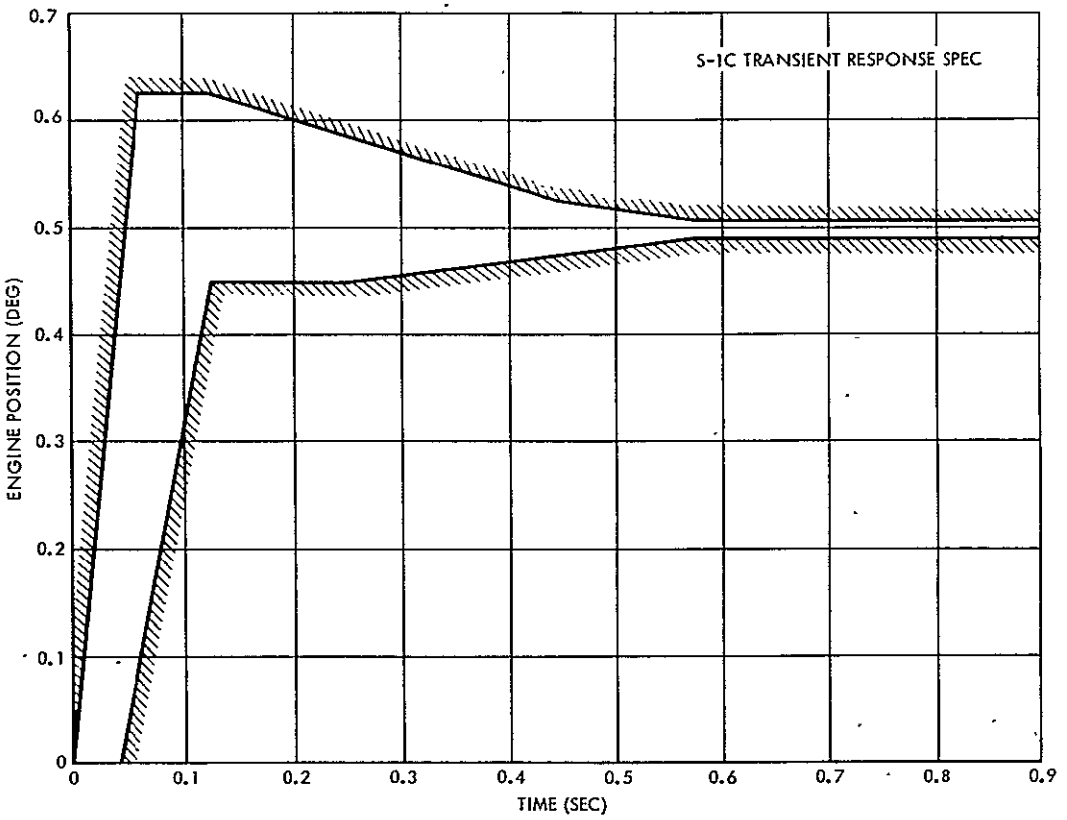

Figure E-10. S-IC Time Response Specification

3.3 S-II STAGE TVC DATA

The linear block diagram for the S-II Stage TVC system is shown in Figure E-11. The nonlinear block diagram and system parameters are shown in Figure E-12 and Table E-2, respectively. The frequency response specification is shown in Figure E-13.

The linear equation describing the S-II Stage thrust vector control system is as follows:

$$\frac{\beta_e}{\beta_c} = \left\{ \frac{0.159\ [0.08\,S + 1]}{\left[\frac{S}{11.02} + 1\right]\left[\frac{S}{421} + 1\right]\left[\frac{S^2}{(33.73)^2} + \frac{2(0.399)S}{33.22} + 1\right]} \right\} \times \left\{ \frac{1}{\left[\frac{S^2}{(94.22)^2} + \frac{2(0.987)S}{94.22} + 1\right]} \right\}$$

where:

β_e is in degrees

β_c is in milliamperes

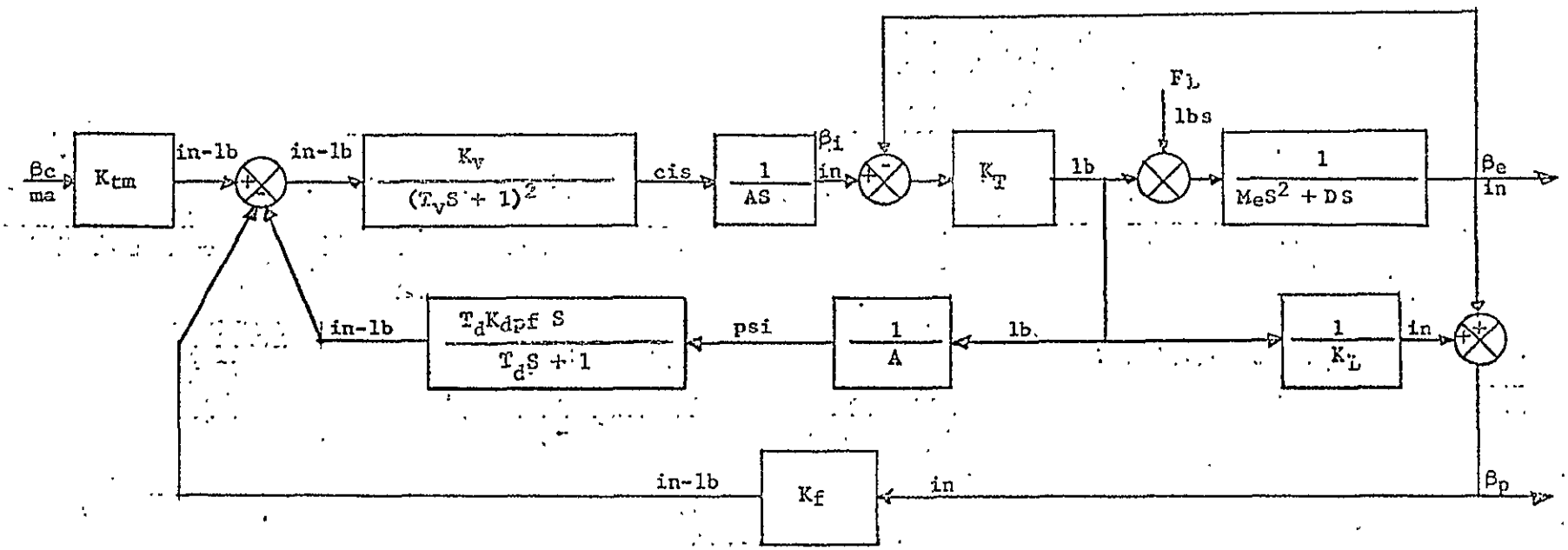

K_{tm} ---------- 0.035 in - lb/ma

K_v ---------- 220 cis/in - lb

T_v ---------- 3.18×10^{-3} sec

A ---------- 13 in^2

K_T ---------- 260,000 lb/in

K_L ---------- 312,000 lb/in

M_e ---------- 125 lb - sec^2/in

D ---------- 625 lb - sec/in

T_d ---------- 0.08 sec

K_{dpf} ---------- 10×10^{-5} in - lb/psi

K_f ---------- 1.06 in - lb/in

δe_{max} = 7 deg

$\dot{\delta} e_{max}$ = 9.6 deg/sec

R_n = 0.991 ft

I_n = 2690 slug ft^2

$\omega_{DWT} = \omega_n$ = 34 rad/sec

ω_{TWD} = 24 rad/sec

Figure E-11. S-II Linear Thrust Vector Control System Block Diagram and System Parameters

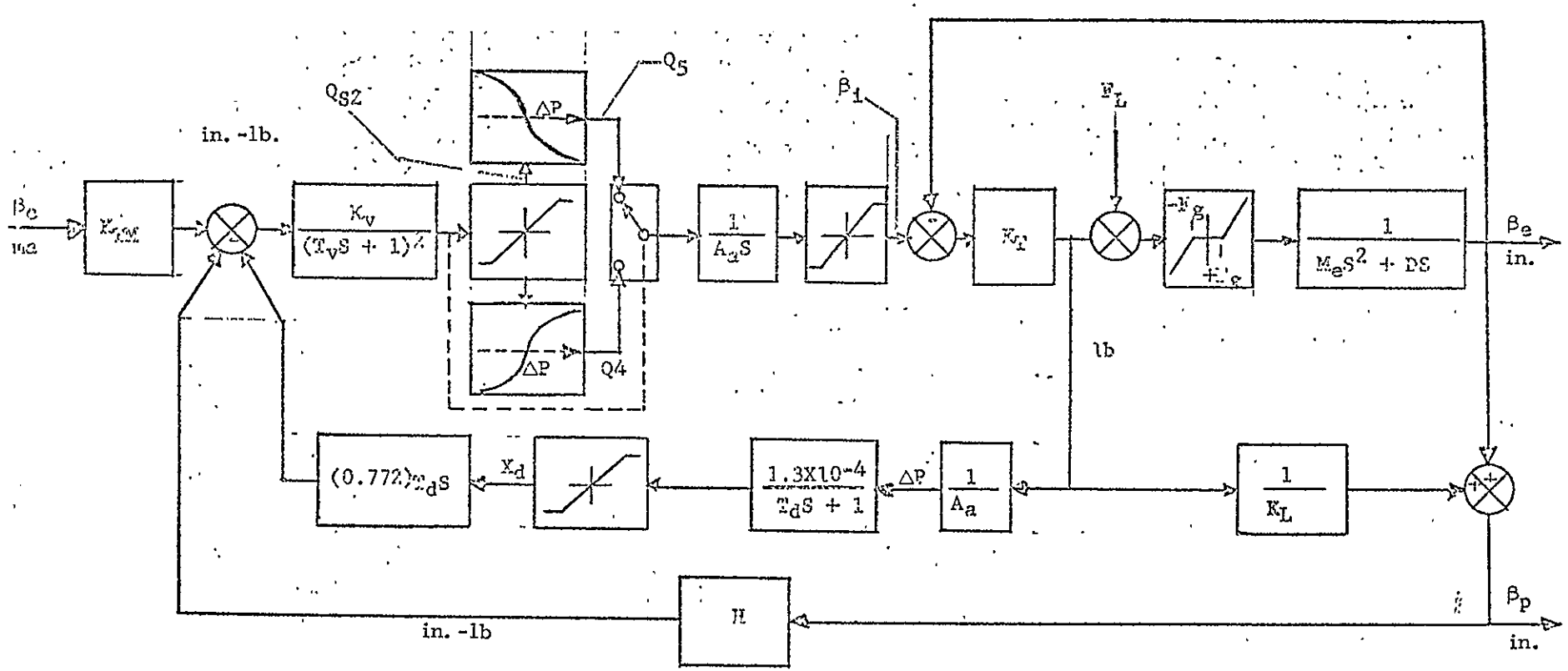

Figure E-12. S-II Thrust Vector Control System Nonlinear Block Diagram

Table E-2

S-II TVC System Block Diagram Parameters

$K_{TM} = 0.035 \frac{\text{in.-lb}}{\text{mA}}$

$K_v = 220 \frac{\text{cis}}{\text{in.-lb}}$

$T_v = 3.18 \times 10^{-3}$ sec

$T_d = 8 \times 10^{-2}$ sec

$H = 1.06 \frac{\text{in.-lb}}{\text{in.}}$

$A_a = 13 \text{ in.}^2$

$M_e = 125 \frac{\text{lb-sec}^2}{\text{in.}}$

$D = 625 \frac{\text{lb-sec}}{\text{in.}}$

$P_s = 3500$ psi (nom)

$K_L = 312,000$ lb/in.

$K_T = 260,000$ lb/in.

(X_d) max. $= \pm 0.26$ in.

(Q_{s2}) max. $= \pm 71$ cis

(β_i) max. $= \pm 1.51$ in.

$F_g = 9000$ lb

$F_L = 20,000 + 40,000 \sin (500\, t)$

$$\frac{Q_5}{Q_{s2}} + \frac{(\Delta P + P_s)}{|\Delta P + P_s|} \left| \frac{\Delta P}{P_s} + 1 \right|^{1/2}$$

$$\frac{Q_4}{Q_{s2}} = \frac{-(\Delta P - P_s)}{|\Delta P - P_s|} \left| \frac{\Delta P}{P_s} - 1 \right|^{1/2}$$

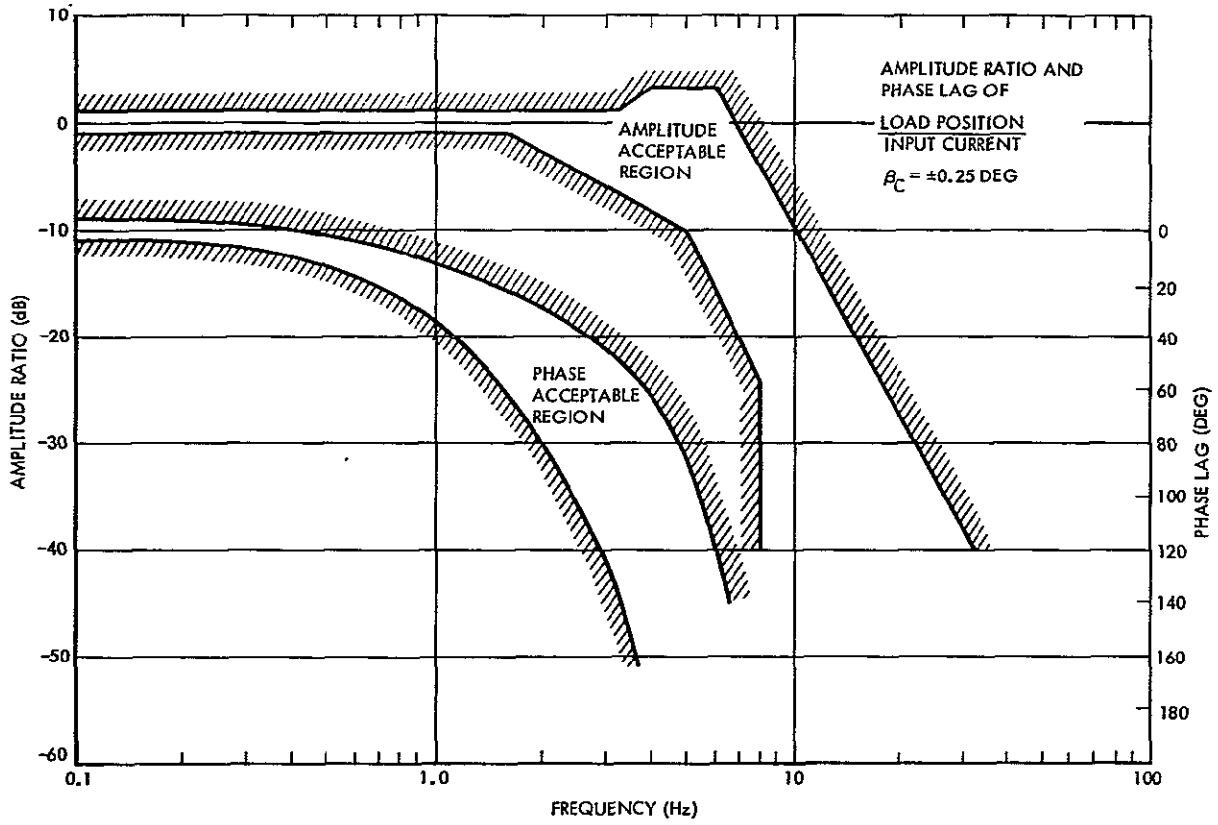

Figure E-13.1 S-II Frequency Response Specification

3.4 S-IVB STAGE TVC DATA

The linear block diagram for the S-IVB Stage TVC system is shown in Figure E-14 The nonlinear block diagram and system parameters are shown in Figure E-15 and Table E-3, respectively. The frequency response specification is shown in Figure E-16.

The linear equation describing the S-IVB Stage thrust vector control system is as follows:

$$\frac{\beta_e}{\beta_c} = \left\{ \frac{0.1496\ [0.08\,S + 1]}{\left[\frac{S}{32.257} + 1\right]\left[\frac{S}{10.49} + 1\right]\left[\frac{S}{405} + 1\right]} \right\} \times \left\{ \frac{1}{\left[\frac{S}{174} + 1\right]\left[\frac{S^2}{(34.68)^2} + \frac{2(0.327)}{(34.68)}\,S + 1\right]} \right\}$$

where:

β_e is in degrees

β_c is in milliamperes

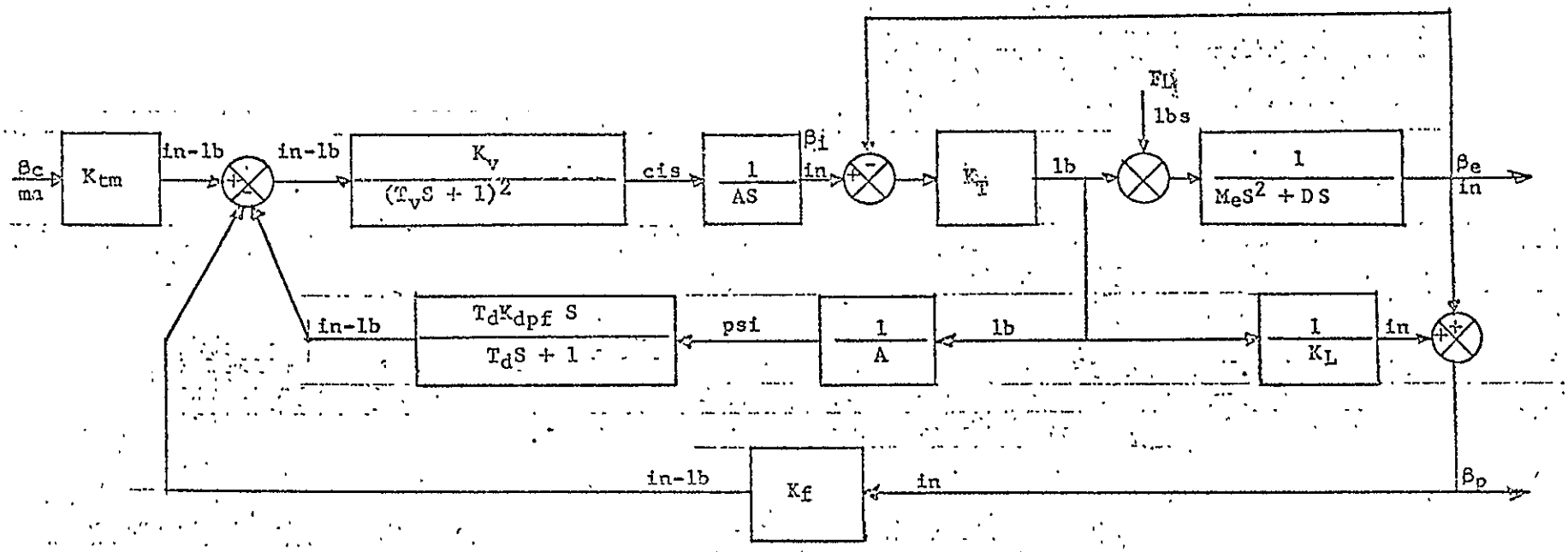

K_{tm} ---------- 0.035 in - lb/ma

K_v ---------- 149.5 cis/in - lb

T_v ---------- 3.18×10^{-3}

A ---------- 11.78 in^2

K_T ---------- 233,000 lb/in

K_L ---------- 284,000 lb/in

M_e ---------- 125 $lb\text{-}sec^2/in$

D ---------- 538. lb-sec/in

T_d ---------- 0.08 sec.

K_{dpf} ---------- 10×10^{-5} in-lb/psi

K_f ---------- 1.129 in-lb/in

R_n = 0.966 ft

I_n = 2660 slug ft^2

$\omega_{DWT} = \omega_n$ = 31 rad/sec

ω_{TWD} = 24 rad/sec

Figure E-14. S-IVB Linear Thrust Vector Control System Block Diagram and System Parameters

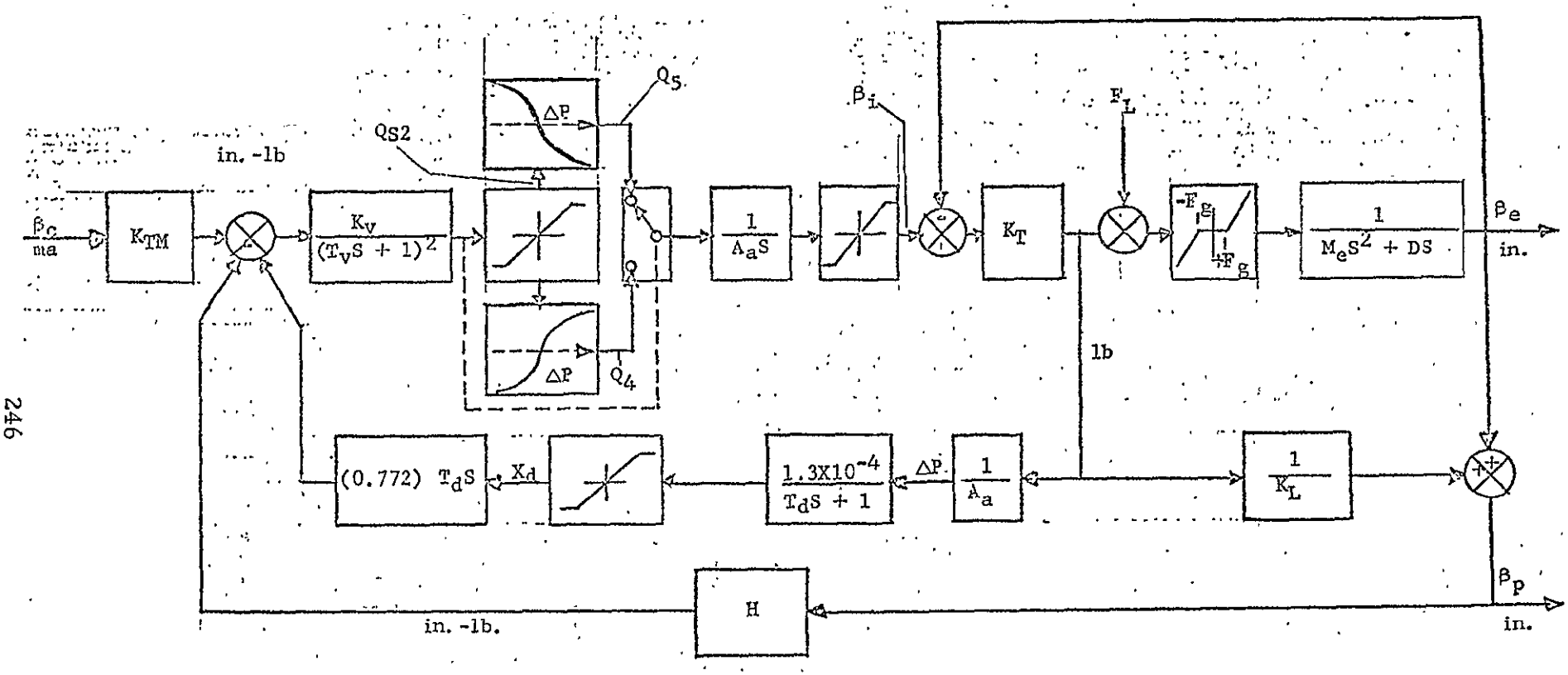

Figure E-15. S-IVB Thrust Vector Control System
Nonlinear Block Diagram

Table E-3

S-IVB TVC System Block Diagram Parameters

$K_{TM} = 0.035 \frac{\text{in.-lb}}{\text{mA}}$

$K_v = 149.5 \frac{\text{cis}}{\text{in.-lb}}$

$T_v = 3.18 \times 10^{-3}$ sec

$T_d = 8 \times 10^{-2}$ sec

$H = 1.129 \frac{\text{in.-lb}}{\text{in.}}$

$A_a = 11.78 \text{ in.}^2$

$M_e = 125.1 \frac{\text{lb-sec}^2}{\text{in.}}$

$D = 538 \frac{\text{lb-sec}}{\text{in.}}$

$P_s = 3650$ psi (nom)

$K_L = 284,000$ lb/in.

$K_T = 233,000$ lb/in.

(X_d) max. $= \pm 0.26$ in.

(Q_{s2}) max. $= \pm 40.4$ cis

(β_i) max. $= \pm 1.45$ in.

$F_g = 9000$ lb

$F_L = 15,000 + 30,000 \sin (500\, t)$

$$\frac{Q_5}{Q_{s2}} = \frac{(\Delta P + P_s)}{|\Delta P + P_s|} \left| \frac{\Delta P}{P_s} + 1 \right|^{1/2}$$

$$\frac{Q_4}{Q_{s2}} = \frac{-(\Delta P - P_s)}{|\Delta P - P_s|} \left| \frac{\Delta P}{P_s} - 1 \right|^{1/2}$$

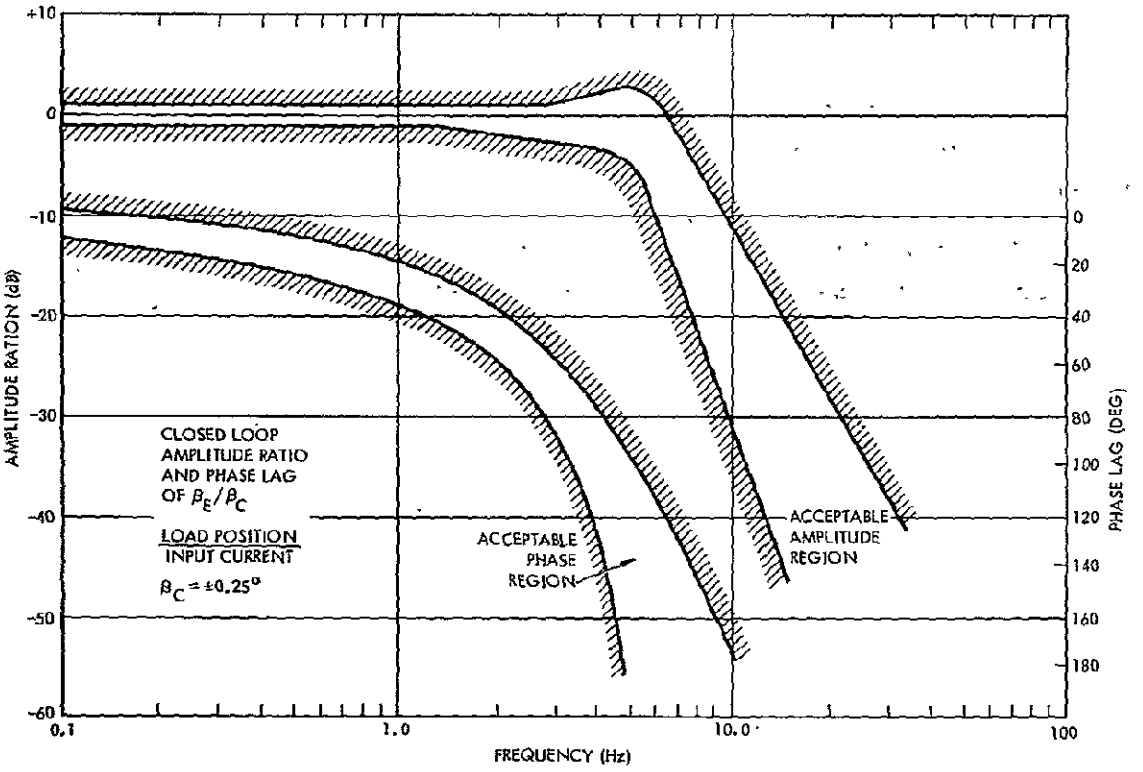

Figure E-16. S-IVB Frequency Response Specification

4. VOYAGER SPACECRAFT DATA

Control system terminology used in analyzing the Voyager control system is given in Table E-4. Values of the control system parameters are given in Tables E-5 and E-6 for two spacecraft configurations (capsule on and off) for four different times of flight during the interplanetary phase.

The Voyager powered flight linear actuation control system model is given in Figure E-17 and the associated data in Table E-7.

Table E-4

Voyager Analysis Data Terminology

Mass Parameters

I = vehicle moment of inertia, slug ft^2

M = vehicle mass, slugs

Engine Parameters

T = engine thrust, lb

M_e = engine mass, slugs

L_e = distance between engine c.g., and engine gimbal, ft

L_T = distance between engine gimbal and vehicle c.g., ft

I_H = inertia of engine about the gimbal point, slug ft^2

Slosh Parameters

L_{BO}, L_{BF}, L_{CO}, L_{CF} = bus and capsule, fuel and oxidizer, slosh mass distances from vehicle c.g., (positive aft of c.g., towards gimbal), ft

M_{BO}, M_{BF}, M_{CO}, M_{CF} = slosh masses, slugs

K_{BO}, K_{BF}, K_{CO}, K_{CF} = slosh mode spring constants, $lb\text{-}ft^{-1}$

ω_{BO}, ω_{BF}, ω_{CO}, ω_{CF} = slosh mode frequencies, rad/sec

ζ_{BO}, ζ_{BF}, ζ_{CO}, ζ_{CF} = slosh mode damping, no dimensions

Bending Parameters

M_1, M_2, M_3, M_4 = bending mode masses (four modes), slugs

ω_1, ω_2, ω_3, ω_4 = bending mode frequencies, rad/sec

ζ_1, ζ_2, ζ_3, ζ_4 = bending mode damping, no dimensions

ϕ_{1T}, ϕ_{2T}, ϕ_{3T}, ϕ_{4T} = bending displacements at the gimbal point (positive values), ft

ϕ_{1T}', ϕ_{2T}', ϕ_{3T}', ϕ_{4T}' = bending slopes at the gimbal point (positive values), ft/ft

Table E-4

Voyager Analysis Data Terminology (con't)

ϕ_{BO1}, ϕ_{BO2}, ϕ_{BO3}, ϕ_{BO4}	= bending displacements at bus oxidizer slosh mass station, ft
ϕ_{BF1}, ϕ_{BF2}, ϕ_{BF3}, ϕ_{BF4}	= bending displacements at bus fuel slosh
ϕ_{CO1}, ϕ_{CO2}, ϕ_{CO3}, ϕ_{CO4}	= bending displacements at capsule oxidizer slosh mass station, ft
$\phi_{1\dot{G}}$, $\phi_{2\dot{G}}$, $\phi_{3\dot{G}}$, $\phi_{4\dot{G}}$	= bending slopes at the position gyro station, ft/ft

Variables

θ	rigid body vehicle attitude angle, rad
λ_{BO}	bus oxidizer slosh mass displacement, ft
λ_{BF}	bus fuel slosh mass displacement, ft
λ_{CO}	capsule oxidizer slosh mass displacement, ft
λ_{CF}	capsule fuel slosh mass displacement, ft
Q_1	first bending mode amplitude, rad
Q_2	second bending mode amplitude, rad
Q_3	third bending mode amplitude, rad
Q_4	fourth bending mode amplitude, rad
δ	engine displacement angle, rad
δ_C	engine command angle, rad
θ_e	attitude error angle, rad
θ_C	integrator feedback attitude command, rad

Station Numbers

Engine gimbal point	111 in.
Bottom of bus propellant tanks	118.25 in.
Gyro location	136 in.
Capsule slosh mass attach points	280 in.

Table E-5

Voyager Spacecraft Data
Parameter Values, Vehicle With Capsule On.

	MCC	Start MOI	End MOI	MOT
I, slug ft^2	26,157	26,623	19,094	19,094
M, slugs	636	595	286	286
T, lb	1,050	7,750	7,750	1,050
M_e, slugs	12.4	12.4	12.4	12.4
L_e, ft	1.88	1.88	1.88	1.88
L_T, ft	4.91	4.91	4.91	4.91
I_H, slug ft^2	50	50	50	50
$L_{BO} = L_{BF}$, ft	1.68	1.68	5.8	5.8
$L_{CO} = L_{CF}$, ft	-9.15	-9.15	-7.35	-7.35
M_{BO}, slugs	75.6	75.6	6.23	6.23
M_{BF}, slugs	47.2	47.0	3.87	3.87
M_{CO}, slugs	2.7	2.7	2.7	2.7
M_{CF}, slugs	0.9	0.9	0.9	0.9
K_{BO}, lb-ft	105	840	76	10.4
K_{BF}, lb-ft	66	555	47	6.4
K_{CO}, lb-ft	9.7	78	160	22
K_{CF}, lb-ft	3.2	26	53	7.4
$\omega_{BO} = \omega_{BF}$, rad/sec	1.18	3.35	3.48	1.29
ω_{CO}, rad/sec	1.89	5.37	7.69	2.87
ω_{CF}, rad/sec	2.30	6.55	9.40	3.49
$\zeta_{BO} = \zeta_{BF}$	0.001	0.001	0.001	0.001
$\zeta_{CO} = \zeta_{CF}$	0.01	0.01	0.01	0.01

Table E-5

Voyager Spacecraft Data
Parameter Values, Vehicle With Capsule On (con't)

	MCC	Start MOI	End MOI	MOT
$M_1 = M_2 = M_3 = M_4$, slug ft^2	1	1	1	1
ω_1, rad/sec	24.70	24.70	24.95	24.95
ω_2, rad/sec	24.97	24.97	25.16	25.16
ω_3, rad/sec	37.50	37.50	39.21	39.21
ω_4, rad/sec	47.13	47.13	47.89	47.89
$\zeta_1 = \zeta_2 = \zeta_3 = \zeta_4$	0.01	0.01	0.01	0.01
ϕ_{1T}, ft	0.00506	0.00506	0.0117	0.0117
ϕ_{2T}, ft	0.00216	0.00216	0.00431	0.00431
ϕ_{3T}, ft	0.00347	0.00347	0.00958	0.00958
ϕ_{4T}, ft	0.00262	0.00262	0.00706	0.00706
$\phi_{1\dot{T}}$	0.000592	0.000592	0.001089	0.001989
$\phi_{2\dot{T}}$	0.000480	0.000480	0.00070	0.00070
$\phi_{3\dot{T}}$	0.000254	0.000254	0.00068	0.00068
$\phi_{4\dot{T}}$	0.000543	0.000543	0.00094	0.00094
$\phi_{BO1} = \phi_{BF1}$, ft	0.00353	0.00353	0.00885	0.00885
$\phi_{BO2} = \phi_{BF2}$, ft	0.000092	0.000092	0.0025	0.0025
$\phi_{BO3} = \phi_{BF3}$, ft	0.00282	0.00282	0.00781	0.00781
$\phi_{BO4} = \phi_{BF4}$, ft	0.00122	0.00122	0.0046	0.0046
ϕ_{CO1}, ϕ_{CF1}, ft	-0.00332	-0.00332	-0.00366	-0.00366
ϕ_{CO2}, ϕ_{CF2}, ft	-0.00466	-0.00466	-0.0056	-0.0056
ϕ_{CO3}, ϕ_{CF3}, ft	-0.000025	-0.000025	0.00013	0.00013
ϕ_{CO4}, ϕ_{CF4}, ft	-0.00525	-0.00525	-0.00648	-0.00648

Table E-5

Voyager Spacecraft Data
Parameter Values, Vehicle With Capsule On (con't)

	MCC	Start MOI	End MOI	MOT
$\phi_{1\dot{G}}$	0.000595	0.000595	0.00109	0.00109
$\phi_{2\dot{G}}$	0.00048	0.00048	0.000070	0.000070
$\phi_{3\dot{G}}$	0.00025	0.00025	0.000068	0.000068
$\phi_{4\dot{G}}$	0.00054	0.00054	0.000094	0.000094
$\phi_{3\dot{T}}$	0.00129	0.00129	0.00172	0.00172
$\phi_{BO1} = \phi_{BF1}$, ft	0.0058	0.0058	0.01112	0.01112
$\phi_{BO2} = \phi_{BF2}$, ft	0.00348	0.00348	0.00107	0.00107
$\phi_{BO3} = \phi_{BF3}$, ft	0.00382	0.00382	0.00118	0.00118
$\phi_{1\dot{G}}$	0.000626	0.000626	0.00112	0.00112
$\phi_{2\dot{G}}$	0.00159	0.00159	0.00137	0.00137
$\phi_{3\dot{G}}$	0.00129	0.00129	0.00172	0.00172

MCC duration ≈ 380 sec for Mars arrival separation

MOI duration ≈ 380 sec

MOT duration ≈ undetermined

Table E-6

Voyager Spacecraft Parameter Values, Vehicle with Capsule Off

	MCC	Start MOI	End MOI	MOT
I, slug-ft^2	14,500	13,523	4,547	4,547
M, slugs	550	500	208	208
T, lb	1,040	7,750	7,750	1,040
M_e, slugs	12.4	12.4	12.4	12.4
L_e, ft	3.19	3.05	2.5	2.5
L_T, ft	3.19	3.05	2.5	2 5
I_H, slug ft^2	50	50	50	50
$L_{BO} = L_{BF}$, ft	0.995	1.142	1.71	1.71
M_{BO}, slugs	75.6	75.6	6.23	6.23
M_{BF}, slugs	47.2	47.0	3.87	3.87
K_{BO}, slugs	121	997	104	14
K_{BF}, slugs	76	624	63	8.7
$\omega_{BO} = \omega_{BF}$, rad/sec	1.26	3.65	4.07	1.50
$\zeta_{BO} = \zeta_{BF}$	0.001	0.001	0.001	0.001
$M_1 = M_2 = M_3 = M_4$	1	1	1	1
ω_1, rad/sec	25.32	25.32	25.32	25.32
ω_2, rad/sec	25.76	25.76	25.76	25.76
ω_3, rad/sec	49.27	49.27	49.27	49.27
$\zeta_1 = \zeta_2 = \zeta_3$	0.01	0.01	0.01	0.01
ϕ_{1T}, ft	0.00741	0.00741	0.0140	0.0140
ϕ_{2T}, ft	0.00678	0.00678	0.00462	0.00462
ϕ_{3T}, ft	0.00118	0.00118	0.00563	0.00563
ϕ_{1T}'	0.000626	0.000626	0.00112	0.00112
ϕ_{2T}'	0.00159	0.00159	0.00137	0.00137

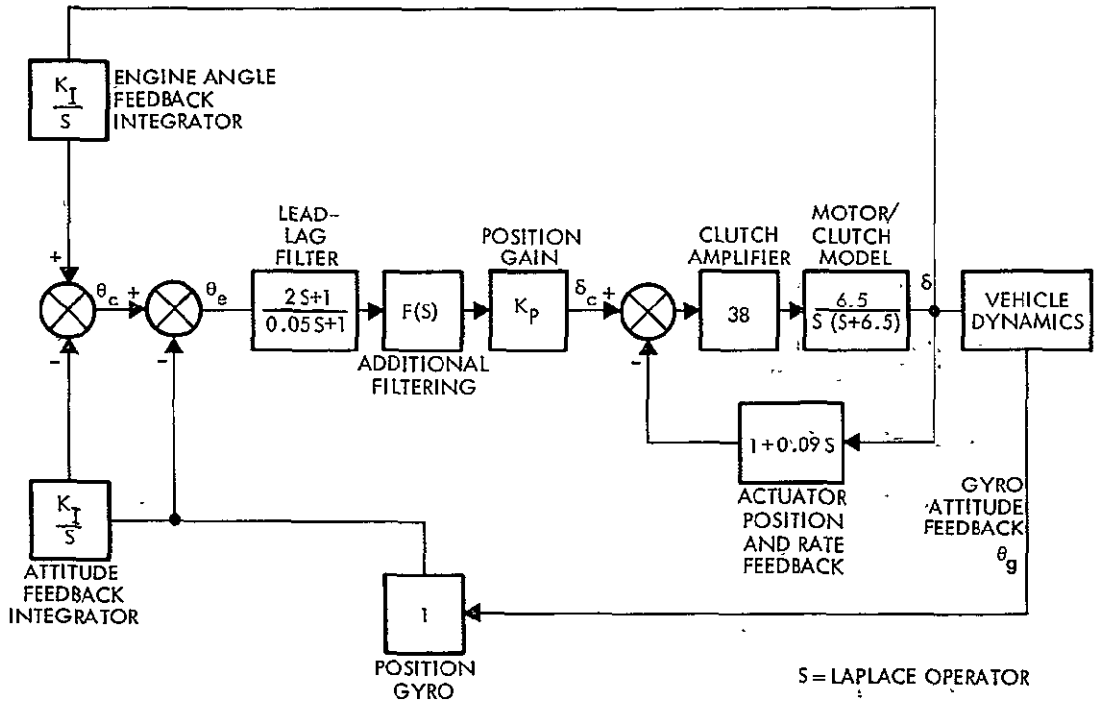

Figure E-17. Block Diagram of Voyager Powered Flight Control System Model